

報告番号 甲 1923 号

Measurement of Radiation Power from the JIPP T-IIU Tokamak Plasma

(JIPP T-IIUトカマクプラズマからの放射強度測定)

名古屋大学大学院
理学研究科物理学専攻

小川 勇

Measurement of Radiation Power from the JIPP T-IIU Tokamak
Plasma

Isamu OGAWA

名古屋大学図書	
洋	917686

Abstract

Characteristics of a pyroelectric detector, a metal-film bolometer and a thermistor are investigated in order to attain high reliability of the bolometric measurement. The spurious signal which appears on a pyroelectric detector is efficiently eliminated by setting a mask close to the detector, which has a function of avoiding the direct incidence of photons on its electrode. This is verified with the consistency of integrated value of the signal. The detector is calibrated with a HeNe laser taking the reflection on the detector surface into account. No temporal change has been seen on the sensitivity of the detector calibrated by this method. We also developed a thin metal-film bolometer with high sensitivity ($12.9 \Omega/\text{mJ}$), high time response ($3 \mu\text{s}$) and well defined thermal characteristics. The calibration of this detector was performed by supplying a bias current through its resistor. We constructed a bolometric system which consisted of twelve pyroelectric detectors and a metal-film bolometer with high time response and high spatial resolution. The radiation power measured with the pyroelectric detector agrees with that measured with the calibrated metal-film bolometer within 10 %.

Spectroscopic and bolometric measurements with spatial and temporal resolution show that large radiation loss brings about the decrease in electron and ion temperature and plasma energy.

Carbon limiters have an effect to suppress the radiation power for ohmic plasma, but are insufficient for ICRF heated plasma.

The main contribution to radiation power may be attributed to Fe impurity released from the ICRF antennae, the Faraday shield and vacuum vessel. By making carbonization of the wall and in-vessel components, the Fe impurity is suppressed to a low level ($n_{\text{Fe}}/n_e \sim 0.04 \%$) and the radiation power is reduced to $P_{\text{rad}} / (P_{\text{OH}} + P_{\text{rf}}) \sim 20 \%$ and emissivity throughout the plasma region is reduced.

This is clearly supported by the observation of Z_{eff} reduction (3.9 \rightarrow 1.2).

Acknowledgements

I must express my sincerest gratitude to Professor Junji Fujita for his continual guidance and constant encouragement during the course of this work.

For the most valuable discussions and help in experiments, I am deeply indebted to thank Professor T. Watari, Dr. K. Kawahata, Dr. K. Masai, and Dr. Y. Ogawa.

I would like to express my grateful appreciation to Dr. N. Noda, for his help in the experiments and the implementation of bolometric system.

I wish to acknowledge helpful discussion with Dr. T. Kato, and Dr. K. Sato.

Very helpful discussions with the member of the Fusion and Plasma Diagnostics Center are gratefully acknowledged.

It is a pleasure to thank the member of the JIPP T-IIU group, in particular, Professor S. Tanahashi, Professor K. Toi, and Messers Y. Kawasumi, E. Kako, R. Ando, S. Hirokura and Y. Taniguchi for operating the JIPP T-IIU device and ICRF heating system.

Table of Contents

Abstract	2
Acknowledgements	4
I Introduction	7
II Theoretical Background	14
(i) Radiation Processes and Radiative Cooling Rates	14
(ii) Measurement of Radiation Power	19
III Characteristics of Detectors	28
(i) Thermistor	28
(ii) Pyroelectric Detector	29
(iii) Metal-film Bolometer	40
(iv) Results and Discussion	51
IV Experimental Equipments for Bolometric Measurement	61
(i) JIPP T-IIU Device	61
(ii) Bolometric System	64
V Experimental Results on a Tokamak Plasma	68

(i) ICRF Heating Experiment with Stainless Steel Limiters ..	68
(ii) ICRF Heating Experiment with Carbon Limiters	70
(iii) ICRF Heating Experiment with Carbonization	77
(iv) Discussion	84
VI Summary	90
References	93

CHAPTER I

Introduction

The radiation losses from a plasma column directly dissipate electron energy and influence electron temperature and power balance in tokamak discharges.¹⁻⁶⁾ It is also associated with instabilities through an influence on the radial profile of electron temperature.⁷⁻⁹⁾

The radiation power is greatly enhanced by the presence of impurity atoms, especially high-Z impurities, because of their high radiative cooling rate.¹⁰⁻¹²⁾ Plasmas are contaminated by both light and heavy elements released from the wall and the limiters. Current research in nuclear fusion is directed towards reduction in the high-Z contamination of the plasma. In recent years, high power ICRF heating experiments up to MW level have been carried out to realize high temperature plasmas. This heating technique has an advantage of having good efficiency for ion heating.¹³⁻¹⁶⁾ However, it has been reported that RF heating brings a relatively large impurity contamination compared to other heating techniques.^{17,18)} Successful heating depends entirely on the effective reduction in the impurity contamination.

A good understanding of the mechanism of impurity production and the origin of impurity is absolutely necessary to find a method to reduce impurity contamination. Several investigations on these problems have been described in the literatures.¹⁹⁻²³⁾ The origin of impurity can be identified by changing the material of in-vessel components. Reduction in the impurity contamination is attempted by replacing high-Z material by low-Z material which has less contribution to the increase in the radiation power. The use of carbon limiter and carbon coating (carbonization) of in-vessel components attract attention recently, because the limiter material and the surface condition of in-vessel components play a critical role in the impurity production.

A discharge using tungsten limiters suffered from serious central radiation cooling.²⁾ Carbon limiters have been found to reduce radiation power from a core plasma.^{20,24)} Furthermore, carbon coating (carbonization)²⁵⁻²⁸⁾ is taken to be a promising method to reduce metal impurity contamination. The effects of low-Z limiter and carbonization on ICRF heated plasma are important subject to be investigated.

Information on the radiation power due to impurity is obtained from spectroscopic^{3,29)} and bolometric^{3,5,29)} measurements. The former method requires information concerning the plasma parameters, namely, the intensity of the impurity lines and the electron density and temperature. On the contrary,

the latter method gives direct results, provided that the power due to charge-exchanged neutral particles can be estimated. In addition, the bolometric system with multichannel detectors gives the information with temporal and spatial resolution in a single discharge.

Investigation on impurities responsible to radiation loss was performed in ohmically heated plasma.³⁾ However, impurity identification in ICRF heated plasma has not been obtained in spite of a great necessity. There is very little quantitative information on the effect of carbonization.

The first bolometric measurement of a tokamak plasma was reported by L.L. Gorelik, et al,^{30,31)} but without spatial resolution. The measurement with spatial resolution was carried out in the TFR tokamak³²⁾ and the DIVA tokamak.³⁾ The quantitative correlation between bolometric and spectroscopic measurements has been obtained in the DIVA tokamak. The spatial information of the radiation power was obtained by scanning the plasma on a shot-to-shot basis, reproducibility of the discharge being an important factor. From the standpoint of reproducibility and the comparison with spectroscopic measurements, it is desired that information is obtained in a single discharge. In the Alcator tokamak,⁵⁾ four collimated bolometers were employed in order to obtain both spatial and temporal resolutions in a single discharge. However, this kind of system does not have high enough spatial resolution to study

the radiation power on the JIPP T-IIU tokamak because of low signal to noise (S/N) ratio.

In order to construct a bolometric system with high temporal and spatial resolution, the detector must have high S/N ratio and high time response. This demand is severe for the measurements on a medium-sized tokamak like JIPP T-IIU, since the behavior of the plasma parameters is rapid and the tolerable spatial resolution is small. In addition, the calibration with high accuracy must be carried out, since multichannel measurements with considerable accuracy are necessary to obtain spatial profile of the radiation power through the Abel inversion. Since the cooling of detector due to thermal conduction produces an error on the measurement, the correction for thermal cooling must also be carried out with high accuracy. For this reason, the detector must have well-defined thermal characteristics.

Thermistors,^{1,33,34)} pyroelectric detectors,^{3,35)} and metal-film bolometers,^{34,36,37)} are employed in fusion devices. Thermistors have been used widely because of its high sensitivity. Pyroelectric detectors give the signal with high sensitivity and high time response. An external circuit for measurements is simple since there is no necessity for a differentiating procedure, which is required for measurements with a thermistor and a metal-film bolometer. However, several problems concerning the detectors are pointed out; the spurious

signal due to the photoelectric effect and temporal change in its characteristics.^{38,39)} A metal-film bolometer is free from the spurious signal and has a long cooling time. Its low sensitivity and slow time response are disadvantages for the application. A resolution of the difficulties which each kind of detector has is essential to perform reliable measurements. Therefore, we investigated the means to eliminate the spurious signal from the pyroelectric detector and the temporal change in its characteristics.⁴⁰⁾ We developed metal-film bolometers with thin structure to improve the sensitivity and time response.⁴¹⁾ They have well-defined characteristics. To select detectors best suited to our bolometric system, we investigated the characteristics of three types of detectors, methods of calibration and correction for thermal cooling with high accuracy. As a result, we constructed a bolometric system which consisted of pyroelectric detectors and metal-film bolometers. By utilizing this bolometric system, we studied the radiation losses due to impurities on the JIPP T-IIU tokamak plasma.⁴²⁾ This study is complemented by the spectroscopic measurements.

In JIPP T-IIU,^{43,44)} high power ICRF heating experiments have been carried out. The decrease in radiation loss from a core plasma is a decisive factor to achieve an effective heating. To serve this purpose, the influences of the limiter material and the carbonization on impurity contamination are investigated.

The ICRF heating experiments have been carried out on discharges

using stainless steel (S.S.) limiters or carbon (C) limiters and on discharges with carbonization using C limiters.

In the experiments with S.S. limiters, the total radiated power is the major fraction of the plasma energy loss and emissivity in a core plasma accounts for the substantial fraction of the total radiation power even for ohmically heated plasma.

Replacing S.S. limiters by C limiters, radiation power from ohmically heated plasma is reduced to 30 % of ohmic input power.

This indicates that the limiters are the major impurity sources in ohmically heated plasma. However, large increase in the total radiation power and emissivity are accompanied by ICRF heating even when C limiters are used. By making carbonization, the increase in radiation power due to ICRF heating is dramatically reduced. The above result indicates that impurity flux released from the antenna, the Faraday shield and the vacuum vessel is mainly responsible to the increase in the radiation power during ICRF heating. By comparing the results of bolometric and spectroscopic measurements in the cases with and without carbonizations, the impurity abundances for both cases are estimated. This estimation is essential for the study of impurity contamination and investigation on the effects of C limiters and carbonization on impurity reduction.

The radiation processes from the plasma, the steady-state

radiative cooling rates and the principle of the radiation measurement are described in Chapter II. The radiative cooling rates are good measure for comparing information from the bolometric measurement with that from the spectroscopic measurement. In Chapter III, characteristics and calibrations of detectors are described. The details of apparatus are described in Chapter IV.

Experimental results on the JIPP T-IIU tokamak plasma are described in Chapter V. Radiation measurements for the three cases are presented. Impurity abundances, the origin of impurity and the effects of C limiters and carbonization on the behavior of radiation power are discussed.

In Chapter VI, the summary of the thesis is presented.

CHAPTER II

Theoretical Background

Most of the radiation power from a tokamak plasma is due to the presence of impurities and is related with impurity abundance by the radiative cooling rate which is a function of electron temperature. The radiation power is directly obtained by means of bolometric measurement, because most of the radiation from a tokamak plasma is efficiently absorbed by various materials and is converted into thermal energy.

(i) Radiation Processes and Radiative Cooling Rates

The radiation mechanism from a magnetically confined plasma falls into three categories: free-free radiation, free-bound (recombination) radiation, bound-bound (line) radiation.

A moving charge radiates whenever it is accelerated or decelerated. The free-free radiation can be divided into two categories: Bremsstrahlung and synchrotron radiation.

Bremsstrahlung is caused by the acceleration of charged particles in the Coulomb field of other charged particles. The major part of the Bremsstrahlung is due to electron-ion

collisions. When the electron velocity distribution is Maxwellian, the classical calculation gives the frequency dependence of the free-free emission as $\exp(-h\nu/T_e)$. The emission per unit frequency interval^{45,46)} is

$$\frac{dE_{\text{ff}}}{d\nu} = \frac{32\pi}{3} \frac{Z_{\text{eff}} e^6}{(4\pi\epsilon_0)^3 c^3 m} \left(\frac{2\pi}{3mT_e}\right)^{1/2} n_e^2 \exp\left(-\frac{h\nu}{T_e}\right) \quad (2-1)$$

Integrating over whole wavelength yields the total emission:

$$P_b = 1.5 \times 10^{-38} Z_{\text{eff}} n_e^2 \left(\frac{T_e}{e}\right)^{1/2} \quad (\text{W/m}^3), \quad (2-2)$$

$$(T_e \text{ in eV, } n_e \text{ in m}^{-3})$$

where, Z_{eff} is the effective ionic charge defined as

$$Z_{\text{eff}} = \sum_i \frac{n_i Z_i^2}{n_e}. \quad (2-3)$$

Bremsstrahlung is properly calculated as the radiation produced by quantum mechanical transitions between unbound state in a continuum. The result obtained by the quantum treatments differs from that by classical theory only by a factor of order unity, which is called the Gaunt factor.

In synchrotron radiation, the acceleration is due to charged particles gyrating in a magnetic field. The major contribution is from electrons and the spectrum of radiation is composed of frequencies that are harmonics of the electron cyclotron frequency.

Synchrotron radiation is calculated starting from the

general expression for radiated emission:

$$\frac{dU}{dt} = \frac{e^4 v_1^2 B^2}{6\pi\epsilon_0 c^3 m^3 (1-\beta^2)}, \quad (2-4)$$

where β is v/c . The total emission from a plasma in thermal equilibrium is obtained from eq.(2-4) by integrating over the Maxwellian distribution. The result⁴⁶⁾ is:

$$P_c = 6.2 \times 10^{-20} B^2 n_e \left(\frac{T_e}{e}\right) \left[1 + \left(\frac{T_e}{e}\right) \frac{1}{2.04 \times 10^5} + \dots \right] \quad (\text{W/m}^3). \quad (2-5)$$

Equation (2-5) is a result for an optically thin plasma. In the case that the plasma is optically thick, the total emission decreases because of the absorption. Therefore, eq.(2-5) gives an upper limit of synchrotron radiation power. Synchrotron radiation from tokamak plasmas ($B \sim 1$ T, $n_e \sim 5 \times 10^{19} \text{ m}^{-3}$, $T_e \sim 1000$ eV) is negligibly small compared with the other radiations.

Recombination radiation occurs when an electron recombines with an ion. Since the upper level is continuous, the radiation is continuous. However, there is some structure due to the discrete nature of the lower energy levels (absorption edge).

For an electron of mass m and velocity v , recombination into state p gives

$$h\nu_p = E(\infty) + \frac{1}{2}mv^2 - E(q), \quad (2-6)$$

where $E(\infty)$ denotes ionization limit. When the electron velocity distribution is Maxwellian, the classical calculation gives the frequency dependence of the recombination radiation as

$\exp(-h\nu/T_e)$.

Line radiation occurs for electron transitions between bound levels, leading to line spectra. When a transition takes place from a level of principal quantum number p with energy $E(p)$ to a level of q with energy $E(q)$, the frequency of the radiation ν_{pq} is expressed by

$$h\nu_{pq} = E(p) - E(q). \quad (2-7)$$

For allowed transitions the usual selection rules of spectroscopy have to be obeyed.

The total radiation power due to the presence of impurity is evaluated from ionization, recombination and excitation rate coefficients. The excited state population for tokamak plasmas are calculated according to the simple corona model, which is usually a good approximation for tokamak plasmas. In this model, excitation and ionization are due to electron collisions on the ground state, de-excitation occurs only by radiation, including radiation and dielectronic recombinations. Direct calculation of the radiative cooling rates have been made¹⁰⁻¹²⁾ for coronal equilibrium. The results for C, O and Fe, which are the most abundant impurities detected in tokamak plasma, are shown in Fig.2-1.¹⁰⁾ These values include also Bremsstrahlung. It is found that line radiations from Fe impurity are dominant in the present tokamak plasma. Among C, O and Fe, a contribution of Fe impurity is largest as a radiator. The total emission from a plasma is obtained as

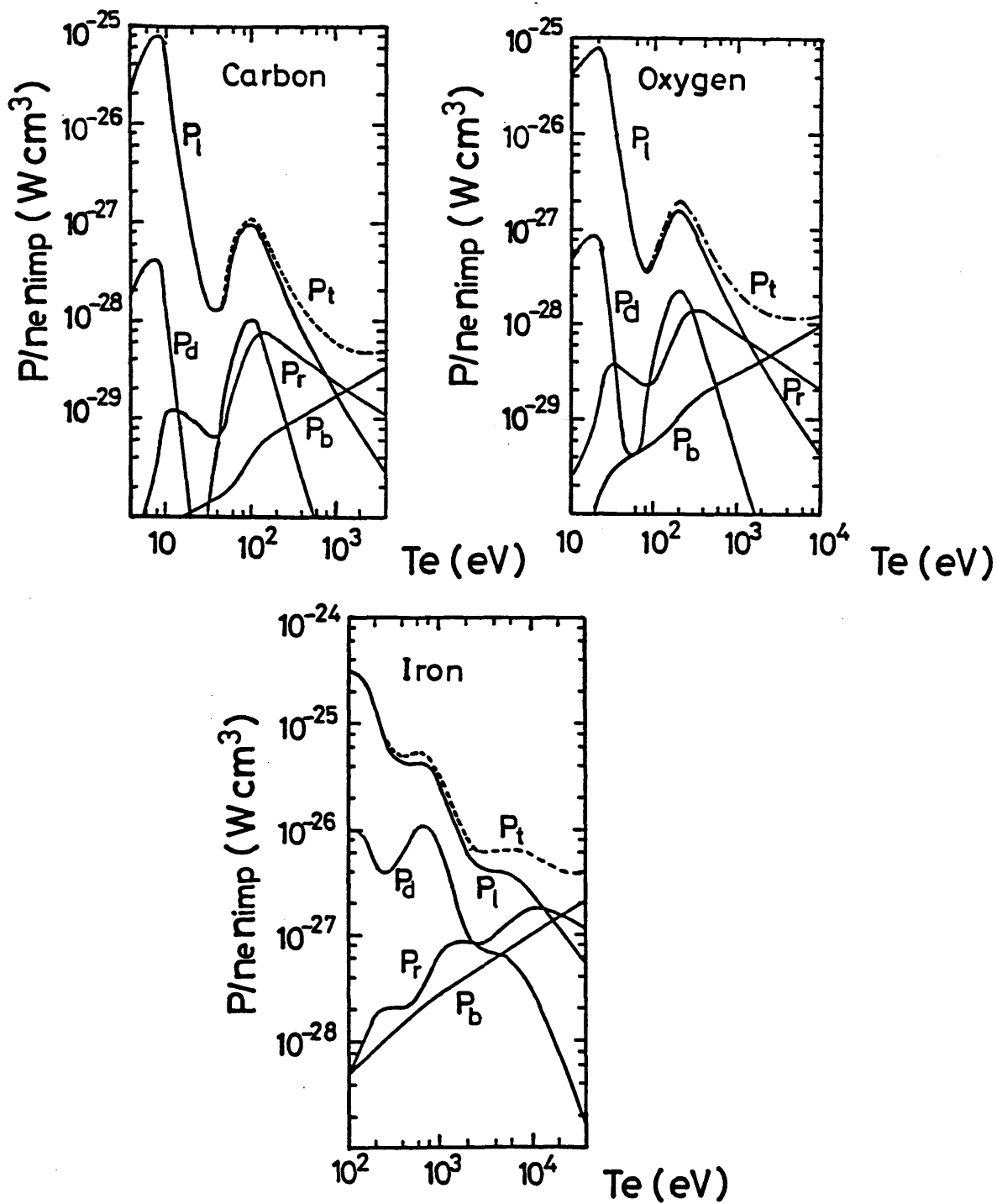


Fig.2-1 Radiative cooling rates as a function of T_e .¹⁰⁾

$$P = n_e n_{imp} L(T_e), \quad (2-8)$$

where $L(T_e)$ is the radiative cooling rate. The impurity density can be inferred from the result of the bolometric measurement by this equation. The effective ionic charge Z_{eff} in eq.(2-3) gives the information to determine the impurity density. According to neoclassical theory, Z_{eff} is related to electron temperature T_e , resistive voltage and plasma current through plasma resistivity η as

$$\eta = 1.03 \times 10^{-4} \frac{Z_{eff} \ln \Lambda}{T_e^{3/2} f_T} \left(\frac{0.457}{1.077 + Z_{eff}} + 0.29 \right), \quad (2-9)$$

where $\ln \Lambda$ is coulomb logarithm, f_T the correction for the trapped electrons. The value of Z_{eff} thus obtained gives that in a core region ($r \leq a/2$) because the plasma current mainly flows in this region.

(ii) Measurement of Radiation Power

Radiation power is measured from the temperature rise of the absorber of a detector on the assumption that the radiation energy is efficiently converted into thermal energy. This assumption is considered to be valid for the photons in VUV region. It seems that the major fraction of radiated power from a tokamak plasma lies in the vacuum ultraviolet region. It is reported that photons in such a region are efficiently absorbed by various materials.⁴⁷⁾ In Fig.2-2, reflectivities of iron

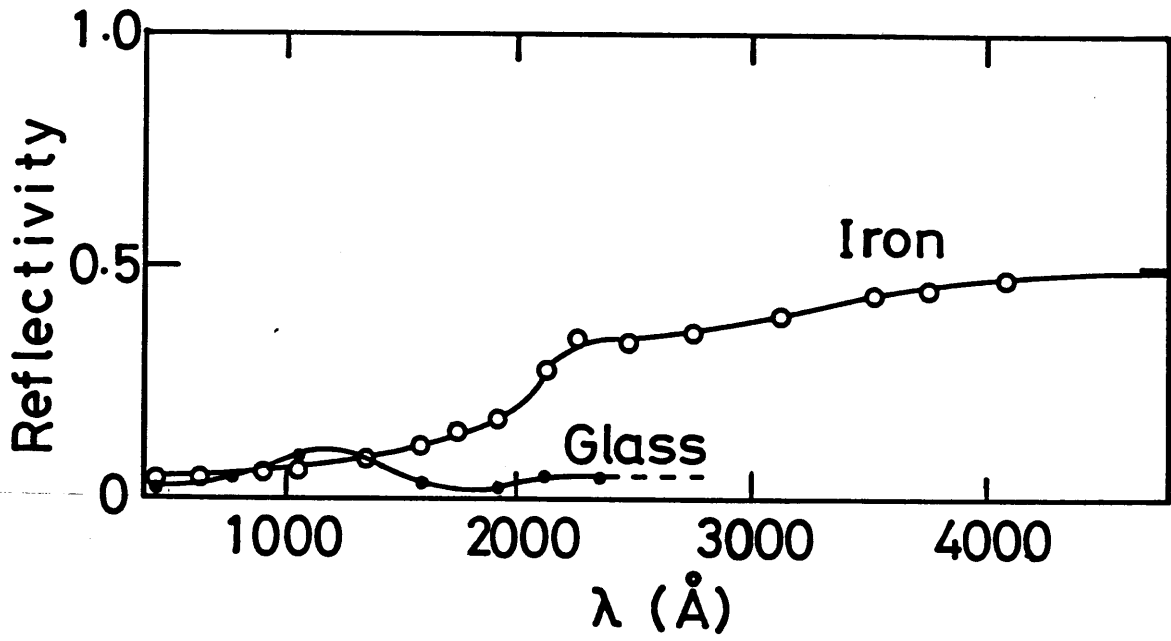


Fig.2-2 Reflectivities of iron and glass as a function of wavelength. 47)

and glass are shown as a function of wavelength. Most of photons up to 2000 Å is absorbed (> 90 %) by these materials. The absorbers are made of these materials. This is supported by the fact that no difference has been observed between bare and coated detectors having layers of carbon black that can absorb nearly 100 % of the incident-light energy.⁴⁸⁾

If a radiation power per volume P_{vol} is incident on the detector, its temperature rise T is governed by

$$c\rho\frac{\partial}{\partial t}T = K\Delta T + P_{vol}, \quad (2-10)$$

where c is the specific heat, ρ the density, K the thermal conductivity. If the first term is negligible, the radiation power is measured from the time differential of T . A detector for the bolometric measurement is so made that the effect of this term is small. The deviation due to this term is the origin of the thermal cooling of the detector. First approximation to input power is written as

$$P = C \left(\frac{dT}{dt} + \frac{T}{\tau_c} \right), \quad (2-11)$$

where C is the thermal capacity and τ_c the cooling time. The temperature rise is measured through the change in resistance or through the change in the surface charge by a pyroelectric effect. The former is the principle of a thermistor and a metal-film bolometer and the latter is that of a pyroelectric detector.

(a) Thermistor and metal-film bolometer

The thermistor and the metal-film bolometer are similar in operation. Both of the detectors combine the functions of a radiation absorber and a resistor for detection. Assuming that the temperature rise T is small, a change in the resistance ΔR can be described as

$$\Delta R = R_0 \alpha T, \quad (2-12)$$

where R_0 is the initial resistance and α the temperature coefficient.

Figure 2-3 shows the circuit used in a total-radiation measurement on the JIPP T-IIU tokamak, where r and c are the resistance and capacitance of the differentiating circuit, respectively. This circuit has the advantage of simpleness and of no signal drift. When a signal is obtained under the condition that the time constant rc is smaller than the required time response τ of measurement and that R_0 is smaller than the impedance determined by r and c , the resulting voltage V can be described as

$$V = Irc \frac{dT}{dt}, \quad (2-13)$$

where I is the current determined by a constant current diode.

From eqs. (2-11), (2-13), P is obtained as

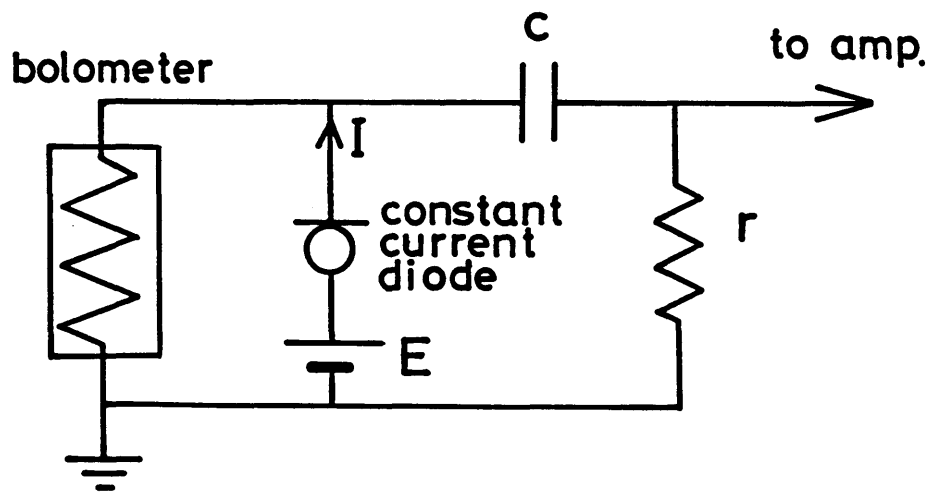


Fig.2-3 Circuit for the metal-film bolometer.

$$P = \frac{C}{I\alpha R_0 r c} \left(V + \frac{1}{\tau_c} \int_0^t V dt \right), \quad (2-14)$$

where $\alpha R_0/C$ is equal to the sensitivity of the detector. In the radiation measurement from a plasma, τ_c is so determined that the radiation is zero immediately after the discharge is terminated.

(b) Pyroelectric detector

When a pyroelectric crystal undergoes a change in temperature, a surface charge is produced as the result of a change in its spontaneous polarization with temperature. This pyroelectric effect is expressed in terms of a pyroelectric coefficient p as,

$$\Delta P_s = pT, \quad (2-15)$$

where P_s is the spontaneous polarization.⁴⁹⁾ The resulting pyroelectric charge-flow i_p in the circuit of the sample (Fig.2-4) is described by

$$i_p = \frac{d}{dt}(A\Delta P_s) = Ap \frac{dT}{dt}, \quad (2-16)$$

where A is the sensitive area of the detector. From eqs.(2-11), (2-16), P is obtained as

$$P = \frac{C}{Ap} \left(i_p + \frac{1}{\tau_c} \int_0^t i_p dt \right), \quad (2-17)$$

where Ap/C is equal to the sensitivity of the detector. In the radiation measurement from a plasma, τ_c is so determined that

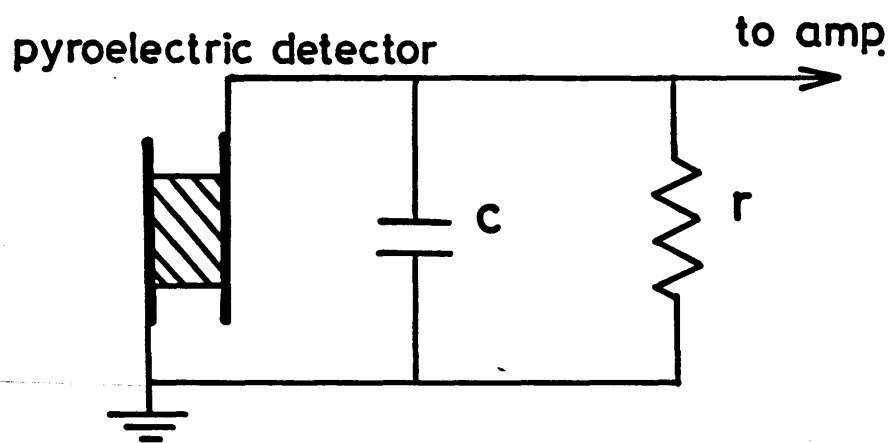


Fig.2-4 Input equivalent circuit of the pyroelectric detector.

the radiation is zero immediately after the discharge is terminated.

The input equivalent circuit of a pyroelectric detector is shown in Fig.2-4. The time response depends on the time constant rc , since the time response determined by the detector is very high. The capacitance c is composed of the capacitance between the electrodes and of a floating capacitance. The resistance r is the load resistance parallel to the detector. This time constant rc is chosen so as to be smaller than the required time response. Under such a condition, this detector operates as a current source whose signal is described by the equation (2-16).

The signal which is obtained through the thermal process should have the following feature. After the incident power on the detector is turned off, the integrated value of this signal becomes zero with a time lapse τ , several times larger than the cooling time τ_c . The integrated value is proportional to the temperature rise of the detector from the initial value. It is derived from the eq.(2-16) as

$$\int_0^{\tau} i_p dt = Ap [T(\tau) - T(0)] . \quad (2-18)$$

After the incident power is turned off, the temperature of the detector gradually decreases with time. Finally it approaches to the initial value. As can be seen from the equation (2-18),

$$\int_0^{\tau} i_p dt = 0. \quad (2-19)$$

A signal which does not satisfy this equation is regarded as the false signal.

CHAPTER III

Characteristics of Detectors

The reliability of a bolometric measurement depends entirely on the performance of the detectors. As a first step, characteristics of three types of detectors are investigated because this is necessary in order to select detectors and to construct a bolometric system best suited to the measurement on the JIPP T-IIU tokamak. As a matter of course, the reliable measurement depends critically on the calibration of detectors.

The accurate measurement of the net input power to the detector is of a primary importance to the calibration.

(i) Thermistor

A thermistor is a small chip of semiconductor material with a standard thickness of 40 μm . It can be free standing or mounted on a metal substrate. The resistance is a sensitive function of temperature, typically 5 % per degree centigrade.

(a) Calibration of Thermistors

The sensitivity of the detector is obtained from the change in resistance when a known power from a HeNe laser is introduced to the detector. The laser power incident on the detector is measured with a calibrated powermeter, with an accuracy of 3 %.

Figure 3-1 shows the laser power and the output signal from the circuit shown in Fig.2-3. The output signal is negative, because the temperature coefficient is negative. The sensitivity obtained without considering the reflected power of HeNe laser light is 1530 Ω/mJ . The reflected power is hard to be measured because of its diffused reflection. The time response of the detector is slow (~ 20 ms). In addition, the sensitivity is observed to be strongly position dependent.

(ii) Pyroelectric Detector

A pyroelectric detector consists of two electrodes and pyroelectric crystal ($LiTaO_3$), whose Curie temperature is $610^\circ C$. Radiation is absorbed by the front electrode with SiO_2 absorber of $50 \mu m$ thick and the crystal of $50 \mu m$ thick. Their absorptive power is shown in Fig.3-2.⁵⁰) Absorbed radiation is converted into heat, which in turn increases the temperature of the crystal. This detector gives the signal due to the heat. The sensitive region of the detector is 2 mm in diameter. This detector has an absorber of smooth surface and incident light onto the absorber undergoes a normal reflection. Therefore,

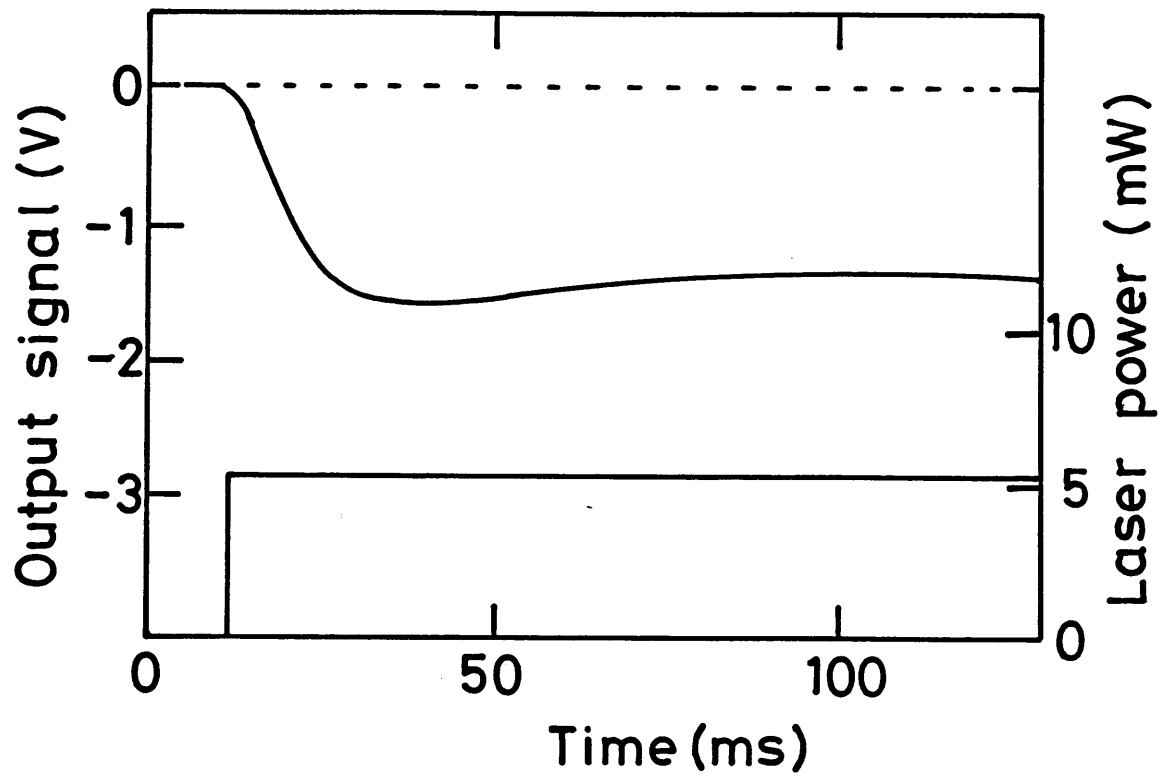


Fig.3-1 Output signal from the thermistor (top) with the incidence of the HeNe laser light (bottom).

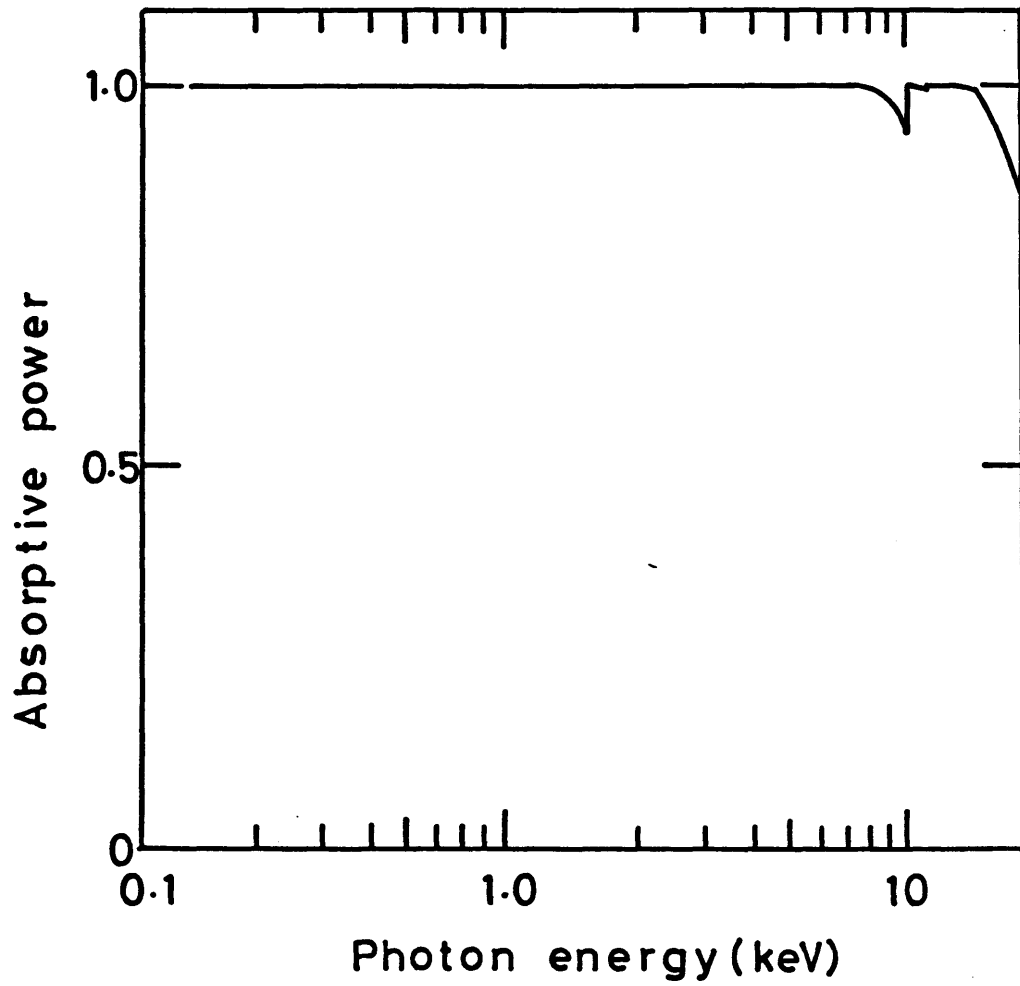


Fig.3-2 Absorptive power of absorber and pyroelectric crystal.50)

the reflected power is easily measured.

(a) Calibration of Pyroelectric Detectors

The beam of the HeNe laser light was conducted nearly normal to the detector (Fig.3-3). The incident power and the reflected power of the laser light were measured with a calibrated powermeter. The net input power is the difference between these powers. The output current from the detector for a net input power of 1.3 mW is shown in Fig.3-4. This signal rises within 1 ms after the power incidence and reaches a maximum value; then it decreases with a cooling time of 185 ms. The sensitivity and cooling time of this detector are obtained from the maximum value and the decay of this signal, respectively.

The sensitivity and the reflectivity thus obtained are 0.95 $\mu\text{A}/\text{mW}$ and 53 %, respectively. This calibrated value is twice as large as the manufacturer's value. The value obtained without considering the reflected power of the HeNe laser light agrees well with the manufacturer's value. The output linearity was checked to be high as shown in Fig.3-5. The incident power was controlled by changing the neutral (ND) filter inserted in front of the detector.

The pyroelectric detector was calibrated each time it was detached from the JIPP T-IIU tokamak. The sensitivity and reflectivity for the HeNe laser light are shown in Fig.3-6.

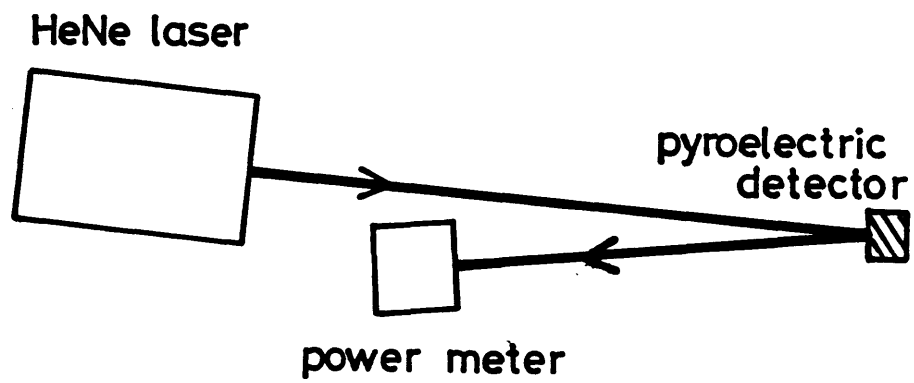


Fig.3-3 Arrangement of a HeNe laser and a calibrated powermeter for the measurement of the reflected power.

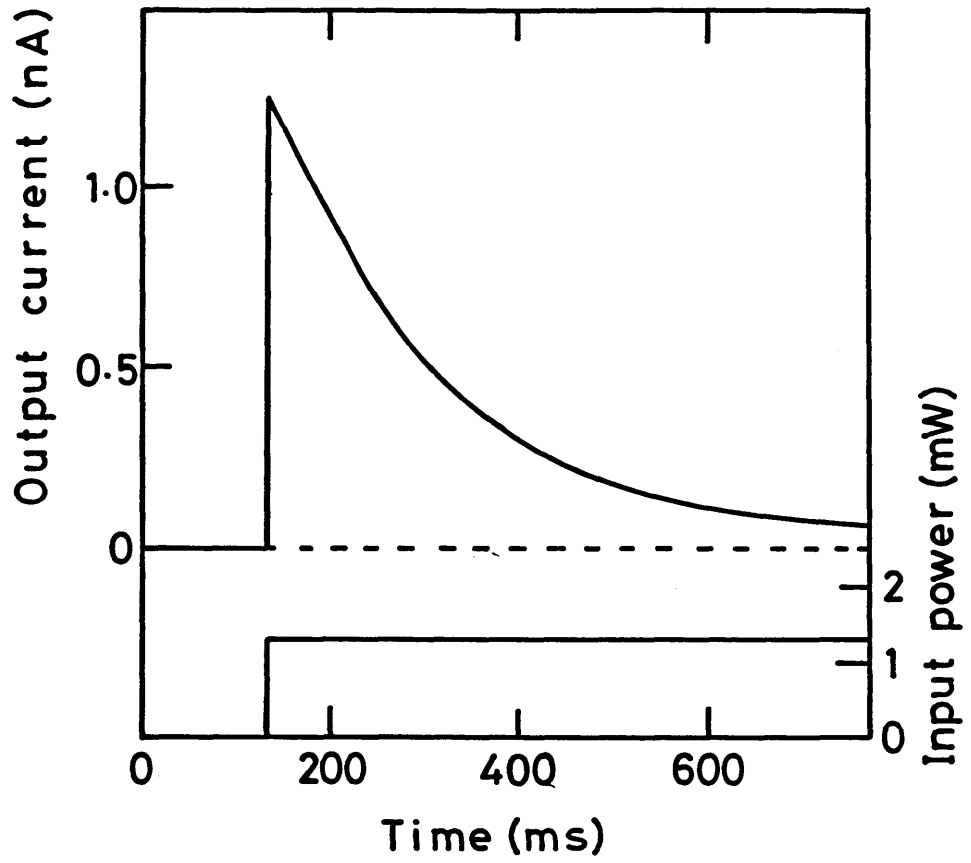


Fig.3-4 Output current from the pyroelectric detector (top) with the incidence of the HeNe laser light and input power to the detector (bottom).

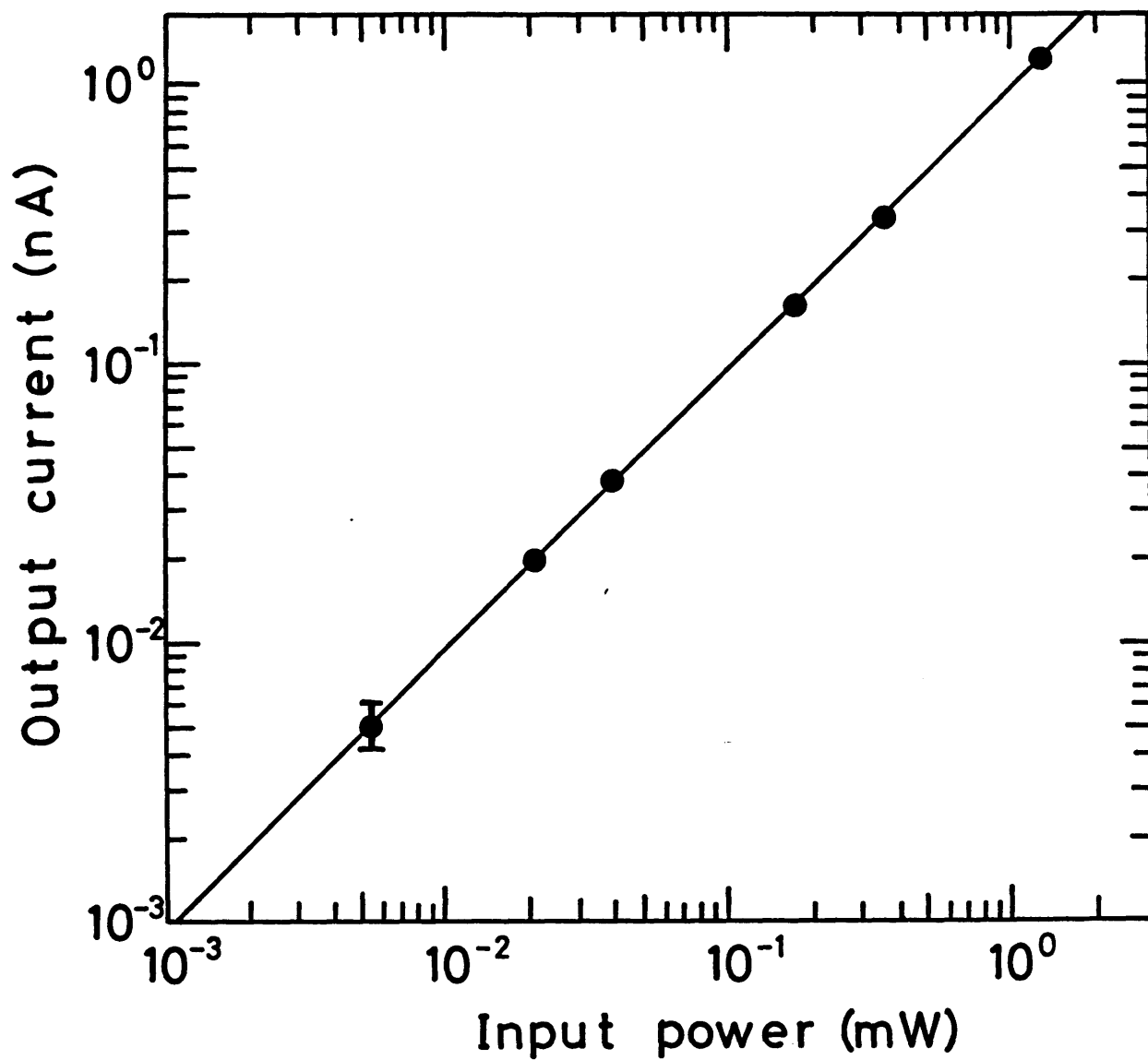


Fig.3-5 A plot of the output current from the pyroelectric detector against the net input power, which shows good linearity.

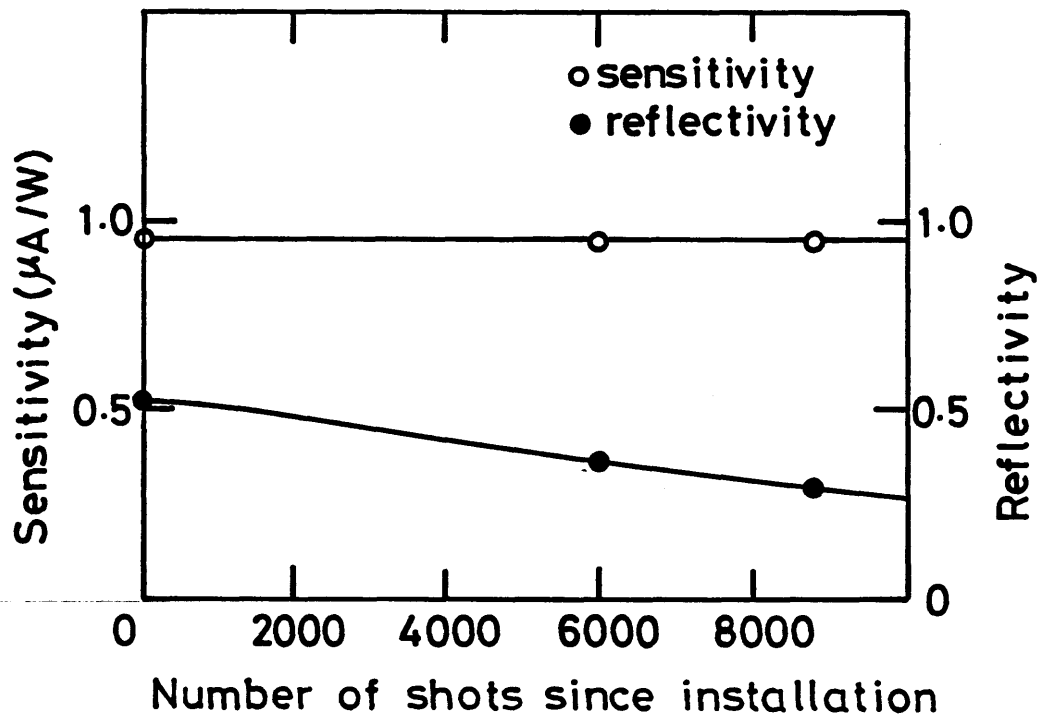


Fig.3-6 Temporal change in the sensitivity (top) and the reflectivity against the HeNe laser light (bottom).

As the detectors are exposed to a plasma discharge, the reflectivity decreases. However, little change in the net sensitivity has been observed (within 1 %). A decrease in the reflectivity is due to the change in the detector surface, since discoloration is found through visual observation.

(b) Spurious Signal

Severe difficulty is already being encountered in interpreting the results measured with pyroelectric detectors.

The problem is the spurious signal due to the electrons produced by secondary emission.^{39,40)} In order to resolve the problem, we investigated on the spurious signal. A pyroelectric detector (bare detector) and a pyroelectric detector with a mask (detector with a mask) were mounted on the JIPP T-IIU device. The mask, which is close to the detector, affords protection against the direct incidence of radiation onto a nongrounded electrode (Fig.3-7). The sensitive region of the bare detector is determined by its intrinsic sensitive region and that of the detector with a mask is determined by the mask.

The signal i_s shown in Fig.3-8(a) was obtained from a bare detector. The magnitude and the behavior of the signal show the possibility of a spurious signal. The magnitude of i_s is too large to do fit with reality, because this value indicates a radiation power which greatly exceeds the input power to plasma.

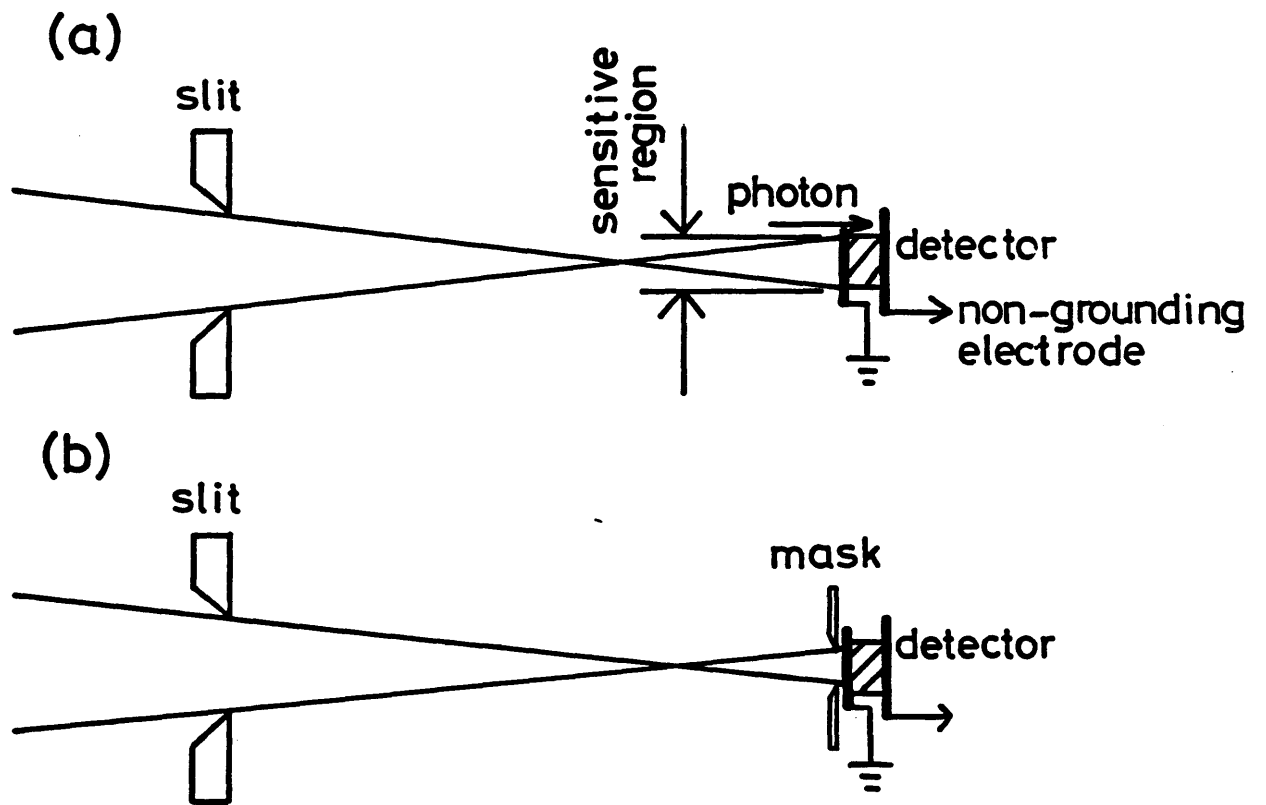


Fig.3-7 Viewing geometry of (a) the bare detector and (b) the detector with a mask.

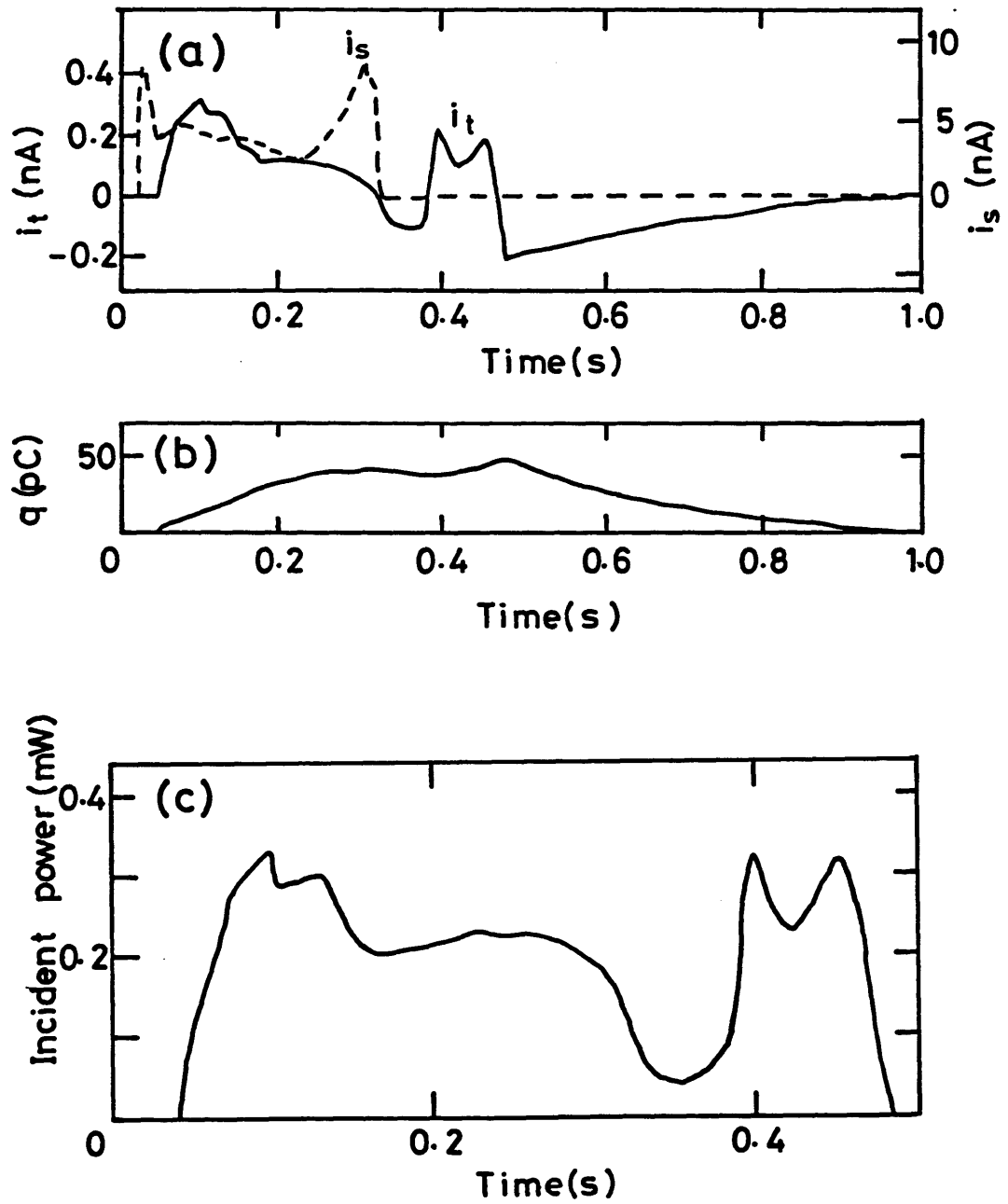


Fig.3-8 (a)Time behaviors of the output from the bare detector (i_s) and the output from the detector with a mask (i_t). The time behaviors of (b) the integrated value of the signal (q) and (c) the incident power on the detector obtained from the signals (i_t, q).

The signal after the discharge has a small negative value, but is too small to explain the decrease in the temperature of the detector due to the heat losses described by the first term of the eq.(2-10). It is obvious that the integrated value of the signal does not return to zero after a long lapse of time. This shows that a positive spurious signal is superposed on the true signal.

The signal i_t shown in Fig.3-8(a) was obtained from a pyroelectric detector with a mask. The magnitude of this signal indicates a radiation power which is about 80 % of the ohmic input power. It is possible that the plasma radiates such a large fraction of the energy loss since this is a radiation-dominant plasma. This signal has a negative part, indicating a decrease in the temperature of the detector. The integrated value of i_t is shown in Fig.3-8(b). It satisfies the condition described in eq.(2-19). Thus the net input power on the detector is obtained through a correction for thermal cooling described in eq.(2-17). The net input power obtained from the signals i_t and q is shown in Fig.3-8(c).

(iii) Metal-film Bolometer

A metal-film bolometer is similar in operation to a thermistor. As the resistor is made of metal and its temperature coefficient is small, the sensitivity is small compared with a

thermistor. In order to improve thermal characteristics and time response as well as sensitivity, we have developed metal-film bolometers with thin structure and axial symmetry. The structure of the metal-film bolometer is shown in Fig.3-9. An absorber is a thin stainless steel plate 20 mm in diameter and 10 μm thick but it is enough thick to absorb photons with high energy up to 3 keV (Fig.3-10).⁵⁰⁾ This absorber is fixed by the holder at 16 mm in diameter (Fig.3-9(a)). Silicon oxide SiO_2 is deposited ($\sim 0.2 \mu\text{m}$) on the absorber in a vacuum, and nickel is also deposited ($\sim 0.1 \mu\text{m}$) on the SiO_2 layer into spiral shape. The SiO_2 layer serves as an electrical insulator between the absorber and the resistor (Ni film). The resistor is a spiral shape and has a resistance of 10 k Ω . It is located on the central region of the absorber and its diameter is 6 mm. A slit is equipped close to the detector in application to the JIPP T-IIU tokamak (Fig.3-9(b)). Its internal diameter is also 6 mm.

Above mentioned structure is designed from the viewpoint of the required characteristics. Thin structure improves time response ($\sim 3 \mu\text{s}$) and sensitivity (12.9 Ω/mJ), since time response is determined by the transit time of a heat from the absorber surface to the resistor and sensitivity is determined by thermal capacity per unit area.

Regarding thermal characteristics, the major fraction of thermal capacity is mainly determined by the absorber because the electrical insulator and the resistor are very thin in

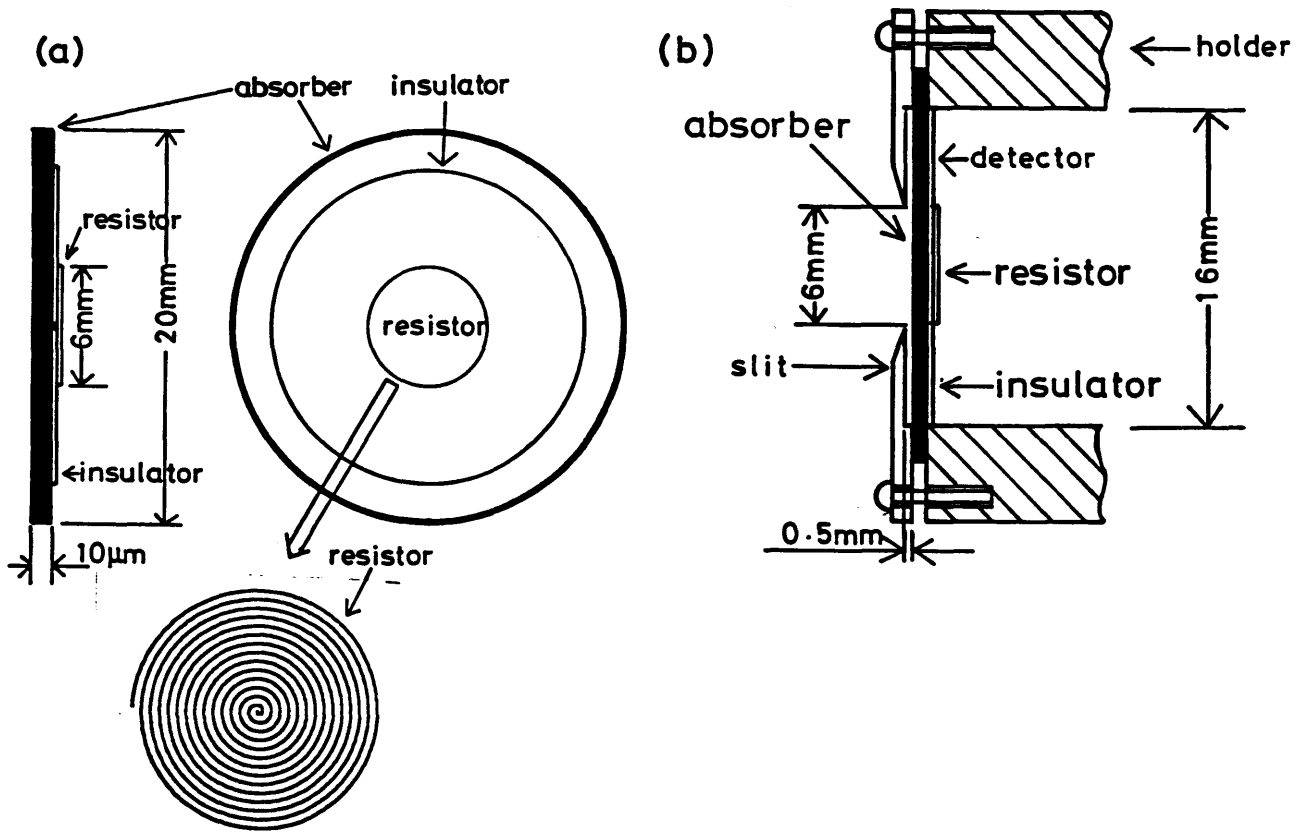


Fig.3-9 (a)Structure of the metal-film bolometer. Thin structure improves sensitivity and time response. A heat conduction equation is easy to be applied because the major fraction of thermal capacity is determined by the absorber. (b) A slit is equipped in the application to JIPP T-IIU tokamak.

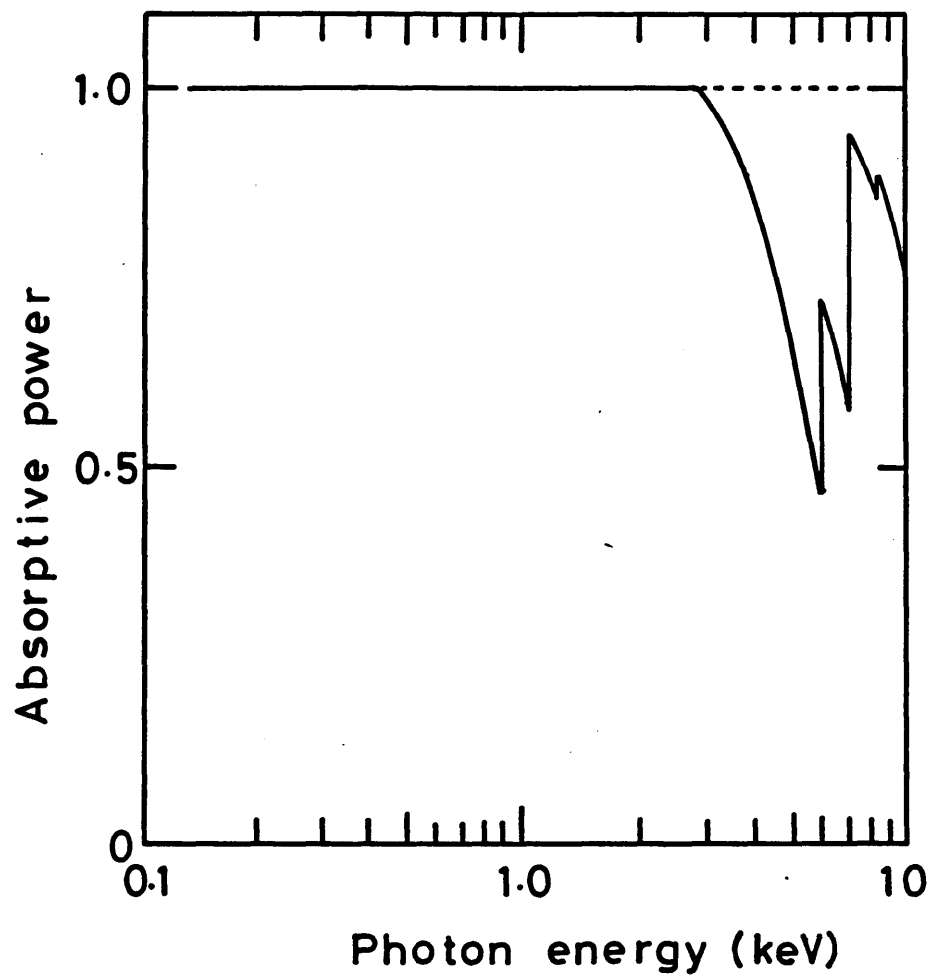


Fig.3-10 Absorptive power of stainless steel absorber in
 thickness of 10 μm as a function of photon energy.⁵⁰⁾

comparison with the absorber. The temperature at periphery of the absorber is held constant because of the large thermal capacity of the holder (Fig.3-9(b)). The resistor serves double functions. One is the function of the sensor for temperature change and the other is that of a heater. As for the former, its resistance is determined as a function of its space averaged temperature in the resistor region because of the shape of the resistor. If a current passes through the resistor, it uniformly heats up the resistor region. The sensitivity of the detector is measured by flowing a bias current through the resistor. The sensitivity thus obtained applies for the experiment on the JIPP T-IIU tokamak, because the diameter of the resistor is as large as internal diameter of the slit.

(a) Calibration of Metal-film Bolometers

The calibration of the metal-film bolometer was performed with the circuit shown in Fig.3-11. This circuit is composed of a Wheatston bridge, a differential amplifier and a differentiating circuit. The net input power to the detector is measured with the voltage drop arising in the bolometer and the current, which flows through the bolometer. The output signal from this circuit and the net input power (P_{in}) are shown in Fig.3-12. This signal reaches a maximum value within 3 ms, and then decreases with a cooling time (~ 1.1 s). The net input

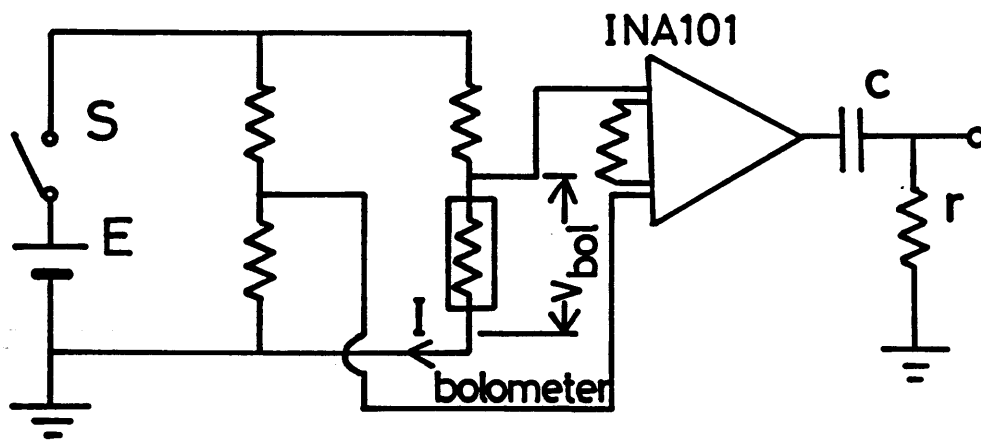


Fig.3-11 Circuit for the calibration of the metal-film bolometer.

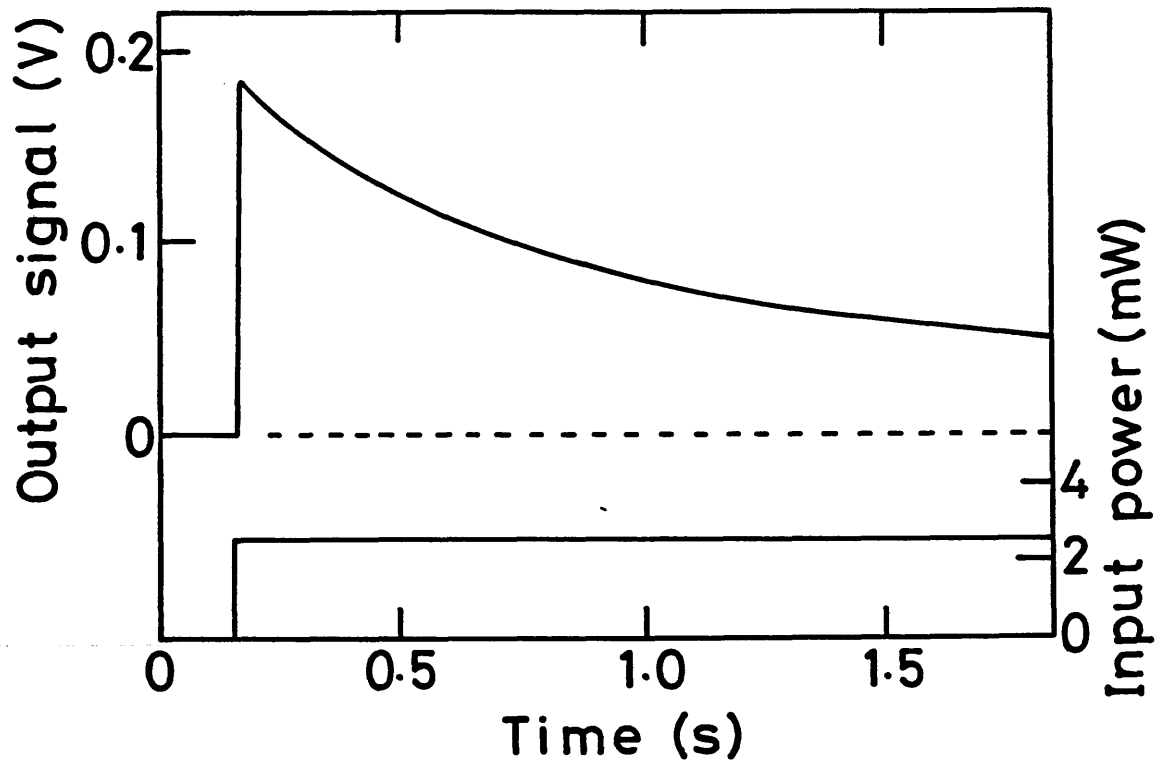


Fig.3-12 Output signal from the metal-film bolometer (top) and the input power to the detector (bottom).

power is 2.50 mW and the sensitivity of this detector is 12.9 Ω/mJ . This method has the advantage of being calibrated *in situ*.

(b) Thermal Characteristics

The thermal characteristics are well expressed by a heat conduction equation because of a simple structure with axial symmetry. As an incident power on the absorber surface is deposited to the resistor in a short time ($\sim 3 \mu\text{s}$), the assumption that a temperature rise is uniform in the direction perpendicular to the detector surface will be allowed for a long time scale ($\gg 3 \mu\text{s}$). In the present case, heat conduction equation (2-10) is modified to a partial differential equation,

$$c\rho\frac{\partial}{\partial t}T(r,t) = K\frac{1}{r}\frac{\partial}{\partial r}\left[r\frac{\partial}{\partial r}T(r,t)\right] + \frac{1}{d}P(r,t), \quad (3-1)$$

where c is the specific heat (0.51 J/gK) of the absorber (stainless steel), ρ the density ($7.9 \times 10^6 \text{ g/m}^3$), K the thermal conductivity (15.1 W/mK), d the thickness (10 μm), $P(r,t)$ the input power density in W/m^2 . This equation is numerically solved by a recurrence method under the boundary and the initial conditions that

$$T(a,t) = T(r,0) = 0, \quad (3-2)$$

where a is the internal radius of the holder (Fig.3-9(b)). The change in resistance R is related with the temperature rise averaged in the resistor region by

$$\Delta R = R_0 \alpha T_{av}(t), \quad (3-3)$$

where $T_{av}(t)$ is the space averaged value of $T(r, T)$, R_0 the initial resistance and α the temperature coefficient of Ni film.

The value of $T_{av}(t)$ is obtained as

$$T_{av}(t) = \frac{1}{\pi a_1^2} \int_0^{a_1} 2\pi r T(r, t) dr, \quad (3-4)$$

where a_1 is the radius of the resistor region. As can be seen from the comparison of eq.(2-12) with eq.(3-3), power measured by the detector is obtained from eq.(2-11) as

$$P_{meas} = C \left[\frac{d}{dt} T_{av}(t) + \frac{1}{\tau_c} T_{av}(t) \right], \quad (3-5)$$

where C is given by $\pi a_1^2 \rho d$. In order to investigate characteristics of a metal-film bolometer, eqs.(3-1)-(3-5) are solved both for the cases of calibration and of radiation measurement.

The calculated results for the case of calibration are shown in Fig.3-13. The value of \dot{T}_{av} (solid line) is shown instead of P_{meas} . The dot denotes the time differential from now on. The value of \dot{T}_{av} corresponds to the output signal in Fig.3-12, that is, \dot{R} . Comparison between time behaviors of both values is made in Fig.3-14. The deviation from a straight line is within 3 % and this supports that thermal characteristics are well expressed by eq.(3-1). A dashed line in Fig.3-13(c) denotes the value with a correction according to eq.(3-5). The value of τ_c in this case is 0.94 s. It is so determined that initial

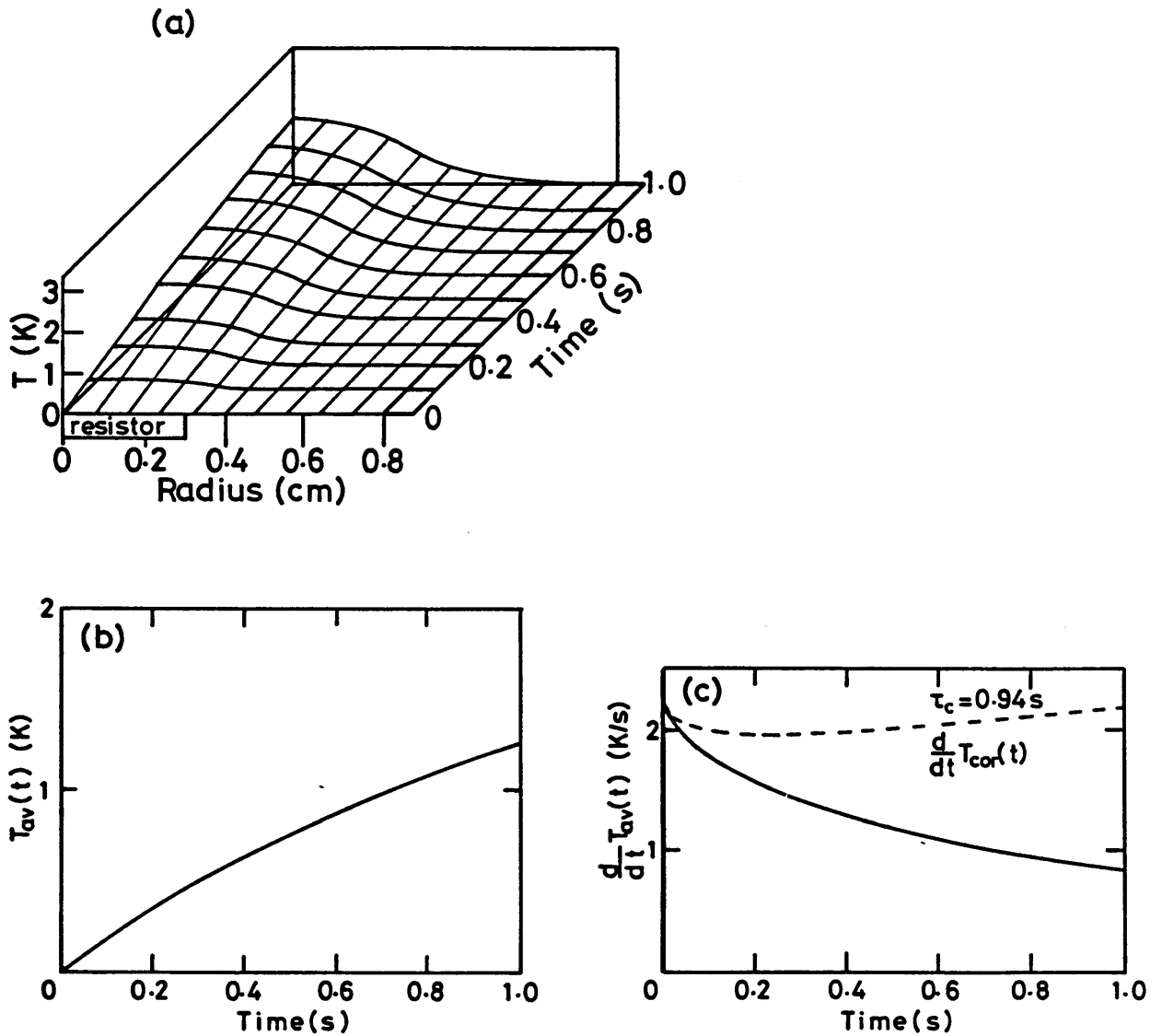


Fig.3-13 Calculated results of (a) temperature rise of the absorber, (b) space-averaged temperature rise ($T_{av}(t)$) in the resistor region. (c) Time behavior of $T_{av}(t)$. The dashed line denotes the value with a simple correction for thermal cooling.

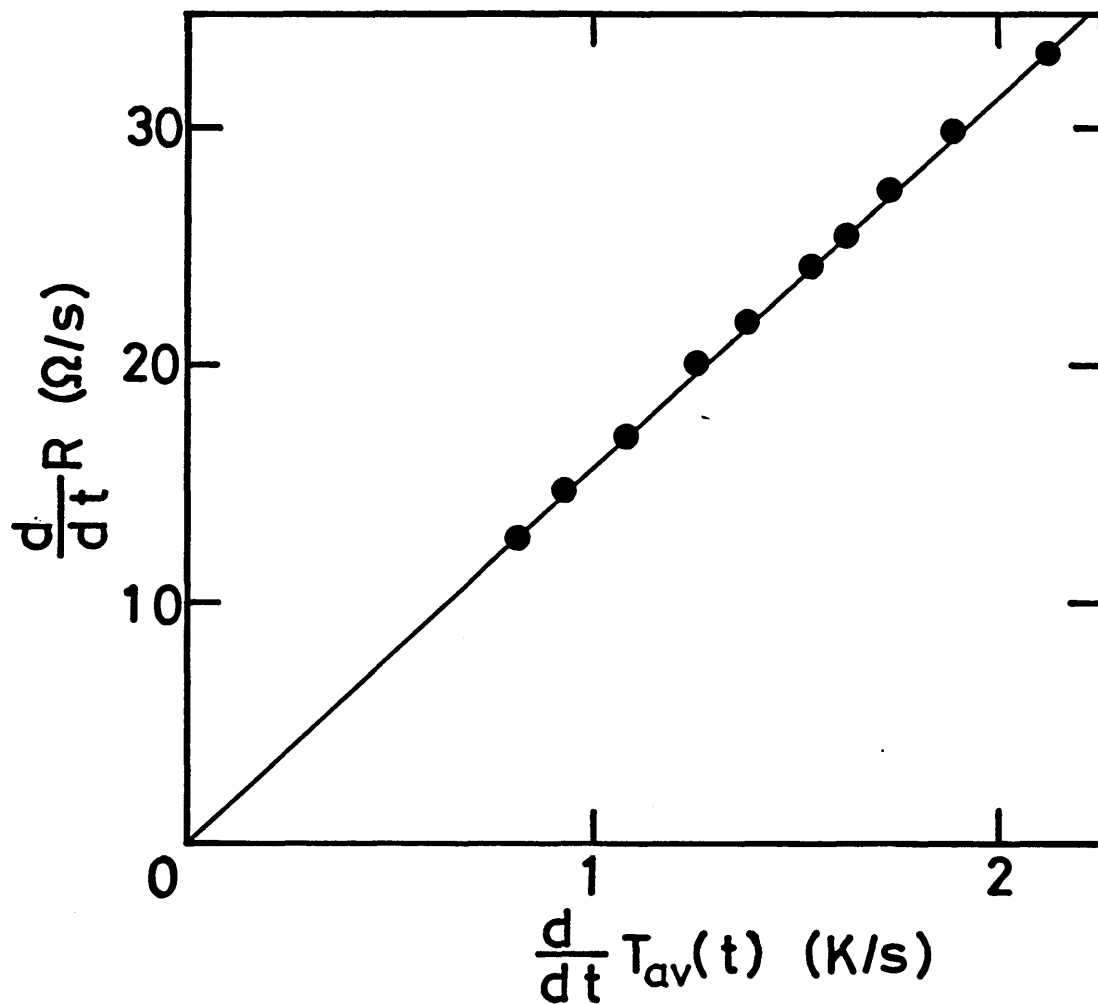


Fig.3-14 A plot of the measured \dot{R} against calculated $\dot{T}_{av}(t)$.

They show a good agreement. The value of \dot{R} corresponds to that of $\dot{T}_{av}(t)$.

value agrees with the value at $t=1.0$ s.

The calculated results for the case of radiation measurement are shown in Fig.3-15. Power density used for calculation of eq.(3-1) is shown in Fig.3-16. In Fig.3-17, T_{av} (solid line) is shown. A dashed line denotes the value with a correction according to eq.(3-5). The value of τ_c in this case is 0.61 s. It is so determined that P_{meas} becomes zero at $t=0.25$ s. Figure 3-18 shows ratio of P_{meas} to P_{in} . The value of P_{in} is the product of power density and the internal area of the slit.

The deviation is reduced by a correction according to eq.(3-5) to 3 % for $t < 180$ ms. This result shows that the correction is effective.

(iv) Results and Discussion

It is important for a bolometric measurement to efficiently absorb the radiation from a plasma. This needs to make sure that photons with long wavelength ($\lambda < 2000$ A) and photons with high energy ($E > 3$ keV for a metal-film bolometer, $E > 10$ keV for a pyroelectric detector) have little contribution to the radiation power because such low energy photons are reflected by an absorber surface of a detector and high energy photons penetrate a detector. In order to investigate the radiation power due to photons with long wavelength ($\lambda > 2000$ A), the radiation power from the JIPP T-IIU tokamak plasma is measured with two

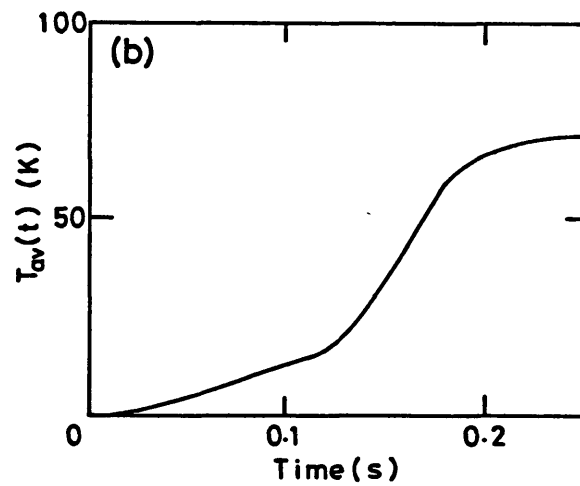
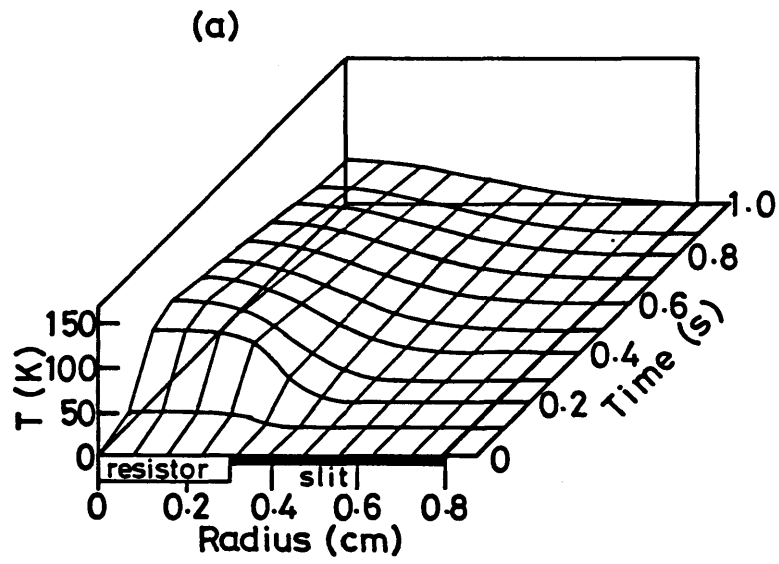


Fig.3-15 Calculated results of (a) temperature rise in the case with a slit, (b) space-averaged temperature rise ($T_{av}(t)$).

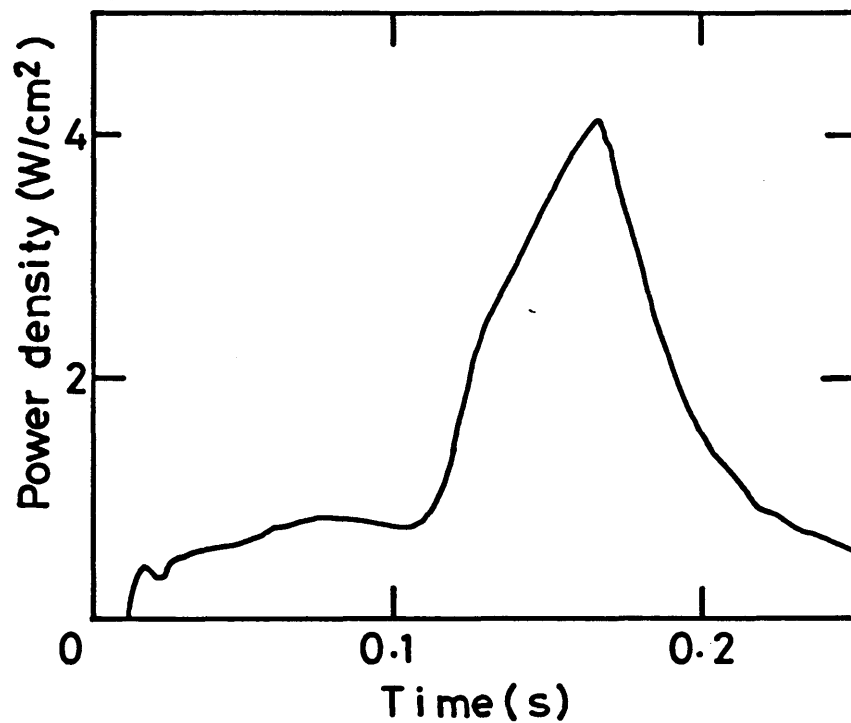


Fig.3-16 The time behavior of the radiation power density measured with the metal-film bolometer ($P_{\text{meas}}(t)$). It includes a simple correction for thermal cooling.

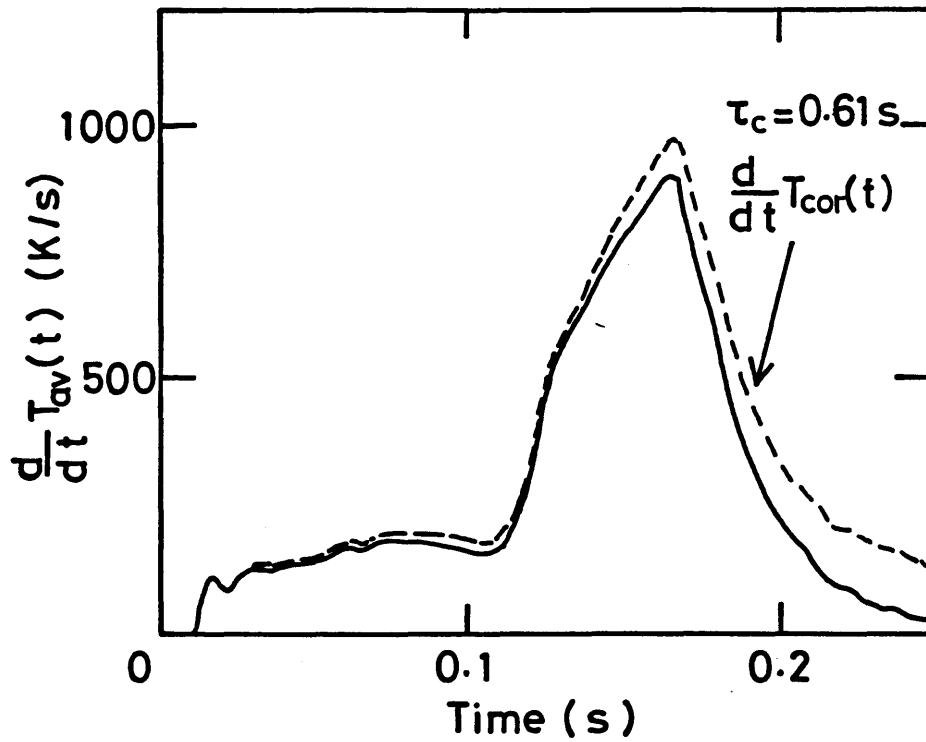


Fig.3-17 The time behavior of $T_{av}(t)$ (solid line). The dashed line denotes the value with a simple correction for thermal cooling.

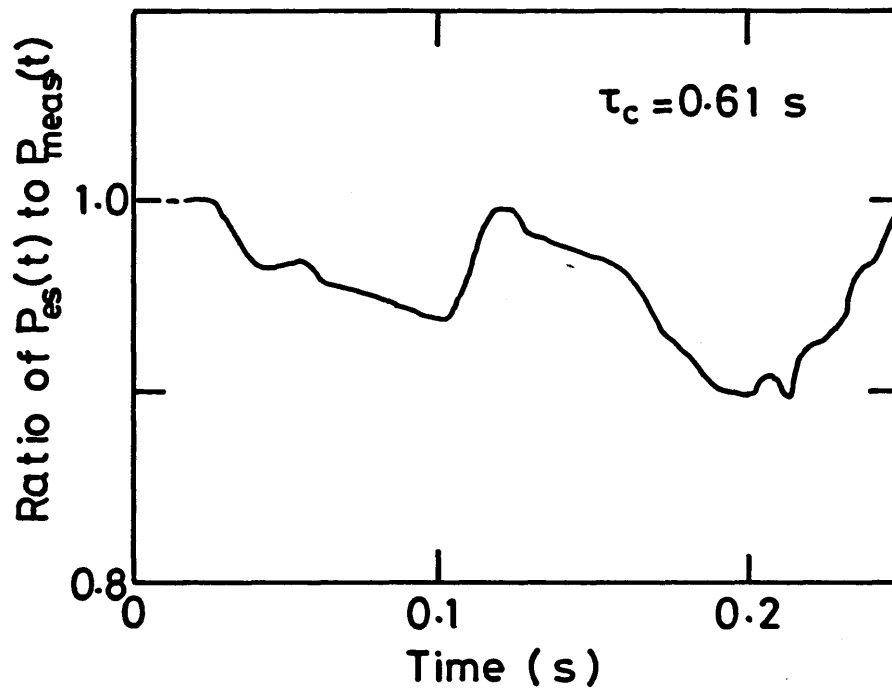


Fig.3-18 Ratio of $P_{es}(t)$ to $P_{meas}(t)$. This value of $P_{es}(t)$ is obtained from the value shown by the dashed line in Fig.3-17 in consideration of thermal cooling.

pyroelectric detectors (Fig.3-19). One of the detectors views the plasma through sapphire window which cuts photons with short wavelength up to 2000 Å (dashed line). These detectors are sufficiently sensitive for photons with long wavelength ($\lambda > 2000$ Å). The above results indicates that photons with long wavelength ($\lambda > 2000$ Å) have little contribution to the radiation power ($< 1\%$). When the electron velocity distribution is Maxwellian, a contribution of photons above 3 keV is estimated to be less than 5% of the total radiation power from the plasma ($T_e \sim 1$ keV). A pyroelectric detector and a metal-film bolometer have high absorption power for photons up to 3 keV (Fig.3-2 and Fig.3-10). Especially, a pyroelectric detector efficiently absorbs the high energy radiation up to 10 keV.

As for a thermistor, slow time response and position dependence of sensitivity are drawback to bolometric measurement. The calibration method using HeNe laser is not suitable for thermistor because of diffused reflection. In addition, thermistor has nonlinear resistance-temperature characteristic and this nonlinearity is also drawback to accurate measurement, since it is almost impossible to correct this nonlinearity accurately.

A pyroelectric detector gives a signal with high S/N ratio (> 100) and high time response (~ 1 ms). Several problems concerning the detector are pointed out, that is, spurious signal and temporal change in sensitivity. The cause of the spurious

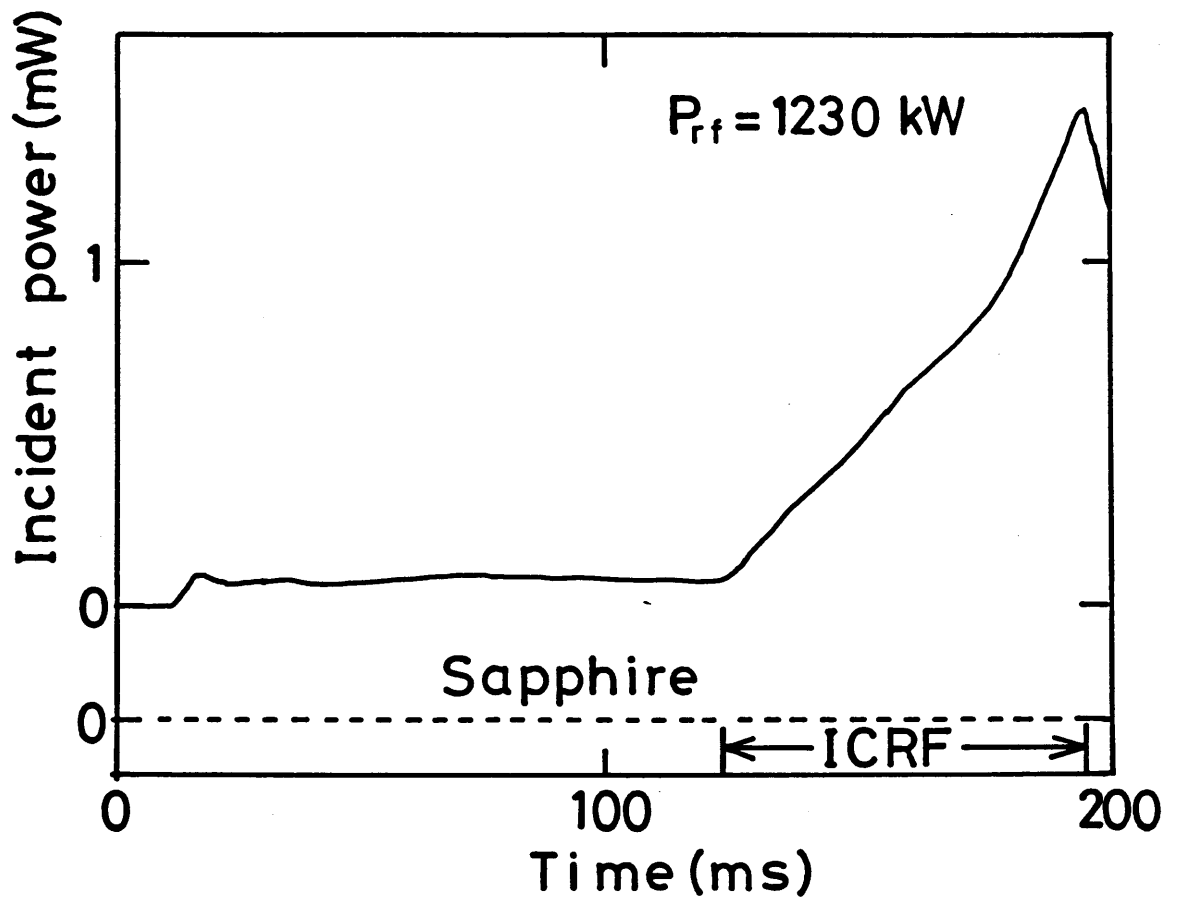


Fig.3-19 Signals from pyroelectric detectors viewing the plasma center. The dashed line shows the signal obtained by a pyroelectric detector viewing through a sapphire window which cuts photons with short wavelength ($\lambda < 2000 \text{ \AA}$).

signal is considered to be due to photoelectric effect. A pyroelectric detector acts as the element of a current source.

The current signal from a pyroelectric detector is of the order of 10^{-10} A in the application to the JIPP T-IIU tokamak. Even a small current due to a non-pyroelectric effect causes a serious spurious signal to the detector. This is the reason why a pyroelectric detector can easily suffer from falsification. A pyroelectric detector without a mask accepts the direct incidence of photons on a non-grounded electrode. Electrons are emitted from the electrode due to the photoelectric effect by these photons and a resulting current is induced. This current would represent the falsification (Fig.3-20). The photons in the vacuum ultraviolet region have a high photoelectric yield efficiency.⁵¹⁾ The value estimated from this efficiency is sufficient to explain the magnitude of the falsification observed in the experiment (i_s in Fig.3-8(a)). It is expected that falsification due to an influx of charged particles and an externally induced electric field (as well as the direct incidence of photons) can be avoided by using a mask.

The results in Fig.3-6 show that the reflectivity of the absorber of the detector for HeNe laser light changes with the change in the detector surface but the sensitivity does not change. Apparently, sensitivity without considering the reflected power shows temporal change. Taking the high absorption of the major fraction of the plasma radiation

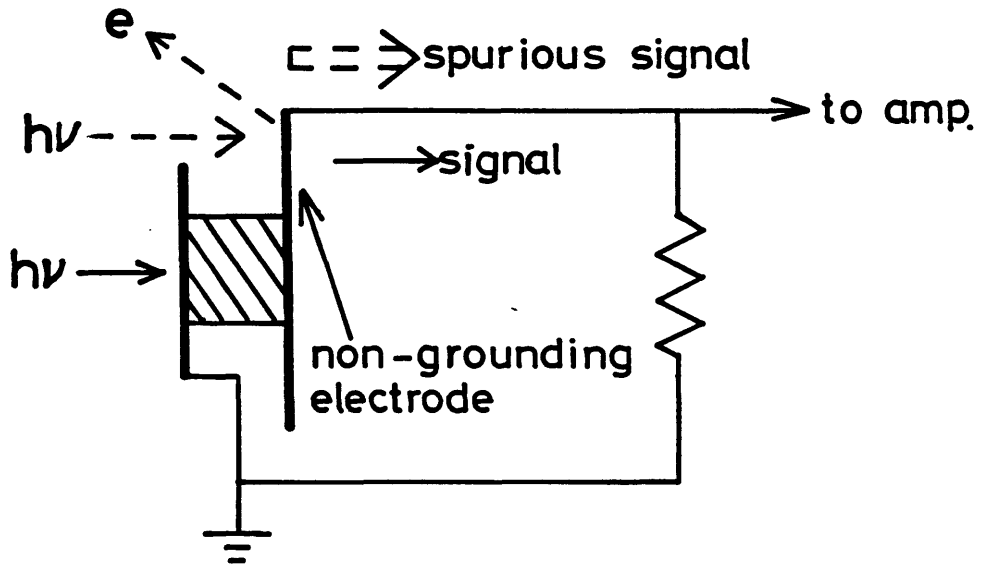


Fig.3-20 Schematic geometry showing the spurious signal from the pyroelectric detector.

into consideration, it can be concluded that the calibration method which takes into account the reflected power is a reasonable method. The change in the reflectivity can be attributed to a contamination of the detector surface. Some of the materials installed inside the vacuum vessel might be deposited on the surface of the detector. However, the deposition is too thin to change the thermal capacity and then the sensitivity of the detector.

Figure 3-14 shows that characteristics of the metal-film bolometer is well expressed by the heat conduction equation.

This fact supports that the detector has well defined characteristics. A correction for thermal cooling is effective for the radiation measurement.

CHAPTER IV

Experimental Equipments for Bolometric Measurement

The present study on radiation power has been carried out on the JIPP T-IIU tokamak plasma. Information on radiation power is directly obtained from the bolometric measurement, provided that a power due to charge-exchanged neutral particles is estimated. It is also complemented by spectroscopic measurement.

We constructed the bolometric system composed of pyroelectric detectors and metal-film bolometers. This selection of detectors is made from the standpoint of high reliability. We applied this bolometric system to the JIPP T-IIU tokamak plasma and investigated the performance of the system.

(i) JIPP T-IIU Device

The objective of the JIPP T-IIU tokamak is to study the confinement and heating of high temperature plasma. Especially, high power ICRF heating experiment is vigorously carried out in the two-ion-hybrid heating regime. The schematic drawing of the JIPP T-IIU experimental arrangement is shown in Fig.4-1. The applied frequency is 40 MHz and hydrogen-to-total ion density

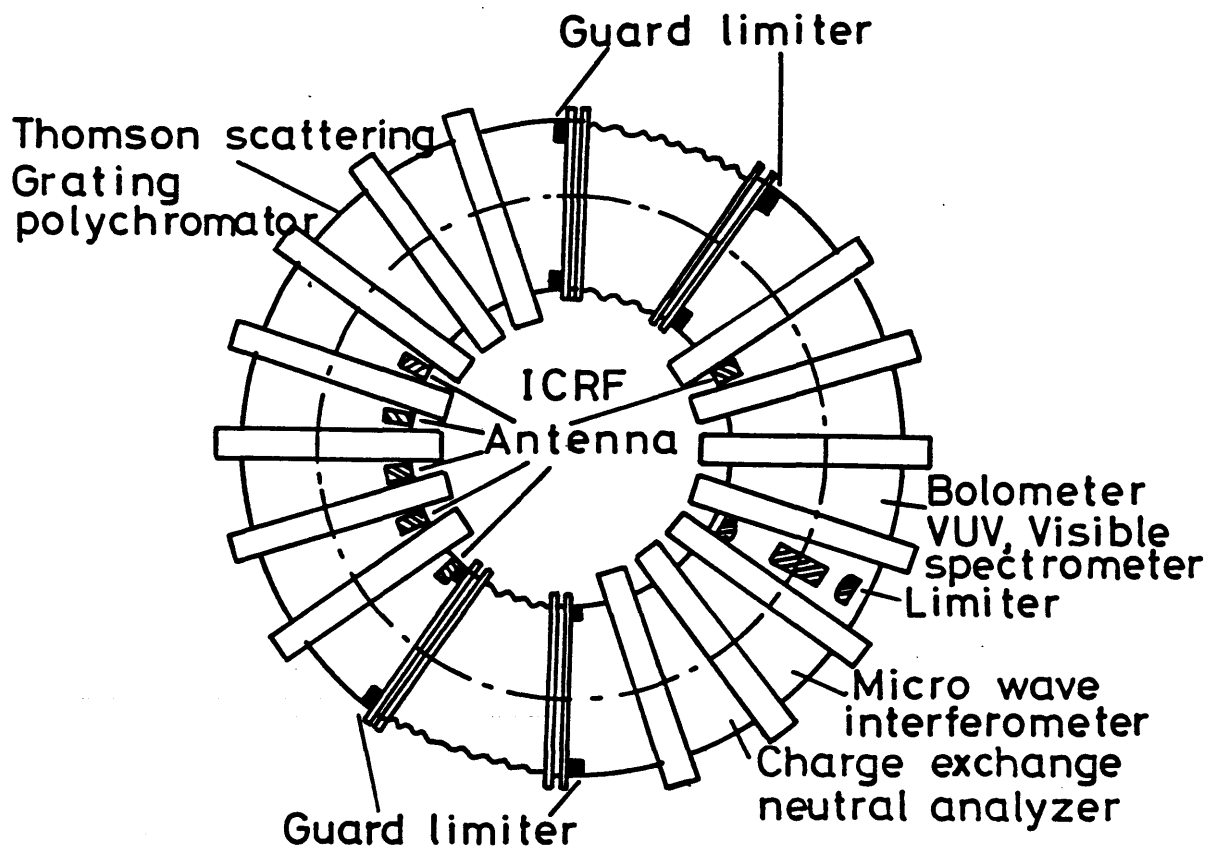


Fig.4-1 Locations of the major diagnostics around JIPP T-IIU in relation to ICRF antennae and limiters.

ratio $n_H/(n_H+n_D)$ is 10 %. The two-ion-hybrid resonance layer for the toroidal magnetic field strength of 3 T in this series of experiments is located near the plasma center. The half-turn antennae are installed in the high field side at six different toroidal positions (Fig.4-1). Each antenna has a capacity to couple the rf power of 0.5 MW to the plasma. Two types of limiters were used. One is stainless steel #304 (S.S.) limiters and the other is carbon (C) limiters. Both of the limiters are of the same shape and size. In order to reduce residual gases, C limiters were baked at temperature around 150 °C for 48 hours.

The vacuum vessel, the antennae and the Faraday shield are made of stainless steel #304. A glow discharge system was prepared for carbonization of inner wall and in-vessel components.

Diagnostics used in the JIPP T-IIU experiments are also shown in Fig.4-1. The line-averaged electron density is measured with 4-mm or 2-mm microwave interferometer. The radial profile of electron density is also measured with HCN laser interferometer by scanning the plasma cross section on a shot-to-shot basis. The temporally and spatially resolved electron temperature is obtained with a multichannel polychromator, which is calibrated by Thomson scattering method with a ruby laser. The ion temperature at the center is measured by analyzing the energy of charge-exchanged neutral atoms emerging from the plasma. The bolometric and the spectroscopic (VUV, visible) measurements are carried out at the same toroidal

section (Fig.4-1). Further details of the bolometric measurement will be described later.

(ii) Bolometric System

The temporally and spatially resolved radiation power (emissivity) is obtained from the signals of the twelve pyroelectric detectors through the Abel inversion. Each pyroelectric detector has a mask to eliminate the spurious signal.

Figure 4-2 shows a schematic diagram of the experimental layout. This enables a simultaneous view of almost an entire vertical cross section, ranging from full plasma radius (23 cm) at the bottom to 20 cm at the top of the plasma. A vertical collimator gives a spatial resolution of 2 cm at the plasma center. The total radiation power is also monitored with a metal-film bolometer which views a solid angle of about 2π steradians.³³⁾ Assuming that the plasma emission is entirely isotropic, the total radiation power is measured directly from the product of the power onto the detector and the areal ratio of vacuum chamber to that of detector sensitive region. The metal-film bolometer and pyroelectric detectors are selected from the viewpoint of a reliable measurement, because these detectors have high time response and well defined thermal characteristics. In addition, the absolute value of the radiation power can be made sure from both of the results, because these detectors

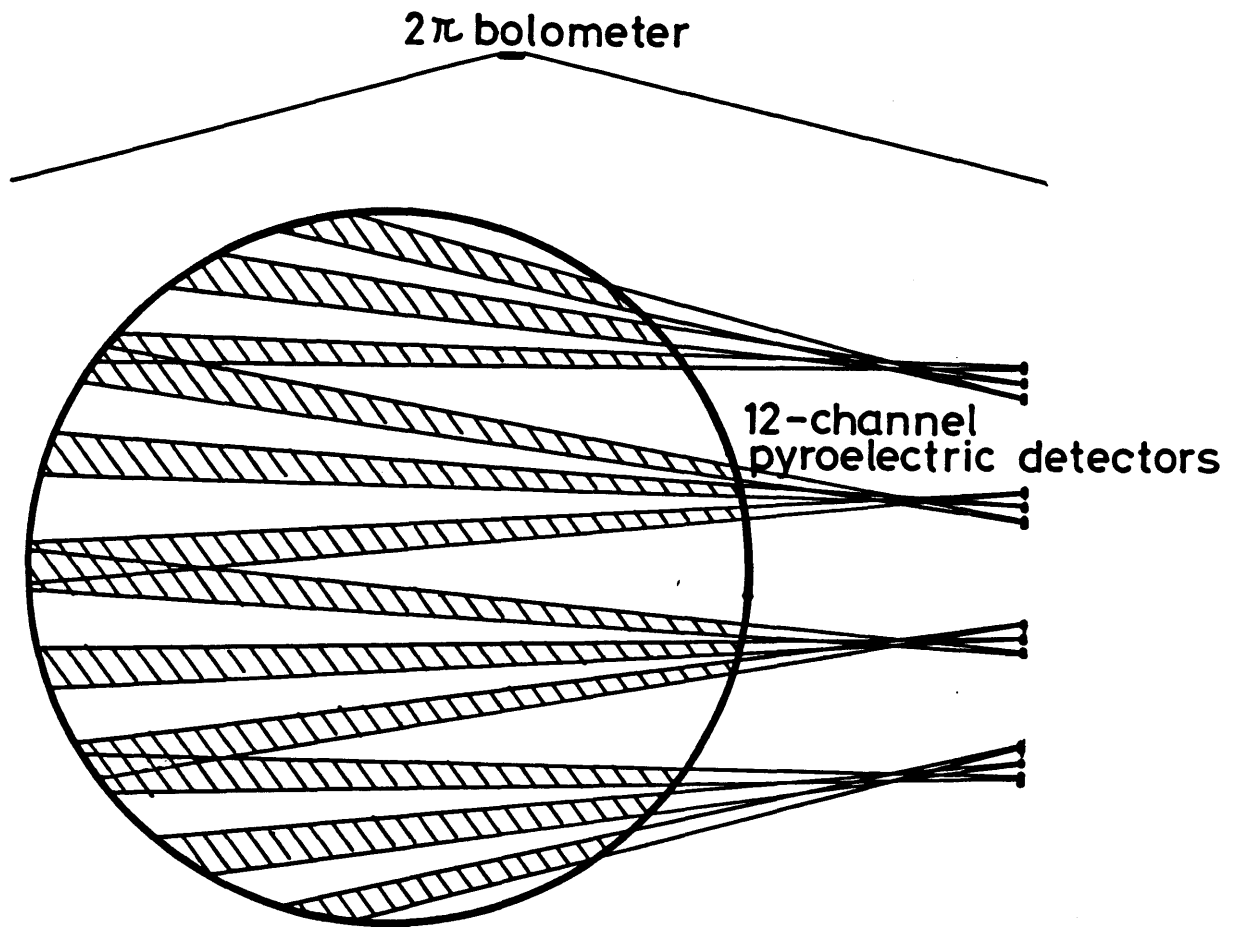


Fig.4-2 Geometric arrangement of the 2π bolometer and the 12-channel detectors with a mask.

are calibrated with several different methods.

Comparison between total radiation power measured with "2 π bolometer" and that with twelve pyroelectric detectors are shown in Fig.4-3. The latter is obtained by integrating over the spatial profile. Both of the values agree with each other within 10 %.

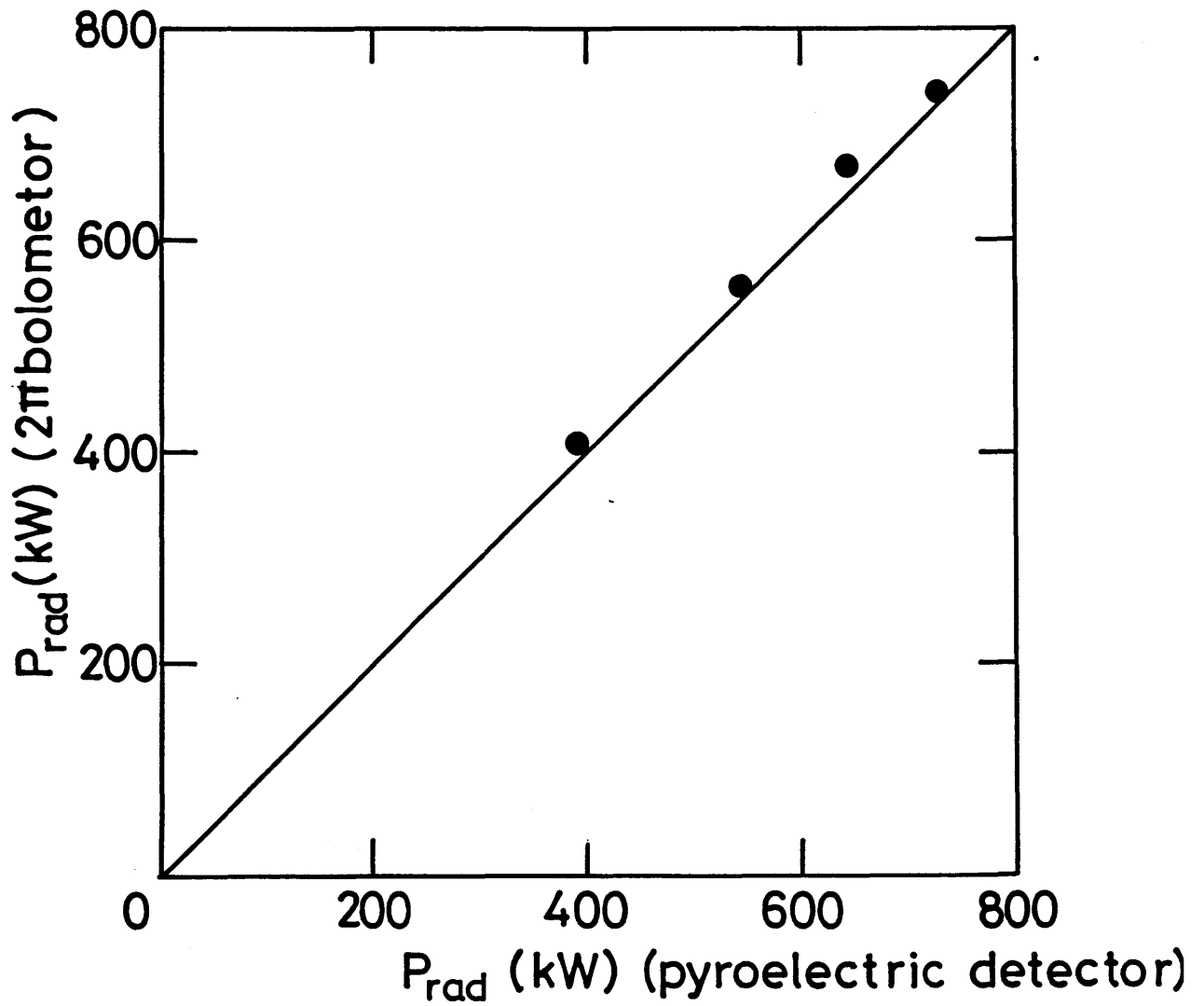


Fig.4-3 A plot of the total radiation power obtained through the integration of the spatial distribution against that obtained with the 2π bolometer.

CHAPTER V

Experimental Results on a Tokamak Plasma

In this chapter, experimental results on the JIPP T-IIU tokamak are described. The experiments were carried out under the following three conditions.

- (i) In use of stainless steel (S.S.) limiters.
- (ii) In use of carbon (C) limiters.
- (iii) With carbonization in use of C limiters.

(i) ICRF Heating Experiment with Stainless Steel Limiters

The first ICRF experiment was carried out with S.S. limiters. The time behaviors of total radiation power P_{rad} measured with the 2π bolometer and emissivity E measured with pyroelectric detectors are shown in Fig.5-1. The ICRF power of 0.15 MW is injected from $t=75$ ms to 110 ms. Even before ICRF injection, that is, during ohmic plasma, radiation loss is the major fraction of the plasma energy loss ($P_{\text{rad}}/P_{\text{OH}} \sim 50\%$).

Emissivity in a core plasma accounts for the substantial fraction of radiation power. Moreover, radiation power continues to increase during ICRF heating and reaches 80 % of input power ($P_{\text{OH}} + P_{\text{rf}}$). Such a radiation dominant plasma is unstable and the injection power of ICRF is limited to 0.4 MW because of a

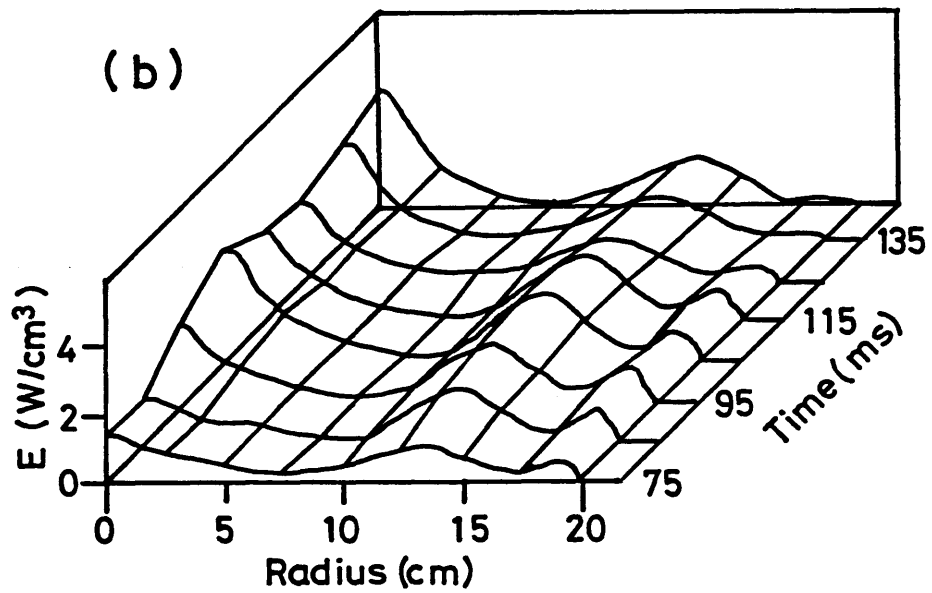
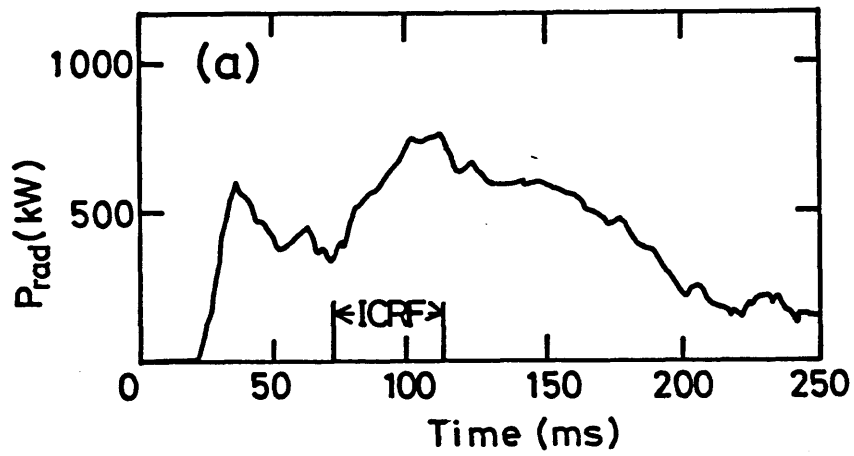


Fig.5-1 (a) Time behavior of total radiation power and (b) spatially and temporally resolved emissivity in the experiment with S.S. limiters.

current disruption.

The effective heating of ion and electron is not observed, because the increment in radiation power due to ICRF injection exceeds the ICRF power ($\Delta P_{\text{rad}} / P_{\text{rf}} \sim 2.8$). The radiation power from a core plasma increases during ICRF heating. The value of Z_{eff} is large (5~7) and supports high emissivity throughout plasma region. The reduction in radiation loss is indispensable to the favorable experiments of both ohmic and ICRF heated plasmas.

(ii) ICRF Heating Experiment with Carbon Limiters

By the use of C limiters, the total radiation power in ohmically heated plasma is remarkably reduced ($P_{\text{rad}} / P_{\text{OH}} \sim 30 \%$) compared with S.S. limiters and the injection power of ICRF is raised to more than 1 MW without a current disruption. A typical plasma discharge at an injection power of 1 MW is shown in Fig.5-2. Electron temperature increases as soon as ICRF power is injected and results in the decrease in loop voltage. Its increment becomes maximum (1340 → 1750 eV) with a lapse of 8 ms.

After its increment, electron temperature begins to decrease with a large rate. Although the decrease becomes small around a lapse of 40 ms, electron temperature again begins to decrease with a large rate till the end of ICRF pulse. Ion temperature increases according to ICRF injection and reaches the maximum

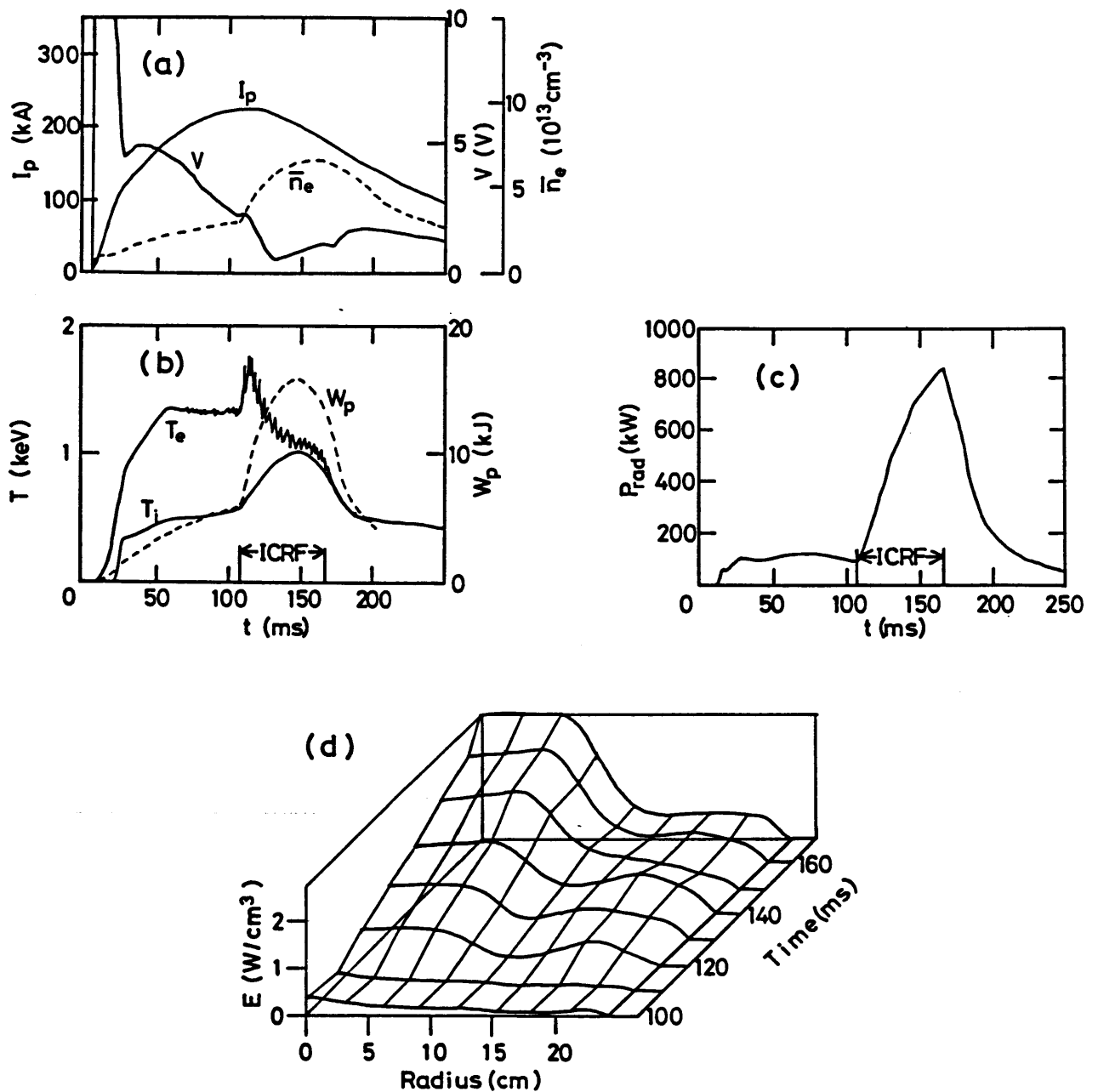


Fig.5-2 A typical discharge in the ICRF experiment ($P_{rf}=1$ MW) with C limiters. Time behaviors of (a) loop voltage V , plasma current I_p , line averaged electron density \bar{n}_e , (b) electron and ion temperatures $T_e(0)$, $T_i(0)$ and plasma energy W_p . (c) Time behavior of total radiation power and (d) spatially and temporally resolved emissivity in the experiment with C limiters.

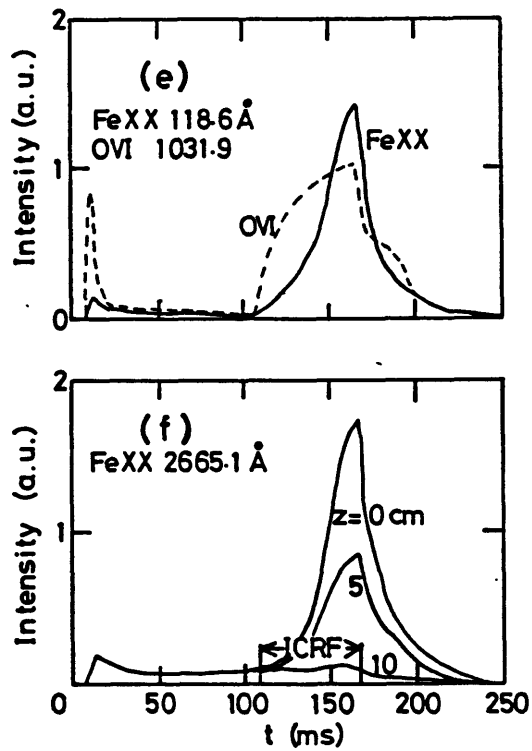


Fig.5-2 A typical discharge in the ICRF experiment ($P_{rf} = 1$ MW) with C limiters. Time behaviors of (e) line intensities (FeXX, OVI) and (f) intensities of forbidden line (FeXX) measured by vertically scanning the plasma in the ICRF experiment with C limiters.

value of 1 keV with a lapse of 40 ms. However, ion temperature do not keep its maximum value during ICRF injection and begin to decrease. Plasma energy W_p reaches the maximum with a lapse of 35 ms and begins to decrease during ICRF heating.

Total radiation power P_{rad} and emissivity E are shown in Fig.5-2(c)(d). In comparison with the case of S.S. limiters, the total radiation power in ohmically heated plasma is remarkably low (370 kW → 130 kW). The ratio of P_{rad}/P_{OH} is about 30 %. In compliance with ICRF injection, however, total radiation power P_{rad} continues to increase during ICRF and reaches $P_{rad}/(P_{OH}+P_{rf}) \sim 50 \%$. Emissivity in central region increases to the level of 2.6 W/cm³ (Fig.5-3). Large radiation loss from a core plasma is quite unfavorable from the viewpoint of the energy confinement.

The value of Z_{eff} slightly increases from 3.3 to 3.9 during ICRF heating. Emissivity in peripheral region reaches a maximum value in 10 ms and keeps a roughly constant value during ICRF.

The VUV and visible spectroscopic measurements are carried out in order to investigate the impurities responsible to the radiation power. The main impurities in the JIPP T-IIU plasma are Fe, O and C. Line intensities of Cr and Ni are small compared with Fe and the estimated Cr density is smaller than that of Fe by a factor of 1/4. The estimated Ni density is found negligible. These estimated values well correspond to component ratio of stainless steel. The time behaviors of impurity lines with low and high ionization potentials (I.P.) are represented

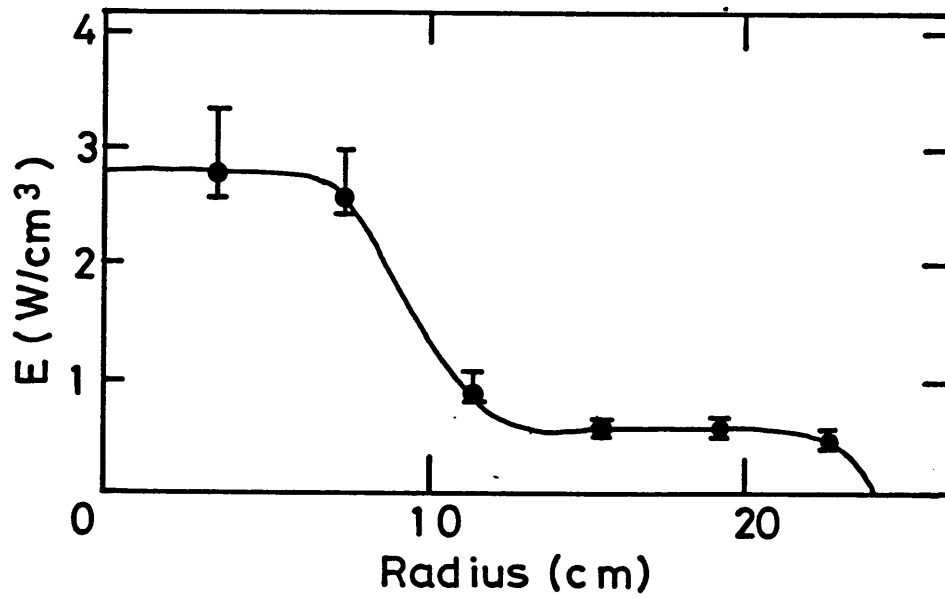


Fig.5-3 Radial profile of radiation power (emissivity) at the end of ICRF pulse ($t=170$ ms).

by those of OVI (I.P.=138 eV) and FeXX (I.P.=1500 eV) in Fig.5-2(e), respectively. The intensity of impurity lines with low I.P. rapidly increases and keeps a roughly constant value during ICRF. The major fraction of such impurities exists in peripheral region. The time behavior of these line intensities agrees with that of emissivity in peripheral region. The line intensities with high I.P. continue to increase during ICRF. In order to investigate the radial density distribution of Fe^{19+} , the intensities of forbidden line are measured by scanning the plasma cross section on a shot-to-shot basis (Fig.5-2(f)). The result shows that the major fraction of Fe^{19+} exists in central region ($r \leq 5$ cm). Emissivity in the same region continues to increase during ICRF pulse. The time behavior of emissivity in the central region and that of line intensities with high ionization states (for example FeXX) agree with each other.

Impurity line intensities against total radiation power are plotted in Fig.5-4 for the case with C limiters. Total radiation is roughly proportional to line intensities of Fe. The Fe impurities of several ionization states may be attributed to the major fraction of radiation power.

Regarding electron temperature, a large decrease after a lapse of 8 ms from ICRF injection may be due to the increase in electron density and that in the equipartition power flow from electron to ion, which results in the increase in ion temperature and makes the difference between electron and ion temperatures

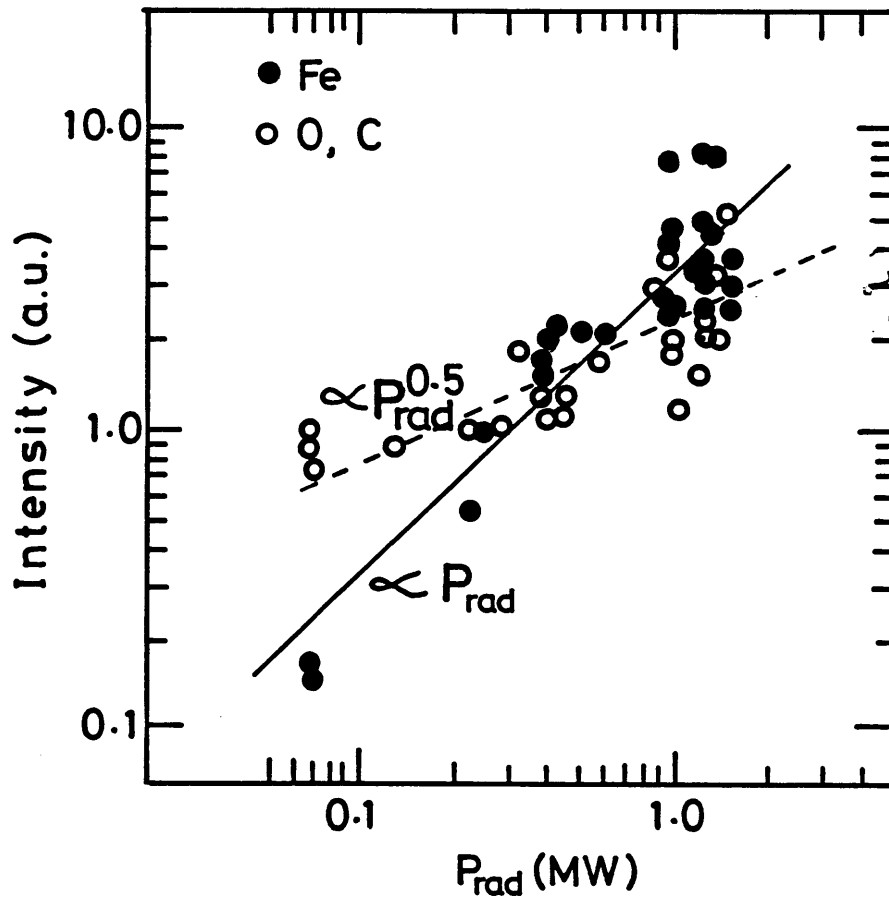


Fig.5-4 Line intensity plotted as a function of total radiation power P_{rad} in the experiment with C limiters.

small. The decrease in electron temperature in the late ICRF pulse may be due to the increase in the radiation loss, which is substantial fraction of plasma energy loss. The decrease in ion temperature in the late ICRF pulse may be due to that in the equipartition power flow from electron to ion, which is caused by the decrease in electron temperature.

(iii) ICRF Heating Experiment with Carbonization

Carbonization is carried out in JIPP T-IIU in expectation of the reduction in metal impurities. Total radiation power is remarkably reduced during ICRF by making carbonization. The maximum power of ICRF system is delivered to plasma (1.35 MW) without the current disruption. A typical plasma discharge at an injection power of 1 MW is shown in Fig.5-5. The decrease in electron temperature in the later part of ICRF pulse is smaller than that of the case without carbonization. The decrease in plasma energy is not seen unlike the case without carbonization.

The ion temperature increases and keeps the maximum value during ICRF. Total radiation power P_{rad} and emissivity E are shown in Fig.5-5(c)(d). The ratio of $P_{\text{rad}} / P_{\text{OH}}$ is 15 % before ICRF pulse.

The maximum value of $P_{\text{rad}} / (P_{\text{OH}} + P_{\text{rf}})$ is 20 %. Emissivity throughout the plasma remains at a low level (0.2 W/cm^3) (Fig.5-6) compared to input power density during ICRF unlike the case without carbonization. This level of emissivity has

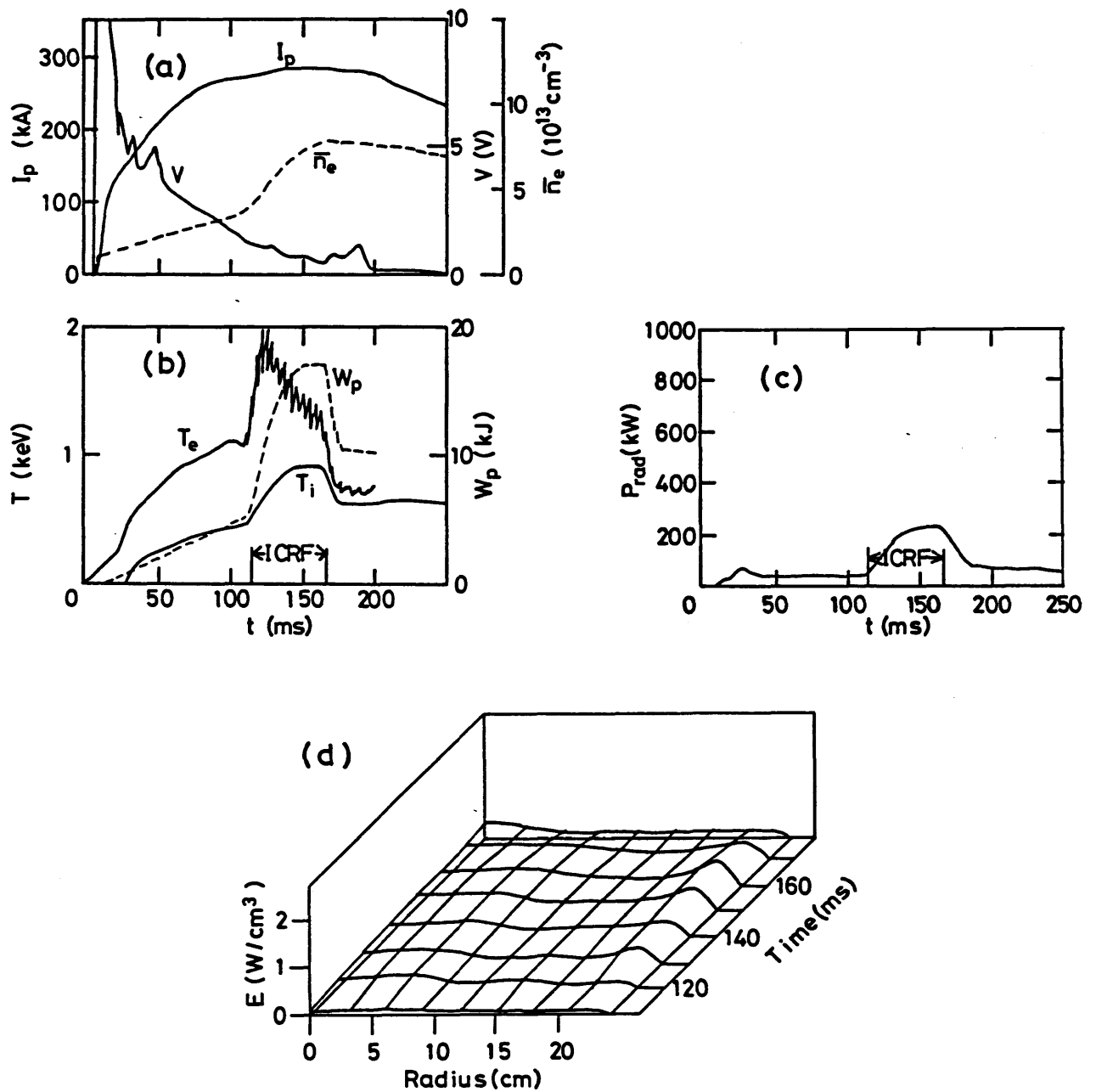


Fig.5-5 A typical discharge in the ICRF experiment ($P_{rf} = 1 \text{ MW}$) with carbonization. Time behaviors of (a) loop voltage V , plasma current I_p , line averaged electron density \bar{n}_e , (b) electron and ion temperatures $T_e(t)$, $T_i(t)$ and plasma energy W_p . (c) Time behavior of total radiation power and (d) spatially and temporally resolved emissivity in the experiment with carbonization.

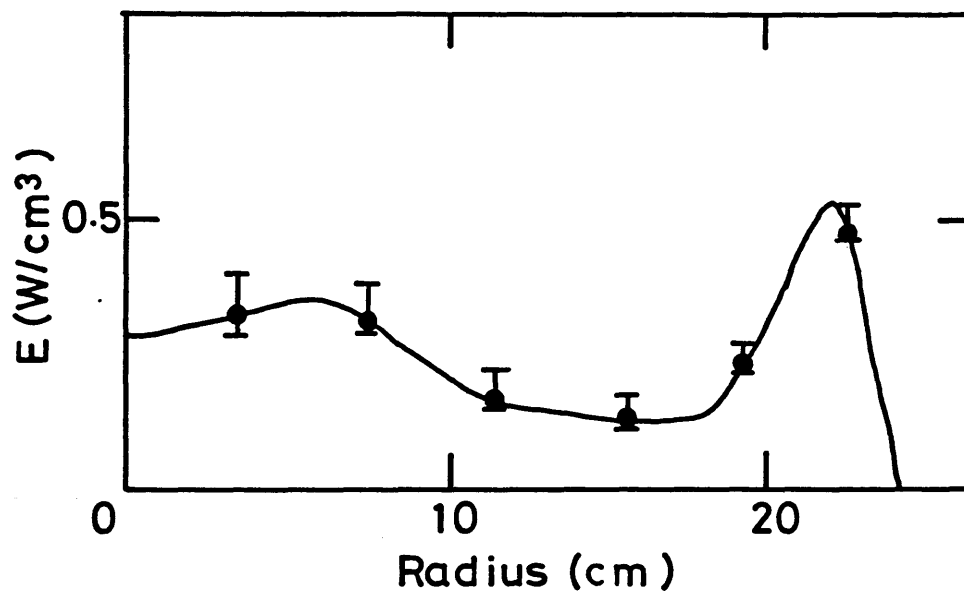


Fig.5-6 Radial profile of radiation power (emissivity) at the end of ICRF pulse ($t=170$ ms).

little effect on the power balance. Low level of central emissivity is favorable from the viewpoint of the energy confinement. The value of Z_{eff} with carbonization remains 1.2 during ICRF heating. The equipartition power flow from electron to ion is larger than that of the case without carbonization because of small decrease in electron temperature. This is the reason why the ion temperature do not decrease during ICRF heating.

The maximum value of radiation power P_{rad} against the ICRF power is plotted in Fig.5-7 for the three cases. Replacing S.S. limiters by C limiters, total radiation power at ohmic plasma phase ($P_{rf}=0$) is reduced by a factor of 1/4. In addition, it is also reduced by a factor of 1/3 by making carbonization. This indicates that the limiters are the major impurity sources in the ohmic phase. The total radiation power linearly increases as the power of ICRF injection is raised. The rate of increase against the ICRF power is little affected by replacing S.S. limiters by C limiters. On the other hand, the rate of increase is reduced by a factor of 1/4 by coating vacuum components with carbon (carbonization). This indicates that the antennae, the Faraday shield and the vacuum vessel are the major impurity sources in the ICRF heating phase. The ratio of line intensity with carbonization to that without carbonization is plotted in Fig.5-8. Considering that the difference between the plasma parameters (electron density and temperature) for the two

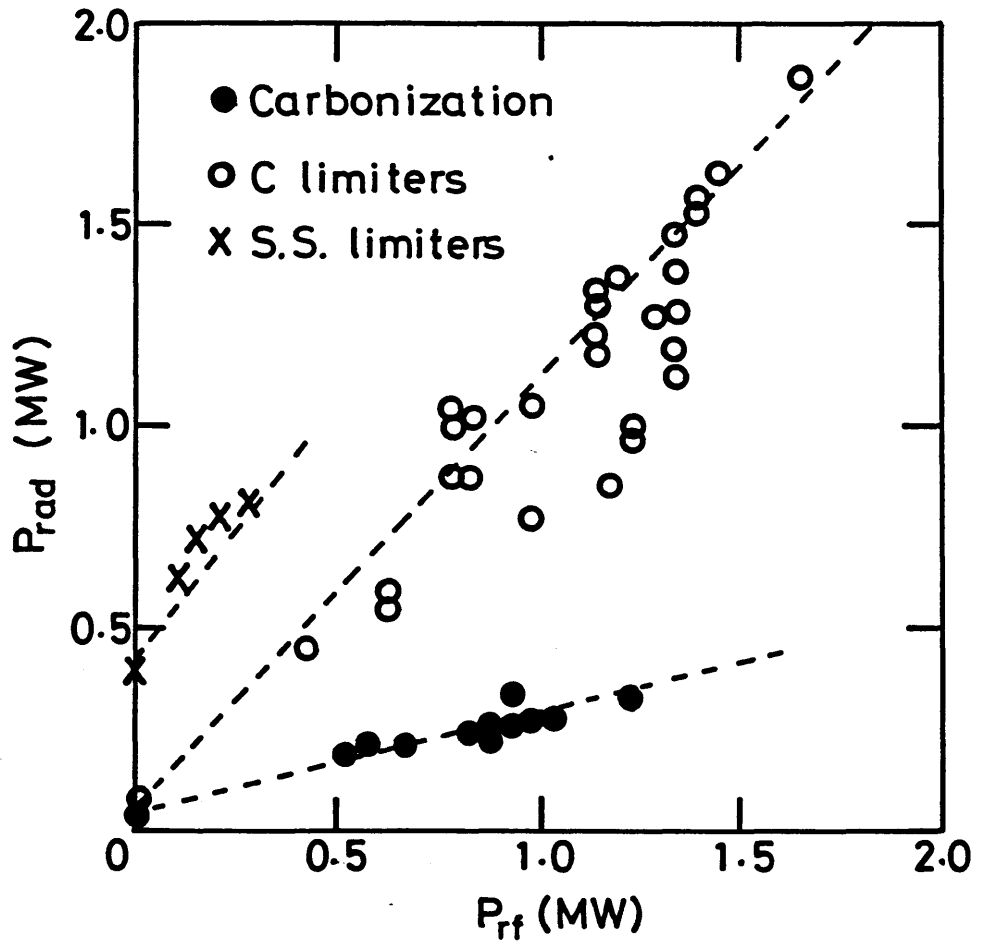


Fig.5-7 Total radiation power P_{rad} plotted as a function of the ICRF power P_{rf} for the three cases; S.S. limiters, C limiters (without carbonization) and Carbonization.

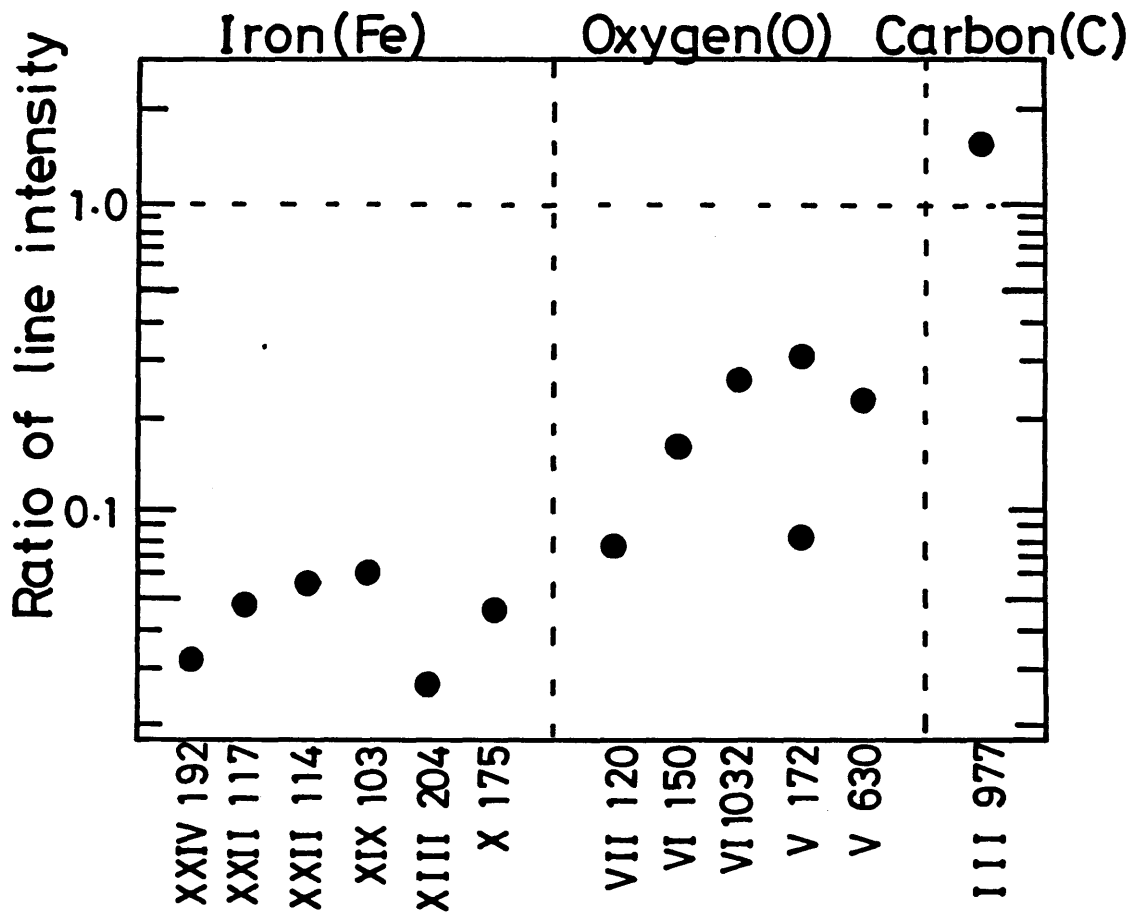


Fig.5-8 Ratio of line intensity with carbonization to that without carbonization.

cases is not so large, the ratio of line intensity is proportional to that of abundance. By making carbonization, impurity abundances of Fe, O and C have changed to 0.05 ± 0.02 , 0.2 ± 0.1 and 1.5, respectively. The scatter of the obtained results is due to poor reproducibility of the discharge.

It is clearly shown from the experimental results that carbonization has an effect of reducing the amount of Fe. The Fe impurities may be responsible to the major fraction of radiation power without carbonization (with C limiters).

(iv) Discussion

The estimation of the power due to charge-exchanged neutral particles (charge-exchange loss) is required before entering into a discussion on the radiation from the tokamak plasma, because information from a bolometric measurement includes the charge-exchange loss. For both of cases with and without carbonization, charge-exchange spectra of deuterium and hydrogen are shown in Fig.5-9. The ratio of the value of hydrogen to that of deuterium reflects the hydrogen-to-deuterium density ratio ($n_H/(n_H+n_D) \sim 10\%$). By making carbonization, neutral particles with low energy ($E > 3.7$ keV for deuterium, $E > 4.3$ keV for hydrogen) increase and neutral particles with higher energy decrease. Estimating the charge-exchange loss due to deuterium and hydrogen, it increases by a factor of 3 by carbonization. On the contrary, the bolometric signal, which views the plasma center like the charge-exchange neutral analyser, decreases by a factor of 1/6 by carbonization (Fig.5-10). The above results show that the charge-exchange loss has less contribution to the bolometric information ($< 6\%$) in the case without carbonization.

The highest amounts of respective impurities are evaluated from the effective ionic charge Z_{eff} . Oxygen and carbon may be fully ionized ($Z=8, 6$) in core plasma ($T_e \sim 1$ keV). The average charge state of Fe is roughly 20 in a core plasma.^{10,11)}

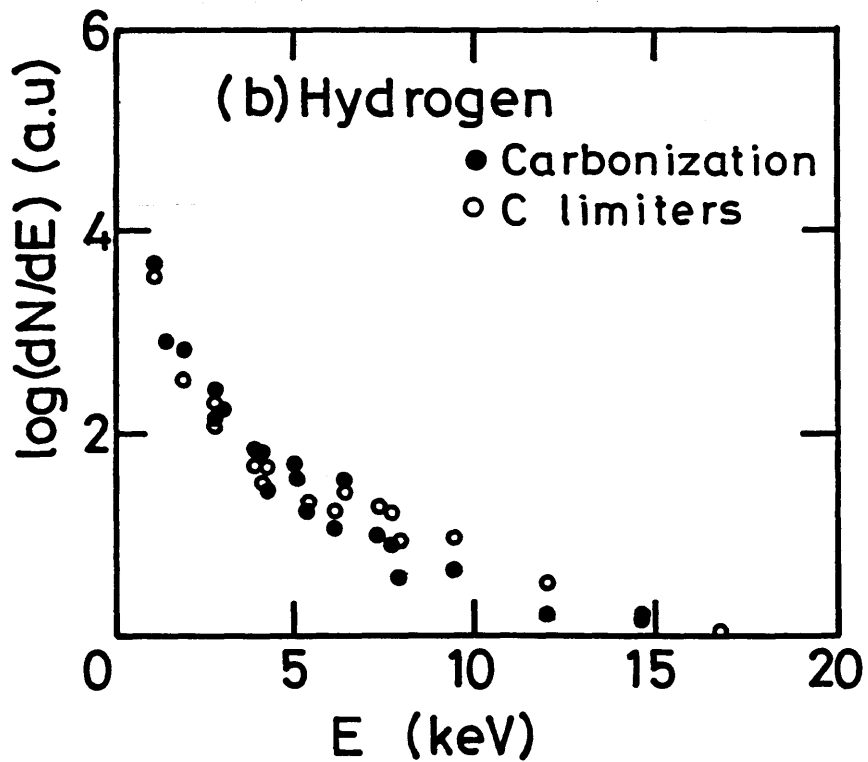
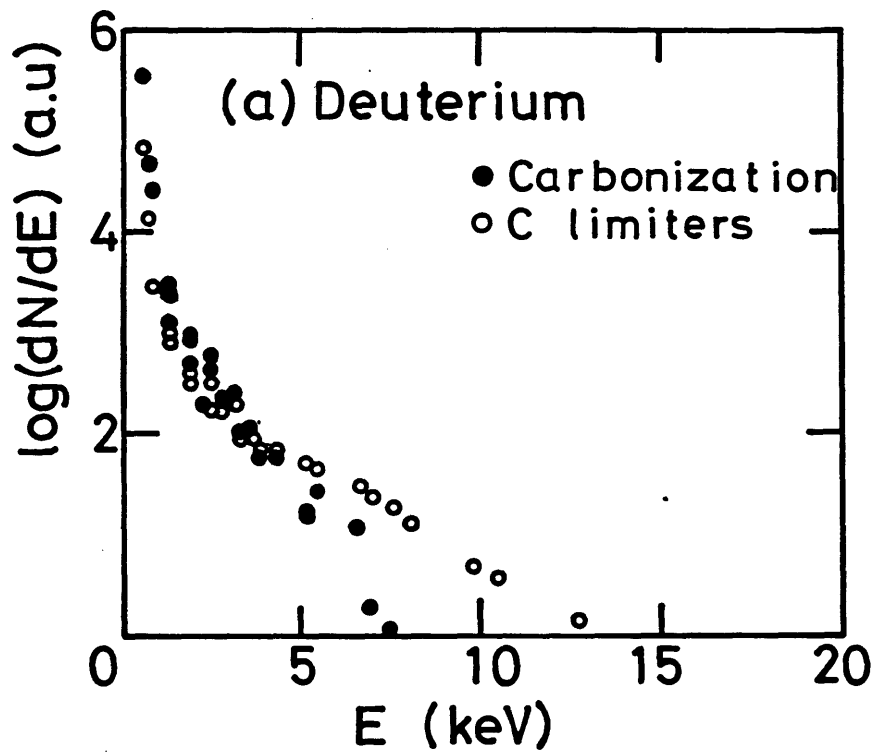


Fig.5-9 Charge-exchange spectra of (a) deuterium and (b) hydrogen. By making carbonization, the charge-exchange loss due to deuterium and hydrogen increases by a factor of 3.

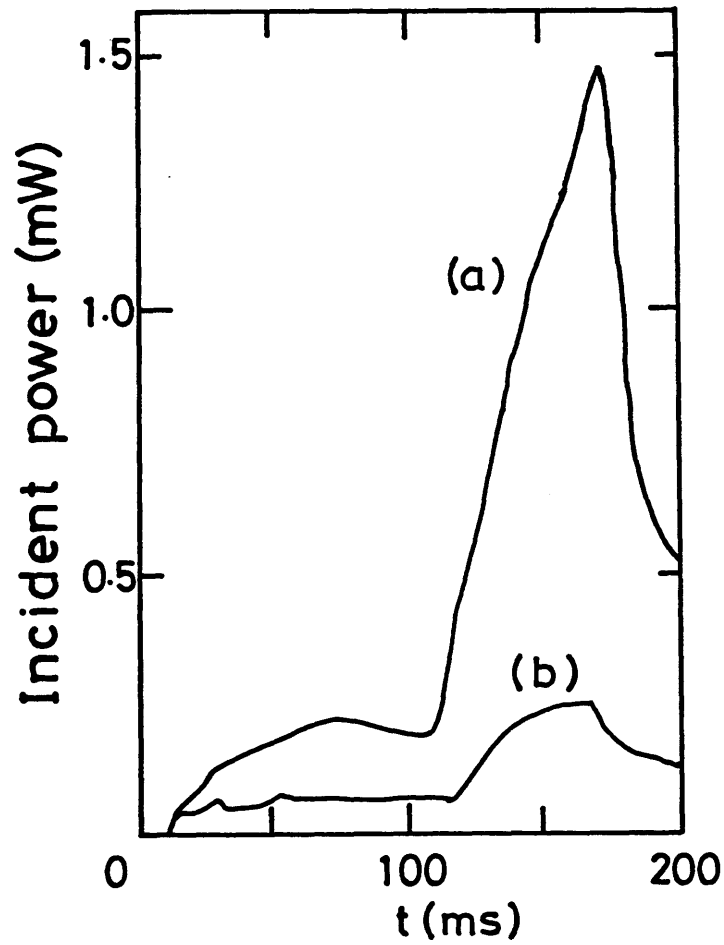


Fig.5-10 Input power to pyroelectric detector (P_{chord}) viewing the plasma center. A symbol of (a) denotes P_{chord} in the case without carbonization (C limiters) and that of (b) denotes P_{chord} in the case with carbonization.

Regarding the ICRF experiment without carbonization (C limiters), the highest amount of Fe, O and C in a core plasma are obtained from $Z_{\text{eff}} = 3.9$ as $n_{\text{Fe}}/n_e \sim 8 \times 10^{-3}$, $n_{\text{O}}/n_e \sim 0.05$ and $n_{\text{C}}/n_e \sim 0.1$, respectively. Assuming that coronal equilibrium holds in core region, abundances of respective impurities are estimated from radiative cooling rates,¹⁰⁻¹²⁾ electron density and emissivity by eq.(2-8). The radiative cooling rates of O and C is too small to explain the central emissivity (2.6 W/cm^{-3}) within their highest amounts and Fe impurities contribute to the major fraction of the central emissivity. The abundance of Fe obtained from its radiative cooling rates ($5.8 \times 10^{-26} \text{ Wcm}^3$ for $T_e \sim 1 \text{ keV}$)¹²⁾ is $n_{\text{Fe}}/n_e \sim 7 \times 10^{-3}$, whose value satisfies its highest amount. The abundance of Fe may contribute to the major fraction of total radiation power because of its high radiative cooling rate, which is several tens times as large as those of O and C in the wide range of electron temperature. Regarding the ICRF experiment with carbonization, the highest amount of Fe, O and C in a core plasma are obtained from $Z_{\text{eff}} = 1.2$ as $n_{\text{Fe}}/n_e \sim 5 \times 10^{-4}$, $n_{\text{O}}/n_e \sim 4 \times 10^{-3}$ and $n_{\text{C}}/n_e \sim 7 \times 10^{-3}$, respectively.

All the impurities remains at a low level. From the ratio of line intensity in Fig.5-8, the abundance of Fe is reduced to 1/20 throughout the plasma region by carbonization. Its central abundance is estimated to be $n_{\text{Fe}}/n_e \sim 3.5 \times 10^{-4}$. The estimated emissivity from this value by eq.(2-8) is 0.13 W/cm^{-3} and agrees with bolometric measurement (0.2 W/cm^{-3}). Emissivity swells in

peripheral region (0.5 W/cm^3). This may be attributed to C, which results from the carbonization. Because the radiative cooling rate of C exceeds that of Fe under the condition that electron temperature is sufficiently low. Such a condition may hold in plasma edge with a swell of emissivity.

Total radiation power of ohmic plasma with S.S. limiters is larger than that with C limiters (without carbonization) by a factor of 5 (Fig.5-7). This difference may be attributed to the impurity flux of Fe released from limiters. On the other hand, the total radiation power increases at the same rate of increase with the ICRF power. The above result indicates that impurity flux of Fe released from the antennae, the Faraday shield and the vacuum vessel is mainly responsible to the increase in total radiation due to ICRF injection. The above-mentioned results are summarized in Table I.

Table I

		S.S. limiters	C limiters	
		Without carbonization	Without carbonization	Carbonization
Ohmic	Z_{eff}	~ 5	~ 3	~ 1.2
	P_{rad}/P_{OH}	$\sim 50\%$	$\sim 30\%$	$\sim 15\%$
ICRF	Z_{eff}	~ 7	~ 4	~ 1.2
	$P_{rad}/(P_{OH}+P_{RF})$	$\sim 80\%$	$\sim 50\%$	$\sim 20\%$
	$E(r=0)$	4.5 W/cm^2	2.6 W/cm^2	0.2 W/cm^2
	n_{Fe}/n_e	—————	$\sim 7 \times 10^{-3}$	$\sim 4 \times 10^{-4}$
	n_O/n_e	—————	$\ll 0.05$	$< 4 \times 10^{-3}$
	n_C/n_e	—————	$\ll 0.1$	$< 7 \times 10^{-3}$

Table I List of Z_{eff} , radiation power and impurity abundances for the three cases; S.S. limiters, C limiters (without carbonization) and Carbonization.

CHAPTER VI

Summary

The characteristics of presently used thermistor, pyroelectric detector and metal-film bolometer were investigated with the aim of attaining a highly reliable bolometric measurement. The spurious signal which appears on a pyroelectric detector was efficiently eliminated by setting a mask close to the detector, thus avoiding the direct incidence of photons at the electrode. This is verified with the consistency of integrated value of the signal. Calibration of a pyroelectric detector was performed with a HeNe laser in consideration of reflections on the detector surface. No temporal change was observed on the sensitivity determined in such a way (within 1 %). Measurements of sensitivity were made over a wide range of input power to detector and proved that the linearity of the signal is high (< 2 %) within range of radiation measurement from the tokamak plasma. A thin metal-film bolometer was developed with high sensitivity ($12.9 \Omega/\text{mJ}$), high time response ($\sim 3 \mu\text{s}$) and well defined thermal characteristics. Calibration of the metal-film bolometer was performed by supplying a bias current

through its resistor. This method has an advantage of being able to measure the input power to detector with high accuracy and of being calibrated *in situ*. Thermal characteristics of this detector are investigated by solving a heat conduction equation fitting in with the detector and well defined thermal characteristics is supported by the fact that the heat conduction equation well explains the time behavior of the signal at calibration.

We constructed a bolometric system which consisted of twelve pyroelectric detectors and a metal-film bolometer. This measurement system gives the information on the total radiation power with high time response (~ 3 ms) and the emissivity with high time response (~ 1 ms) and high spatial resolution (2 cm).

The total radiation power agrees with that obtained by integrating over the spatial profile within 10 %.

We studied the radiation due to impurities on the tokamak plasma by means of this bolometric system. The radiation loss from a plasma core plays an important role on tokamak discharges with S.S. and C limiters (without carbonization). The radiation power increases during ICRF heating, and electron and ion temperatures and plasma energy decrease. The increase in the radiation power is brought about by Fe impurities.

Although C limiters have an effect to suppress radiation power from the ohmic plasma ($P_{\text{rad}} / P_{\text{OH}} \sim 30$ %), it is still high for the ICRF heated plasma ($P_{\text{rad}} / (P_{\text{OH}} + P_{\text{rf}}) \sim 50$ %). This is

because the antennae, the Faraday shield and the vacuum vessel may become sources of Fe impurities. Carbonization suppresses Fe impurities and radiation power even for high power ICRF heated plasma. Radiation loss is no longer major fraction of plasma energy loss ($< 20\%$). The major impurity, Fe decreases to a negligible level ($n_{Fe}/n_e \sim 0.04\%$) and is reduced to $1/20$ throughout the plasma region. This results well explain the measured emissivity in a core plasma. It is worth while to note that C impurity in a core plasma remains at a low level ($n_C/n_e < 0.7\%$) even with carbonization.

References

- 1) H. Hsuan, K. Bol and R.A. Ellis:
Nucl. Fusion 15 (1975) 657.
- 2) V. Arunasalam, C. Barnes, K. Bol, D. Boyd,
K. Brau, N. Bretz, M. Brusati, S. Cohen,
S. Davis, D. Dimock, F. Dylla, D. Eames,
P. Efthimion, H. Eubank, H. Furth, R. Goldston,
R. Hawryluk, K. Hill, E. Hinnov, R. Horton,
J. Hosea, H. Hsuan, D. Ignat, F. Jobes,
D. Johnson, M. Mattioli, E. Mazzucato, E. Meservey,
P. Moriette, N. Sauthoff, J. Schivell, G. Schmidt,
R. Smith, F. Stauffer, W. Stodiek, J. Strachan,
S. Suckewer and S. von Goeler:
in Controlled Fusion and Plasma Physics
1977 (Proc. 8th Eur. Conf. Plague, 1977)
(Institut of Plasma Physics) Vol.2, p.17.
- 3) K. Odajima, H. Maeda, M. Shiho, H. Kimura,
S. Yamamoto, M. Nagami, S. Sengoku, T. Sugie,
S. Kasai, M. Azumi and Y. Shimomura:
Nucl. Fusion 18 (1978) 1337.
- 4) A.N. Vertiporokh, S.Yu. Luk'yanov and Yu.S. Maksimov:
Sov. J. Plasma Phys. 6 (1980) 7.
- 5) L.S. Scaturro and M.M. Pickrell.

- Nucl. Fusion 20 (1980) 527.
- 6) E.R. Müller, K. Behringer and H. Niedermeyer:
Nucl. Fusion 22 (1982) 1651.
 - 7) R.A. Jacobsen:
Plasma Phys. 17 (1975) 547.
 - 8) L.R. Grisham and K. Bol:
Nucl. Fusion 18 (1978) 315.
 - 9) C.E. Bush, S.C. Bates, J.L. Dunlap,
E.A. Lazarus, M. Murakami, V.K. Pare
and C.E. Thomas:
Nucl. Fusion 23 (1983) 67.
 - 10) C. Breton, C. De Michelis and M. Mattioli:
J. Quan. Spectrosc. Radiat. Transfer. 19 (1978) 367.
 - 11) D.E. Post and R.V. Jensen:
Atomic Data and Nuclear Data Tables
20 (1977) 397.
 - 12) H.P. Summers and M.B. Hooper:
Plasma Phys. 25 (1983) 1311.
 - 13) T. Amano, J. Fujita, Y. Hamada, M. Ichimura,
O. Kaneko, K. Kawahata, Y. Kawasumi, S. Kitagawa,
T. Kuroda, K. Matsuoka, K. Matsuura, Y. Midzuno,
K. Miyamoto, H. Naitou, Y. Nagayama, A. Nishizawa,
N. Noda, I. Ogawa, Y. Ogawa, K. Ohkubo, Y. Oka,
K. Sakurai, M. Sasao, K. Shimizu, S. Shinohara,
R. Sugihara, S. Tanahashi, T. Tetsuka, K. Toi,

- S. Tsuji and T. Watari:
in Plasma Physics and Controlled Nuclear Fusion Research
1982 (Proc. 9th Int. Conf. Baltimore, 1982)
(IAEA, Vienna, 1983) Vol.1, p.219.
- 14) D. Hwang, M. Bitter, R. Bundy, A. Cavallo, R. Chrien,
S. Cohen, P. Colestock, C. Daughney, S. Davis,
D. Dimock, P. Efthimion, H. Eubank, D. Gambier,
R. Goldston, D. Herndon, E. Hinnov, J. Hosea, J. Hovey,
R. Kaita, D. Manos, E. Mazzucato, D. Mcneill,
D. Mikkelsen, D. Mueller, A.L. Pecquet, D. Post,
G. Schilling, C. Singer, J. Strachan, S. Suckewer,
H. Thompson, S. Von Goeler and J. Wilson:
in Plasma Physics and Controlled Nuclear Fusion Research
1982 (Proc. 9th Int. Conf. Baltimore, 1982)
(IAEA, Vienna, 1983) Vol.2, p.3.
- 15) H. Kimura, K. Odajima, S. Iizuka, S. Sengoku,
T. Sugie, K. Takahashi, H. Takeuchi, T. Yamauchi,
K. Kumagai, H. Matsumoto, T. Matsuda, K. Ohasa,
S. Yamamoto, K. Anno, T. Shibata, H. Sunaoshi,
H. Hiratsuka, K. Yokoyama, A. Funahashi, T. Nagashima,
H. Maeda and Y. Shimomura:
in Plasma Physics and Controlled Nuclear Fusion Research
1980 (Proc. 8th Int. Conf. Brussels, 1980)
(IAEA, Vienna, 1981) Vol.2, p.105.
- 16) Equipe TFR:

in Plasma Physics and Controlled Nuclear Fusion Research
1980 (Proc. 8th Int. Conf. Brussels, 1980)
(IAEA, Vienna, 1981) Vol.1, p.75.

- 17) S. Suckewer, E. Hinnov, D. Hwang, J. Schivell,
G.L. Schmidt, K. Bol, N. Bretz, P.L. Colestock,
D. Dimock, H.P. Eubank, R.J. Goldston, R.J. Hawryluk,
J.C. Hosea, H. Hsuan, D.W. Johnson, E. Meservey and
D. Mcneill:
Nucl. Fusion 21 (1981) 981.
- 18) R. Behn, A. de Chambrier, G.A. Collins, P.A. Duperrex,
A. Heym, F. Hofmann, Ch. Hollenstein, B. Joye,
R. Keller, A. Lietti, J.B. Lister, J.M. Moret,
S. Nowak, J. O'Rourke, A. Pochelon and W. Simm:
Plasma Physics and Controlled Fusion
26 (1984) 173.
- 19) Equipe TFR, EUR-CEA-FC-1206(1983)
- 20) N. Noda, T. Watari, K. Toi, E. Kako, K. Sato,
K. Okubo, K. Kawahata, I. Ogawa, T. Tetsuka,
S. Tanahashi, S. Hirokura, Y. Taniguchi, Y. Kawasumi,
R. Ando and J. Fujita:
J. Nucl. Mater. 128 & 129 (1984) 304.
- 21) H. Kimura, H. Matsumoto, K. Odajima, S. Konoshima,
T. Yamamoto, N. Suzuki, K. Hoshino, Y. Miura,
T. Matsuda, H. Takeuchi, T. Sugie, S. Kasai,
T. Yamauchi, H. Kawashima, T. Ogawa, T. Kawakami,

- T. Shoji, M. Mori, H. Ogawa, Y. Uesugi, K. Ohasa,
 S. Yamamoto, M. Maeno, S. Sengoku, H. Nakamura,
 H. Ohtsuka, T. Matoba, A. Funahashi and Y. Tanaka:
 in Plasma Physics and Controlled Nuclear Fusion Research
 1982 (Proc. 9th Int. Conf. Innsbruck, 1982)
 (IAEA, Vienna, 1983) Vol.2, p.113.
- 22) H. Ogawa, K. Odajima, H. Ohtsuka, H. Matsumoto,
 H. Kimura, K. Hoshino, S. Kasai, T. Kawakami,
 H. Kawashima, M. Maeno, T. Matoba, T. Matsuda,
 Y. Miura, M. Mori, T. Ogawa, K. Ohta, T. Shoji,
 N. Suzuki, H. Tamai, Y. Uesugi, S. Yamamoto,
 T. Yamauchi, I. Yanagisawa, H. Nakamura
 and M. Katagiri:
 J. Nucl. Mater. 128 & 129 (1984) 298.
- 23) K.H. Behringer, B. Denne, M.J. Forrest, N.C. Hawkes,
 A. Kaye, P.D. Morgan, N.J. Peacock, M.F. Stamp,
 H.P. Summers and G. Tallents:
 Proc. 13th Europ. Conf. Controlled Fusion and Plasma Heating,
 1986 (European Physical Society, Schliersee 1986)
 Vol.10, p.176.
- 24) K. Bol, V. Arunasalam, M. Bitter, D. Boyd,
 K. Brau, N. Bretz, J. Bussac, S. Cohen,
 P. Colestock, S. Davis, D. Dimock, F. Dylla,
 D. Eames, P. Efthimion, H. Eubank, R.J. Goldston,
 R.J. Hawryluk, K.W. Hill, E. Hinnov, J. Hosea,

- H. Hsuan, F. Jobes, D. Johnson, E. Mazzucato,
 S. Medley, E. Meservey, N. Sauthoff, G. Schmidt,
 F. Stauffer, W. Stodiek, J. Strachan, S. Suckewer,
 G. Tait, M. Ulrickson and S. Von Goeler:
 in Plasma Physics and Controlled Nuclear Fusion Research
 1978 (Proc. 7th Int. Conf. Innsbruck, 1978)
 (IAEA, Vienna, 1979) Vol.1, p.11.
- 25) S. Sengoku, T. Matsuda, H. Matsumoto,
 T. Abe, H. Otsuka, T. Arai, K. Ohasa,
 S. Yamamoto, K. Odajima, H. Kimura,
 S. Kasai, K. Kumagai, K. Takahashi
 and Y. Shimomura:
 J. Nucl. Mater 93 & 94 (1980) 178.
- 26) A. Pospiesznyk, H.L. Bay, P. Bogen, D. Rusbüldt,
 U. Samm, J. Schlüter, B. Schweer:
 Proc. 12th Europ. Conf. Controlled Fusion and Plasma Physics,
 1985 (European Physical Society, Budapest 1985)
 Vol.9, p.523.
- 27) J. Schlüter, E. Graffmann, L. Könen, F. Waelbroeck,
 G. Waidmann, J. Winter and the TEXTOR Team:
 Proc. 12th Europ. Conf. Controlled Fusion and Plasma Physics,
 1985 (European Physical Society, Budapest 1985)
 Vol.9, p.627.
- 28) N. Noda, Y. Ogawa, K. Masai, I. Ogawa, R. Ando,
 S. Hirokura, E. Kako, Y. Taniguchi, R. Akiyama,

- Y. Kawasumi, K. Kawahata, K. Toi, T. Watari,
S. Tanahashi, K. Matsuoka and Y. Hamada:
Jpn. J. Appl. Phys. 25 (1986) L397.
- 29) E. Hinnov, J. Hosea, H. Hsuan, F. Jobes,
E. Meservey, G. Schmidt and S. Suckewer:
Nucl. Fusion 22 (1982) 325.
- 30) L.L. Gorelik, K. A. Razumova, V. V. Sinitsyn:
in Plasma Physics and Controlled Nuclear Fusion Research
1965 (Proc. Int. Conf. Culham, 1965)
(IAEA, Vienna, 1966) Vol.2, p.647.
- 31) L. L. Grelik, S. V. Mirnov, V. G. Nikolaevsky:
Nucl. Fusion 12 (1972) 185.
- 32) Equipe TFR:
in Plasma Physics and Controlled Nuclear Fusion Research
1976 (Proc. 6th Int. Conf. Berchtesgaden, 1976)
(IAEA, Vienna, 1977) Vol.1, p.647.
- 33) M. M. Pickrell: MIT Plasma Fusion Center Report
No.PFC/RR-82-30(1982)
Nucl. Fusion 20 (1980) 527.
- 34) J. Schivel, G. Renda, J. Lowrance, and H. Hsuan:
Rev. Sci. Instrum. 53 (1982) 1527.
- 35) TFR Group : J. Nucl. Sci. Tech. 16(1979) 847.
- 36) S. Besshou, S. Morimoto, O. Motojima, T. Obiki,
A. Iiyoshi, and K. Uo : Jpn. J. Appl. Phys. 23 (1984)L839 .
- 37) K. F. Mast, and H. Krause: Rev. Sci. Instrum. 56 (1985) 969.

- 38) H. Kawamura, M. Seki, and M. Maeno:
J. Nucl. Sci. Tech. 16 (1979) 847.
- 39) E. R. Müller: Max-Planck-Institut für Plasmaphysik Report
No. IPP III/56, 1980.
- 40) I. Ogawa, K. Kawahata, N. Noda, T. Watari, S. Tanahashi,
K. Toi and J. Fujita:
Jpn. J. Appl. Phys. 25 (1986) 1057.
- 41) I. Ogawa, N. Noda, K. Kawahata, Y. Ogawa and J. Fujita:
Jpn. J. Appl. Phys. (1987) .
- 42) I. Ogawa, K. Kawahata, Y. Ogawa and T. Watari,
N. Noda, K. Masai, E. Kako, S. Tanahashi,
K. Toi and J. Fujita:
J. Phys. Soc. Jpn. 56 (1987) 535.
- 43) M. Ichimura, J. Fujita, S. Hirokura, E. Kako,
K. Kawahata, Y. Kawasumi, A. Nishizawa, N. Noda,
I. Ogawa, K. Okubo, Y. Ono, M. Sasao, S. Shinohara,
S. Tanahashi, T. Tetsuka, K. Toi, T. Watari,
T. Aoki and S. Hidekuma:
Nucl. Fusion 24 (1984) 709.
- 44) K. Toi, T. Watari, K. Okubo, K. Kawahata, N. Noda,
S. Tanahashi, T. Amano, R. Ando, J. Fujita, Y. Hamada,
S. Hirokura, K. Ida, E. Kako, O. Kaneko, Y. Kawasumi,
S. Kitagawa, T. Kuroda, K. Matsuoka, K. Matsuura,
Y. Midzuno, M. Mimura, H. Naitou, A. Nishizawa, I. Ogawa,
Y. Ogawa, Y. Oka, M. Okamoto, M. Ono, K. Sakurai,

- M. Sasao, K. Sato, K.N. Sato, Y. Taniguchi,
T. Tetsuka and K. Yamazaki:
in Plasma Physics and Controlled Nuclear Fusion Research
1984 (Proc. 10th Int. Conf. Culham, 1984)
(IAEA, Vienna, 1985) Vol.1, p.523.
- 45) McWhirter, R.W.P., in Plasma Diagnostic Techniques,
Huddleston, R.H. Leonard, S.L. eds:
Academic Press, New York, (1965).
- 46) K. Miyamoto: Plasma Physics for Nuclear Fusion,
Iwanami Shoten Publishers, Tokyo (1976).
- 47) G. B. Sabine: Pys. Rev. 55 (1939) 1064.
- 48) J. Schivel: Rev. Sci. Instrum. 56 (1985) 972.
- 49) S. T. Liu, and D. Long : Proc. IEEE 66(1978) 14.
- 50) Frank Biggs and Ruth Lighthill:
Weapons Effects Research Department
(Sandia Laboratories) SC-RR-710507 (1971)
- 51) James A. R. Samson: Thechniques of Vacuum Ultraviolet
Spectroscopy,
(GCA Corporation, New York, London, Sydney, 1967) p224.

Radiation Loss and Impurity Abundance during ICRF Heating
in the JIPP T-IIU Tokamak

Isamu OGAWA, Kazuo KAWAHATA, Yuichi OGAWA,
Tetsuo WATARI, Nobuaki NODA*, Kuniaki MASAI,
Eiji KAKO, Shyugo TANAHASHI, Kazuo TOI,
and Junji FUJITA

Institute of Plasma Physics, Nagoya University, Nagoya 464

(Received August 15, 1986)

Spectroscopic and bolometric measurements with spatial and temporal resolution show that large radiation loss brings about the decrease in electron and ion temperature and plasma energy. Regarding emissivity in a core plasma, the result by bolometric measurements well agrees with that estimated from impurity abundance and radiative cooling rates. Carbon limiters have an effect to suppress the radiation loss for Ohmic plasma, but is insufficient for ICRF heated plasma. The main contribution to radiation loss may be attributed to Fe impurity released from the ICRF antennae, the Faraday shield and vacuum vessel. By making carbonization, the Fe impurity is suppressed to a low level ($n_{\text{Fe}}/n_e \sim 0.03\%$) and the radiation loss is reduced to

*Present address: Plasma Physics Laboratory, Kyoto University
Gokasho, Uji, Kyoto 611

$P_{\text{rad}} / (P_{\text{OH}} + P_{\text{rf}}) \sim 20\%$. This is clearly supported by the observation of Z_{eff} (3.9 \rightarrow 1.2).

§1 Introduction

The radiation loss from a plasma column directly disperses electron energy and plays an important role regarding the determination of electron temperature and power balance in tokamak discharges.¹⁻⁶⁾ It is also associated with instabilities through an influence on a radial profile of electron temperature.⁷⁻⁹⁾ The magnitude and the spatial profile of the radiation loss depend entirely on the sort of impurities and the abundance. Therefore, the limiter material and the surface condition of in-vessel component play a critical role.

Recent studies on radiation loss have shown that high-Z impurities bring about high radiation loss because of its high radiative cooling rate. A discharge using tungsten limiters suffered from central radiation cooling.²⁾ Carbon limiters have been found to reduce radiation loss from a core plasma.^{10,11)}

Furthermore, carbon coating (carbonization)¹²⁻¹⁵⁾ is taken to be a promising method to reduce metal impurity contamination.

A good grasp of the mechanism of impurity production and the origin of impurity is absolutely necessary to find a method to reduce impurity contamination. Several investigations on them have been described in the literature.^{*,11,16-18)} The origin of impurity can be identified by changing the material of vacuum components, but clear results are hard to be obtained because of

mutual impurity deposition on vacuum components. All the more, experimental results are necessary to clarify the origin of impurity.

*Equip TFR, EUR-CEA-FC-1206(1983)

In JIPP T-IIU, 19,20) high power ICRF heating experiments have been carried out. The decrease in radiation loss from a core plasma is a decisive factor to achieve an effective heating.

In order to make clear the influence of the radiation loss on the ICRF heating and to identify impurities responsible to the radiation loss and to clarify the origin of impurity, the experiments were carried out under the following three conditions.

- (1) In use of stainless steel (S.S.) limiters.
- (2) In use of carbon (C) limiters.
- (3) With carbonization in use of C limiters.

In these experiments, principal diagnostics are bolometric and spectroscopic measurements. Bolometric system employs a metal-film bolometer and 12 pyroelectric detectors. This selection of detectors is made from the standpoint of high reliability (accuracy in absolute value, spatial and temporal resolution).21)

Investigations on impurities responsible to radiation loss were performed in Ohmically heated plasma.3,22) However,

impurity identification in ICRF heated plasma has not been obtained and there is very little quantitative information on carbonization. It is the purpose of the present paper to describe (1) the influence of radiation loss on a plasma, (2) the effect of low-Z (C) limiters and the carbonization on the ICRF heating characteristics, and (3) an experimental basis to clarify the origin of impurities.

§2 Experimental Setup

The JIPP T-IIU tokamak has a major radius of $R=0.91$ m and a minor radius of $a=0.23$ m. The ICRF heating experiment is carried out in the two-ion-hybrid heating regime. The applied frequency is 40 MHz and the hydrogen-to-ion density ratio $n_H/(n_H+n_D)$ is 10 %. The two-ion-hybrid resonance layer for the toroidal magnetic field $B_T = 3$ T in this series of experiments is located near the plasma center. The half-turn antennae are installed in the high field side at six different toroidal positions (Fig.1).

Each antenna has a capability to couple the rf power of 0.5 MW to the plasma. Two types of limiters were used. One is stainless steel SuS 304 (S.S.) limiters and the other is carbon (C) limiters. Both of the limiters are of the same shape and size. In order to reduce residual gases, C limiters were baked at temperature around 150 °C for 48 hours. The vacuum vessel, the antennae and the Faraday shield are made of stainless steel

SuS 304. A glow discharge system was prepared for carbonization.

The bolometric and the spectroscopic (VUV, visible) measurements are carried out at the same toroidal section (Fig.1). The bolometric system²¹⁾ consists of 2π bolometer (metal-film bolometer) and pyroelectric detectors. The radial profile of radiation loss (emissivity) is obtained through Abel inversion of the signals from 12 pyroelectric detectors. Each pyroelectric detector is calibrated with a HeNe laser and a powermeter which has an accuracy of 3 %. The total radiation loss is measured with the 2π bolometer. The sensitivity of 2π bolometer is calibrated with the change in resistance due to a heat produced by a bias current. The total radiation loss agrees with the value obtained through a volume integration of the radial profile of radiation loss.

§3 Experimental results

3.1 ICRF heating experiment with S.S. limiters

The first ICRF experiment was carried out with S.S. limiters. The time behaviors of total radiation loss P_{rad} measured with the 2π bolometer and emissivity E measured with pyroelectric detectors are shown in Fig.2. The ICRF power of 0.15 MW is injected from $t=75$ ms to 110 ms. Even before ICRF injection, radiation loss is the major fraction of the plasma

energy loss ($P_{\text{rad}}/P_{\text{OH}} \sim 50\%$). Emissivity in a core plasma accounts for the substantial fraction of radiation loss.

Moreover, radiation loss continues to increase during ICRF heating and reaches 80 % of input power ($P_{\text{OH}}+P_{\text{rf}}$). Such a radiation dominant plasma is unstable and the injection power of ICRF is limited to 0.4 MW because of a current disruption.

The effective heating of ion and electron is not observed, because the increment in radiation loss due to ICRF injection exceeds the ICRF power ($\Delta P_{\text{rad}}/P_{\text{rf}} \sim 2.8$). The radiation loss from a core plasma increases during ICRF heating. The reduction in radiation loss is indispensable to the favorable experiments of both Ohmic and ICRF heated plasmas.

3.2 ICRF heating experiment with C limiters

By the use of C limiters, the total radiation loss in Ohmically heated plasma is remarkably reduced ($P_{\text{rad}}/P_{\text{OH}} \sim 30\%$) compared with S.S. limiters and the injection power of ICRF is raised to more than 1 MW without a current disruption. A typical plasma discharge at an injection power of 1 MW is shown in Fig.3.

Electron temperature increases as soon as ICRF power is injected and results in the decrease in loop voltage. Its increment becomes maximum (1340 \rightarrow 1750 eV) with a lapse of 8 ms. After its increment, electron temperature begins to decrease with a large rate. Although the decrease becomes small around a lapse of 40

ms, electron temperature again begins to decrease with a large rate till the end of ICRF pulse. Ion temperature increases according to ICRF injection and reaches the maximum value of 1 keV with a lapse of 40 ms. However, ion temperature do not keep its maximum value during ICRF injection and begin to decrease.

Plasma energy W_p reaches the maximum with a lapse of 35 ms and begins to decrease during ICRF heating.

Total radiation loss P_{rad} and emissivity E are shown in Fig.3(c)(d). In comparison with the case of S.S. limiters, the total radiation power in Ohmically heated plasma is remarkably low (370 kW \rightarrow 130 kW). The ratio of P_{rad}/P_{OH} is about 30 %. In compliance with ICRF injection, however, total radiation loss P_{rad} continues to increase during ICRF and reaches $P_{rad}/(P_{OH}+P_{rf}) \sim 50$ %. Emissivity in central region increases to the level of 2.6 W/cm³. Large radiation loss from a core plasma is quite unfavorable from the viewpoint of the energy confinement.

Emissivity in peripheral region reaches a maximum value in 10 ms and keeps a roughly constant value during ICRF.

The VUV and visible spectroscopic measurements are carried out in order to investigate the impurities responsible to the radiation loss. The main impurities the JIPP T-IIU plasma are Fe, O and C. Line intensities of Cr, Ni are small compared with Fe and the estimated Cr density is smaller than that of Fe by a factor of 1/4. The estimated Ni density is found negligible.

These estimated values well correspond to component ratio of

stainless steel. The time behaviors of impurity lines with low and high ionization potentials (I.P.) are represented by those of OVI (I.P.=138 eV) and FeXX (I.P.=1500 eV) in Fig.3(e),

respectively. The intensity of impurity lines with low I.P. rapidly increases and keeps a roughly constant value during ICRF.

The major fraction of such impurities exists in peripheral region. The time behavior of these line intensities agrees with that of emissivity in peripheral region. The line intensities with high I.P. continue to increase during ICRF. In order to investigate the radial distribution of FeXX, the intensities of forbidden line are measured by scanning the plasma cross section on a shot-to-shot basis (Fig.3(f)). The result shows that the major fraction of FeXX exists in central region ($r \leq 5$ cm).

Emissivity in the same region continues to increase during ICRF pulse. The time behavior of emissivity in the central region and that of line intensities with high ionization states (for example FeXX) agree with each other. Impurity line intensities against total radiation loss are plotted in Fig.4 for the case with C limiters. Total radiation is roughly proportional to line intensities of Fe. The Fe impurities of several ionization states may be attributed to the major fraction of radiation loss.

Regarding electron temperature, a large decrease after a lapse of 8 ms from ICRF injection may be due to the increase in electron density and that in the equipartition power from electron to ion, which results in the increase in ion temperature

and makes the difference between electron and ion temperatures small. The decrease in electron temperature in the late ICRF pulse may be due to the increase in the radiation loss, which is substantial fraction of plasma energy loss then. The decrease in ion temperature in the late ICRF pulse may be due to that in the equipartition power from electron to ion, which is caused by the decrease in electron temperature.

3.3 ICRF heating experiment with carbonization

Carbonization is carried out in JIPP T-IIU in expectation of the reduction in metal impurities. Total radiation loss is remarkably reduced during ICRF by making carbonization. The maximum power of ICRF system is delivered to plasma (1.35 MW) without the current disruption. A typical plasma discharge at an injection power of 1 MW is shown in Fig.5. The decrease in electron temperature in the later part of ICRF pulse is smaller than that of the case without carbonization. The decrease in plasma energy is not seen unlike the case without carbonization.

The ion temperature increases and keeps the maximum value during ICRF. Total radiation loss P_{rad} and emissivity E are shown in Fig.5(c)(d). The ratio of $P_{\text{rad}} / P_{\text{OH}}$ is 15 % before ICRF injection. The maximum value of $P_{\text{rad}} / (P_{\text{OH}} + P_{\text{rf}})$ is 20 %.

Emissivity throughout the plasma remains at a low level (0.2 W/cm^3) compared to input power density during ICRF unlike the case without carbonization. This level of emissivity has little

effect on the power balance. Low level of central emissivity is favorable from the viewpoint of the energy confinement. The equipartition power from electron to ion is larger than that of the case without carbonization because of small decrease in electron temperature. This is the reason why the ion temperature do not decrease during ICRF heating.

The maximum value of radiation loss P_{rad} against the ICRF power is plotted in Fig.6 for all three cases. Replacing S.S. limiters by C limiters, total radiation loss at Ohmic plasma phase ($P_{\text{rf}}=0$) is reduced to a factor of 1/4. In addition, it is also reduced to a factor of 1/3 by making carbonization. This indicates that the limiters are the major impurity sources in the Ohmic phase. The total radiation losses linearly increase as the power of ICRF injection is raised. The rate of increase against the ICRF power is little affected by replacing S.S. limiters by C limiters. On the other hand, the rate of increase is reduced to a factor of 1/4 by coating vacuum components with carbon (carbonization). This indicates that the antennae, the Faraday shield and the vacuum vessel are the major impurity sources in the ICRF heating phase. The ratio of line intensity with carbonization to that without carbonization are plotted in Fig.7. Considering that the difference between the plasma parameters (electron density and temperature) for two cases is not so large, the ratio of line intensity is proportional to that of abundance. By making carbonization, impurity abundances of Fe, O and C have

changed to 0.05 ± 0.02 , 0.2 ± 0.1 and 1.5, respectively. The scatter of the obtained results is due to poor reproducibility of the discharge.

It is clearly shown from the experimental results that carbonization has an effect of reducing the amount of Fe. The Fe impurities may be responsible to the major fraction of radiation loss without carbonization (with C limiters).

§4 Discussion

Impurity abundances are evaluated from the ratio of line intensity (Fig.7) and the effective ion charge Z_{eff} . According to neoclassical resistivity, Z_{eff} is obtained from the electron temperature $T_e(r)$, resistive voltage and the plasma current. The value of Z_{eff} thus obtained gives that in a core region ($r \leq a/2$) because the plasma current mainly flows in this region.

The value of Z_{eff} is $5 \sim 7$ with S.S. limiters and supports high emissivity throughout plasma region. With C limiters (without carbonization), Z_{eff} slightly increases from 3.3 to 3.9 during ICRF heating. The value of Z_{eff} with carbonization remains 1.2 during ICRF heating. Oxygen and carbon may be fully ionized ($Z=8, 6$) in core plasma ($T_e \sim 1.5$ keV). The average charge state of Fe is roughly 20 in a core plasma.²³⁾ The highest amount of respective impurities are obtained from Z_{eff} and impurity abundance ratios described in § 3.3, assuming that

only oxygen or carbon besides Fe exists in a plasma. Assuming that Z_{eff} is determined by Fe and C only, $n_{\text{Fe}}/n_e \sim 7 \times 10^{-3}$, $n_{\text{C}}/n_e \sim 2 \times 10^{-3}$ for the ICRF experiment without carbonization, and $n_{\text{Fe}}/n_e \sim 3 \times 10^{-4}$, $n_{\text{C}}/n_e \sim 3 \times 10^{-3}$ for the ICRF experiment with carbonization. On the other hand, assuming that Z_{eff} is determined by Fe and O only, $n_{\text{Fe}}/n_e \sim 6 \times 10^{-3}$, $n_{\text{O}}/n_e \sim 9 \times 10^{-3}$ for the ICRF experiment without carbonization, and $n_{\text{Fe}}/n_e \sim 3 \times 10^{-4}$, $n_{\text{O}}/n_e \sim 2 \times 10^{-3}$ for the ICRF experiment with carbonization. There is little difference between abundances of Fe for both cases. The abundance of Fe without carbonization may contribute to the major fraction of total radiation loss because of its high radiative cooling rate,²³⁾ which is several tens times as large as those of O, C in the wide range of electron temperature. The contribution of Fe to radiation loss is the largest among Fe, O and C impurities except for extremely peripheral region. The high-Z impurities (Fe, Cr) are responsible to the major fraction of total radiation loss (> 90 %). Among the high-Z impurities, Fe dominates the total radiation loss.

Assuming that coronal equilibrium holds in core region, emissivity due to respective impurities is estimated from radiative cooling rates,²³⁾ abundances and electron density. In the ICRF experiment without carbonization (with C limiters), emissivity in core region due to the Fe impurities is estimated at 1.8 W/cm^3 and those due to O and C are 0.02 W/cm^3 and 0.002

W/cm^3 , respectively. The contribution of Fe is dominant and agrees with bolometric measurement (2.6 W/cm^3). In the ICRF experiment with carbonization, emissivity in the core region due to the impurities of Fe, O and C are estimated to be 0.1 W/cm^3 , 0.01 W/cm^3 and 0.002 W/cm^3 , respectively. These estimated values agree with bolometric measurement (0.2 W/cm^3). In the experiment with carbonization, emissivity swells in peripheral region (0.5 W/cm^3). This may be attributed to C, which results from the carbonization. Because the radiative cooling rate of C exceeds that of Fe under the condition that electron temperature is sufficiently low. Such a condition may hold in plasma edge with a swell of emissivity.

Total radiation loss of Ohmic plasma with S.S. limiters is larger than that with C limiters (without carbonization) by a factor of 5 (Fig.6). This difference may be attributed to the impurity flux of Fe released from limiters. On the other hand, the total radiation losses increase at the same rate of increase with the ICRF power. The above result indicates that impurity flux of Fe released from the antennae, the Faraday shield and the vacuum vessel is mainly responsible to the increase in total radiation due to ICRF injection.

§6 Conclusion

The radiation loss from a plasma core plays an important role on

tokamak discharges with S.S. and C limiters (without carbonization). The radiation loss increases during ICRF heating and electron and ion temperature and plasma energy decrease. The increase in the radiation loss is brought about by Fe impurities.

Although C limiters have an effect to suppress radiation loss from the Ohmic plasma ($P_{\text{rad}}/P_{\text{OH}} \sim 30\%$), it is still high for the ICRF heated plasma ($P_{\text{rad}}/(P_{\text{OH}}+P_{\text{rf}}) \sim 50\%$). This is because the antennae, the Faraday shield and the vacuum vessel may become a source of Fe impurities. Carbonization suppresses Fe impurities and radiation loss even for high power ICRF heated plasma. Radiation loss is no longer major fraction of plasma energy loss ($< 20\%$). This is supported by the impurity abundances spectroscopically determined. The major impurity, Fe decreases to a negligible level ($n_{\text{Fe}}/n_{\text{e}} \sim 0.03\%$). This results well explain the measured emissivity in a core plasma. It is worth while to note that C impurity remains at a low level ($n_{\text{C}}/n_{\text{e}} \sim 0.3\%$) even with carbonization. The above-mentioned results are summarized in Table 1.

Acknowledgements

The authors wish to thank the JIPP T-IIU group, in particular, Messrs Y. Kawasumi, S. Hirokura, Y. Taniguchi, H. Ishiguro and M. Mugishima for assistance of the experiments.

References

- 1) H. Hsuan, K. Bol and R.A. Ellis:
Nucl. Fusion 15 (1975) 657.
- 2) V. Arunasalam, C. Barnes, K. Bol, D. Boyd,
K. Brau, N. Bretz, M. Brusati, S. Cohen,
S. Davis, D. Dimock, F. Dylla, D. Eames,
P. Efthimion, H. Eubank, H. Furth, R. Goldston,
R. Hawryluk, K. Hill, E. Hinnov, R. Horton,
J. Hosea, H. Hsuan, D. Ignat, F. Jobes,
D. Johnson, M. Mattioli, E. Mazzucato, E. Meservey,
P. Moriette, N. Sauthoff, J. Schivell, G. Schmidt,
R. Smith, F. Stauffer, W. Stodiek, J. Strachan,
S. Suckewer and S. von Goeler:
in Controlled Fusion and Plasma Physics
1977 (Proc. 8th Eur. Conf. Prague, 1977)
(Institut of Plasma Physics) Vol.2, p.17.
- 3) K. Odajima, H. Maeda, M. Shiho, H. Kimura,
S. Yamamoto, M. Nagami, S. Sengoku, T. Sugie,
S. Kasai, M. Azumi and Y. Shimomura:
Nucl. Fusion 18 (1978) 1337.
- 4) A.N. Vertiporokh, S.Yu. Luk'yanov and Yu.S. Maksimov:
Sov. J. Plasma Phys. 6 (1980) 7.
- 5) L.S. Scaturro and M.M. Pickrell:
Nucl. Fusion 20 (1980) 527.

- 6) E.R. Müller, K. Behringer and H. Niedermeyer:
Nucl. Fusion 22 (1982) 1651.
- 7) R.A. Jacobsen:
Plasma Phys. 17 (1975) 547.
- 8) L.R. Grisham and K. Bol:
Nucl. Fusion 18 (1978) 315.
- 9) C.E. Bush, S.C. Bates, J.L. Dunlap,
E.A. Lazarus, M. Murakami, V.K. Pare
and C.E. Thomas:
Nucl. Fusion 23 (1983) 67.
- 10) K. Bol, V. Arunasalam, M. Bitter, D. Boyd,
K. Brau, N. Bretz, J. Bussac, S. Cohen,
P. Colestock, S. Davis, D. Dimock, F. Dylla,
D. Eames, P. Efthimion, H. Eubank, R.J. Goldston,
R.J. Hawryluk, K.W. Hill, E. Hinnov, J. Hosea,
H. Hsuan, F. Jobs, D. Johnson, E. Mazzucato,
S. Medley, E. Meservey, N. Sauthoff, G. Schmidt,
F. Stauffer, W. Stodiek, J. Strachan, S. Suckewer,
G. Tait, M. Ulrickson and S. Von Goeler:
in Controlled Fusion and Plasma Physics
1977 (Proc. 7th Int. Conf. Innsbruck, 1977)
(IAEA, Vienna, 1978) Vol.1, p.11.
- 11) N. Noda, T. Watari, K. Toi, E. Kako, K. Sato,
K. Okubo, K. Kawahata, I. Ogawa, T. Tetsuka,
S. Tanahashi, S. Hirokura, Y. Taniguchi, Y. Kawasumi,

- R. Ando and J. Fujita:
J. Nucl. Mater. 128 & 129 (1984) 304.
- 12) S. Sengoku, T. Matsuda, H. Matsumoto,
T. Abe, H. Otsuka, T. Arai, K. Ohasa,
S. Yamamoto, K. Odajima, H. Kimura,
S. Kasai, K. Kumagai, K. Takahashi
and Y. Shimomura :
J. Nucl. Mater 93 & 94 (1980) 178.
- 13) A. Pospiesznyk, H.L. Bay, P. Bogen, D. Rusbüldt,
U. Samm, J. Schlüter, B. Schweer:
Proc. 12th Europ. Conf. Controlled Fusion and Plasma Physics,
1985 (European Physical Society, Budapest 1985)
Vol.9, p.523.
- 14) J. Schlüter, E. Graffmann, L. Könen, F. Waelbroeck,
G. Waidmann, J. Winter and the TEXTOR Team:
Proc. 12th Europ. Conf. Controlled Fusion and Plasma Physics,
1985 (European Physical Society, Budapest 1985)
Vol.9, p.627.
- 15) N. Noda, Y. Ogawa, K. Masai, I. Ogawa, R. Ando,
S. Hirokura, E. Kako, Y. Taniguchi, R. Akiyama,
Y. Kawasumi, K. Kawahata, K. Toi, T. Watari,
S. Tanahashi, K. Matsuoka and Y. Hamada:
Jpn. J. Appl. Phys. 25 (1986) L397.
- 16) H. Kimura, H. Matsumoto, K. Odajima, S. Konoshima,
T. Yamamoto, N. Suzuki, K. Hoshino, Y. Miura,

- T. Matsuda, H. Takeuchi, T. Sugie, S. Kasai,
 T. Yamauchi, H. Kawashima, T. Ogawa, T. Kawakami,
 T. Shoji, M. Mori, H. Ogawa, Y. Uesugi, K. Ohasa,
 S. Yamamoto, M. Maeno, S. Sengoku, H. Nakamura,
 H. Ohtsuka, T. Matoba, A. Funahashi and Y. Tanaka:
 in Controlled Fusion and Plasma Physics
 1982 (Proc. 9th Int. Conf. Baltimore, 1982)
 (IAEA, Vienna, 1983) Vol.2, p.113.
- 17) H. Ogawa, K. Odajima, H. Ohtsuka, H. Matsumoto,
 H. Kimura, K. Hoshino, S. Kasai, T. Kawakami,
 H. Kawashima, M. Maeno, T. Matoba, T. Matsuda,
 Y. Miura, M. Mori, T. Ogawa, K. Ohta, T. Shoji,
 N. Suzuki, H. Tamai, Y. Uesugi, S. Yamamoto,
 T. Yamauchi, I. Yanagisawa, H. Nakamura
 and M. Katagiri:
 J. Nucl. Mater. 128 & 129 (1984) 298.
- 18) K.H. Behringer, B. Denne, M.J. Forrest, N.C. Hawkes,
 A. Kaye, P.D. Morgan, N.J. Peacock, M.F. Stamp,
 H.P. Summers and G. Tallents:
 Proc. 13th Europ. Conf. Controlled Fusion and Plasma Heating,
 1986 (European Physical Society, Schliersee 1986)
 Vol.10, p.176.
- 19) M. Ichimura, J. Fujita, S. Hirokura, E. Kako,
 K. Kawahata, Y. Kawasumi, A. Nishizawa, N. Noda,
 I. Ogawa, K. Okubo, Y. Ono, M. Sasao, S. Shinohara,

- S. Tanahashi, T. Tetsuka, K. Toi, T. Watari,
T. Aoki and S. Hidekuma:
Nucl. Fusion 24 (1984) 709.
- 20) K. Toi, T. Watari, K. Okubo, K. Kawahata, N. Noda,
S. Tanahashi, T. Amano, R. Ando, J. Fujita, Y. Hamada,
S. Hirokura, K. Ida, E. Kako, O. Kaneko, Y. Kawasumi,
S. Kitagawa, T. Kuroda, K. Matsuoka, K. Matsuura,
Y. Midzuno, M. Mimura, H. Naitou, A. Nishizawa, I. Ogawa,
Y. Ogawa, Y. Oka, M. Okamoto, M. Ono, K. Sakurai,
M. Sasao, K. Sato, K.N. Sato, Y. Taniguchi,
T. Tetsuka and K. Yamazaki:
in Controlled Fusion and Plasma Physics
1984 (Proc. 10th Int. Conf. London, 1984)
(IAEA, Vienna, 1985) Vol.1, p.523.
- 21) I. Ogawa, K. Kawahata, N. Noda, T. Watari, S. Tanahashi,
K. Toi and J. Fujita:
Jpn. J. Appl. Phys. 25 (1986) 1057.
- 22) E. Hinnov, J. Hosea, H. Hsuan, F. Jobes,
E. Meservey, G. Schmidt and S. Suckewer:
Nucl. Fusion 22 (1982) 325.
- 23) D.E. Post and R.V. Jensen:
Atomic Data and Nuclear Data Tables
20 (1977) 397.

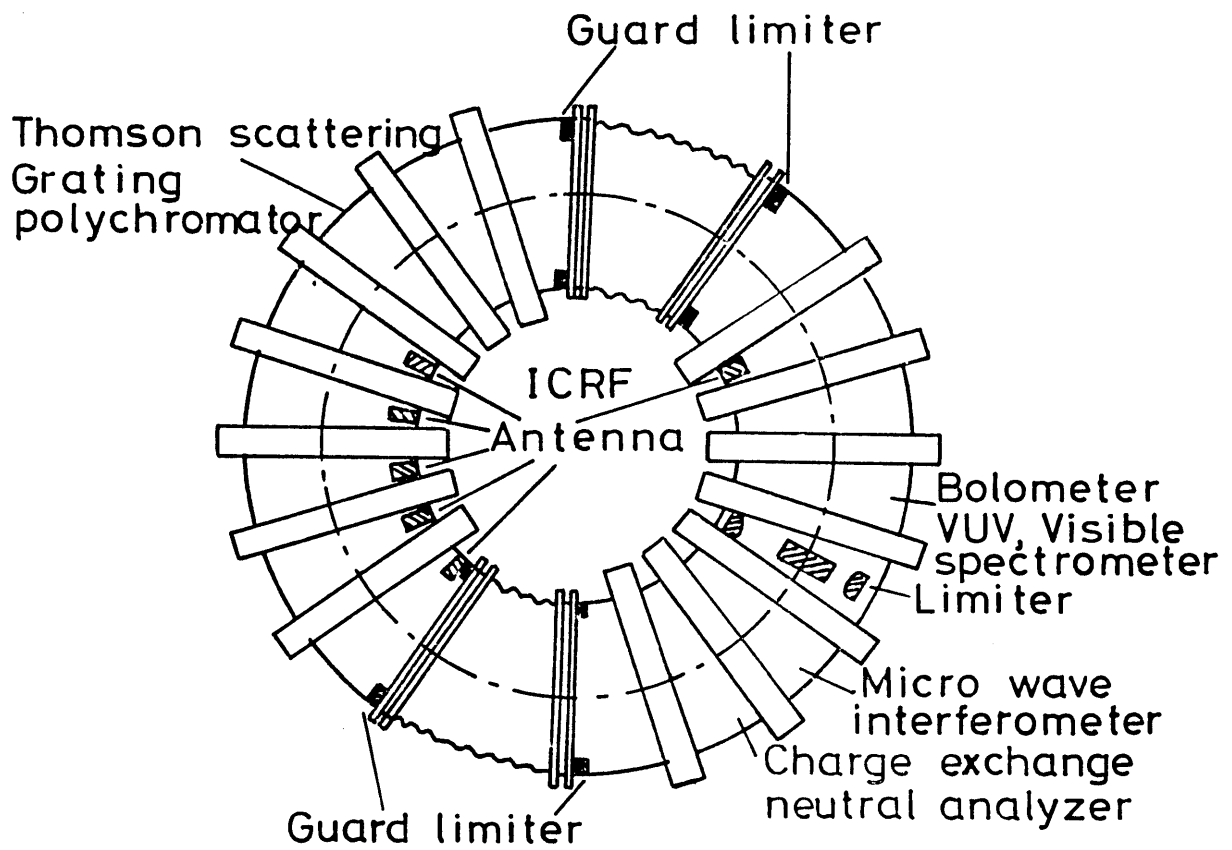


Fig.1 Locations of major diagnostics around JIPP T-IIU in relation to ICRF antennae and limiters.

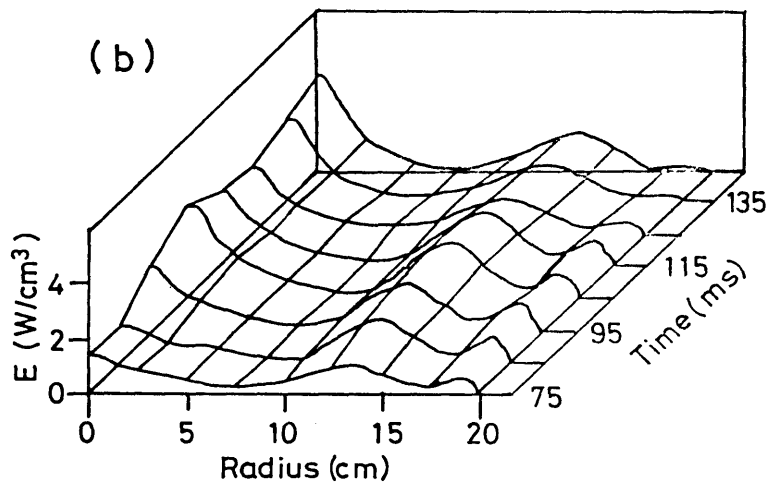
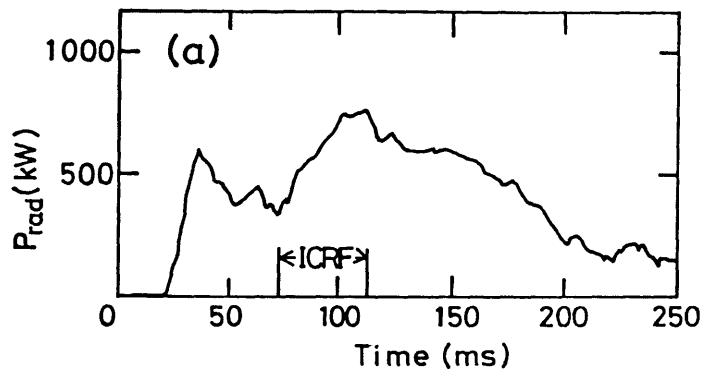


Fig.2 (a) Time behavior of total radiation power and (b) spatially and temporally resolved emissivity in the experiment with S.S. limiters.

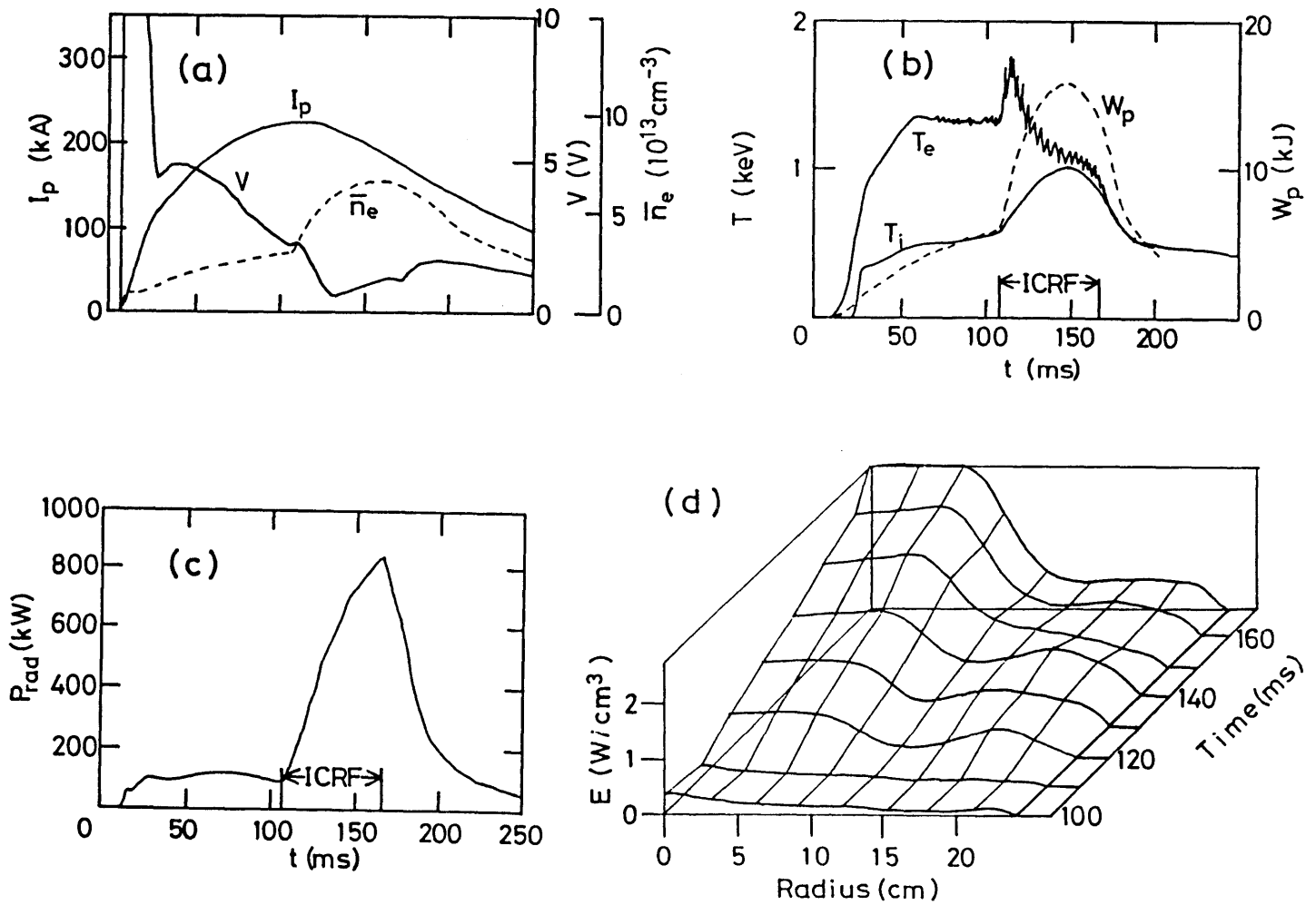


Fig.3 A typical discharge in the ICRF experiment ($P_{\text{rf}} = 1 \text{ MW}$) with C limiters. Time behaviors of (a) loop voltage V , plasma current I_p , line averaged electron density \bar{n}_e , (b) electron and ion temperatures $T_e(t)$, $T_i(t)$ and plasma energy W_p . (c) Time behavior of total radiation power and (d) spatially and temporally resolved emissivity in the experiment with C limiters.

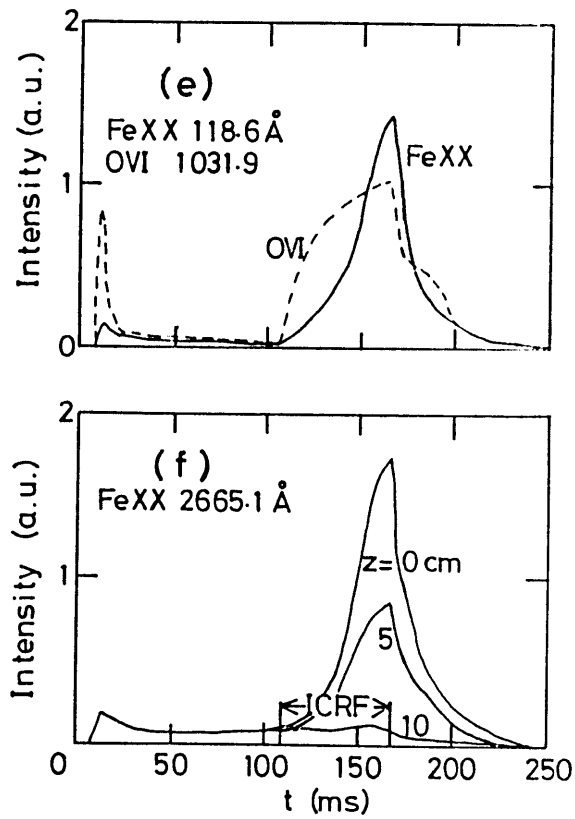


Fig.3 A typical discharge in the ICRF² experiment ($P_{rf} = 1$ MW) with C limiters. Time behaviors of (e) line intensities (FeXX, OVI) and (f) intensities of forbidden line (FeXX) measured by vertically scanning the plasma in the ICRF² experiment with C limiters.

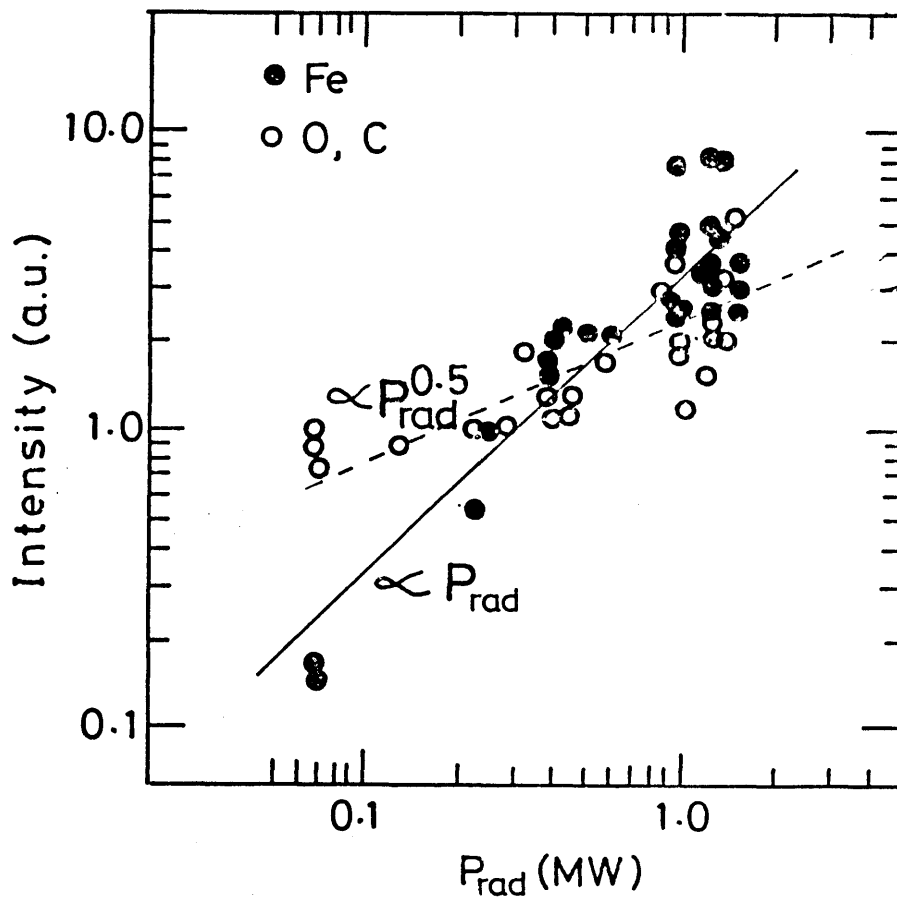


Fig.4 Line intensity plotted as a function of total radiation power P_{rad} with C limiters.

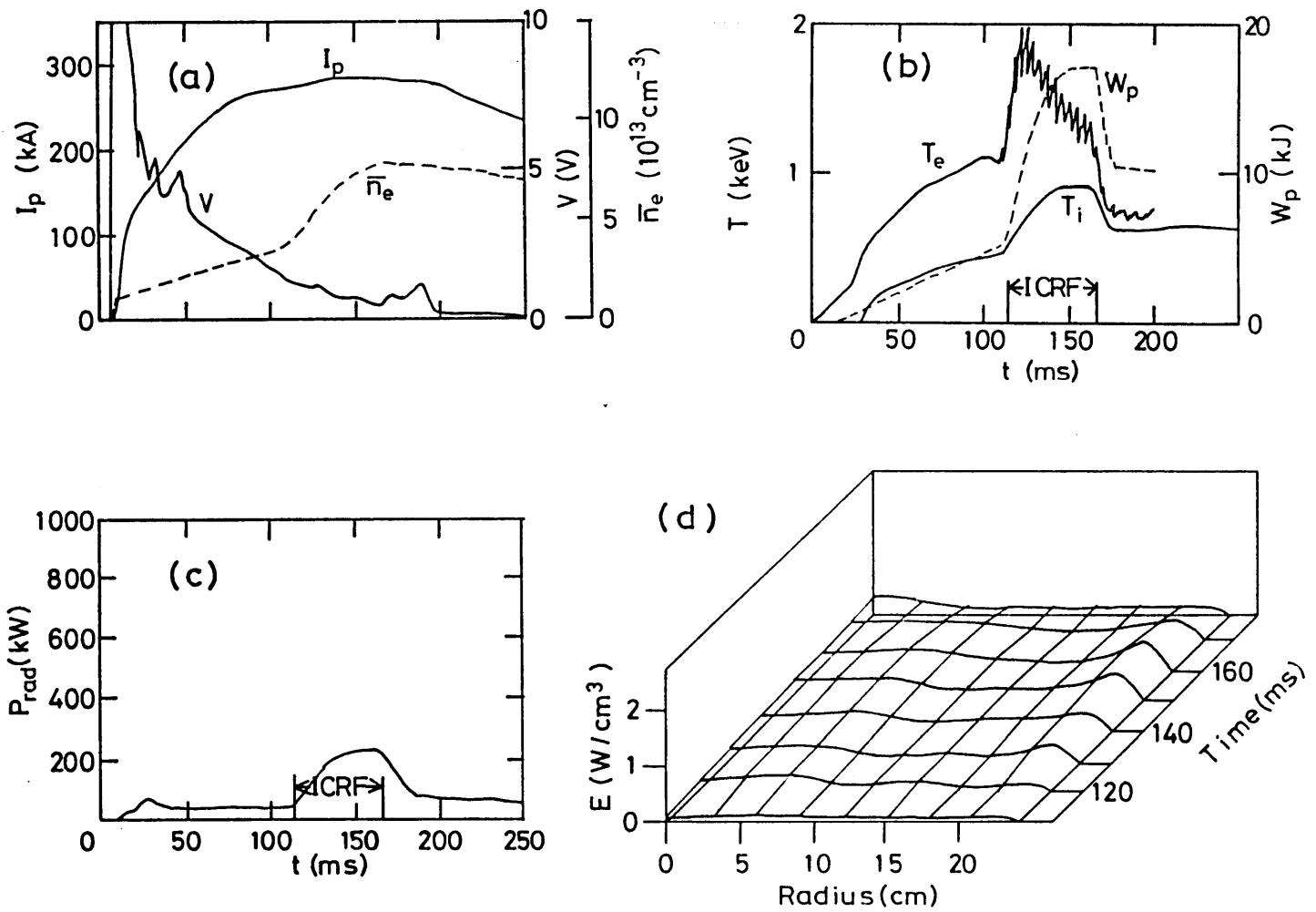


Fig.5 A typical discharge in the ICRF experiment ($P_{\text{rf}}=1 \text{ MW}$) with carbonization. Time behaviors of (a) loop voltage V , plasma current I_p , line averaged electron density \bar{n}_e , (b) electron and ion temperatures $T_e(t)$, $T_i(t)$ and plasma energy W_p . (c) Time behavior of total radiation power and (d) spatially and temporally resolved emissivity in the experiment with carbonization.

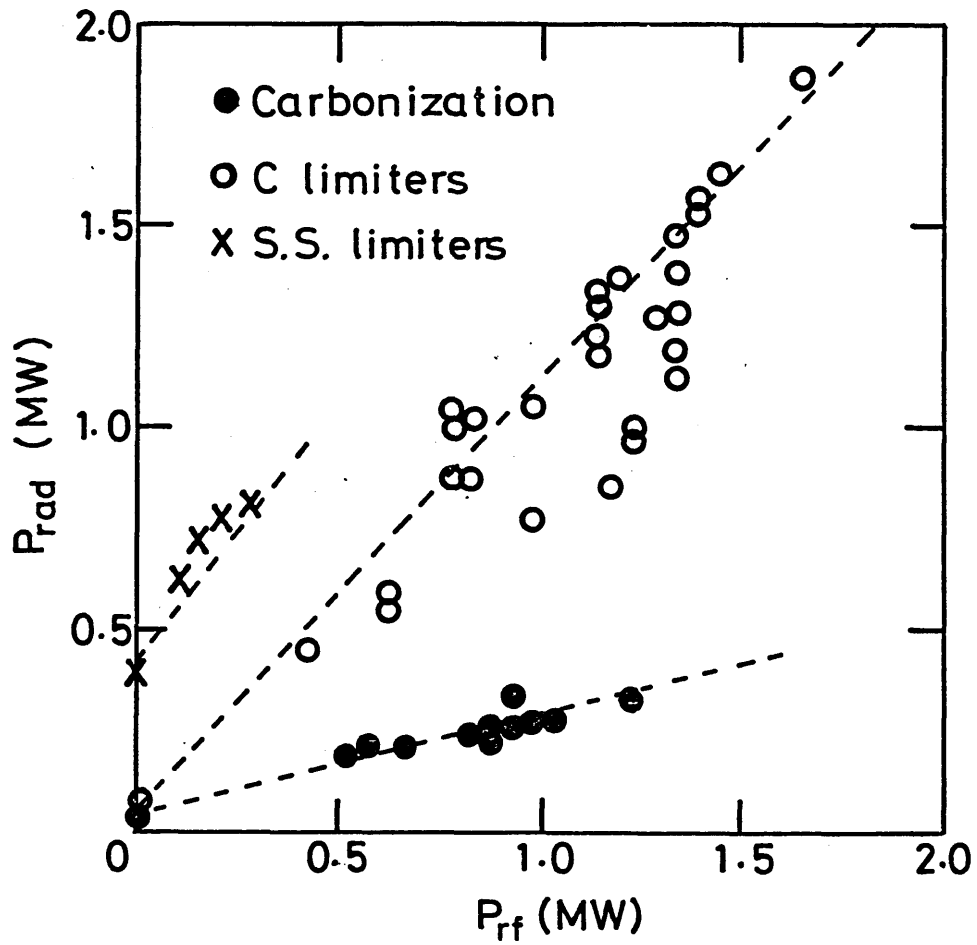


Fig.6 Total radiation power P_{rad} plotted as a function of the ICRF power P_{rf} for three cases; S.S.limiters, C limiters (without carbonization) and Carbonization.

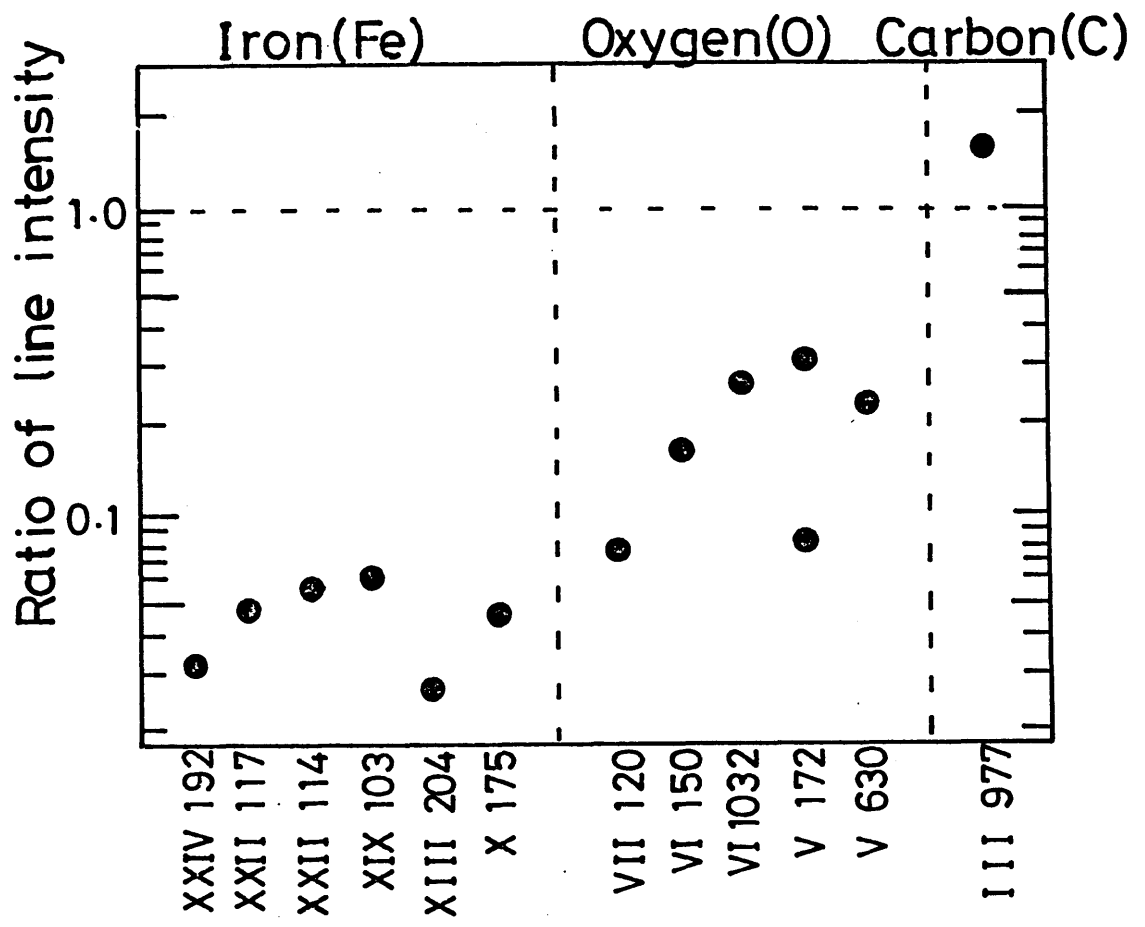


Fig.7 Ratio of line intensity with carbonization to that without carbonization.

Table I

		S.S. limiters	C limiters	Carbonization
Ohmic	Z_{eff}	~ 5	~ 3	~ 1.2
	P_{rad}/P_{OH}	$\sim 50\%$	$\sim 30\%$	$\sim 15\%$
ICRF	Z_{eff}	~ 7	~ 4	~ 1.2
	$P_{rad}/(P_{OH}+P_{rf})$	$\sim 80\%$	$\sim 50\%$	$\sim 20\%$
	$E(r=0)$	4.5 W/cm^3	2.6 W/cm^3	0.2 W/cm^3
	n_{Fe}/n_e	—	$\sim 7 \times 10^{-3}$	$\sim 3 \times 10^{-4}$
	n_o/n_e	—	$\sim 9 \times 10^{-3}$	$\sim 2 \times 10^{-3}$
	n_c/n_e	—	$\sim 2 \times 10^{-3}$	$\sim 3 \times 10^{-3}$

Thermal Characteristics of a Metal-film Bolometer

Isamu OGAWA, Nobuaki NODA*, Kazuo KAWAHATA,

Yuichi OGAWA and Junji FUJITA

Institute of Plasma Physics, Nagoya University, Nagoya 464

(Received)

A metal-film bolometer has been developed for the reliable measurement of the radiation power from a high temperature plasma. Its sensitivity and time response are improved by reducing an absorber thickness ($10\ \mu\text{m}$) to the minimum limit to sufficiently absorb photons with high energy up to 3 keV. In addition, this detector has well defined thermal characteristics.

The deviation of the measured value arising from thermal cooling is investigated by numerically solving a heat conduction equation fitting in with the detector. The calculated results well explain the thermal characteristics for a temporally constant power (at calibration) and show that the deviation of the measured radiation power from its calculated value is reduced by a precise correction to the extent of 0.5 %.

*Present address: Plasma Physics Laboratory Kyoto University
Gokasho, Uji, Kyoto 611

§1 Introduction

In tokamak devices, the radiation loss from a plasma column is an important role regarding the determination of electron temperature, power balance¹⁻⁶⁾ and instabilities.⁷⁻⁹⁾

Measurements of the magnitude, time behavior and spatial profile of the radiation power are required in order to investigate these phenomena.

Reliable measurements lie entirely on the performance of detectors. Characteristics imposed on them are ratio of high signal to noise (S/N), sharp time response. Thermistors^{1,10)}, pyroelectric detectors^{3,11,12)} and metal-film bolometers^{10,12,13)} are used to measure the radiation power. A thermistor has high sensitivity but large position dependence of sensitivity and slow time response (~ 5 ms) are drawback to bolometric measurements.¹²⁾ In addition, the change in characteristics and their deterioration are observed under a high temperature circumstance expected on the device.¹⁰⁾ A pyroelectric detector gives the signal with high S/N ratio and sharp time response.

Several problems concerning the detector pointed out, that is, the spurious signal due to the photoelectric effect and temporal change in sensitivity but they are not so serious ones.¹²⁾ A metal-film bolometer is free from the spurious signal and has a long cooling time. Its low sensitivity (a low S/N ratio) is

drawback to the application.

It is desired that several types of detectors are employed from the viewpoint of a reliable measurement. In that case, one complements another and the absolute value is cross checked.

Especially, adoption of metal-film bolometers and pyroelectric detectors is considered to be a pointed selection for an evaluation of the absolute value because their calibrations are carried out by different methods. In addition, a metal-film bolometer is suitable for a measurement of the total radiation power (2π bolometer) and will tolerate the radiation damage under high hard X-ray and neutron dose.

In order to attain a reliable measurement, we have developed metal-film bolometers which have the following features :

- (1) High sensitivity
- (2) Sharp time response
- (3) Well defined thermal characteristics

Although high sensitivity and sharp time response are important as a matter of course, well defined thermal characteristics are the basis of the reliable measurement, since they are associated with a correction for thermal cooling. There are very few quantitative results on them except for those for temporally and spatially constant input power on a detector¹⁴⁾.

It is the purpose of the present paper to describe the design of a detector and its thermal characteristics associated with a correction for thermal cooling.

§2 Design of Metal-film Bolometer

The metal-film bolometer is shown in Fig.1(a). An absorber is a thin stainless steel plate of 20 mm in diameter and 10 μm thick. This absorber is fixed by the holder of 16 mm in diameter (Fig.1(b)). Silicon oxide SiO_2 is deposited ($\sim 0.2 \mu\text{m}$) on the absorber in a vacuum, and nickel is also deposited ($\sim 0.1 \mu\text{m}$) on the SiO_2 layer into close spiral shape. The SiO_2 layer serves as an electrical insulator between the absorber and the resistor (Ni film). The resistor has a resistance of 10 k Ω . It is located in the central region of the absorber and its diameter is 6 mm. A slit is equipped close to the detector in application to the JIPP T-IIU tokamak (Fig.1(b)). Its internal diameter is also 6 mm.

Above mentioned structure is designed from the viewpoint of the required characteristics described in § 1. Thin structure improves time response ($\sim 3 \mu\text{s}$) and sensitivity (12.9 Ω/mJ), since time response is determined by the transit time of a heat from the absorber surface to the resistor and sensitivity is determined by thermal capacity per unit area. The absorber of 10 μm is enough thick to absorb photons with high energy up to 3 keV. In addition, the slit plays a role of raising sensitivity, since all incident power passing through the slit heats only the region in thermal contact with the resistor.

Regarding thermal characteristics, the major fraction of

thermal capacity is mainly determined by the absorber because the electrical insulator and the resistor are very thin in comparison with the absorber. The temperature at periphery of the absorber is held constant because of the large thermal capacity of the holder (Fig.1(b)). The resistor serves double functions. One is the function of the resistor for detection and the other is that of a heater. As for the former, its resistance is determined as a function of its space averaged temperature in the resistor region because of the shape of the resistor. If a current passes through the resistor, it is considered to uniformly produces a heat in the resistor region. This uniformity is justified under the condition that Ni film has a constant cross section along the pattern and is closely wound with same interval. In such a situation, a heat produced by the resistor flows the gap between the patterns and the temperature difference between the pattern and the gap becomes small in a short time.

§3 Thermal characteristics

The thermal characteristics are well expressed by a heat conduction equation because of a simple structure with axial symmetry of the detector. As an incident power on the absorber surface is conducted to the resistor in a short time ($\sim 3 \mu\text{s}$), the treatment that a temperature rise is uniform in the direction perpendicular to the detector surface will be allowed for a long

time scale ($\gg 3 \mu\text{s}$). An equation of temperature rise $T(r,t)$ in the present case is a partial differential equation of

$$c\rho\frac{\partial}{\partial t}T(r,t) = K\frac{1}{r}\frac{\partial}{\partial r}\left[r\frac{\partial}{\partial r}T(r,t)\right] + \frac{1}{d}P(r,t), \quad (1)$$

where c is the specific heat (0.51 J/gK) of the absorber (stainless steel), ρ the density ($7.9 \times 10^6 \text{ g/m}^3$), K the thermal conductivity (15.1 W/mK), d the thickness (10 μm), $P(r,t)$ the input power density in W/cm^2 . This equation is numerically solved by a recurrence method under the boundary and the initial conditions of

$$T(a,t) = T(r,0) = 0, \quad (2)$$

where a is the internal radius of the holder (Fig.1(b)). There exists an analytic solution¹⁴⁾ under the condition that the incident power density $P(r,t)$ is temporally and spatially constant. In order to check an accuracy in the numerical solution, it is compared with the analytic solution. It well agrees with the analytic solution.

The information on the radiation loss, which is approximately proportional to the time differential of temperature rise of the central absorber region, is obtained from the change in resistance (R). The value of R is related with the temperature rise $T(r,t)$ by

$$R = \int \frac{\rho_e \alpha}{A} T(r,t) dl, \quad (3)$$

where ρ_e is the specific resistance, α the temperature

coefficient, A the cross section of Ni film and dl the line element along Ni film pattern. If ρ_e , α and A are constant along Ni film pattern, eq.(3) is rewritten as

$$R = \frac{\rho_e \alpha}{A} \int T(r, t) dl = \frac{\rho_e \alpha l}{A} T_{av}(t), \quad (4)$$

where l is the length of Ni film pattern and $T_{av}(t)$ the temperature rise averaged in the resistor region. As the pattern is close spiral shape, representative temperature rise is space-averaged value in the resistor region. Equation (4) is rewritten by initial resistance R_0 as

$$R = R_0 \alpha T_{av}(t). \quad (5)$$

The value of $T_{av}(t)$ is obtained as

$$T_{av}(t) = \frac{1}{\pi a_1^2} \int_0^{a_1} 2\pi r T(r, t) dr, \quad (6)$$

where a_1 is the radius of the resistor region. In the measurement with a metal-film bolometer, information on radiation power is obtained from \dot{R} , that is, $\dot{T}_{av}(t)$. The dot denotes the time differential from now on. In order to correct thermal cooling due to a heat dispersion, a correction term must be added to $\dot{T}_{av}(t)$. The corrected value of $\dot{T}_{av}(t)$ is described as

$$\frac{d}{dt} T_{cor}(t) = \frac{d}{dt} T_{av}(t) + \frac{1}{\tau_c} T_{av}(t), \quad (7)$$

where $T_{cor}(t)$ is the corrected value and τ_c the cooling time. If the value of $\dot{T}_{cor}(t)$ is given at a certain time, τ_c in eq.(7) is determined. Such a situation applies to the calibration of the

detector and measurement of the radiation loss from a plasma. In the usual way of calibration, temporally constant power is incident on the detector. As a matter of course, the radiation power becomes zero after discharge finish.

3.1 Thermal characteristics during calibration

The calibration is carried out from the increase in resistance due to a heat produced by a bias current passing through the resistor. An electric power (dashed line) dissipated in the resistor and the increase in the resistance \dot{R} (solid line) are shown in Fig.2. An electric power is 2.5mW.

As can be seen from eq.(5), \dot{R} corresponds to $\dot{T}_{av}(t)$ and changes with time. In order to investigate this thermal cooling, eq.(1) is solved for the input power density of

$$P(r,T) = \begin{cases} 2.5 \times 10^{-3} / \pi a_1^2 \text{ W/m}^2 & \text{for } r \leq a_1. \\ 0 \text{ W/m}^2 & \text{for } r > a_1. \end{cases}$$

The form of $P(r,t)$ will be justified because of the resistor shape. The temperature rise $T(r,t)$ and space averaged temperature rise ($T_{av}(t)$) are shown in Fig.3. The value of $\dot{T}_{av}(t)$ is shown in Fig.4 and is the value which corresponds to \dot{R} in Fig.2. Comparison between time behaviors of both values is shown in Fig.5. A plot with the maximum \dot{R} corresponds to the initial value immediately after power input. Sensitivity is

obtained from the value of this plot. The solid line shows the relation between \dot{R} and $\dot{T}_{av}(t)$, which is derived from the sensitivity ($s=\alpha R_0/C$) and eq.(5). The value of C is the heat capacity in the resistor region ($C=\pi\alpha_1^2 c\rho d$). The relation is described as

$$\frac{d}{dt}R = \pi\alpha_1^2 c\rho d s \frac{d}{dt}T_{av}(t). \quad (8)$$

The deviation from a straight line is within 3 % and this supports that thermal characteristics are well expressed by eq.(1). A dashed line in Fig.4 denotes the value with a correction according to eq.(7). The value of τ_c in this case is 0.94 s. It is so determined that initial value agrees with the value at $t=1.0$ s. The time interval of the correction is 1.0 s.

In Fig.6, the maximum deviation of $\dot{T}_{cor}(t)$ from the value which corresponds to the input power to detector and τ_c are plotted as a function of time interval of a correction. The deviation increases with time interval. For a short interval (≤ 0.2 s), the deviation is within 5 %.

3.2 Thermal characteristics of the detector without a slit

As the usual way of using, the radiation power is incident to all over the absorber surface.^{5,13,14)} If radiation power is temporally constant, thermal cooling characteristics are understood by an analytic solution.¹⁴⁾ In the measurement of

radiation power with time variation, it is necessary for investigating thermal characteristics to numerically solve eq.(1). The measured radiation power density $P_{\text{meas}}(t)$ from the plasma is shown in Fig.7. It is measured with the metal-film bolometer with a slit and a correction according to eq.(7) is made.

The calculated results ($T(r,t)$, $T_{\text{av}}(t)$) for $P_{\text{meas}}(t)$ are shown in Fig.8. The value of $\dot{T}_{\text{av}}(t)$ is shown in Fig.9. In this case, a correction term according to eq.(7) is much smaller than the value of $\dot{T}_{\text{av}}(t)$ ($< 0.04\%$). The value of τ_c in this case is so determined that the corrected value becomes zero immediately after $t=0.25\text{s}$, since this discharge finishes about $t=0.25\text{s}$.

The incident power density ($P_{\text{es}}(t)$) to the detector is estimated from the corrected value ($\dot{T}_{\text{cor}}(t)$), since the sensitivity and the increase in resistance R of eq.(5) relate $\dot{T}_{\text{cor}}(t)$ with $P_{\text{es}}(t)$. The ratio of $P_{\text{es}}(t)$ to $P_{\text{meas}}(t)$ is plotted as a function of time (Fig.10). The deviation is not so large ($< 3\%$). The value of $P_{\text{es}}(t)$ never exceeds that of $P_{\text{meas}}(t)$ and exhibits a tendency to decrease at the time when $P_{\text{meas}}(t)$ has the large rate of decrease.

3.3 Thermal characteristics of the detector with a slit

A slit is equipped close to the detector in application to the JIPP T-IIU tokamak (Fig.1(b)). When the detector operates as

a 2π bolometer (measurement of total radiation power), the slit plays a role to reduce the incident power and to shield it from the noise circumstance. When it operates as a collimated detector, the slit plays a role to raise spatial resolution as will be described later.

In order to make sure thermal characteristics of the detector, eq.(1) is solved for the input power of the form

$$P(r,T) = \begin{cases} P_{\text{meas}}(t) \text{ W/m}^2 & \text{for } r \leq a_1, \\ 0 \text{ W/m}^2 & \text{for } r > a_1, \end{cases}$$

where $P_{\text{meas}}(t)$ is the input power density shown in Fig.7.

The calculated results ($T(r,t)$, $T_{\text{av}}(t)$) are shown in Fig.11. In comparison with the results in the case of the detector without a slit, the temperature rise at the central region begins decreasing with large rate after incident power is over. A sufficient correction for thermal cooling is necessary. The value of $\hat{T}_{\text{av}}(t)$ is shown in Fig.12. The dashed line denotes its corrected value according to eq.(7). The value of τ_c is so determined that the corrected value becomes zero immediately after $t=0.25\text{s}$, since this discharge finishes about $t=0.25\text{s}$. The value of τ_c is 0.61s . The correction term $T_{\text{av}}(t)/\tau_c$ increases with time because $T_{\text{av}}(t)$ monotonically increases with time. The ratio of $P_{\text{es}}(t)$ to $P_{\text{meas}}(t)$ is plotted as a function of time (Fig.13). The value of $P_{\text{es}}(t)$ is the incident power density estimated from the corrected value ($\hat{T}_{\text{cor}}(t)$). It exhibits a

tendency to decrease at the time when $P_{\text{meas}}(t)$ has the large rate of decrease. The deviation from $P_{\text{meas}}(t)$ arrives to 10 % at $t=0.2$ s. Such an accuracy is far from the reliable measurement.

The input power density $P_{\text{meas}}(t)$ already includes the deviation due to thermal cooling. In order to evaluate the deviation due to thermal cooling, eq.(1) is solved by putting $P_{\text{es}}(t)$ in the place of $P(r,t)$. The ratio of $\tilde{P}_{\text{es}}(t)$ to $P_{\text{es}}(t)$ is similarly plotted as a function of time (Fig.14). The value of $\tilde{P}_{\text{es}}(t)$ is the power density estimated from the calculated results for $P_{\text{es}}(t)$. The ratio in Fig.13 agrees within 0.5% with that in Fig.14. This agreement is explained as follows. The deviation of the corrected value from its input power depends on the shape of the time behavior of input power. Although a correction according to eq.(7) is insufficient to evaluate the absolute value, it correctly reproduces the shape of the time behavior.

The relation between the absorbed power to the detector and the measured power $P_{\text{meas}}(t)$ may be assimilated to that between $P_{\text{meas}}(t)$ and $P_{\text{es}}(t)$. This assumption is supported by the agreement between the value of $P_{\text{es}}(t)/P_{\text{mes}}(t)$ in Fig.13 and the value of $\tilde{P}_{\text{es}}(t)/P_{\text{es}}(t)$ in Fig.14, because the same procedure according to eq.(7) is taken for obtaining the results of $P_{\text{meas}}(t)$, $\tilde{P}_{\text{es}}(t)$ and $P_{\text{es}}(t)$. Therefore, $P_{\text{meas}}(t)$ multiplied by the value of $P_{\text{meas}}(t)/P_{\text{es}}(t)$ is more accurate value of the measured input power density.

§4 Discussion

The metal-film bolometer is designed so that it has high sensitivity, sharp time response and well defined thermal characteristics. The sensitivity and the time response are raised as the absorber is thinned to the minimum limit to absorb photons with high energy. The selection of the material is restricted. Especially, it is of primary importance to overcome lack of sensitivity in the measurement of radial profile. This problem is all the more serious in the small size device because of the necessity for high spatial resolution and sharp time response. If a slit is equipped close to the detector, a spatial resolution is raised. However, the equipment has only a significance on the assumption that the deviation due to thermal cooling is sufficiently reduced by a correction. Unless the detector has well defined thermal characteristics, it is impossible to make such a precise correction.

Spatial resolution is determined by a viewing geometry, which is an arrangement of an entrance slit and an exit slit.

The entrance slit determines the input power density and the exit slit determines the detection area of the detector. The magnitude of the signal is determined by input power density as can be seen from Fig.9 and Fig.12. The slit close to the detector operates as the exit slit and plays a role to raise spatial resolution. This effect increases as the entrance slit

is stopped down. As the toroidal dependence of the radiation power from the tokamak plasma is much smaller than the radial dependence, the entrance slit has a rectangle shape which gathers the radiation power from a toroidally wide region. In such a situation, the slit is poloidally narrowed and to equip the slit is effective.

Regarding thermal characteristics, the designed detector has a simple structure with axial symmetry. The well defined thermal characteristics are supported by the fact that the measured value at calibration agrees within 3 % with the calculated results (Fig.5). The measured value is \dot{R} and the calculated value is $\dot{T}_{av}(t)$. The deviation due to thermal cooling is reduced to the extent of this agreement, since the correction according to the calculation result (ratio of $P_{es}(t)$ to $P_{meas}(t)$) reduced the deviation to the extent of 0.5 % as mentioned above.

In the case of the detector with a slit, thermal cooling characteristics are given for two cases of the input power density. The input power density shown in Fig.7 has the large rate of decrease which produces the large deviation due to thermal cooling. Even in this case, the deviation is reduced by a precise correction. Therefore, this correction is effective for any case. On the contrary, the results for constant power have the minimum deviation.

In the case without a slit, the deviation is sufficiently small ($< 3\%$) and more precise correction is considered not to

be necessary.

§5 Summary

The thin metal-film bolometer has been developed with high sensitivity ($12.9 \Omega/\text{mJ}$), sharp time response ($\sim 3 \mu\text{s}$) and well defined thermal characteristics. Thermal characteristics are investigated by numerically solving a heat conduction equation fitting in with the detector and the well defined thermal characteristics is supported by the fact that the heat conduction equation well explains the time behavior of the signal at calibration (results for a temporally constant power). The equipment of a slit close to the detector plays a role to raise spatial resolution. The deviation due to thermal cooling increases according to the equipment but is reduced by the calculation of the equation to the extent of 0.5 %.

Acknowledgements

The authors wish to thank the JIPP T-IIU group, in particular, Messrs. Y. Kawasumi, S. Hirokura, Y. Taniguchi, H. Ishiguro and M. Mugishima for assistance of the experiments. It is a pleasure to acknowledge useful discussion with Dr.S.Besshou of Kyoto University.

References

- 1) H. Hsuan, K. Bol and R.A. Ellis:
Nucl. Fusion 15 (1975) 657.
- 2) V. Arunasalam, C. Barnes, K. Bol, D. Boyd,
K. Brau, N. Bretz, M. Brusati, S. Cohen,
S. Davis, D. Dimock, F. Dylla, D. Eames,
P. Efthimion, H. Eubank, H. Furth, R. Goldston,
R. Hawryluk, K. Hill, E. Hinnov, R. Horton,
J. Hosea, H. Hsuan, D. Ignat, F. Jobses,
D. Johnson, M. Mattioli, E. Mazzucato, E. Meservey,
P. Moriette, N. Sauthoff, J. Schivell, G. Schmidt,
R. Smith, F. Stauffer, W. Stodiek, J. Strachan,
S. Suckewer and S. von Goeler:
in Controlled Fusion and Plasma Physics
1977 (Proc. 8th Europ. Conf. Prague, 1977)
(Institut of Plasma Physics) Vol.2, p.17.
- 3) K. Odajima, H. Maeda, M. Shiho, H. Kimura,
S. Yamamoto, M. Nagami, S. Sengoku, T. Sugie,
S. Kasai, M. Azumi and Y. Shimomura:
Nucl. Fusion 18 (1978) 1337.
- 4) A.N. Vertiporokh, S.Yu. Luk'yanov and Yu.S. Maksimov:
Sov. J. Plasma Phys. 6 (1980) 7.
- 5) L.S. Scaturro and M.M. Pickrell:
Nucl. Fusion 20 (1980) 527.

- 6) E.R. Müller, K. Behringer and H. Niedermeyer:
Nucl. Fusion 22 (1982) 1651.
- 7) R.A. Jacobsen:
Plasma Phys. 17 (1975) 547.
- 8) L.R. Grisham and K. Bol:
Nucl. Fusion 18 (1978) 315.
- 9) C.E. Bush, S.C. Bates, J.L. Dunlap,
E.A. Lazarus, M. Murakami, V.K. Pare
and C.E. Thomas:
Nucl. Fusion 23 (1983) 67.
- 10) J. Schivell, G. Renda J. Lowrance
and H. Hsuan:
Rev. Sci. Instrum. 53 (1982) 1527.
- 11) TFR Group (Presented by A.L. Pecquet):
J. Nucl. Mater. 93 (1980) 377.
- 12) I. Ogawa, K. Kawahata, N. Noda, T. Watari, S. Tanahashi,
K. Toi and J. Fujita:
Jpn. J. Appl. Phys. 25 (1986) 1057
- 13) S. Besshou, S. Morimoto, O. Motojima, T. Obiki,
A. Iiyoshi and K. Uo:
Jpn. J. Appl. Phys. 23 (1984) L839.
- 14) H. Kawamura, M. Seki and M. Maeno:
J. Nucl. Sci. Tech. 16 (1979) 847.

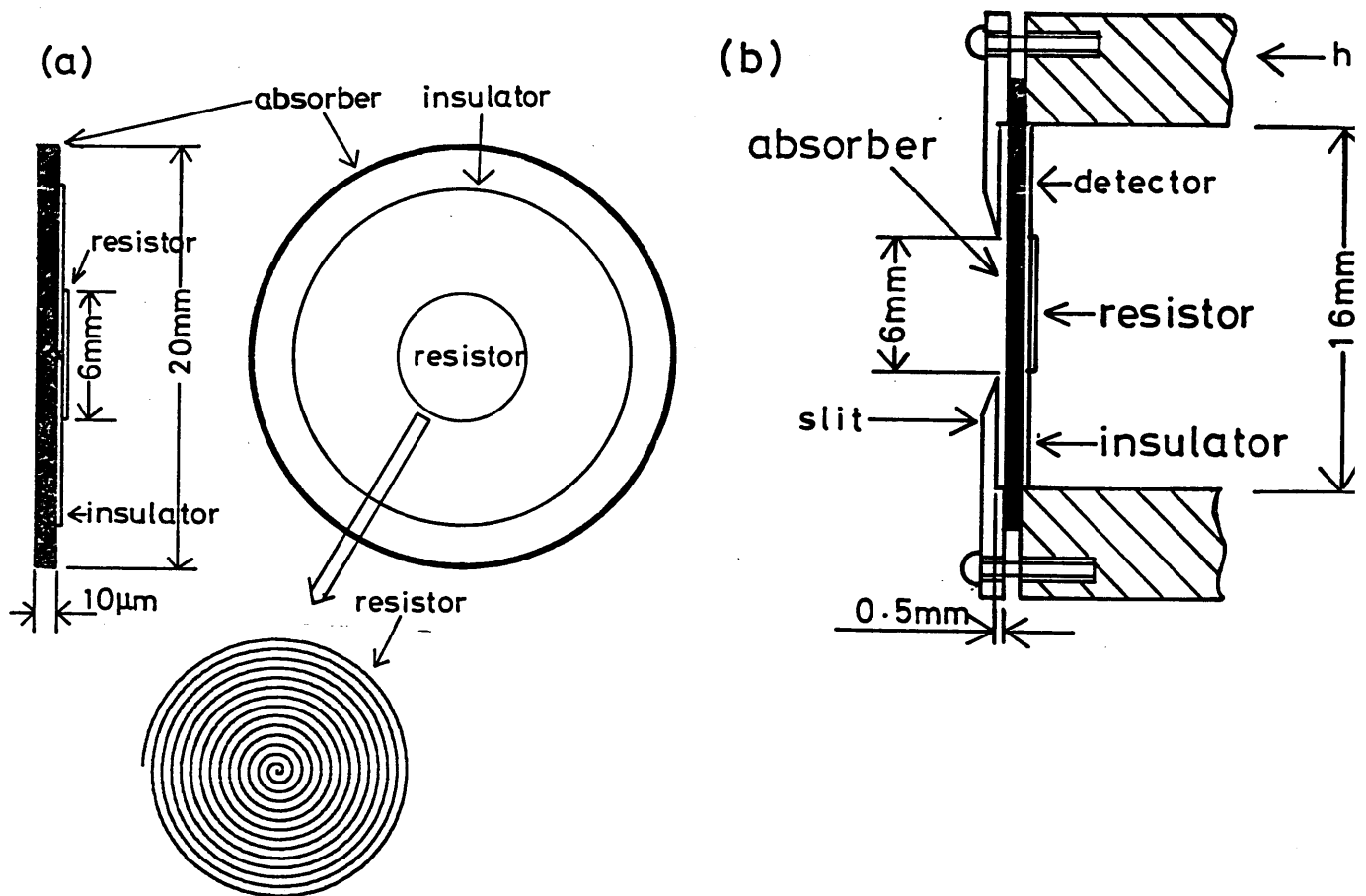


Fig.1 (a) Structure of the metal-film bolometer. Thin structure improves sensitivity and time response. A heat conduction equation is easy to be applied because the major fraction of thermal capacity is determined by the absorber. (b) A slit is equipped in expectation of high sensitivity and high spatial resolution.

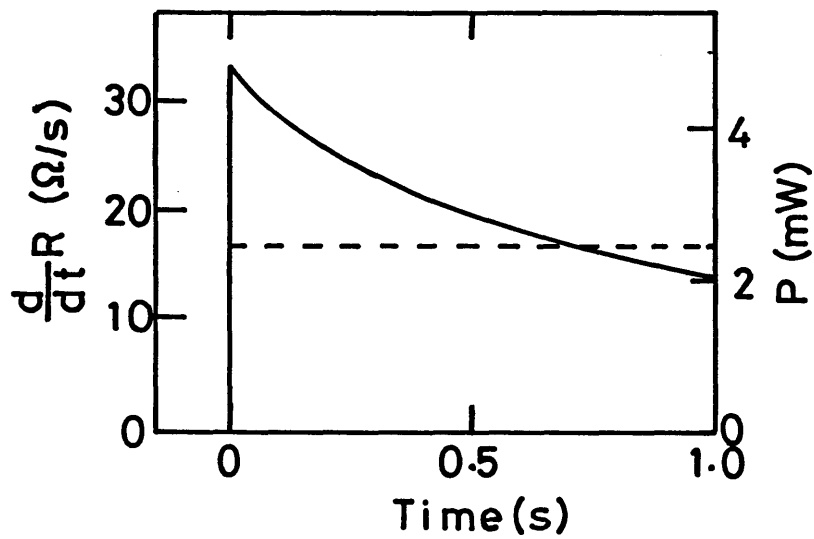


Fig.2 Time behaviors of the input power (dashed line) and \dot{R} (solid line) at calibration. A heat produced by a bias current passing through the resistor changes its resistance.

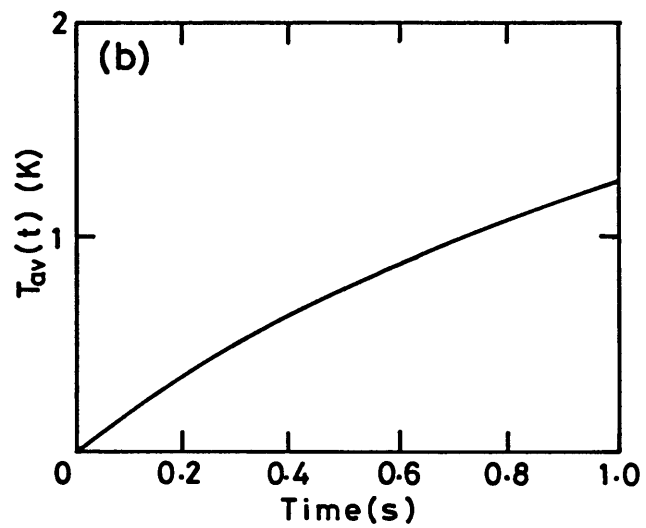
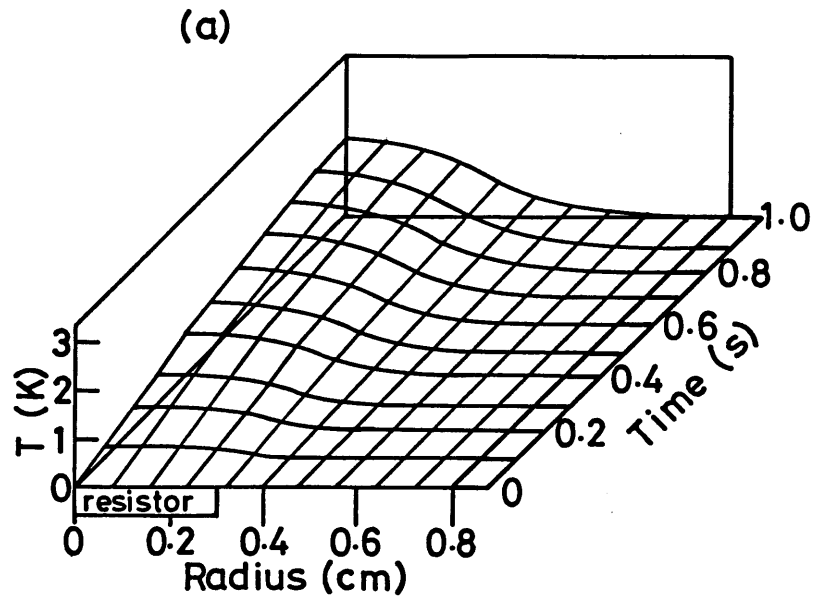


Fig.3 Calculated results of (a) temperature rise of the absorber, (b) its space averaged ($T_{av}(t)$) in the resistor region.

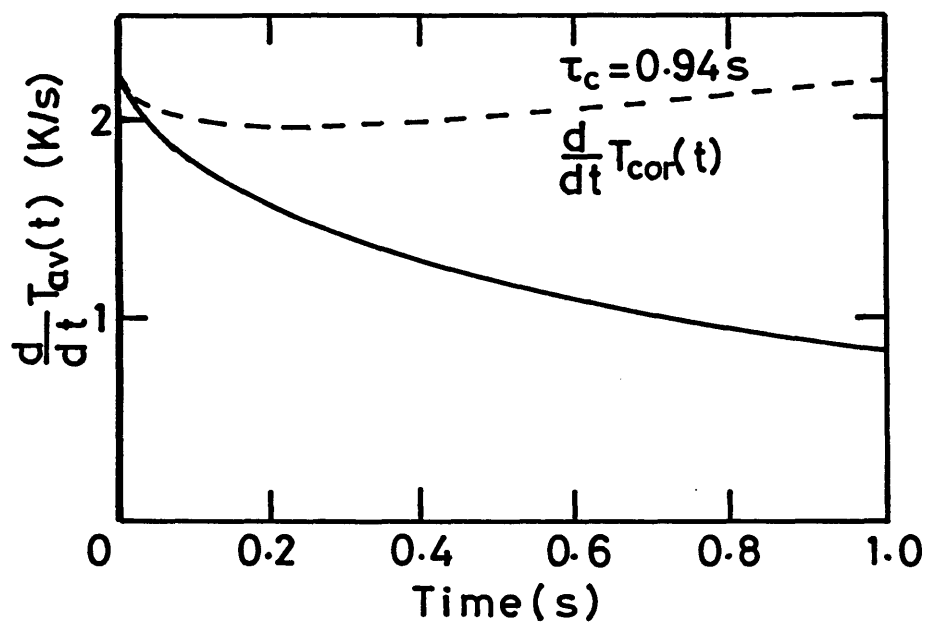


Fig.4 Time behavior of $T_{av}(t)$. The dashed line denotes the value with a simple correction for thermal cooling.

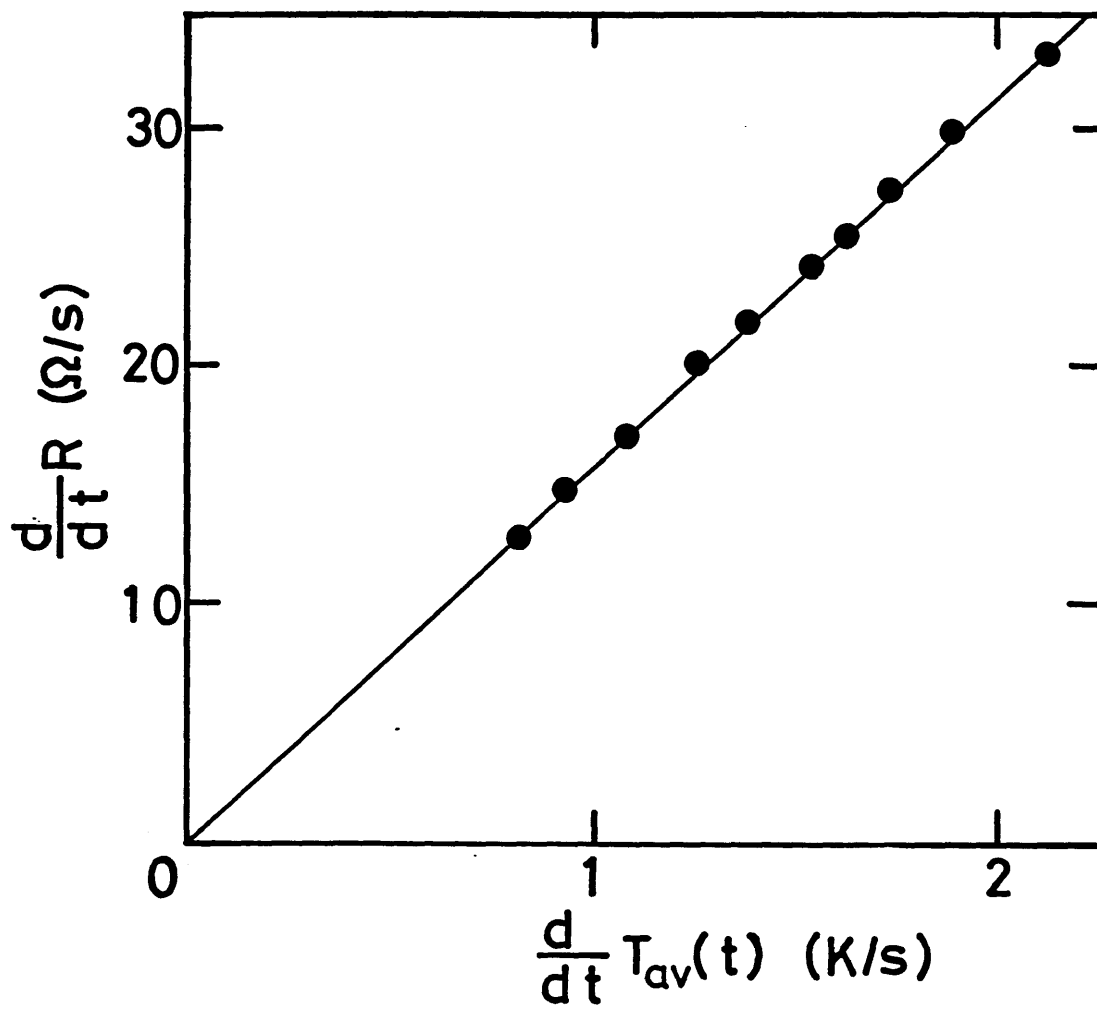


Fig.5 A plot of the measured \dot{R} against calculated $\dot{T}_{av}(t)$. The solid line shows the relation between \dot{R} and $\dot{T}_{av}(t)$, which is described by eq.(8).

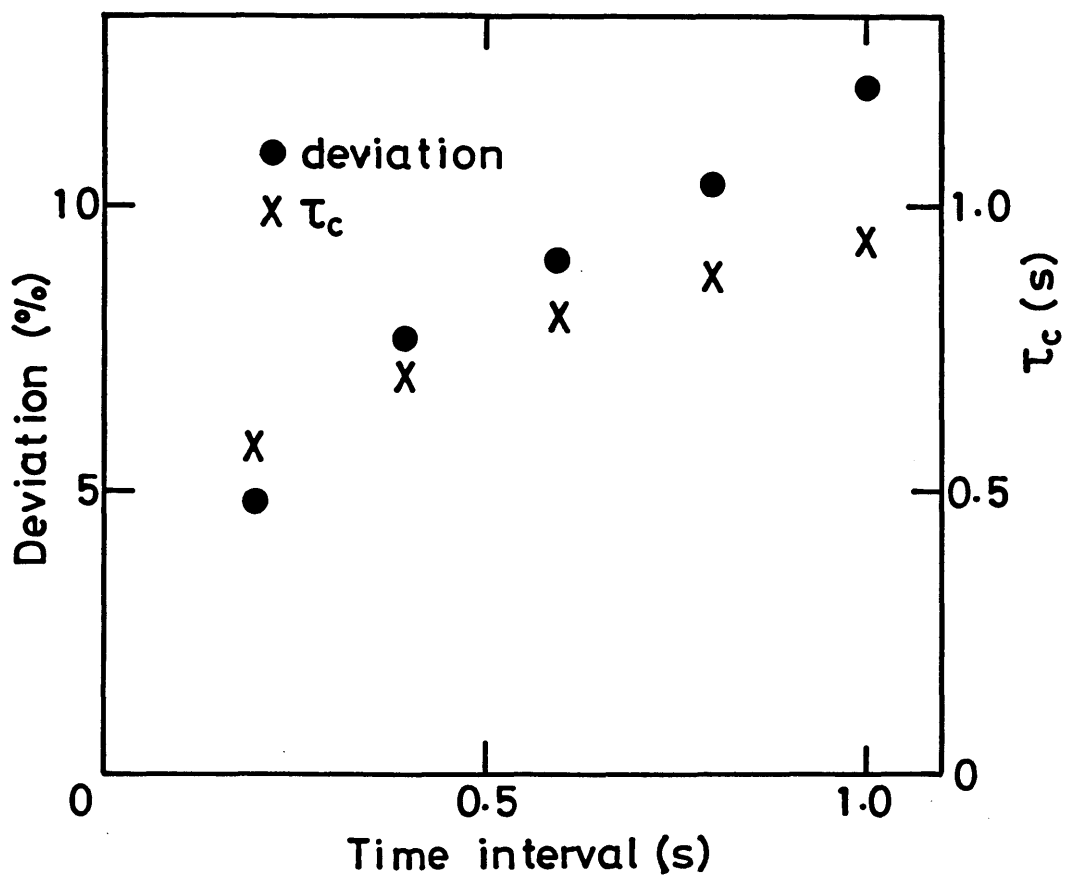


Fig.6 The maximum deviation of $T_{cor}(t)$ and the cooling time τ_c are plotted as a function of time interval of a correction for thermal cooling.

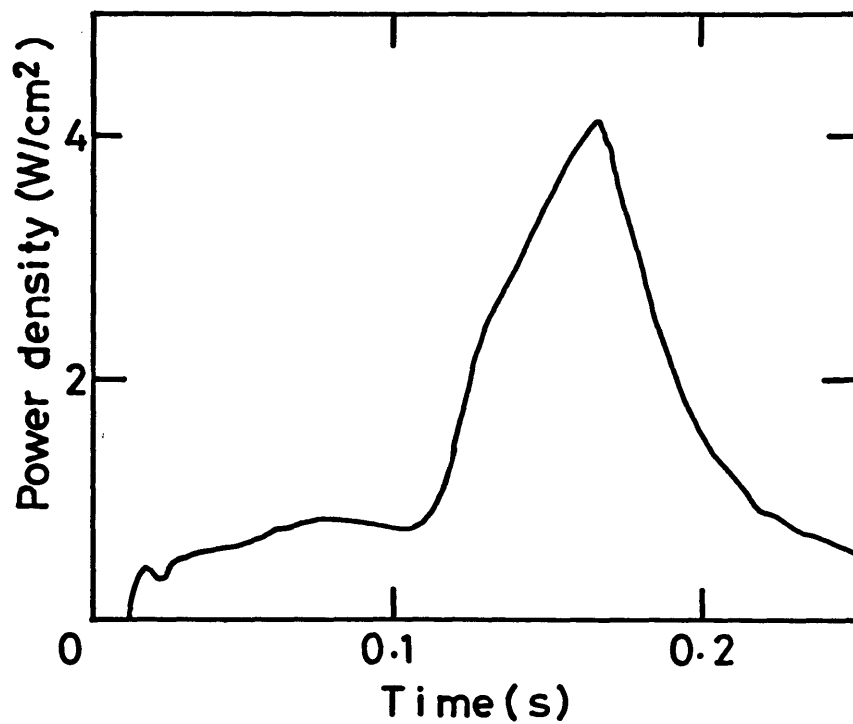


Fig.7 Time behavior of the radiation power density measured with the metal-film bolometer ($P_{\text{meas}}(t)$). It includes a simple correction for thermal cooling.

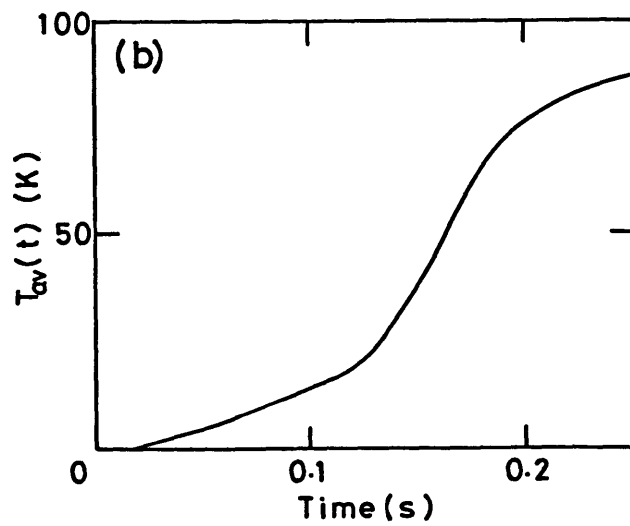
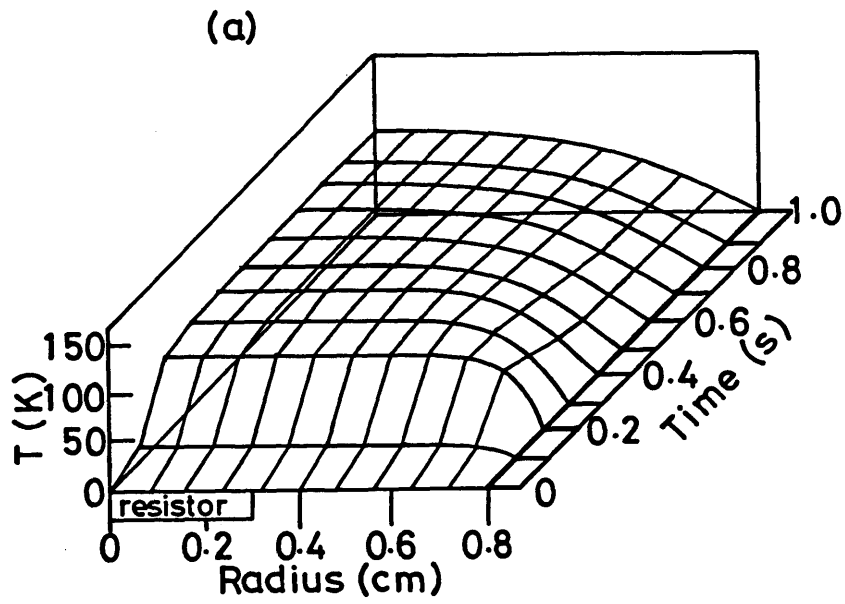


Fig.8 Calculated results of (a) temperature rise in the case without a slit, (b) its space averaged ($T_{av}(t)$).

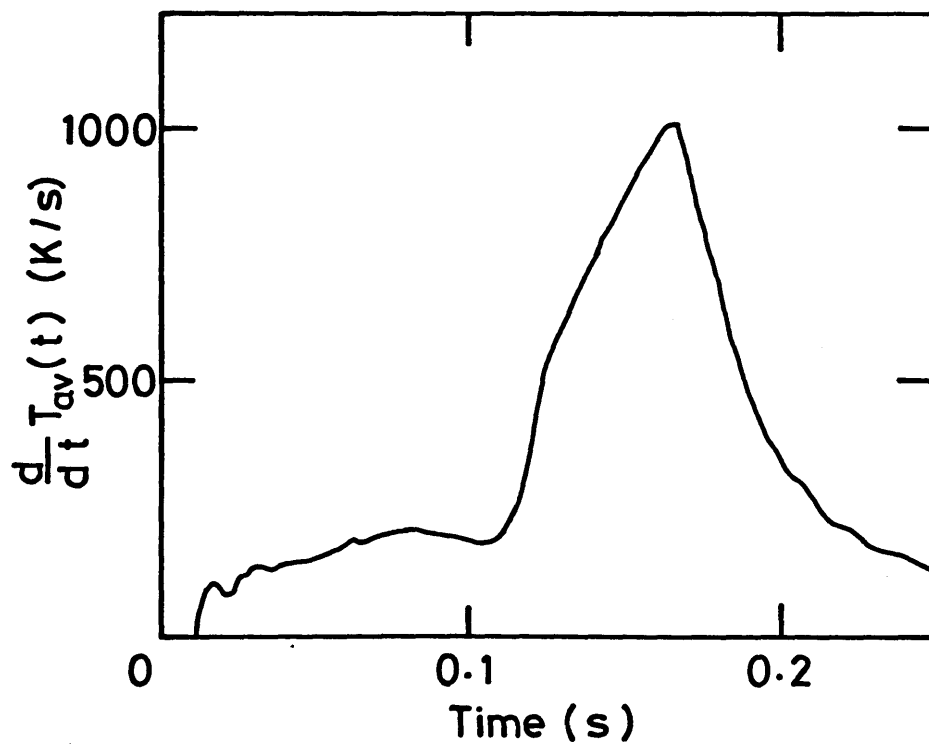


Fig.9 The time behavior of $T_{av}(t)$. A correction for thermal cooling has little effect on its value ($< 0.04\%$).

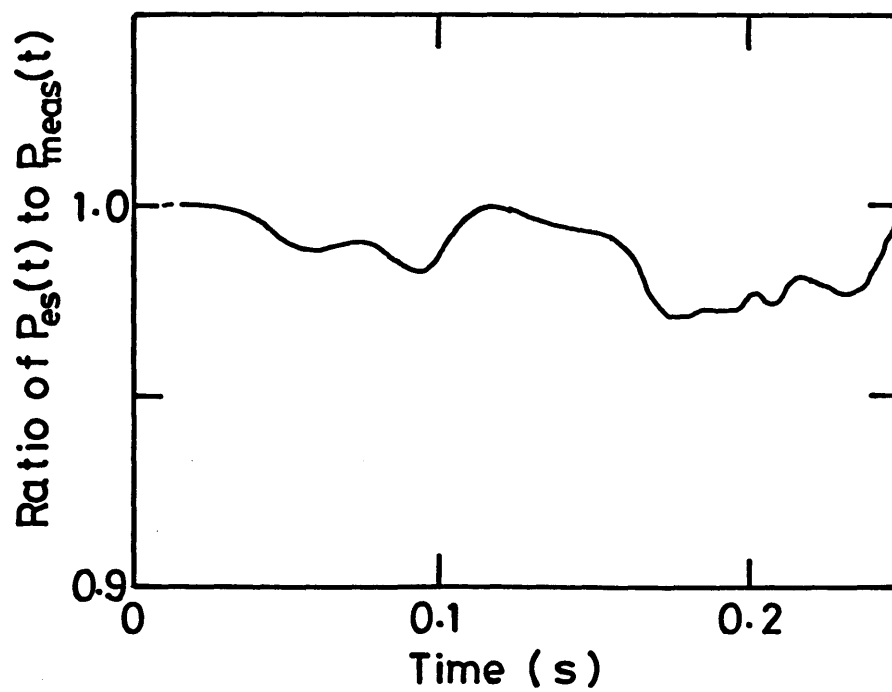


Fig.10 Time behavior of ratio of $P_{es}(t)$ to $P_{meas}(t)$. The value of $P_{es}(t)$ is obtained from the value of $T_{cor}(t)$ in consideration of thermal cooling.

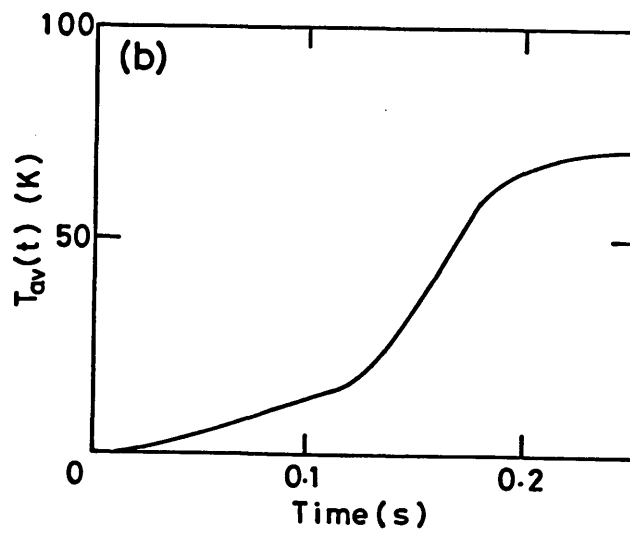
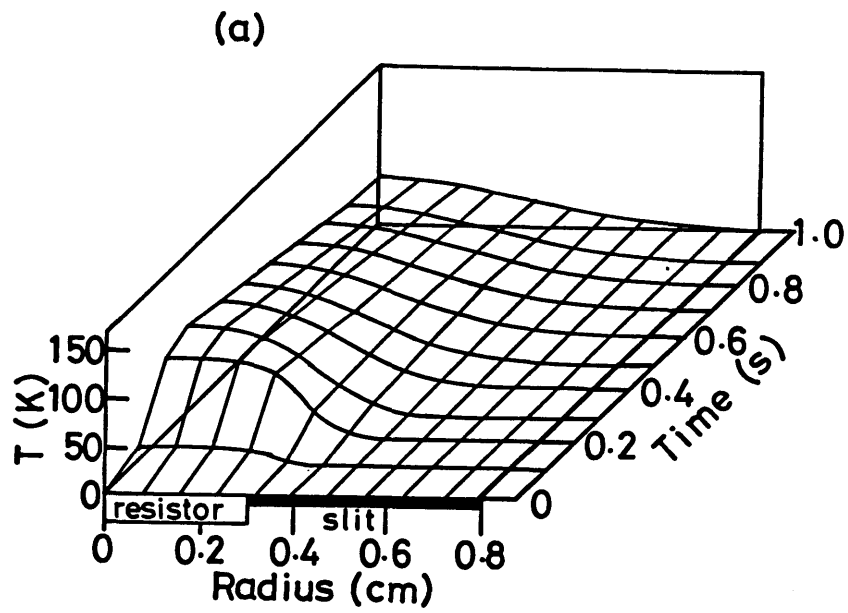


Fig.11 Calculated results of (a) temperature rise in the case with a slit, (b) its space averaged ($T_{av}(t)$).

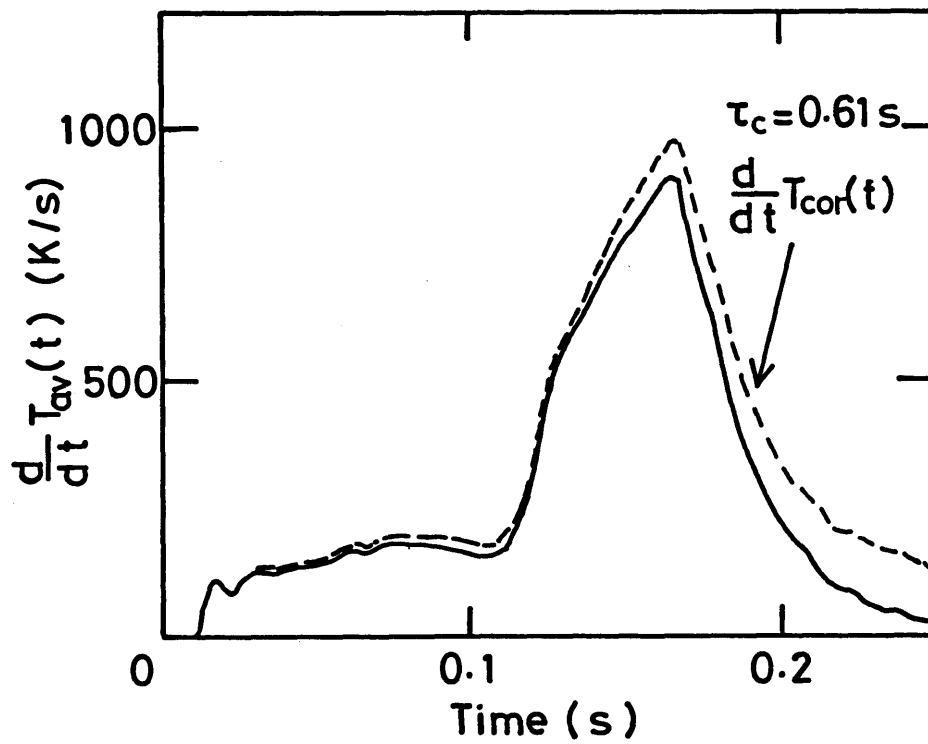


Fig.12 The time behavior of $T_{av}(t)$ (solid line). The dashed line denotes the value with a simple correction for thermal cooling.

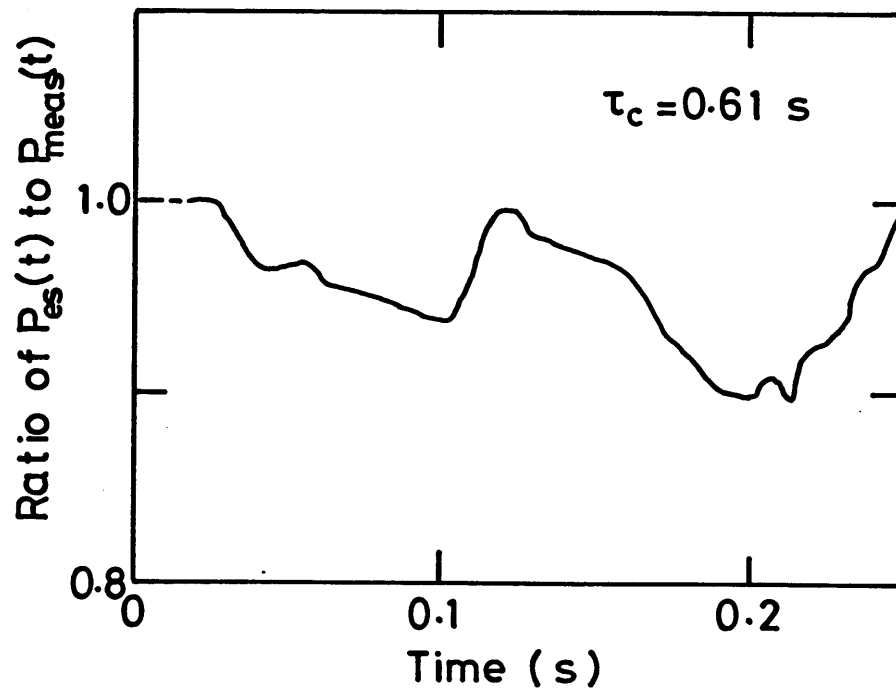


Fig.13 Time behavior of ratio of $P_{es}(t)$ to $P_{meas}(t)$. The value of $P_{es}(t)$ is obtained from the value shown by the dashed line in Fig.12 in consideration of thermal cooling.

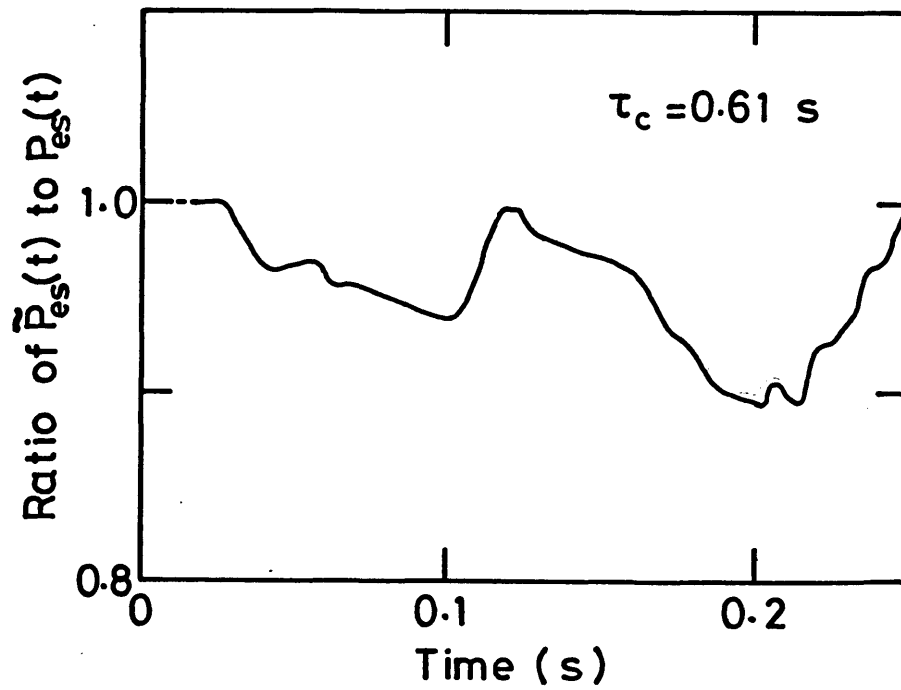


Fig.14 Time behavior of ratio of $\tilde{P}_{es}(t)$ to $P_{es}(t)$. The value of $\tilde{P}_{es}(t)$ is calculated by putting $P_{es}(t)$ in the place of $P(r,t)$ of eq.(1).

Characteristics of the Detectors for Bolometric Measurement in Application to High Temperature Plasma

Isamu OGAWA, Kazuo KAWAHATA, Nobuaki NODA,
Tetsuo WATARI, Shuugo TANAHASHI, Kazuo TOI
and Junji FUJITA

Institute of Plasma Physics, Nagoya University, Nagoya 464

(Received September 17, 1985; accepted for publication April 26, 1986)

The characteristics of a thermistor, a metal-film bolometer, and a pyroelectric detector were investigated with the aim of attaining a highly reliable bolometric measurement. The spurious signal which appears on a pyroelectric detector was sufficiently eliminated by setting a mask close to the detector, thus avoiding the direct incidence of photons at the electrode. Whether a signal was true or false could be determined from the integrated value of the signal. Calibrations were performed with a HeNe laser in consideration of reflections on the detector surface. No time drift was observed on the sensitivity determined in such a way. The radiation power measured with a pyroelectric detector agreed within 10% with that measured with a calibrated metal-film bolometer.

§1. Introduction

In present-day tokamak research, radiation loss plays an important role regarding the radial distribution of temperature, power balance, and stability of the plasma.¹⁻⁴⁾ In order to investigate these phenomena, measurements of the magnitude, time behavior, and spatial distribution of the radiation power are required. They are measured spectroscopically^{3,5)} and bolometrically.³⁻⁵⁾ The former method requires information concerning the plasma parameters, namely, the intensity of the impurity lines and the electron density and temperature. The latter method gives direct results, provided that the power due to charge-exchanged neutral particles is estimated.

Information on the radiation power profile is obtained through an Abel inversion, which requires measurements with considerable accuracy. Therefore, the calibration of these detectors is of primary importance. The reliability of a bolometric measurement depends entirely on the performance of the detectors. The requisite detector characteristics are a rapid time response (several ms), a high signal to noise (S/N) ratio, and a cooling time which is sufficiently longer than the plasma discharge duration.

Thermistors,^{1,6)} metal-film bolometers,⁶⁻⁸⁾ and pyroelectric detectors^{3,5)} are employed in fusion devices. A pyroelectric detector gives signals with a high S/N ratio and a rapid response. An external circuit for measurements is simple since there is no necessity for a differentiating procedure, which is required for measurements with a metal-film bolometer or a thermistor. In measurements with a pyroelectric detector, a high spatial resolution is expected for the following reason. Spatial resolution is determined by the viewing geometry of the detector, which is an arrangement of the entrance slit and the exit slit. The entrance slit determines the input power density and the exit slit determines the detective area. The spatial resolution increases as both slits are stopped down. Taking the S/N ratio into consideration, the spatial resolution is determined by the detection limit against the minimum input power. The

small size of the sensitive part, as well as the high S/N ratio increases the spatial resolution. However, several problems concerning these detectors are pointed out:

- (1) Sensitivity at short wavelengths¹⁰⁾
- (2) Spurious signal due to electrons produced by secondary emission*
- (3) Temporal changes in its characteristics*

A resolution of these difficulties is essential before reliable measurements of the radiation power can be obtained. In this paper, a reduction of the falsification, a calibration method with high accuracy, and the characteristic of other type detectors are investigated.

§2. Principle of the Detector for Bolometric Measurement

Radiation power is measured as a function of the temperature rise of the absorber of a detector on the assumption that the radiation energy from a plasma is efficiently converted into thermal energy. This assumption is justified for the following reason. It seems that the main fraction of radiated power from a tokamak plasma lies in the vacuum ultraviolet region. It is reported that photons in such a region are efficiently absorbed by various materials.¹¹⁾ This is supported by the fact that no difference has been observed between bare and coated detectors having layers of carbon black that can absorb nearly 100% of the incident-light energy.¹²⁾

If a radiation power P is incident on the foil, its temperature rise ΔT is governed by

$$P = C \frac{d}{dt} \Delta T + C \frac{\Delta T}{\tau_c}, \quad (1)$$

where C is the thermal capacity of the foil and τ_c the cooling time. The temperature rise is measured through the change in a resistance or through the change in the surface charge by a pyroelectric effect. The former is the principle of a thermistor and a metal-film bolometer and the latter is that of a pyroelectric detector.

*E. R. Müller: Max-Planck-Institut für Plasmaphysik Report No. IPP III/56, 1980.

2.1 Thermistor and metal-film bolometer

The thermistor and the metal-film bolometer are similar in operation. Both of the detectors combine the functions of a radiation absorber and a resistor for detection. Assuming that the temperature rise ΔT is small, a change in the resistance ΔR can be described as

$$\Delta R = R_0 \alpha \Delta T, \quad (2)$$

where R_0 is the initial resistance and α the temperature coefficient.

Figure 1 shows the circuit used in a total-radiation measurement on the JIPP T-IIU tokamak, where r and c are the resistance and capacitance of the differentiating circuit, respectively. This circuit has the advantage of simplicity and of no signal drift. When a signal is obtained under the condition that the time constant rc is smaller than the required time response τ of measurement and that R_0 is smaller than the impedance determined by r, c , the resulting voltage V can be described as

$$V = Irc \frac{d}{dt} \Delta R, \quad (3)$$

where I is the current determined by a constant current diode.

When τ_c is much longer than the duration time of the discharge, equation (1) can be rewritten as

$$P = C \frac{d}{dt} \Delta T. \quad (4)$$

From eqs (2), (3), and (4), V is obtained as

$$V = \frac{I \alpha R_0 r c}{C} P. \quad (5)$$

This shows that the signal is proportional to the incident power P .

2.2 Pyroelectric detector

When a pyroelectric crystal undergoes a change in temperature, a surface charge is produced as the result of a change in its spontaneous polarization with temperature. This pyroelectric effect is expressed by a pyroelectric coefficient p ,

$$\Delta P_s = p \Delta T, \quad (6)$$

where P_s is the spontaneous polarization.¹³⁾ The resulting pyroelectric charge-flow i_p in the circuit of the sample (Fig. 2) is described by

$$i_p = \frac{d}{dt} (A \Delta P_s) = A p \frac{d}{dt} \Delta T, \quad (7)$$

where A is the area of the sensitive region of the detector.

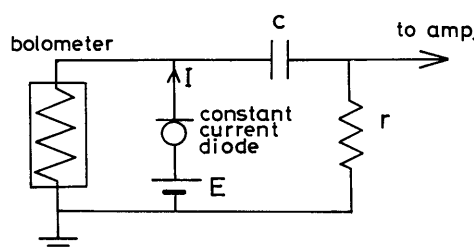


Fig. 1. Circuit for a metal-film bolometer.

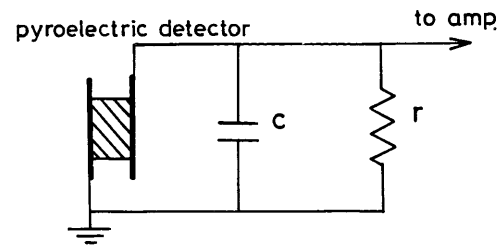


Fig. 2. Input equivalent circuit of a pyroelectric detector.

The input equivalent circuit of a pyroelectric detector is shown in Fig. 2. The time response depends on the time constant rc , since the time response determined by the detector is very rapid. The capacitance c is composed of the capacitance between the electrodes and that of a floating capacitance. The resistance r is the load resistance parallel to the detector. This time constant rc is chosen to be smaller than the required time response. Under such a condition, this detector operates as a current source whose signal is described by eq. (7).

A signal which is obtained through the thermal process should have the following feature. After the incident power on the detector is turned off, the integrated value of this signal becomes zero with a time lapse τ , several times larger than the cooling time τ_c . The integrated value is proportional to the temperature rise of the detector from the initial value. It is derived from eq. (7) as

$$\int_0^{\tau} i_p dt = A p [\Delta T(\tau) - \Delta T(0)]. \quad (8)$$

After the incident power becomes off, the temperature of the detector gradually decreases with time. Finally, it approaches the initial value. As can be seen from eq. (8),

$$\int_0^{\tau} i_p dt = 0. \quad (9)$$

A signal which does not satisfy this equation is regarded as a false signal.

§3. Calibration

It is important for a calibration to accurately determine the net input power to the detector since a bolometric measurement requires a total absorption of the radiation power from the plasma. A HeNe laser was used as the light source. The net input was obtained in consideration of the reflection from the detector. This method is suitable for a pyroelectric detector with a smooth surface, since the light undergoes a normal reflection and the reflected power is easy to measure. There is another method for calibrating a metal-film bolometer. If a current passes through the resistor of the detector, it produces heat. The sensitivity is obtained from the change in the resistance due to this heat.

3.1 Calibrations of the pyroelectric detector and the thermistor

The beam of the HeNe laser light was conducted to the detector at nearly right angles (Fig. 3). The power of the incident light and the reflection were measured with a calibrated power meter, with an accuracy of 3%. The net input power is the difference between these powers. The

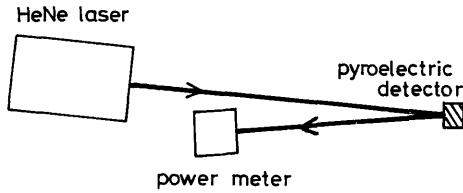


Fig. 3. Arrangement of a HeNe laser and a calibrated power meter for measurements of the reflected power.

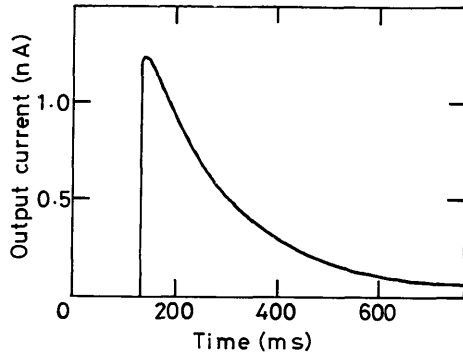


Fig. 4. Output current from a pyroelectric detector with incident HeNe laser light.

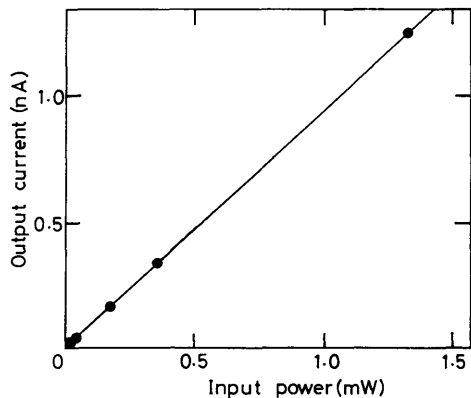


Fig. 5. A plot of the output current from a pyroelectric detector against the net input power, showing good linearity between them.

output current from the detector for a net input power of 1.3 mW is shown in Fig. 4. This signal rises within 1 ms after the power incidence and reaches a maximum value; then it decreases with a cooling time of 185 ms. The sensitivity and cooling time of this detector are obtained from the maximum value and the decay of this signal, respectively. The sensitivity and the reflectivity are $0.95 \mu\text{A}/\text{mW}$ and 53%, respectively. This calibrated value is twice as large as the manufacturer's value. The value obtained without regard to the reflected power of the HeNe laser light agrees well with the manufacturer's value. The high linearity of the output was checked as shown in Fig. 5. The incident power was controlled by changing the optical filter.

In a calibration of the thermistor, the circuit shown in Fig. 1 was used for the thermistor. The time behavior of the output signal for incident HeNe laser light was similar to that from a pyroelectric detector, except for an opposite polarity. This is because the thermistor has a negative temperature coefficient. The sensitivity obtained without regard to the reflected power of the HeNe laser

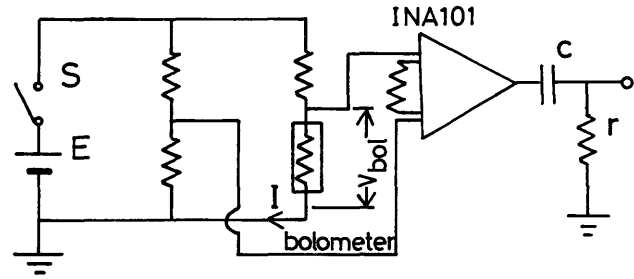


Fig. 6. Circuit for the calibration of a metal-film bolometer.

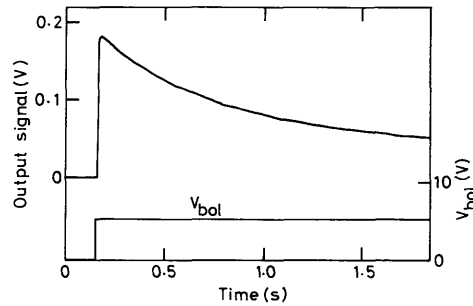


Fig. 7. Output signal from a metal-film bolometer with an input electric power and the voltage drop arising in this detector.

light was $1530 \Omega/\text{mJ}$. The reflected power is hard to be measured because of its diffused reflection. The cooling time is 0.92 s.

3.2 Calibration of the metal-film bolometer

The calibration of the metal-film bolometer was performed with the circuit shown in Fig. 6. This circuit is composed of a Wheatstone bridge, a differential amplifier, and a differentiating circuit. The net input power to the detector is measured with the voltage drop (V_{bol}) arising in the bolometer and the current I , which flows through the bolometer. The output signal from this circuit and V_{bol} are shown in Fig. 7. This signal reaches a maximum value within 3 ms, and then decreases with the cooling time (about 1.1 s). The net input power is 2.50 mW and the sensitivity of this detector is $12.9 \Omega/\text{mJ}$. This method has the advantage of being calibrated *in situ*.

§4. Arrangement of the Detectors to the JIPP T-IIU Tokamak

A pyroelectric detector (bare detector), a pyroelectric detector with a mask (detector with the mask) and a thermistor were mounted in order to investigate spurious signals due to the photoelectric effect. The mask, which is close to the pyroelectric detector, affords protection against the direct incidence of radiation onto a non-grounded electrode (Fig. 8). The sensitive region of the bare detector is determined by its intrinsic sensitive region and that of the detector with the mask is determined by the mask. The thermistor, which is free standing, is so arranged that it views the same plasma region as a detector with a mask. The effect of the mask against spurious signals was investigated from the signals from a detector with a mask and from the thermistor. This is because any spurious signal due to the photoelectric

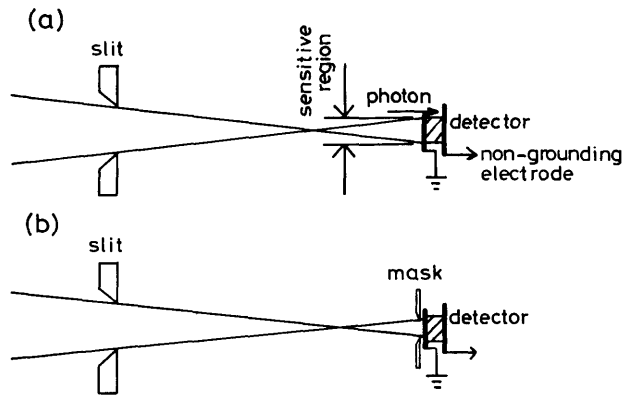


Fig. 8. Geometry of (a) a bare detector and (b) the detector with a mask.

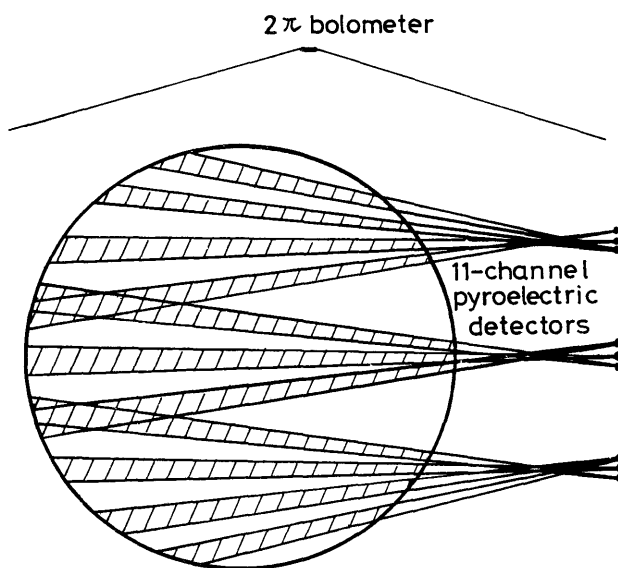


Fig. 9. Geometric arrangement of 11-channel detectors with masks and a 2π bolometer.

effect has little effect on the signal of the thermistor (discussed below).

In order to measure the total and spatial profile of the radiation, a so-called " 2π bolometer"* and eleven pyroelectric detectors (detectors with the mask) were employed (Fig. 9). The shaded portion in Fig. 9 shows the plasma region viewed by the detectors with a mask. The maximum value in breadth of the shaded portion (spatial resolution) is 2 cm. This " 2π bolometer" is a metal-film bolometer and views the plasma with a solid angle of about 2π .

§5. Results of the Measurement in the JIPP T-IIU Tokamak

The signal (i_s) shown in Fig. 10(a) was obtained from a bare detector (Fig. 8(a)). The magnitude and the behavior of the signal show the possibility of a spurious signal. The magnitude of i_s is too large to do fit with reality. Because this value indicates a radiation loss which greatly exceeds the input power to the plasma. The

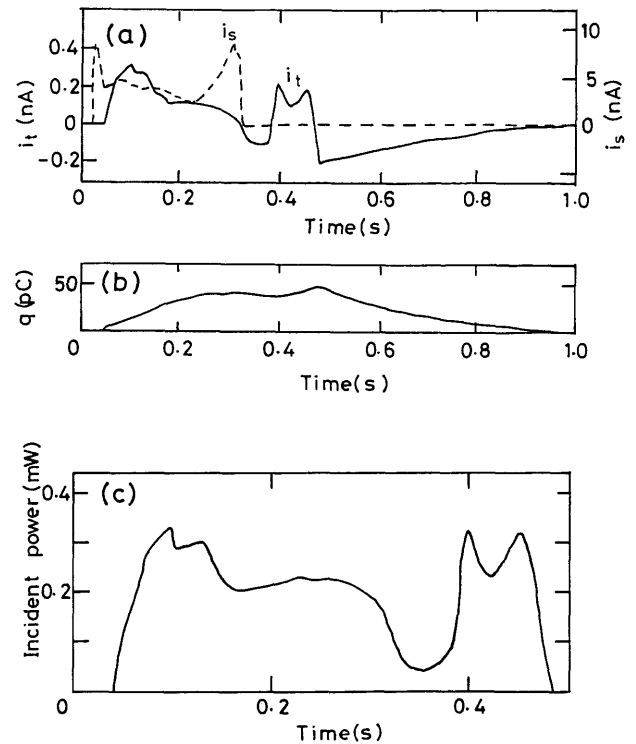


Fig. 10. (a) Time behaviors of the output from a bare detector (i_s) and the output from a detector with a mask (i_t). The time behavior of (b) the integrated value of a signal and (c) the incident power on a detector obtained with a detector with a mask through a correction for the cooling time.

signal after the discharge has a small negative value, but is too small to explain the decrease in the temperature of the detector due to the heat losses described by the second term of the equation (1). It is obvious that the integrated value of the signal does not return to zero with a long lapse of time. This shows that a positive spurious signal is superposed on the true signal.

The signal (i_t) shown in Fig. 10(a) was obtained from a pyroelectric detector with a mask (Fig. 8(b)). The magnitude of this signal indicates a radiation loss which is about 80% of the ohmic input power. It is possible that the plasma radiates such a large fraction of the energy loss since this is a radiation-dominant plasma. This signal has a negative part, indicating a decrease in the temperature of the detector. The integrated value of i_t is shown in Fig. 10(b). It satisfies the condition described in eq. (9). Thus the net input power on the detector is obtained through a correction regarding the cooling time. As can be seen from eqs. (1) and (7),

$$P = \frac{C}{Ap} \left(i_p + \frac{1}{\tau_c} \int_0^t i_p dt \right), \quad (10)$$

where Ap/C is equal to the sensitivity of this detector. The net input power obtained from the signals i_t and q shown in Fig. 10(a) (b) is shown in Fig. 10(c).

The signals from the detector with a mask and a thermistor are shown in Fig. 11 for a comparison. This comparison is restricted to the initial magnitudes and the time variations, since the zero levels of these signals without any corrections for the cooling times decrease with time. The time variation of the signal from a detector with a mask is consistent with that from a thermistor. The

*M. M. Pickrell: MIT Plasma Fusion Center Report No. PFC/RR-82-30 (1982).

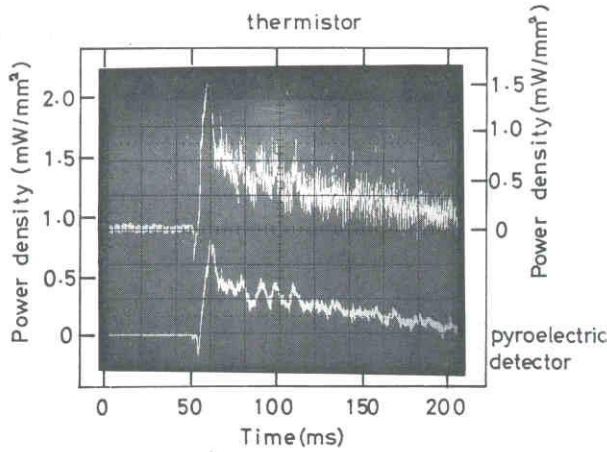


Fig. 11. Time behavior of the incident power per unit area obtained with a thermistor and a detector with a mask, respectively.

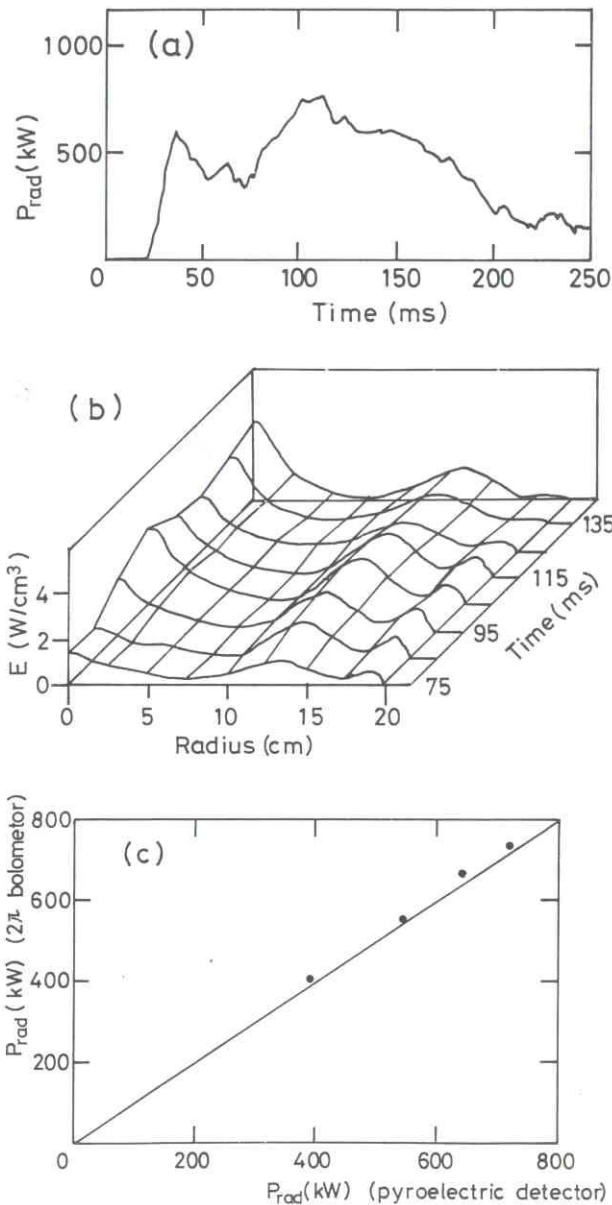


Fig. 12. (a) Time behavior of the total radiation power measured with a 2π bolometer. (b) Spatial distribution of the radiation every ten ms. (c) A plot of the total radiation power obtained through the integration of the spatial distribution against that obtained with a 2π bolometer.

magnitude of the latter is larger than that of the former by 30% for the initial 100 ms. This discrepancy seems to be rather reasonable since the calibration data of this thermistor was obtained without any consideration of the reflection of HeNe laser light because of the difficulty in measuring the reflected power. Therefore, the signal obtained by a pyroelectric detector would show a more accurate value. The pyroelectric detector gives a signal with a higher S/N ratio and a greater time response. The time response of the pyroelectric detector is 1 ms, the time constant of the differentiating circuit of the thermistor is 3 ms and the time response determined by the thermistor is about 5 ms.

The total radiation power is obtained with the 2π bolometer through a correction for the cooling time (Fig. 12(a)). This correction procedure is made from eqs. (1), (2) and (3),

$$P = \frac{C}{I\alpha R_0 r c} \left(V + \frac{1}{\tau_c} \int_0^t V dt \right), \quad (11)$$

where $\alpha R_0/C$ is equal to the sensitivity of the detector. This cooling time is not simply defined because of the temperature nonuniformity of the detector surface. This nonuniformity causes a deviation from the true value, depending on the time behavior of the total radiation. The adequate value of τ_c in equation (11) varies case by case; it is so determined that the total radiation is zero immediately after the plasma duration. The value in the case of Fig. 12(a) is 470 ms. The accuracy of the correction is estimated by solving the heat-conduction equation which is related to this detector (a thin disk shape (10 μm). The resistor for the detection is positioned at the center region. The heat-conduction equation gives the time behavior and the spatial distribution of the temperature rise $\Delta T(t, r)$ against the input power (Fig. 12(a)). Equations (2) and (3) relate $\Delta T(t, r)$ with V . The input power used in the heat-conduction equation and the value of P obtained in eq. (11) give the deviation. The deviation in the total radiation power, caused by a correction using a value of 470 ms, was less than 5%. The total radiation power was also obtained by integrating the spatial profile (Fig. 12(b)).

These signals were obtained with a high S/N ratio (more than 20). Both of the values agree with each other

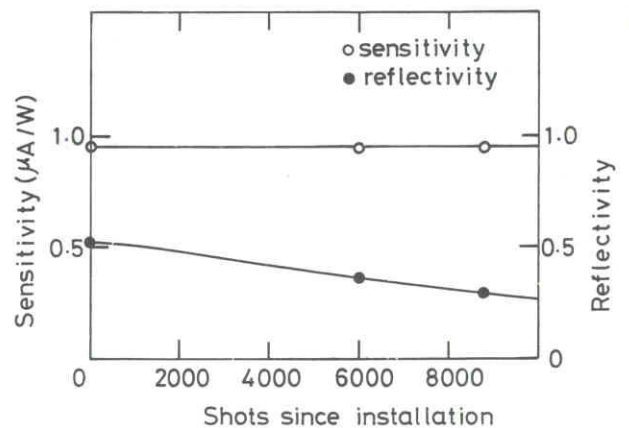


Fig. 13. Temporal change in the sensibility and the reflectivity for He-Ne laser light.

within 10%, as shown in Fig. 12(c).

The pyroelectric detector was calibrated each time it was detached from the JIPP T-IIU tokamak. The sensitivity and reflectivity for the HeNe laser light are shown in Fig. 13. As the detectors are exposed to a plasma discharge, the reflectivity decreases. However, little change in the sensitivity has been observed (within 1%). A decrease in the reflectivity is due to a change in the surface condition of the detector, since discolorations are found through visual observations.

§6. Discussion

There are two methods for calibrating bolometric detectors. One is a method in which the output against the known input power is obtained. The other is a method in which data of the thermal process and of detection process are used for calculations. The sensitivities of the thermistor and the metal-film bolometer are calculated from their thermal capacity and the temperature coefficient of their resistor. The thickness of a detector with a specific accuracy and a specific heat need to be determined. Moreover, the effective thermal capacity which is used for a calibration depends on the geometric form of the detector. To obtain this effective thermal capacity is a difficult problem if the detector has a complicated geometry. A calibration using the known input power is an easy method and gives a value for the total system. An accurate measurement of the input power is of primary importance in this method. The sensitivity obtained in this method is expected to be accurate, because it is possible to measure the electric input power to the detector with accuracy.

Concerning the cooling time, that of a pyroelectric detector is well-defined. This is because of the small non-uniformity of the temperature profile of the detector surface. A correction for the initial 300 ms is quite effective and reproduces the constant HeNe laser power within 5%, in case of the calibration shown in Fig. 4. The same accuracy probably applies to a measurement of the radiation power from the plasma. Concerning the metal-film bolometer, its cooling time is influenced by the nonuniformity of the detector temperature. The heat-conduction equation suitable for a metal-film bolometer gives the effective cooling time in individual cases. A correction using this cooling time is accurate (within 5%) for the case shown in Fig. 12(a).

The total radiation power from a 2π bolometer and from pyroelectric detectors are given on the assumption that detector surfaces absorb 100% of the incident radiation from the plasma. The agreement between these radiation powers show that this assumption is good. This assumption is also supported by the fact that the main radiation, which lies in vacuum ultraviolet region, is highly absorbed by various kinds of materials.

The results shown in Fig. 13 show that the reflectivity for the He-Ne laser light is changeable according to the condition of the detector surface. On the other hand, a small difference between the radiation powers of the plasma under similar conditions can be seen. This indicated that the reflectivity for the photons responsible to the main fraction of the radiation power from the plasma

is not so changeable as that for the HeNe laser light. This tendency is consistent with the high absorbance of such photons. The calibration without regard to the reflected power of HeNe laser light causes an overestimation and a changeable evaluation of the radiation power from the plasma. Taking the high absorption of the main fraction of the plasma radiation into consideration, it can be concluded that the calibration method with regard to the reflected power of the He-Ne laser light is a reasonable method. It is likely that the cause of the above-mentioned temporal change in the characteristics represents a change in the reflectivity for the photons at longer wavelengths. This change in the reflectivity can be attributed to a contamination of the detector surface. Some of the materials installed inside the vacuum vessel might become deposited on the surface of the detector. However, it is too thin to change its thermal capacity and the sensitivity is unchanged. The same phenomenon applies to a metal-film bolometer.

The calibration method using a He-Ne laser is not suitable for a thermistor and a metal-film bolometer, since the reflected power of the HeNe laser light is hard to measure because of diffused reflections. In addition, there is an obstacle in calibrating the thermistor, the position dependence of the sensitivity. Measurements of the thermal capacity and the temperature coefficient are the only calibration methods for a thermistor.

A pyroelectric detector gives a signal as the element of a current source. On the other hand, a thermistor and a metal-film bolometer give voltage signals which represent a voltage drop due to an external current. The current signal from a pyroelectric detector is of the order of 10^{-10} A and the bias currents supplied to a metal-film bolometer and a thermistor are of the order of 10^{-3} A in the application to the JIPP T-IIU tokamak. Even a small current due to a non-pyroelectric effect causes a serious falsification of the signal to the pyroelectric detector. This is the reason why a pyroelectric detector can easily suffer from falsification. A pyroelectric detector without a mask accepts the direct incidence of photons on a non-grounded electrode. Electrons are emitted from the electrode through the photoelectric effect by these photons and a resulting current is induced. This current would represent the falsification (Fig. 14). The photons of the vacuum ultraviolet region have a high photoelectric-effect efficiency.¹⁴⁾ The value estimated from this efficiency is sufficient to explain the magnitude of the falsification observed in this experiment (i_s in Fig. 10(a)). Even the signal in the case without a mask includes the true

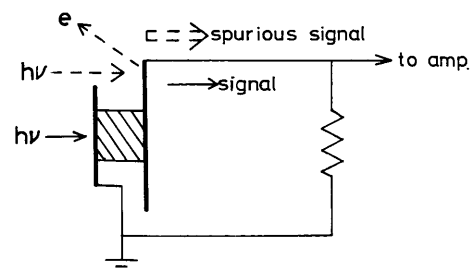


Fig. 14. Schematic geometry showing the spurious signal from the pyroelectric detector.

signal, since this signal becomes a little negative at the end of a plasma discharge. This negative signal indicates the process of the decrease in temperature of the detector and is regarded as the signal through thermal process. The magnitude of the falsification must be sufficiently suppressed to less than that of the true signal. It is expected that falsification due to an influx of charged particles and an externally induced electric field (as well as the direct incidence of photons) can be avoided by using a mask. However, there is a possibility of falsification due to the penetration of photons with energies greater than 10 keV. This may be an obstacle in the measurement of a high-temperature plasma in future devices. However, the efficiency of the photoelectric effect becomes low for such photons.

§7. Summary

The characteristics of presently used pyroelectric detectors, metal-film bolometers, and thermistors are summarized. The time resolution in a radiation measurement obtained with pyroelectric detectors was 1 ms, and that of a metal-film bolometer was 3 ms. The time response is determined by both the arrival time of the heat at the sensitive part and from the time constant of the external circuit. The time response, determined by the detector, became rapid as the thickness of the detector was reduced. The response time of a signal obtained with a thermistor was long because of its thick absorber. Concerning the S/N ratio, the results for a pyroelectric detector and a thermistor were satisfactory (more than 20). That of a metal-film bolometer is high (more than 20) as long as the total radiation is measured. Although the cooling time of the pyroelectric detector is short (~ 200 ms), it can be amply covered by a correction for the cooling time (Fig. 10(c)).

Acknowledgements

The authors wish to thank the JIPP T-IIU group,

in particular, Messrs Y. Kawasumi, and E. Kako, S. Hirokura, Y. Taniguchi, H. Ishiguro and M. Mugishima for assistance during the experiments. It is a pleasure to acknowledge valuable discussions with Dr. S. Besshou of Kyoto University.

References

- 1) H. Hsuan, K. Bol, and R. A. Ellis: *Nucl Fusion* **15** (1975) 657.
- 2) V. Arunasalam, C. Barnes, K. Bol, D. Boyd, K. Brau, N. Bretz, M. Brusati, S. Cohen, S. Davis, D. Dimock, F. Dylla, D. Eames, P. Efthimion, H. Eubank, H. Furth, R. Goldston, R. Hawryluk, K. Hill, E. Hinnov, R. Horton, J. Hosea, H. Hsuan, D. Ignat, F. Jobes, D. Johnson, M. Mattioli, E. Mazzucato, Meservey, P. Moriette, N. Sauthoff, J. Schivell, G. Schmidt, R. Smith, F. Stauffer, W. Stodiek, J. Strachan, S. Suckewer, and S. von Goeler: *Proc. 8th Europ Conf. Controlled Fusion & Plasma Physics, 1977* (Institut of Plasma Physics, Prague, 1977) Vol. 2, p. 17.
- 3) K. Odajima, H. Maeda, M. Shiho, H. Kimura, S. Yamamoto, M. Nagami, S. Sengoku, T. Sugie, S. Kasai, M. Azumi, and Y. Shimomura: *Nucl. Fusion* **18** (1978) 1337.
- 4) L. S. Scaturro, and M. M. Pickrell: *Nucl. Fusion* **20** (1980) 527.
- 5) E. Hinnov, J. Hosea, H. Hsuan, F. Jobes, E. Meservey, G. Schmidt, and S. Suckewer: *Nucl. Fusion* **22** (1982) 325.
- 6) J. Schivell, G. Renda, J. Lowrance, and H. Hsuan: *Rev. Sci. Instrum.* **53** (1982) 1527.
- 7) S. Besshou, S. Morimoto, O. Motojima, T. Obiki, A. Iiyoshi, and K. Uo: *Jpn. J. Appl. Phys.* **23** (1984) L839.
- 8) K. F. Mast, and H. Krause: *Rev. Sci. Instrum.* **56** (1985) 969.
- 9) TFR Group (Presented by A. L. Pecquet): *J. Nucl. Mater.* **93** (1980) 377.
- 10) H. Kawamura, M. Seki, and M. Maeno: *J. Nucl. Sci. Tech.* **16** (1979) 847.
- 11) G. B. Sabine: *Phys. Rev.* **55** (1939) 1064.
- 12) J. Schivell: *Rev. Sci. Instrum.* **56** (1985) 972.
- 13) S. T. Liu, and D. Long: *Proc. IEEE* **66** (1978) 14.
- 14) James A. R. Samson: *Techniques of Vacuum Ultraviolet Spectroscopy*, (GCA Corporation, New York, London, Sydney, 1967) p. 224.

Reprinted from

Journal of the Physical Society of Japan
Vol. 53, No. 5, May, 1984, pp. 1590-1593

Growing and Damping of Space Charge Waves of an Electron Beam due to Nonlinear Landau Damping

Reiji SUGAYA, Hideki FUJITA and Isamu OGAWA

*Department of Physics, Faculty of Science,
Ehime University, Matsuyama 790*

Growing and Damping of Space Charge Waves of an Electron Beam due to Nonlinear Landau Damping

Reiji SUGAYA, Hideki FUJITA* and Isamu OGAWA*

*Department of Physics, Faculty of Science,
 Ehime University, Matsuyama 790*

(Received December 12, 1983)

We have observed experimentally damping and growing of fast and slow space charge waves of an electron beam due to nonlinear Landau damping in an electron beam-plasma system by using spectrum analysis. The former with positive energy damps and the latter with negative energy grows by nonlinear interaction with the Trivelpiece-Gould mode and the electron beam. The lowest and higher modes of the Trivelpiece-Gould modes with respect to a radial wavelength grow by this nonlinear wave-particle interaction satisfying the resonant condition.

Nonlinear wave-particle interaction (nonlinear Landau damping) is one of fundamental mechanisms for energy transfer between waves and particles in plasma turbulence.^{1,4)} Recently, many experimental observations of nonlinear Landau damping have been reported for various electrostatic waves.²⁻⁶⁾ We have also reported experimental studies of nonlinear Landau damping in an electron beam-plasma system immersed in a magnetic field, where the space charge wave of an electron beam and other electrostatic wave interact with an electron beam or plasma electrons.^{7,8)} In this letter, we present the detailed experimental observations of the behaviours of fast and slow space charge waves of an electron beam (fast and slow beam modes) due to nonlinear Landau damping in an electron beam-plasma system in a magnetic field where the fast or slow beam mode decays into the Trivelpiece-Gould mode (T-mode) by nonlinear interaction with an electron beam. We have carried out simultaneous observations of damping of the fast beam mode with positive energy and growing of the slow beam

mode with negative energy by using spectrum analysis of wave number.

The resonant condition for such a nonlinear interaction is given by^{7,8)}

$$\omega_1 - \omega_2 - (k_{//1} - k_{//2})v_b = m\omega_c, \quad (1)$$

where ω_1 and ω_2 are the frequencies of two waves, $k_{//1}$ and $k_{//2}$ the components of wave vectors parallel to the magnetic field, v_b the velocity of the beam, ω_c the electron cyclotron frequency and m an integer. The subscripts 1 and 2 denote the fast (or slow) beam mode and T-mode, respectively. Based on the general wave kinetic equations,⁹⁾ the following equations for nonlinear Landau damping of electrostatic waves in an infinite uniform plasma in a uniform magnetic field are obtained:⁸⁾

$$\frac{\partial |E_{\omega_1}|^2}{\partial z} = -2\gamma_1 |E_{\omega_1}|^2 - S\alpha_1 |E_{\omega_1}|^2 |E_{\omega_2}|^2, \quad (2)$$

$$\frac{\partial |E_{\omega_2}|^2}{\partial z} = -2\gamma_2 |E_{\omega_2}|^2 + \alpha_2 |E_{\omega_1}|^2 |E_{\omega_2}|^2, \quad (3)$$

with nonlinear wave-particle coupling coefficients given as follows:

$$\alpha_1 \left| \frac{\partial \varepsilon}{\partial k_{//1}} \right| = \alpha_2 \left| \frac{\partial \varepsilon}{\partial k_{//2}} \right| = -\frac{4\pi\omega_o^4 m\omega_c}{k_1^2 k_2^2 m_e n_o} \int_{-\infty}^{\infty} dv_{//} \int_0^{\infty} dv_{\perp} \frac{\partial f_o(v_{\perp}, v_{//})}{\partial v_{\perp}} \delta(\omega' - m\omega_c - k'_{//} v_{//}) \times \left| \sum_{p=-\infty}^{\infty} \frac{k_{\perp 1} k_{\perp 2} J_p(k_{\perp 1} v_{\perp} / \omega_c) J_{p-m}(k_{\perp 2} v_{\perp} / \omega_c)}{(\omega_1 - p\omega_c - k_{//1} v_{//})^2 - \omega_c^2} \right|^2, \quad (4)$$

where ε is the linear dielectric constant given by

* Present address: Institute of Plasma Physics, Nagoya Univ., Nagoya 464.

$$\varepsilon = 1 + \frac{\omega_p^2}{k^2 v_t^2} \left[1 + \sum_{n=-\infty}^{\infty} e^{-\lambda} I_n(\lambda) \frac{\omega}{\sqrt{2} k_{//} v_t} Z \left(\frac{\omega - n\omega_c}{\sqrt{2} k_{//} v_t} \right) \right] - \frac{\omega_b^2}{\omega_c^2} \sum_{n=-\infty}^{\infty} \left[\frac{e^{-\mu} I_n(\mu) \omega_c^2}{(\omega - n\omega_c - k_{//} v_b)^2} \frac{k_{//}^2}{k^2} + \frac{n\omega_c e^{-\mu} I_n(\mu) / \mu}{\omega - n\omega_c - k_{//} v_b} \frac{k_{\perp}^2}{k^2} \right], \quad (5)$$

and f_0 is the electron velocity distribution function showing the mixture of the Maxwellian plasma with the electron temperature T_e and the electron beam with the velocity v_b and the temperature T_b . Here, E is the wave electric field as a function of the axial distance z , γ the linear damping rate, $\omega' = \omega_1 - \omega_2$, $\mathbf{k}' = \mathbf{k}_1 - \mathbf{k}_2$, $\omega_0^2 = \omega_p^2 + \omega_b^2$, $\lambda = k_{\perp}^2 v_t^2 / \omega_c^2$, $\mu = k_{\perp}^2 v_{tb}^2 / \omega_c^2$, $v_t = \sqrt{T_e / m_e}$, $v_{tb} = \sqrt{T_b / m_e}$, n_0 the total electron density, I_n the modified Bessel function of the n -th order, Z the plasma dispersion function,¹⁰⁾ and S is the sign of the wave energy for the fast and slow beam modes. The other notations are standard. Since, $\alpha_1, \alpha_2 > 0$, it is proved that when the first wave is the fast beam mode with the positive energy ($S=1$), this wave damps and the second wave (T-mode) grows. On the other hand, when the first wave is the slow beam mode with the negative energy ($S=-1$), this wave and the second one grow simultaneously (explosive instability⁸⁾).

In this experiment a monoenergetic beam with energy $U_b \cong 140$ eV, current $I_b \cong 1.5$ mA, and diameter $D_b \cong 6$ mm is continuously injected along a uniform magnetic field into a beam-generated plasma with electron density $n_e \cong 2 \times 10^9$ cm⁻³, $T_e \cong 5$ eV and diameter $D_p \lesssim 4$ cm at argon gas pressure of 0.4 mTorr. The uniformity of the magnetic field is 2.7 percent over a length of 60cm. The electron-neutral collision frequency of beam and plasma electrons are $\nu \cong 1 \sim 2$ MHz giving a mean free path of 1 m. On opposite side of the electron gun, a Faraday cup is placed to measure the parallel energy of the electron beam U_b . A coaxial antenna, axially movable, is placed in the plasma in order to detect the wave. The first wave and/or the second one are excited by applying one or two external hf signals with frequencies ω_1 and ω_2 (voltages $V_1, V_2 \cong 0-5$ V) to the electrode of the electron gun. The spatial evolution of the small amplitude space charge wave of the beam excited by the weak external hf signal (ω_1) changes by

the presence of the large amplitude T-mode launched by the strong external signal (ω_2). On the other hand, in order to identify this nonlinear interaction, the small amplitude T-mode excited nonlinearly by the large amplitude space charge wave of the beam is investigated. To determine the wave number components $k_{//}$ of the obtained wave patterns, the interferometer outputs are analyzed by the method of fast Fourier transform (FFT) and maximum entropy method (MEM).¹¹⁾ Analysis by maximum entropy method has a high resolving power of spectrum and it is possible to make a spectrum analysis even if the length of data is very short.

In Fig. 1(a), we exhibit typical interferometer traces of the first wave. The traces A and B are the small amplitude space charge waves with the second wave ($V_2 = 2$ V), and without the second one, respectively. These traces are the results of interference of fast and slow beam modes,^{7,8)} whose dispersion relation is derived approximately by $\varepsilon = 0$ and given as follows:

$$\omega_1 = k_{//1} v_b \pm \frac{k_{//1}}{k_1} \omega_b, \quad (6)$$

where the upper and lower signs correspond to the fast and slow beam modes, respectively. To obtain the wave number components $k_{//1}$ of these traces the spectrum analysis of the interferometer outputs is carried out, and their spectra obtained by the methods of FFT and MEM are shown in Fig. 1(b). The spectrum of the interferometer trace B by MEM (curve B₂) has two peaks f and s which correspond to the fast and slow beam modes, respectively. However, in the spectrum of the trace B by FFT shown by the curve B₁, there appears only one peak f which corresponds to the fast beam mode. The spectrum analysis by FFT cannot separate the fast and slow beam modes, because the trace is too short to resolve them. In Fig. 4(b), the values $k_{//1}$ for the peaks f and s in Fig. 1(b) are plotted by the open circles. The solid curves F and S show the

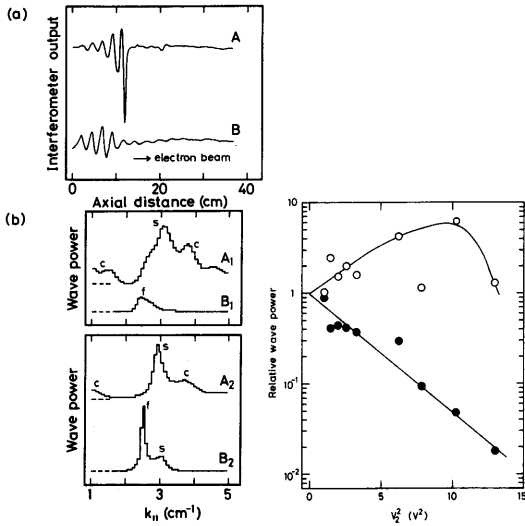


Fig. 1. (a) Interferometer traces of the first wave. (b) Spectra of wave number for the traces A and B in Fig. 1(a). The curves A_1 , B_1 are obtained by FFT, and A_2 , B_2 by MEM. The horizontal dotted lines indicate the zero level. $\omega_1/2\pi=315$ MHz, $\omega_2/2\pi=230$ MHz, $\omega_c/2\pi=253$ MHz, $V_2=2$ V for A, A_1 and A_2 , $V_2=0$ V for B, B_1 and B_2 , and $V_1=0.2$ V.

Fig. 2. Relative wave powers of the fast and slow beam modes obtained from the components of the spectra of the interferometer outputs of the first wave by FFT are shown versus V_2^2 , where the wave powers are normalized by those with $V_2=0$. The solid circles correspond to the fast beam mode and the open ones to the slow beam mode. It is found that the wave powers of the fast beam mode decrease exponentially with V_2^2 and those of the slow beam mode increase exponentially with $V_2 \lesssim 2$ V, saturate and decrease with $V_2 \gtrsim 2$ V. This exponential increase and decrease of the wave power agree with the theoretical prediction, because from eqs. (2) and (3) the following equation can be obtained when $|E_{\omega_1}| \ll |E_{\omega_2}|$:

dispersion relations of the fast and slow beam modes, respectively, which are derived from

$$|E_{\omega_1}|^2 = |E_{\omega_1}(0)|^2 \exp \left\{ -\frac{S\alpha_1}{2\gamma_2} |E_{\omega_2}(0)|^2 [1 - \exp(-2\gamma_2 z)] - 2\gamma_1 z \right\}. \quad (7)$$

Since it may be considered that $|E_{\omega_2}(0)| \propto V_2$, it can be proved from eq. (7) that $\ln |E_{\omega_1}/E_{\omega_1}(V_2=0)|^2 \propto -SV_2^2$. It seems that the saturation and decrease of the slow beam mode with $V_2 \gtrsim 2$ V arise from the more higher-order nonlinear process.

In order to confirm that these damping and growing of the fast and slow beam modes are caused by the nonlinear Landau damping due to nonlinear interaction with the T-mode and the beam electrons, we identified the resonant condition and the dispersion relation of the second wave. The observation of interferometer traces of the second waves in the presence and absence of the first wave was made and the similar result as that shown in ref. 7 was

obtained. Traces A and B in Fig. 3(a) are the small amplitude second waves with the first ($V_1=5$ V) and without the first one, respectively. The trace B shows only a space charge wave of the beam with the frequency ω_2 . But, the excitation of the T-mode by the first wave is observed in the region D in the trace A, where the short wavelength wave is superimposed on the space charge wave of the beam. In Fig. 3(b), the spectra of these interferometer traces are shown by the curves A_1 , B_1 (by FFT) and A_2 , B_2 (by MEM). When the first wave does not exist, the T-mode is hardly excited, as shown in the curves B_1 and B_2 . But, the large peak p and small peak q of the curves A_1 and A_2 show that the T-modes are excited strongly

eq. (6) under the present experimental condition. It is found that the open circles fit well to the dispersion relations F and S. As shown by the curves A_1 and A_2 in Fig. 1(b), the spectrum of the interferometer trace A shows that the peak s for the slow beam mode is enhanced extremely and the peak f for the fast beam mode is suppressed (or disappears). This means, as predicted theoretically, that the fast beam mode damps and the slow beam mode grows by the presence of the T-mode. The other peaks C observed in A_1 and A_2 may be considered to be an electrostatic electron cyclotron harmonic waves excited by other coupling of nonlinear Landau damping.

obtained. Traces A and B in Fig. 3(a) are the small amplitude second waves with the first ($V_1=5$ V) and without the first one, respectively. The trace B shows only a space charge wave of the beam with the frequency ω_2 . But, the excitation of the T-mode by the first wave is observed in the region D in the trace A, where the short wavelength wave is superimposed on the space charge wave of the beam. In Fig. 3(b), the spectra of these interferometer traces are shown by the curves A_1 , B_1 (by FFT) and A_2 , B_2 (by MEM). When the first wave does not exist, the T-mode is hardly excited, as shown in the curves B_1 and B_2 . But, the large peak p and small peak q of the curves A_1 and A_2 show that the T-modes are excited strongly

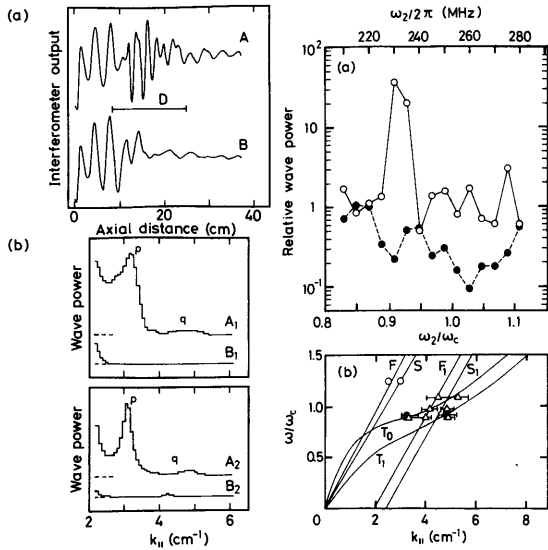


Fig. 3. (a) Interferometer traces of the second wave. (b) Spectra of wave number for the traces A and B in Fig. 3(a). The curves A_1, B_1 are obtained by FFT, and A_2, B_2 by MEM. The horizontal dotted lines indicate the zero level. $V_1=5$ V for A, A_1 and A_2 , $V_1=0$ V for B, B_1 and B_2 , and $V_2=0.1$ V. The other parameters are the same as Fig. 1.

Fig. 4. (a) Relative wave power of the first wave obtained by FFT is shown versus ω_2/ω_c or $\omega_2/2\pi$. The open and solid circles correspond to the fast and slow beam modes, respectively. $\omega_1/2\pi=315$ MHz, $\omega_c/2\pi=253$ MHz, $V_1=0$ V, $V_2=2$ V, $k_{||1}\cong 2.6$ cm^{-1} (\bullet) and $k_{||1}=3.2$ cm^{-1} (\circ). (b) Locations of the interferometer traces and resonant conditions on the dispersion diagram. The curves T_0 and T_1 exhibit the dispersion relation of the T-mode calculated from $\epsilon=0$. The straight lines F_1 and S_1 are the resonant condition eq. (1) for the fast and slow beam modes, respectively. That is, $(\omega_2, k_{||2})$ are variables, $(\omega_1, k_{||1})$ are given by the open circles, and $m=1$. Calculations are carried out under the present experimental condition: $\omega_p^2/\omega_c^2=3$, $\omega_b^2/\omega_c^2=0.06$, $v_b/v_i=7.5$, $k_{\perp 1}=4.8/D_b$ for F and S, $k_{\perp 2}=4.8/D_p$ for T_0 , and $k_{\perp 2}=11/D_p$ for T_1 . Here, $D_p=4$ cm is employed so that the curves T_0 and T_1 fit well to the experimental data of the second wave.

by the presence of the first wave. The values of $k_{||2}$ for the peaks p and q are plotted by the solid circles on the dispersion diagram of Fig. 4(b). It can be found that the peak p corresponds to the dispersion curve T_0 which is the T-mode for the lowest mode with respect to radial wavelength, and the peak q to the dispersion curve T_1 for the higher mode. The values of $k_{||2}$ for the nonlinearly excited T-modes with the other frequencies are also

shown by the open triangles. It is seen that the solid circles and the open triangles satisfy the resonant condition eq. (1) with $m=1$ which is shown by the lines F_1 and S_1 and the dispersion relation of the T-modes.

In Fig. 4(a), relative wave powers of the fast and slow beam modes with $V_2=2$ V obtained from the components of the spectra of the interferometer outputs of the first wave by FFT are shown versus ω_2/ω_c or $\omega_2/2\pi$, where the wave powers are normalized by those with $V_2=0$. The solid circles show the wave power of the fast beam mode and the open circles show that of the slow beam mode. It is found that the fast beam mode is suppressed and the slow beam mode is enhanced by the lowest and higher T-modes in the region satisfying the resonant condition.

In conclusion, the damping of the fast beam mode and the growing of the slow beam mode due to nonlinear Landau damping are observed simultaneously using the spectrum analysis. It is confirmed that the fast and slow beam modes interact nonlinearly with the lowest and higher modes of the Trivelpiece-Gould modes, causing their growth.

The authors thank Professor T. Dodo and Dr. M. Sugawa for their discussions. Computer calculations were made using Facom M-200 of the Data Processing Center, Kyushu University. This work was partially supported by a Grant-in-Aid from the Ministry of Education, Science and Culture in Japan.

References

- 1) R. Sugaya: Phys. Fluids **26** (1983) 2698.
- 2) R. P. H. Chang and M. Porkolab: Phys. Rev. Lett. **25** (1970) 1262.
- 3) K. W. Gentle and A. Malein: Phys. Rev. Lett. **26** (1971) 625.
- 4) G. Matthieussent and J. Olivain: Phys. Rev. Lett. **34** (1975) 1610.
- 5) H. Ikezi and Y. Kiwamoto: Phys. Rev. Lett. **27** (1971) 718.
- 6) R. P. H. Chang and M. Porkolab: Phys. Rev. Lett. **32** (1974) 1227.
- 7) R. Sugaya, M. Sugawa and H. Nomoto: Phys. Fluids **19** (1976) 1829; J. Phys. Soc. Jpn. **42** (1977) 1373; J. Phys. Soc. Jpn. **45** (1978) 1716.
- 8) R. Sugaya, M. Sugawa and H. Nomoto: Phys. Rev. Lett. **39** (1977) 27; J. Phys. Soc. Jpn. **47** (1979) 966.
- 9) M. Porkolab and R. P. H. Chang: Phys. Fluids **15** (1972) 283.
- 10) B. D. Fried and S. D. Conte: *The Plasma Dispersion Function* (Academic Press, New York, 1961).
- 11) M. Anderson: Geophys. **39** (1974) 69.

ICRF HEATING EXPERIMENTS ON JIPP T-II

M. ICHIMURA*, J. FUJITA, S. HIROKURA,
E. KAKO, K. KAWAHATA, Y. KAWASUMI,
A. NISHIZAWA, N. NODA, I. OGAWA, K. OHKUBO,
Y. ONO, M. SASAO, S. SHINOHARA**,
S. TANAHASHI, T. TETSUKA, K. TOI, T. WATARI,
T. AOKI, S. HIDEKUMA

Institute of Plasma Physics,
Nagoya University,
Nagoya, Japan

ABSTRACT. Data of JIPP T-II ICRF heating experiments are presented. The experiment covers three typical cases: the low-concentration hydrogen minority case, the high-concentration hydrogen minority case, and the ^3He -minority case. The best heating efficiency is obtained for the ^3He -minority case. It is shown through power balance analysis that the two H-minority cases are different in the wave energy deposition profile. The difference is explained by the presence of a local cavity mode in the high-concentration minority case. The ion temperature stops rising at a power density level of $0.65 \text{ W}\cdot\text{cm}^{-3}$ for the hydrogen minority experiments. No such deterioration is found in the case of the ^3He minority experiment up to a power density level of $0.45 \text{ kW}\cdot\text{cm}^{-3}$. This is the maximum possible to attain within the maximum power injection (180 kW) up to which the experiment is conducted. An analytic solution of the Fokker-Planck equation is derived in order to interpret the deterioration of the heating efficiency.

1. INTRODUCTION

For the heating of thermonuclear fusion plasma, the use of waves in the ion cyclotron range of frequency (ICRF) offers several advantages. Recent high-power ICRF heating experiments [1-4] have demonstrated the practicability of fast-wave heating with a variety of heating regimes. Based on the success in handling MW level ICRF power injection, the application of ICRF heating to future large tokamaks is becoming realistic. In the Institute of Plasma Physics, Nagoya University, ICRF heating is projected in the R-project proposal. The experiment presented here was carried out on JIPP T-II as a preparatory experiment intended to aid in designing the R-tokamak. One of our interests is the clarification of the wave propagation and absorption mechanisms, which is important in deciding the heating regime best suited to the R-tokamak.

Another interest is in the mechanism of deterioration of the heating efficiency which occurs with high-power ICRF heating. It is particularly important to derive a scaling to estimate how much ICRF power will be injected in future devices without deterioration of the heating efficiency. We have reason to believe that the power density will play a key role in limiting the injection power. It is shown in Section 4 through an analysis of experimental data that slipping of minority ions gives rise to a reduced heating efficiency with heating power densities higher than a certain level.

2. EXPERIMENTAL RESULTS

JIPP T-II [5] in the Institute of Plasma Physics, Nagoya University, is a stellarator-tokamak hybrid device with a major radius of $R=91 \text{ cm}$ and a minor radius of $a=15 \text{ cm}$. The ICRF heating experiment is carried out in a tokamak operating at a toroidal magnetic field of around 2.7 T and a plasma density ranging from 2 to $5 \times 10^{13} \text{ cm}^{-3}$. The plasma current is around 90 kA, and the Joule input power is about 100 kW throughout this experiment. The deuterium

Present and permanent addresses:

* Plasma Research Center, Tsukuba University, Ibaraki 305, Japan.

** Department of Physics, University of Tokyo, Tokyo 113, Japan.

plasma with minority ions of hydrogen or ^3He is heated in a two-ion hybrid regime. Frequencies of 40 MHz for the hydrogen minority and 26.7 MHz for the ^3He minority are used so that the ion-ion hybrid resonance layer is located near the plasma centre. Two all-metal antennas with Faraday shields are set in the vacuum vessel and each receives RF power from its own oscillator. Each antenna has an all-metal structure with a Faraday shield and consists of a top and a bottom half-turn pair. RF currents are fed from the low-field side near the equatorial plane in order to produce a poloidal $m=0$ current loop. The antenna configuration is very similar to that of TFR except that the present antenna covers a greater portion of the low-field side. The experiment is carried out for three cases: 4%H, 10%H, and 10% ^3He . The concentrations of the minority ions are measured spectroscopically in the H-minority experiments, whereas, in the ^3He -minority experiments, they are deduced from an analysis of the gas dynamics.

We regard 4%H and 10%H as typical cases representing low and high concentrations of minority hydrogen ions. A favourable result is obtained in the 4%H experiment: the heating is successful up to a net input power of 260 kW, where the power density is $0.65 \text{ W}\cdot\text{cm}^{-3}$; this power corresponds to twice the Joule input power. The deuterium and hydrogen temperatures are measured by a mass-discriminating fast-neutral-particle analyser. As is shown in Fig. 1, the deuterium temperature T_D increases from 270 to 570 eV. The heating rate is $1.2 \text{ eV}\cdot\text{kW}^{-1}$. The increase in the electron temperature T_e is also found by measuring the electron cyclotron emission calibrated by pulse height analysis of soft X-rays (Fig. 2). In this figure, the electron temperature rises with time from 0.78 keV but begins to decrease after reaching a maximum value of 1.1 keV (before the RF pulse is turned off). Application of higher power up to 400 kW (power density of $1 \text{ W}\cdot\text{cm}^{-3}$) does not bring about any further increase in T_D , and a deterioration of the confinement is observed. A similar heating rate is also obtained with the 10%H experiment. The deterioration of the heating efficiency occurs, however, at a power level as low as 150 kW. In both cases, the deterioration of heating efficiency is preceded by a deterioration of the electron energy confinement, along with an increased influx of heavy ion impurities.

In the ^3He minority case (27 MHz), the maximum injection power is limited to 180 kW because of arcing at high-power injection in the tuner, which has primarily been designed for 40 MHz. However, this power is large enough to allow a reasonable comparison with

H-minority experiments as far as heating efficiency is concerned. In the ^3He -minority experiment, a heating efficiency ($\text{eV}\cdot\text{kW}^{-1}\cdot\text{cm}^{-3}$) twice as high as in the H-minority case is observed, demonstrating the superiority of ^3He as a minority species for fixed toroidal magnetic field strength. Within this power level, no deterioration of heating efficiency was observed. In Fig. 3, the relationship between the power applied and the increase in the deuterium temperature is summarized in terms of $\Delta T_D \bar{n}$.

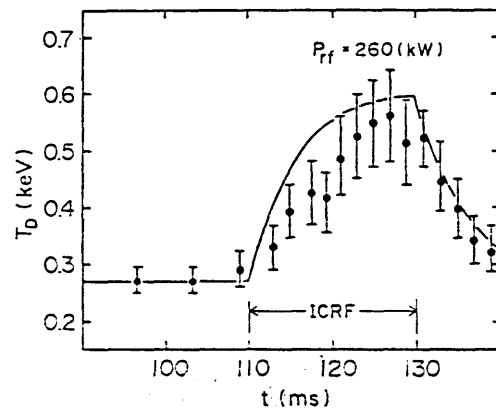


FIG. 1. Time evolution of deuterium temperature; solid line is obtained in computing Eq. (1).

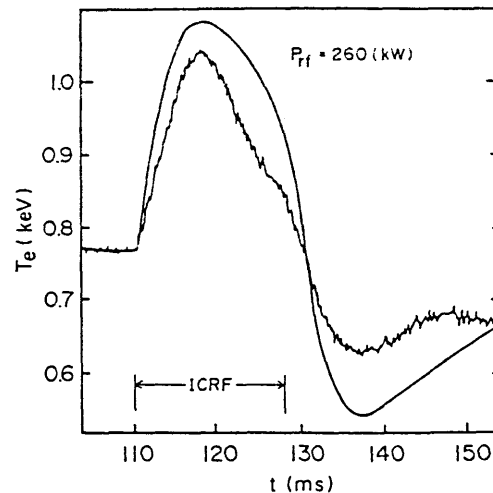


FIG. 2. Time evolution of electron temperature; electron temperature rises rapidly with higher RF power and begins to decrease later when RF is still on. Dotted line shows result of simulation calculations with measured radiation loss as input.

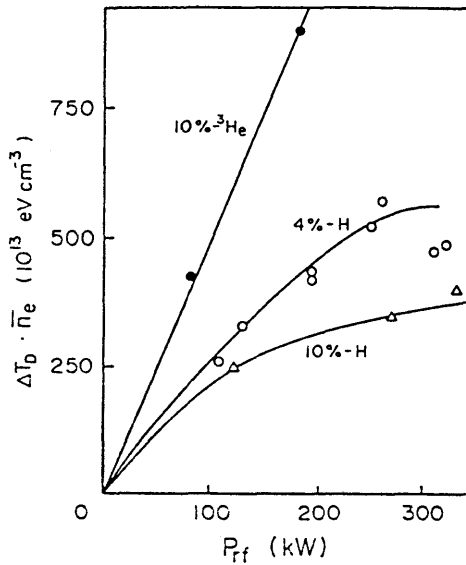


FIG.3. Power dependence of deuterium temperature.

3. ANALYSIS

The reason for the difference between the 4%H and 10%H cases can be understood from an analysis of the usual power balance equations:

$$\begin{aligned} \frac{d}{dt} (n_H T_H) &= - \frac{n_H (T_H - T_D)}{\tau_{HD}} - \frac{n_H (T_H - T_e)}{\tau_{He}} \\ &\quad - \frac{n_H T_H}{\tau_H} + \frac{2}{3} \langle P_{RF} \rangle_H \\ \frac{d}{dt} (n_D T_D) &= - \frac{n_D (T_D - T_H)}{\tau_{DH}} - \frac{n_D (T_D - T_e)}{\tau_{De}} - \frac{n_D T_D}{\tau_D} \\ &\quad + \frac{2}{3} \langle P_{RF} \rangle_D \\ \frac{d}{dt} (n_e T_e) &= - \frac{n_e (T_e - T_D)}{\tau_{eD}} - \frac{n_D (T_e - T_H)}{\tau_{eH}} \end{aligned}$$

$$- \frac{n_e T_e}{\tau_e} - \langle P_{rad} \rangle + \frac{2}{3} \langle P_{RF} \rangle_e + \frac{2}{3} \langle P_J \rangle \tag{1}$$

Here, n_H , n_D and n_e are the densities, and T_H , T_D and T_e the temperatures of H, D and e, respectively. τ_H , τ_D and τ_e are the energy confinement times of the respective species. $\langle P_{RF} \rangle_H$, $\langle P_{RF} \rangle_D$ and $\langle P_{RF} \rangle_e$ are the averaged heating power densities on H, D and e, respectively. τ_{HD} and τ_{He} are energy relaxation times from H to D and e, respectively. Similarly, τ_{De} and τ_{DH} are such relaxation times from D to e and H, and τ_{eD} and τ_{eH} are those from e to D and H. $\langle P_{rad} \rangle$ and $\langle P_J \rangle$ are the averaged radiation loss and the Joule input power, respectively. Without RF, the set of Eqs (1) can be solved for τ_H , τ_D and τ_e in the Ohmic-heating phase because $\langle P_{RF} \rangle_H$, $\langle P_{RF} \rangle_D$ and $\langle P_{RF} \rangle_e$ are zero and all the other necessary quantities are easily measured or calculated from them. In the presence of RF, Eq.(1) is solved for $\langle P_{RF} \rangle_H$, $\langle P_{RF} \rangle_D$ and $\langle P_{RF} \rangle_e$, on the assumption that transport coefficients τ_H , τ_D and τ_e do not change on the application of RF. We measure the quantities involved in Eq.(1), waiting for 5 ms after the ICRF heating has been turned on. This time-scale, which is not long compared to the heating time, is chosen so as to be able to neglect possible changes in the transport parameters which might be due to impurity influx or some other unknown reasons. 5 ms is much longer than the time-scales associated with wave propagations (about 2 s) or the

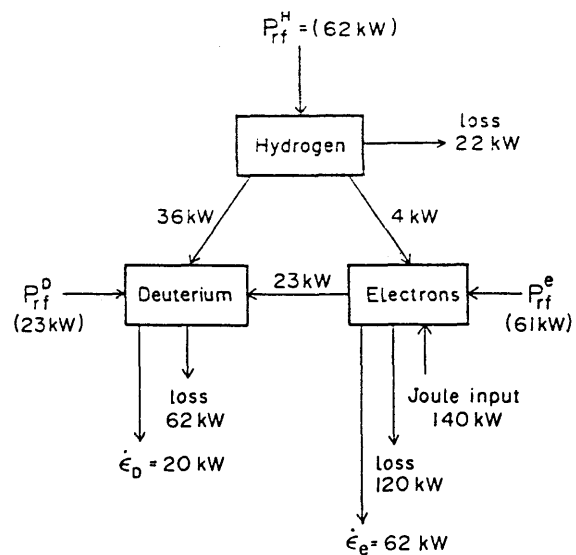


FIG.4. Power balance analysis for 4%H minority case. $\epsilon_D = (3/2) n_D T_D V$, $\epsilon_e = (3/2) n_e T_e V$ (V - plasma volume).

peripheral re-cycling time (about 1 ms); this fact is necessary for minimizing errors arising in estimating the derivative terms in Eq.(1), which might be caused by fluctuations. Throughout this discussion, which is based on a zero-dimensional analysis, a parabolic electron density profile is assumed, and squared parabolic profiles are assumed for T_e , T_H and T_D . An example for the power balance is shown in Fig.4 for the case of the 4%H experiment. The RF powers absorbed by the species as given in the parentheses are calculated on the basis of the known power transfer data. Among the dominant features we find is the fact that not only minority ions but also electrons and deuterons absorb wave energy in the 4%H experiment, while only minority ions absorb a significant amount of wave energy in the 10%H experiments. These results are different from those of TFR and PLT: TFR reports direct heating of electrons in the high-concentration H-experiment, while PLT states that only minority ions are directly heated in the low-concentration H-experiment. Our experimental results are the other way round, in the sense that electron heating is rather observed in low- than in high-concentration H-experiments. The reason for this difference between their and our results can be understood in terms of a wave propagation analysis keeping the differences in the antenna configurations in mind. Our antenna is very similar to the TFR antenna in shape but differs from it in performance. Our antenna is smaller and operates on a lower frequency than that of TFR. So, the RF current on the antenna is shaped to be perfectly uniform in our experiment. The question from which side the wave is incident depends, however, on the local structure of the wave propagation. One of the important parameters characterizing the wave propagation is defined by [4]

$$\epsilon_H^c = \left(\frac{k_{\parallel}^2 c^2}{\omega_{pD}^2} + \frac{4}{3} \right) \frac{k_{\parallel} v_T}{\omega} \quad (2)$$

If the H-concentration ϵ_H , is higher than this critical value ϵ_H^c , there is a mode conversion layer present. Here, ω_{pD} is the deuterium ion plasma frequency, k_{\parallel} the parallel wave number, v_T the thermal velocity of the hydrogen ions, c the velocity of light, and ω the applied RF frequency. Substituting the values relevant for our experiment on the right-hand side of Eq.(2), we obtain $\epsilon_H^c \approx 2\%$, which is smaller than any H-concentrations we use in this experiment. Therefore, we may assume the presence of a mode conversion layer throughout this experiment. Another important parameter,

$$\eta = \pi \frac{\sqrt{3}}{2\sqrt{2}} R_H \frac{\omega_{pD}}{c} \quad (3)$$

is known to be a quantity which can be used to measure the separation between a resonance layer and a cut-off layer [6, 8]. Here, R is the major radius. When the value of η becomes larger than unity, a wave incident from the low-field side is completely reflected, and one from the high-field side is almost completely mode-converted. On the other hand, with a value of η less than unity, the mode conversion process is attainable both from the low- and the high-field sides. An examination of Eq.(3) with experimental parameters yields η -values of 0.5 and 1.3 for the 4%H and 10%H cases, respectively. Thus, we interpret the electron part of the wave absorption in the 4%H experiment as a consequence of the mode conversion of a wave to an electrostatic mode. Theoretically, a certain amount of electron heating is expected in the 10%H experiment, as well. This is because the wave energy is incident from the high- as well as from the low-field side: the former has a chance to be mode-converted and to heat the electrons. However, no electron heating is observed experimentally. We assume that the wave radiation primarily consists of waves coming from the low-field side. An indication of this fact is found in the following experimental data: the wave excitation and the propagation characteristics are related to the loading resistance of the antenna. In Fig.5, measured loading resistances are plotted versus

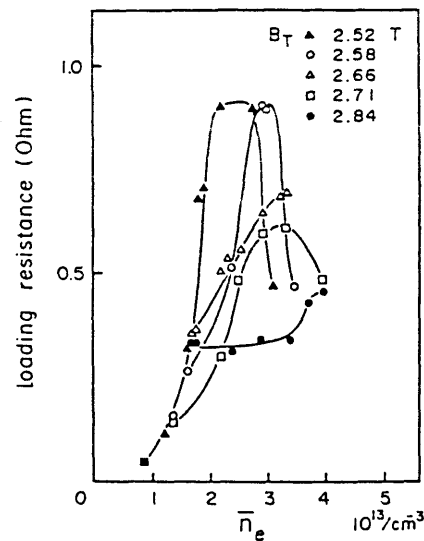


FIG.5. Loading resistance versus \bar{n}_e .

the plasma density for the high-concentration minority case. It is an outstanding characteristic of this case that the plasma density which yields the maximum loading resistance increases with increasing toroidal magnetic field strength. This tendency is well understood, provided the local cavity mode predicted by the theory [8–11] is really present; as the toroidal magnetic field B_T increases, the resonance cut-off double layer shifts towards the low-field side, thereby reducing the volume of the cavity. For the RF frequency kept constant, the cavity resonance can only be satisfied by the shorter wavelength realized in the case of higher plasma density. On the basis of this physical picture, we shall draw an analogy with a plasma-filled waveguide of rectangular cross-section. A mean Alfvén wave number $k_{\perp,\omega}$, for fast-wave oscillation is defined by

$$k_{\perp,\omega} = \omega (\mu_0 \bar{n} m_D / \bar{B}^2)^{1/2} \quad (4)$$

where the averaged number density, \bar{n} , and the averaged magnetic field, \bar{B} , are calculated from the experimental data at the cavity resonance. Here, m_D is the deuteron mass. A geometric wave number $k_{\perp,g}$, which characterizes the cross-section of the cavity and the fundamental resonance condition, is defined by

$$k_{\perp,g} = \frac{\pi}{2} (a^{-2} + b^{-2})^{1/2} \quad (5)$$

where a and b are the dimensions of the cavity as estimated from the computed cut-off surfaces. This simple model would predict a linear relationship between $k_{\perp,\omega}$ and $k_{\perp,g}$ at the fundamental resonance. The relationship between $k_{\perp,\omega}$ and $k_{\perp,g}$ obtained experimentally is plotted in Fig.6, where the straight line represents a best-fit relationship of $k_{\perp,\omega}/k_{\perp,g} = 0.6$. These results confirm the presence of a cavity mode on the low-field side, in the case of high-H minority concentration. The increase in the loading resistance of the low-field side part of an antenna when a local cavity mode is present is consistent with the results obtained by running Lapière's code [9]. Thus, it is possible that the major part of the wave energy is emitted from the low-field side. The wave energy is then absorbed in the cyclotron layer by minority ions. Thus the reason for the difference between the JIPP T-II and TFR results is comprehensible. This contrasts with the case where the concentration of the minority ions is low; there is only a weak connection between $k_{\perp,\omega}$ and $k_{\perp,g}$. In this case, the wave is not localized, and it is then absorbed in the mode conversion layer.

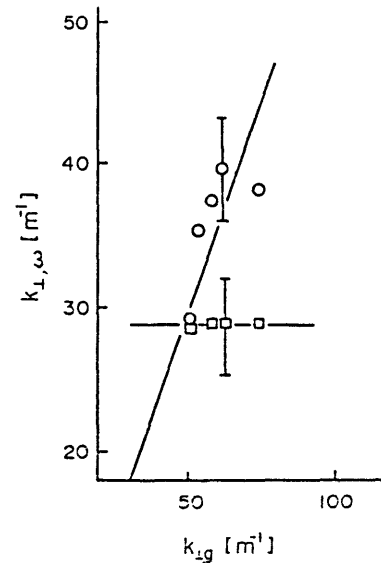


FIG.6. Relation between Alfvén wave number $k_{\perp,\omega}$ and geometric wave number $k_{\perp,g}$.

4. DISCUSSION

The sum of the RF powers absorbed by the respective species is less than that radiated from the antennas. If efficiency is defined by

$$\gamma = \frac{\langle P_{RF} \rangle_e + \langle P_{RF} \rangle_H + \langle P_{RF} \rangle_D}{\langle P_{RF} \rangle} \quad (6)$$

We obtain $\gamma = 0.56$ for the 4%H and $\gamma = 0.23$ for the 10%H case. In the following discussions, the Fokker-Planck equation is used to interpret an efficiency smaller than unity. It is well known that the particle confinement is determined by the plasma current, which is only 90 kA in this experiment; particles with an energy of more than 20 keV cannot be confined. It is, therefore, important to gain some insight into the behaviour of the minority ions which are intensively heated and finally lost. An analytic steady-state solution of the linear Fokker-Planck equation was first given by Stix [12]. It is, however, not complete because the particle flow through velocity space is neglected. According to the Stix notation, the isotropic linear Fokker-Planck equation with a quasi-linear collision term is written in the form:

$$\frac{\partial A}{\partial t} = \frac{1}{v^2} \frac{\partial}{\partial v} [-v^2 \Gamma] \quad (7)$$

where

$$\Gamma = -\frac{1}{v^2} \left[-\alpha v^2 + \frac{1}{2} \frac{\partial}{\partial v} (\beta v^2) A + \left(\frac{1}{2} \beta + K \right) v^2 \frac{\partial A}{\partial v} \right] \quad (8)$$

The first integral of Eq.(7) gives

$$-v^2 \Gamma = c_1 \quad (9)$$

Here, c_1 has a physical meaning of particle flow through the velocity space, which has been ignored in Ref.[10]. If it is retained, the solution of Eq.(7) has the form

$$A(v) = c_1 \int_v^{v_0} \frac{1}{\left(\frac{1}{2}\beta + K\right)v^2} \frac{1}{A_0(V)} dV A_0(V) \quad (10)$$

where

$$A_0(V) = \exp \left(-\int_0^V \frac{-V^2}{\frac{1}{2}\beta + K} dV \right) \quad (11)$$

is the solution from Ref.[10], and

$$v_0 = (2E_{\max}/m)^{1/2} \quad (12)$$

with E_{\max} the maximum energy of particles which can be confined in the system. A numerical comparison of analytical expressions (10) and (11) with experimental parameters yields $A(v)$ quite different from $A_0(v)$, implying the importance of the particle flow through the velocity space. The distribution function of the minority ions $A(v)$ is far from a Maxwellian distribution. We deduce an effective ion temperature from the inclination of the theoretically obtained distribution function around the energy range where the fast-neutral-particle analyser works in the experiment. The power dependence of the hydrogen temperature is compared to the dependence as predicted by theory in Fig.7; we see that there is a qualitative agreement. The particle energies transferred from hydrogen to deuterium by the relaxation process, P_{DH} , and from hydrogen to the electrons, P_{eH} , are given by

$$P_{DH} = \int_0^{v_0} 4\pi \frac{m}{2} v^2 \frac{\partial}{\partial v} \left[-\alpha_D v^2 + \frac{1}{2} \frac{\partial}{\partial v} (\beta_D v^2) A + \frac{1}{2} \beta_D v^2 \frac{\partial A}{\partial v} \right] dv \quad (13)$$

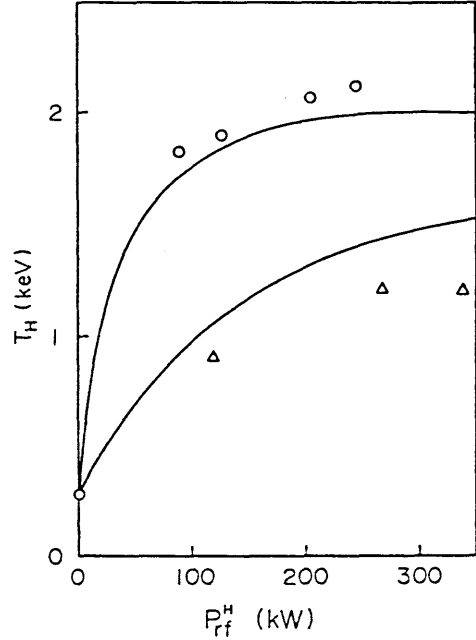


FIG.7. Temperature of minority ions versus input RF power. Open circles and triangles show measured minority ion temperature for 4%*H* and 10%*H* cases, respectively. Solid lines designate theoretical calculations from Eq.(10).

$$P_{eH} = \int_0^{v_0} 4\pi \frac{m}{2} v^2 \frac{\partial}{\partial v} \left[-\alpha_e v^2 A + \frac{1}{2} \frac{\partial}{\partial v} (\beta_e v^2) A + \frac{1}{2} \beta_e v^2 \frac{\partial A}{\partial v} \right] dv \quad (14)$$

$$\langle P_{RF} \rangle = \frac{3}{2} \text{ mW} \quad (15)$$

and we notice an obvious relation

$$\langle P_{RF} \rangle = \langle P_{DH} \rangle + \langle P_{eH} \rangle + c_1 E_{\max} \quad (16)$$

where the last term is the portion of the energy lost as energetic ions. The portion of the wave energy absorbed by hydrogen and then transferred to deuterium ions and electrons is given by

$$\xi = \frac{\langle P_{DH} + P_{eH} \rangle}{\langle P_{RF} \rangle_H} = \frac{\langle P_{RF} \rangle - c_1 E_{\max}}{\langle P_{RF} \rangle_H} \quad (17)$$

Since the loss term $c_1 E_{\max}/\langle P_{RF} \rangle_H$ is an increasing function of $\langle P_{RF} \rangle_H$, ξ becomes small on high-power heating. The result of the numerical computation of ξ

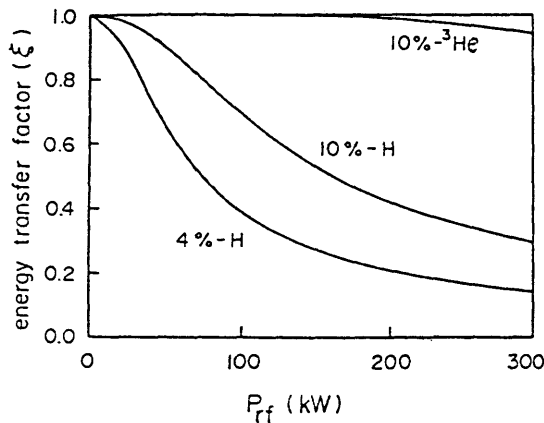


FIG. 8. Energy transfer factors of minority ions.

is shown in Fig. 8 for three cases: 4%H, 10%H and 10%³He. It is worthwhile mentioning that, for the 10%H case, the application of a power over 150 kW does not serve to heat D but only to increase the particle loss of minority hydrogen. This may be the reason why we observe a deterioration of the heating efficiency in the experiment at a higher power level. We also find that the threshold is as low as 30 kW in the case of the 4%H experiment. However, the ion temperature continues to rise together with increasing power from this power level up to 260 kW because the wave deposits its energy not only on H but also on e and D. The 10%³He experiment belongs to the high-concentration minority case and compares well with the 10%H experiment. In this case, the threshold is high enough for no deterioration to occur, and the high heating efficiency is maintained. This superiority of ³He as a minority species is attributed to the larger collisional cross-section of ³He than that of H.

We observe in this experiment that the deteriorating effect of R.F first affects the electron energy confinement. This is due to the enhanced radiation loss. The origin of the impurity is sought by examining the visible light emission which is indicative of the impurity influx and the characteristic lines in soft-X-ray emission which yield information on the core impurity. The radiation loss is mainly due to impurities of the heavy metals Ti and Mo, the former coming from the vacuum wall and the latter from the limiter. The bolometrically measured radiation loss increases gradually with time for about 10 ms; this is in contrast with the rise-time for visible light, which is 1 ms. A simulation using Eq.(1) with the measured radiation loss gives the solid curves shown in Figs 1 and 2. Thus, the behaviour

of the electron temperature is well understood in terms of the radiation loss. Though the deterioration of electron energy confinement does not affect the ion heating significantly, impurities are another problem to be solved in experiments in the near future.

5. SUMMARY

The experimental results of ICRF heating on JIPP T-II were described and three typical heating regimes were compared. The highest heating efficiency was achieved in the ³He-minority experiment. In the H-minority experiment, low- (4%H) and high-concentration minority (10%H) cases were compared. Differences were found in the wave energy deposition profile on each species derived through power balance analysis. This difference was explained in terms of mode conversion theory; this model was consistent with the measured loading resistance. The behaviour of the plasma under high-power ICRF heating was also investigated with power levels of up to 400 kW. A deterioration in the heating efficiency was observed in both cases with a heating power density less than $0.65 \text{ W} \cdot \text{cm}^{-3}$. The mechanism of the heating deterioration was explained in terms of a relaxation process with a solution of the Fokker-Planck equation.

ACKNOWLEDGEMENTS

The authors are indebted to Drs T. Sato and K. Adati for providing us with the RFC-XX RF power sources. They are grateful to Drs T. Hamada, K. Matsuura, R. Sugihara, and T. Amano for continuous encouragement and useful discussions. They also would like to thank M. Mugishima and H. Ishiguro for the operation of the FW generator.

REFERENCES

- [1] HWANG, D., BITTER, M., BUDNY, R., CAVALLO, A., CHRIEN, R., et al., in Plasma Physics and Controlled Nuclear Fusion Research (Proc. 9th Int. Conf. Baltimore, 1982), Vol.2, IAEA, Vienna (1983) 3.
- [2] EQUIPE TFR, *ibid.*, 17.
- [3] KIMURA, H., MATSUMOTO, H., ODAJIMA, K., KONOSHIMA, S., YAMAMOTO, T., et al., *ibid.*, 113.
- [4] JACQUINOT, J., McVEY, B.D., SCHARER, J.E., *Phys. Rev. Lett.* **39** (1977) 88.

- [5] FUJITA, J., ITOH, S., KADOTA, K., KAWAHATA, K., KAWASUMI, Y., et al., in Plasma Physics and Controlled Nuclear Fusion Research (Proc. 8th Int. Conf. Brussels, 1980), Vol.1, IAEA, Vienna (1981) 209.
- [6] SWANSON, D.G., Phys. Rev. Lett. 36 (1976) 316.
- [7] SCHARER, J.E., McVEY, B.D., MAU, T.K., Nucl. Fusion 17 (1977) 297.
- [8] COTSFTIS, M., SY, W.N-C., Phys. Lett. 93A (1983) 193.
- [9] LAPIERRE, T., in Heating in Toroidal Plasmas (Proc. 2nd Joint Grenoble-Varenna Int. Symp., Como), Vol.1 (1980) 549.
- [10] FUKUYAMA, A., NISHIYAMA, S., ITOH, K., ITOH, S-I., Nucl. Fusion 23 (1983) 1005.
- [11] ITOH, K., ITOH, S-I., FUKUYAMA, A., Nucl. Fusion 24 (1984) 13.
- [12] STIX, T., Nucl. Fusion 15 (1975) 737.

(Manuscript received 11 October 1983

Final manuscript received 2 May 1984)

Reprinted from

PHYSICAL REVIEW A

GENERAL PHYSICS

Volume 34

Third Series

Number 2

AUGUST 1986

Impurity accumulation spectroscopically observed during ion
cyclotron resonance frequency heating experiments in the JIPP T-II-U tokamak

K. Ono, T. Oomori, and Y. Ueda

Central Research Laboratory, Mitsubishi Electric Corporation, Tsukaguchi-honmachi, Amagasaki 661, Japan

K. Sato, K. Ito, I. Watari, I. Ogawa, K. Kawahata, R. Ando,

Y. Kawasumi, N. Noda, and S. Tanahashi

Institute of Plasma Physics, Nagoya University, Chikusa-ku, Nagoya 464, Japan

pp. 1328-1337

Published by

THE AMERICAN PHYSICAL SOCIETY

through the

AMERICAN INSTITUTE OF PHYSICS

Impurity accumulation spectroscopically observed during ion cyclotron resonance frequency heating experiments in the JIPP T-II-U tokamak

K. Ono, T. Oomori, and Y. Ueda*

Central Research Laboratory, Mitsubishi Electric Corporation, Tsukaguchi-honmachi, Amagasaki 661, Japan

K. Sato, K. Toi, T. Watari, I. Ogawa, K. Kawahata, R. Ando,
Y. Kawasumi, N. Noda, and S. Tanahashi

Institute of Plasma Physics, Nagoya University, Chikusa-ku, Nagoya 464, Japan

(Received 21 February 1986)

Spectroscopic investigations of iron-ion line radiation (Fe X-XXIV) in the extreme-ultraviolet region have been carried out during ion cyclotron resonance frequency (ICRF) heating experiments in the JIPP T-II-U tokamak, at the Japanese Institute of Plasma Physics (JIPP), Nagoya University, Nagoya. The central-chord radiances of the iron-ion resonance lines were observed to increase during ICRF heating. After the radiance of the highest ionization stage attained the peak toward the end of ICRF heating, the radiances of the lower stages were observed to attain their peaks at successively later times. The rf-power injection was accompanied by strong gas puffing and additional current rise, which raised the electron density and concurrently lowered the central electron-temperature. The electron-temperature decrease in the central region, which was further promoted by radiative losses due to metallic impurities, continued after ICRF heating. The spectroscopic observations are interpreted as showing that the ICRF heating causes a large additional influx of iron into the plasma, and that the iron accumulates preferentially in the plasma interior with long confinement times. The sequential peaking of the radiation from the highest to the lowest ionization stages reflects the decrease in the electron temperature and the concurrent recombination into successively lower stages. These interpretations are supported by the soft-x-ray and bolometric measurements, and confirmed by the modeling calculations that reproduce the iron-ion line radiances.

I. INTRODUCTION

Impurity effects still constitute one of the most important problems in tokamak plasmas.¹ Impurities can adversely affect the overall energy confinement and the local power balance of such plasmas, through their line radiation and their contribution to the plasma resistivity. In recent years these impurity effects have been considerably reduced; relatively pure plasmas are currently obtained in all tokamaks by various impurity control techniques such as discharge cleaning, titanium gettering, use of graphite limiters, and precise plasma-position control. Nevertheless, the typical influxes of metallic impurities encountered in many tokamaks would be unacceptable if the impurities accumulated preferentially in the interior of the plasma. Interior accumulation of metallic impurities leads to plasma disruptions or to excessive radiation losses in the plasma interior. Such impurity accumulation, predicted to occur from neoclassical transport theory, has been observed in some tokamak experiments with Ohmic heating only²⁻⁷ and with auxiliary heating by neutral-beam injection (NBI).^{6,8-11} However, it has been generally possible to operate the tokamak in such a way that no accumulation occurs. Anomalous transport is often invoked to explain this lack of accumulation.

As a means of auxiliary heating alternative to NBI, ion cyclotron resonance frequency (ICRF) heating has been recently carried out in a number of tokamak experiments. In earlier experiments with ICRF heating where intermediate- Z metals were used for limiters,^{12,13} the lev-

els of metallic impurities were so high that central radiated power densities reached a level comparable to the ICRF heating power density; in some cases,¹³ the plasma interior started to cool during ICRF heating and then disruptions occurred. In more recent ICRF heating experiments with low- Z graphite limiters,¹⁴⁻²⁰ the metallic impurity concentrations have been considerably reduced; currently, the central radiation losses do not play a major role in the discharge power balance and the heating efficiency is not affected substantially. However, the levels of metallic impurities are still higher during ICRF heating than during Ohmic heating or NBI at similar power levels. In general, auxiliary heating tends to strongly enhance metallic impurity generation at internal structures such as walls, limiters, and antennas, leading to large additional influxes of such impurities which then penetrate to the plasma interior. So far, a great deal of attention has been focused on the source and its rates of metallic impurities during ICRF heating; however, their rapid penetration to the plasma interior has not come into question.

In this paper, we describe and analyze spectroscopic observations of iron-ion line radiation in the extreme-ultraviolet (xuv) region during ICRF heating experiments in the JIPP T-II-U tokamak.^{18,20} Emphasis is placed on the radiation increase during ICRF heating and on the subsequent sequential peaking of the radiation from the highest to the lowest ionization stages. These observations are interpreted as showing that iron ions accumulate preferentially in the central region of the plasma with

long confinement times. In the present experiments, impurity levels are relatively low and accumulation is not serious; however, the present results emphasize that a deeper understanding of impurity transport and confinement as well as of impurity generation may be needed for near-future tokamak experiments with higher-power, longer-pulse ICRF heating. The next section gives a brief description of the machine, the operation, and the diagnostics used in this study. Section III presents the results of spectroscopic measurements, together with those of soft-x-ray and bolometric ones, for both discharges with and without ICRF heating. Finally, Sec. IV contains modeling calculations that reproduce the iron-ion line radiances measured in the experiments.

II. EXPERIMENTAL ARRANGEMENT

The JIPP T-II-U tokamak was operated with graphite limiters, a nominal minor radius $a=23$ [cm, a nominal major radius $R=91$ cm, a toroidal magnetic field $B_T=26.4\text{--}30.0$ kG, and stainless-steel walls. Typical plasma parameters during the quasisteady part of the Ohmically heated discharges were the following: working gas D_2 with 3–20% H_2 minority, plasma current $I_p=170$ kA, line-average electron density $\bar{n}_e \approx 2 \times 10^{13}$ cm^{-3} , central electron density $n_e(0) \approx 3 \times 10^{13}$ cm^{-3} , central electron temperature $T_e(0) \approx 1$ keV, and central ion temperature $T_i(0) \approx 0.5$ keV. In the JIPP T-II-U ICRF heating experiments, rf-power injection was accompanied by strong gas puffing and additional current rise, in order to suppress impurity influxes and growth of $m=2$ magnetohydrodynamic (MHD) activity.^{18,20} Strong puffing of the working gas was initiated at 100 ms during the above quasisteady discharge condition, and the gas was continuously bled into the discharge until 140 ms; additional current rise was initiated at 117 ms, and the current was increased up to $I_{pm}=240\text{--}290$ kA in about 25 ms. Then ICRF heating in the H minority regime was carried out between 118 and 153 ms at an rf power $P_{rf}=500\text{--}800$ kW (exceeding the Ohmic power input $P_{Ohmic} \approx 300$ kW) having the 40 MHz frequency. Two of the three ICRF antennas had stainless-steel Faraday shields, and the remaining one had titanium Faraday shields.

Spectral line emission intensities in the xuv region, 30–1100Å, were measured with a 2-m grazing-incidence monochromator and a CsI-cathode electron multiplier. The wavelength resolution was about 0.2 Å, and the line of sight was along a chord through the center of the plasma. The sensitivity of this monochromator system was relatively calibrated over the entire wavelength range and absolutely calibrated at two wavelengths of the H L_β and L_γ lines by the branching-ratio technique.²¹ The line-average electron density along the central chord was measured by microwave interferometry, and the central electron temperature from second-harmonic electron cyclotron emission. The radial profiles of electron density and temperature were measured by ruby-laser Thomson scattering. The near-central ion temperature was measured from the charge-exchanged D^0 energy distribution. The energy emitted from the plasma, consisting of photons mostly in the xuv region and charge-exchanged neu-

tral atoms, was measured with an array of bolometers viewing different chords. The soft-x-ray emission at photon energies above 1 keV was monitored with an array of silicon detectors viewing different chords.

III. EXPERIMENTAL RESULTS AND INTERPRETATIONS

Figures 1(a)–4(a) show typical results for the Ohmically heated discharges including strong gas puffing and additional current rise. These data provide a reference for later comparison with the results obtained when ICRF heating was carried out. Figure 1(a) shows the time evolution of the plasma current I_p , the line-average electron density \bar{n}_e , the central electron density $n_e(0)$, and the central electron temperature $T_e(0)$ for a D_2 discharge with 3% H_2 minority, $B_T=28.8$ kG, and $I_{pm}=240$ kA. The density increases from $\bar{n}_e \approx 2 \times 10^{13}$ to 6×10^{13} cm^{-3} in about 60 ms after the initiation of gas puffing at 100 ms. The density profile was slightly hollow with the maximum at $r \approx 7$ cm during the steep part of the density increase. The central electron temperature reaches the maximum value $T_e(0) \approx 1.4$ keV at about 120 ms, and then decreases to $T_e(0) \approx 1$ keV during the density increase. However, the electron temperature remained almost unchanged at intermediate radii, so that the centrally peaked

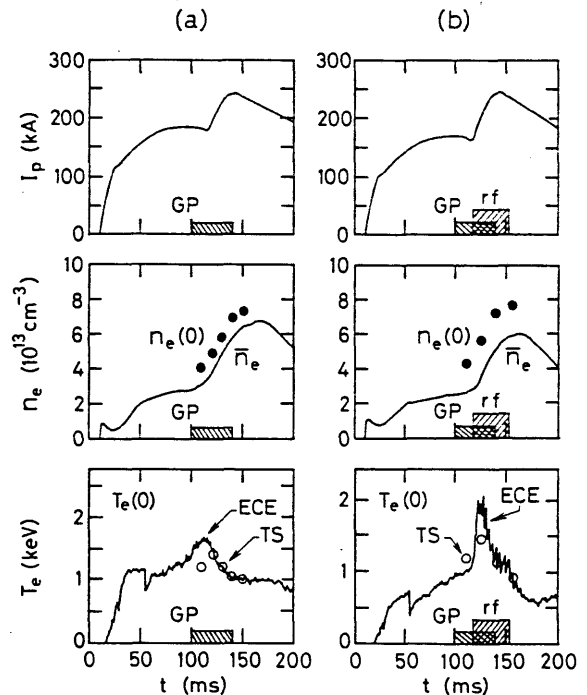


FIG. 1. Time evolutions of the plasma current I_p , the line-average electron density \bar{n}_e , the central electron density $n_e(0)$, and the central electron temperature $T_e(0)$ for JIPP T-II-U discharges (a) with Ohmic heating only and (b) with ICRF heating; $T_e(0)$ was measured by Thomson scattering (TS) and from second-harmonic electron cyclotron emission (ECE). These discharges include strong gas puffing (GP) and additional current rise; in (b), ICRF heating (rf) lasts 35 ms from 118 to 153 ms. Discharge conditions: working gas D_2 with 3% H_2 minority, $B_T=28.8$ kG, $I_{pm}=240$ kA, and $P_{rf}=500$ kW.

profile of the electron temperature flattened gradually inside $r \approx 7$ cm after about 120 ms. The central ion temperature fell by about 50 eV after about 120 ms during the density increase, and thereafter returned to its initial level.

Figure 2(a) shows the time evolution of the emission intensities of several iron-ion resonance lines for the Ohmically heated discharge of Fig. 1(a). These signals are central-chord radiances. The FeXXIII resonance line at 132.83 Å overlaps with a FeXX resonance line at 132.85 Å. The FeXX 132-Å line intensity is estimated to be about twice as large as the FeXX 118-Å line intensity. In

this estimation, the Boltzmann distribution is assumed between upper-level populations of the two FeXX resonance transitions, and the atomic data are taken from the tables of Fuhr *et al.*²² Thus, around 120 ms when the FeXXIII 132-Å signal attains the peak, about half of the FeXXIII 132-Å signal is a contribution from FeXX; in the early and late parts of the discharge, however, most of it is a contribution from FeXX. Between the start of the discharge and about 120 ms, higher ionization stages are seen to appear and attain peak intensities at successively later times. Each line intensity drops after reaching its own peak. The high ionization stages FeXX–XXIV, which radiate in the central region of the plasma, attain their peak intensities after the initiation of gas puffing at 100 ms. This is consistent with the result that the central electron temperature does not decrease until about 20 ms after the initiation of gas puffing.

All the line intensities show a substantial drop during gas puffing, in spite of the increasing electron density, indicating a large decrease of the iron concentration. This intensity drop is more noticeable in the higher ionization stages. Such a substantial drop in metallic impurity line intensities due to gas puffing has been observed in a number of tokamak experiments;^{23–27} the intensity drop has been ascribed mostly to a large decrease of the metallic impurity concentrations in the discharge following the lowering of the peripheral electron temperature. Gas puffing raises the electron density and concurrently lowers the electron temperature, since the energy content of a plasma remains almost unchanged by this operation. The lowered temperature at the plasma periphery leads to reduced impurity generation at the limiters and walls, resulting in reduced impurity influxes into the plasma. The larger intensity drop in the higher ionization stages has been ascribed to a lowering of the electron temperature with consequent changes in the ionization balance. A more detailed account of the spectroscopic observations in this type of discharge will appear in another paper.²⁰

Figures 1(b)–4(b) show typical results from the ICRF heating experiments, where ICRF heating at $P_{rf} = 500$ kW was applied to the Ohmically heated discharge of Figs. 1(a)–4(a) between 118 and 153 ms. Figure 1(b) shows the time evolution of the same plasma parameters as shown in Fig. 1(a). It is natural that the time evolutions of the plasma condition are almost the same in the two cases with Ohmic heating only and with ICRF heating at least up to 118 ms when the ICRF heating is initiated. The evolutions of the plasma current I_p , the line-average electron density \bar{n}_e , and the central electron density $n_e(0)$ are very similar in both cases during the whole period of the discharge. The density profiles were also similar in both cases. It is therefore evident that the ICRF heating itself makes no appreciable contribution to the density increase; the density increases by about a factor of 3 in about 60 ms owing to the strong gas puffing initiated at 100 ms.

The time evolution of the electron and ion temperatures in the ICRF heating case differs markedly from that in the Ohmic heating one. The central electron temperature increases rapidly to $T_e(0) \approx 1.8$ keV within about 5 ms after the initiation of ICRF heating, because the ICRF power can be coupled with electrons as well as ions.²⁸

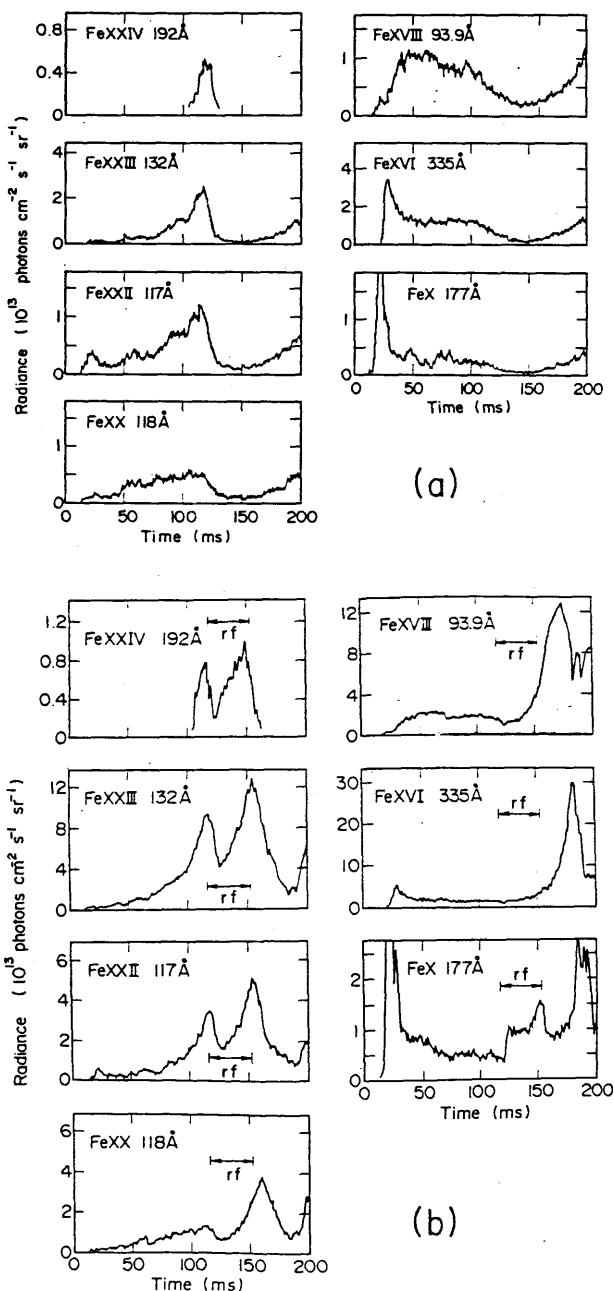


FIG. 2. Time evolutions of the central-chord radiances of several iron-ion resonance lines for (a) the Ohmically heated and (b) the ICRF heated discharges of Fig. 1. The FeXXIII 132-Å signal includes a contribution from FeXX, owing to the blending of the FeXXIII 132.83-Å and FeXX 132.85-Å lines.

However, the central electron temperature begins to decrease at about 125 ms during ICRF heating; it decreases to $T_e(0) \approx 0.5$ keV in about 50 ms during and after ICRF heating. This decreasing rate of $T_e(0)$ is much faster than that in the Ohmic heating case where the decrease in $T_e(0)$ is ascribed mostly to the density increase due to gas puffing. The electron temperature continued increasing or remained almost unchanged at intermediate radii, in spite of the rapid decrease in $T_e(0)$; consequently, the centrally peaked profile of the electron temperature flattened rapidly after about 125 ms, leading to a slightly hollow profile with the maximum at $r \approx 7-10$ cm around 155 ms. Such hollow temperature profiles have been observed in some tokamak experiments,^{9,11,24,29} and are now known to be caused by large radiative losses due to metallic impurities in the central region of the plasma. It is therefore probable that the rapid decrease in $T_e(0)$ during and after ICRF heating is attributable both to gas puffing and to radiative losses. The signal of the electron cyclotron emission shows a large sawtooth oscillation during ICRF heating. The central ion temperature rose by $\Delta T_i(0) \approx 0.5$ keV during ICRF heating, and thereafter returned to its initial level. The ion heating efficiency is relatively high:

$$\Delta T_i(0)\bar{n}_e/P_{\text{rf}} \approx (3-6) \times 10^{13} \text{ eV cm}^{-3} \text{ kW}^{-1}.$$

Figure 2(b) shows the time evolution of the iron-ion line intensities for the ICRF heated discharge of Fig. 1(b). These signals are central-chord radiances of the same spectral lines as shown in Fig. 2(a) for the Ohmic heating case. The evolutions of the emission intensity of each line are very similar in both cases up to about 120–125 ms, about 2–7 ms after the initiation of ICRF heating, aside from the difference in the absolute radiance. The absolute line radiances depend on the discharge conditions and the condition of the vacuum vessel; the data in Figs. 2(a) and 2(b) were obtained at separate days during a long series of experiments. All the line intensities show a substantial drop due to the gas puffing initiated at 100 ms. After this drop, which is more noticeable in the higher ionization stages, the evolution of the line intensities in the ICRF heating case differs strikingly from that in the Ohmic heating one. The line intensity of the low ionization stage Fe X, which radiates near the edge of the plasma, rises by about a factor of 2–3 after about 120 ms during ICRF heating, and thereafter returns to its slowly rising base level. This result indicates a large additional influx of iron into the plasma during ICRF heating.

The line intensities of the intermediate and high ionization stages Fe XVI–XXIV, which radiate near the middle and center of the plasma, begin to rise at about 125 ms; they rise by about a factor of 3–4 during ICRF heating. This intensity rise that is much faster than the electron-density increase may, in a sense, be ascribed to a considerable increase of the iron concentration in the discharge due to the additional influx. The line intensities depend on the electron temperature T_e as well as on the electron density and the iron concentration along the spectrometer line of sight. All the iron-ion lines in Fig. 2 originate from $\Delta n = 0$ resonance transition; their excitation rate coefficients by electron impact are practically independent

of T_e over the range 0.2–2 keV where the ions exist. Consequently, the line intensities depend on T_e only through the fractional abundances of iron ionization stages. While all the line intensities show a substantial rise after about 125 ms during ICRF heating, the electron temperature decreases from $T_e \approx 1.8$ to 1 keV in the central region where the high ionization stages radiate. This T_e decrease should result in a marked decrease of the abundances of high stages such as Fe XXIV. Therefore, if the iron concentration did not increase preferentially in the central region, but increased at almost the same rate throughout the plasma, the intensity rise during ICRF heating would be less noticeable in the higher ionization stages. This is contrary to the present observations. Preferential accumulation of iron must be taken into account in the central region of the plasma, in order to explain the substantial rise in the line intensities of high ionization stages such as Fe XXIV during ICRF heating.^{4,6,8,9,11}

The highest ionization stage Fe XXIV attains the peak intensity at about 150 ms, about 3 ms before the termination of ICRF heating; then the lower stages attain their peak intensities at successively later times while the electron temperature decreases from $T_e \approx 1$ to 0.5 keV in the central region. Each line intensity drops after reaching its own peak. This sequential peaking of the emission reflects the decrease in T_e and the concurrent recombination into successively lower stages without substantial changes in the iron concentration.^{4,6,8,9,11} If a large decrease of the iron concentration took place in the discharge after ICRF heating, all the line intensities would show a substantial drop without sequential peaking. An influx of iron into the plasma after ICRF heating is probably much smaller than that during ICRF heating. Therefore, it appears that the iron, which has flowed into the plasma and accumulated in its central region during ICRF heating, is retained in the plasma with relatively long confinement times after ICRF heating.

Soft-x-ray and bolometric measurements support the spectroscopic observations on the impurity behavior. Figures 3(a) and 3(b) show the time evolution of the central-chord soft-x-ray emission and the total radiated power P_{rad} for (a) the Ohmically heated and (b) the ICRF heated discharges of Fig. 1.

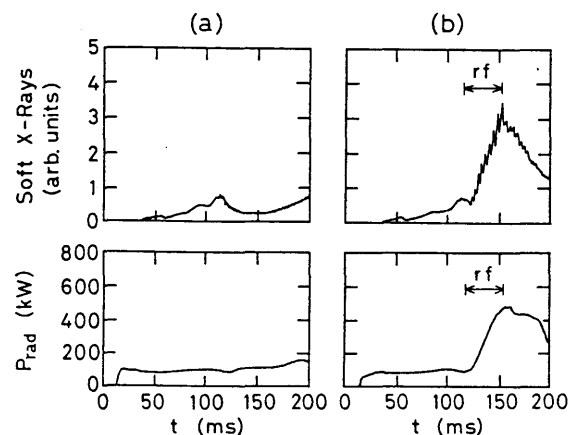


FIG. 3. Time evolutions of the central-chord soft-x-ray emission and the total radiated power P_{rad} for (a) the Ohmically heated and (b) the ICRF heated discharges of Fig. 1.

P_{rad} for the Ohmically and the ICRF heated discharges of Fig. 1, respectively. In each case, the central-chord soft-x-ray signal has a similar time evolution to the signals of the high ionization stages Fe XX–XXIII in Fig. 2; a substantial drop due to gas puffing is seen around 120 ms. The soft-x-ray emission depends on the electron temperature T_e and density n_e , and also on the level of impurities; the T_e dependence is so strong that most of the emission along the detector line of sight tends to be localized where T_e is highest. The central-chord soft-x-ray emission comes mostly from the central region of the plasma. After the drop due to gas puffing, it rises continuously at a rate much faster than the n_e increase during ICRF heating, though T_e is decreasing in the central region. This emission rise was noticeable on all detectors viewing different chords. The soft-x-ray emission drops following the termination of ICRF heating. These results indicate that the impurity levels in the discharge increase considerably during ICRF heating owing to large additional influxes of impurities into the plasma, and that this increase occurs preferentially in the central region. If impurities did not accumulate preferentially in the central region of the plasma, the emission rise during ICRF heating would be less noticeable on detectors viewing the chords nearer to the central one, because of the T_e decrease in the central region. It is also evident that the impurity levels in the discharge do not continue to increase considerably after ICRF heating. The central-chord soft-x-ray signal, together with the signal of the electron cyclotron emission in Fig. 1(b), shows a large sawtooth oscillation during ICRF heating.

Such a substantial rise in the central-chord soft-x-ray emission has been observed in some tokamak experiments,^{2,4–8,10} and has been ascribed to central accumulation of metallic impurities. In some cases, the onset of accumulation was accompanied by the disappearance of the sawteeth.² Theoretical calculations have also shown that sawtooth oscillations (periodic internal disruptions) can significantly reduce impurity accumulation (impurity confinement times) if inward convection is large enough relative to diffusion in the impurity flux.³⁰ In some cases,^{4,6} however, accumulation took place concurrently with well-defined sawtooth activity as in the present experiments.

The total radiated power in the Ohmic heating case remains almost constant during the whole period of the discharge; a very little drop due to gas puffing is seen around 120 ms. After this drop, the total radiated power in the ICRF heating case increases continuously from $P_{\text{rad}} \approx 100$ to 500 kW during ICRF heating, and thereafter maintains a relatively constant value for about 20–30 ms. The value of P_{rad} toward the end of ICRF heating is nearly equal to the ICRF heating power P_{rf} , corresponding to about 60% of the total input power $P_{\text{tot}} = P_{\text{Ohmic}} + P_{\text{rf}}$ ($P_{\text{Ohmic}} \approx 300$ kW, $P_{\text{rf}} \approx 500$ kW) to the plasma.

Figures 4(a) and 4(b) show the time evolution of the radial profile of the radiated power density W_{rad} for the Ohmically and the ICRF heated discharges of Fig. 1, respectively. The radiation profile $W_{\text{rad}}(r)$ in the Ohmic heating case remains fairly flat between 100 and 170 ms, whereas that in the ICRF heating case evolves toward a

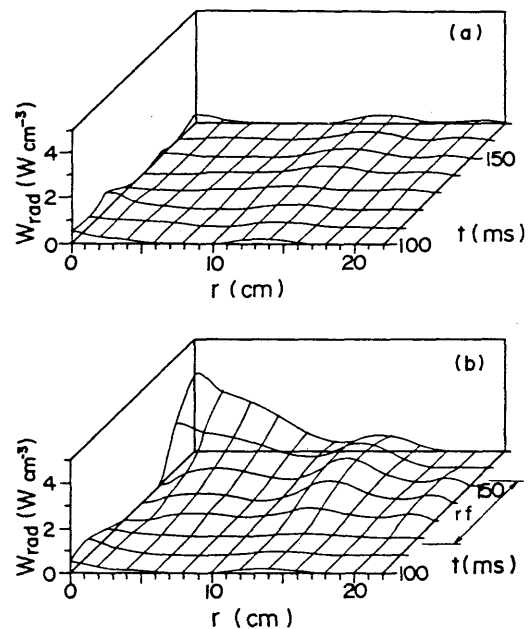


FIG. 4. Time evolutions of the radial profile of the radiated power density W_{rad} for (a) the Ohmically heated and (b) the ICRF heated discharges of Fig. 1.

centrally peaked profile. In each case, the near-central radiation at $r \lesssim 10$ cm, largely due to metallic impurities, has a similar time evolution to a superposition of the signals of the intermediate and high ionization stages Fe XVI–XXIV in Fig. 2; a substantial drop due to gas puffing is seen around 120 ms. After this drop, which is more noticeable at smaller radii, the near-central radiation increases gradually during ICRF heating without appreciable profile modifications. The values of $W_{\text{rad}}(r)$ within $r \approx 10$ cm toward the end of ICRF heating are comparable to or exceeding the volume-average density $\bar{W}_{\text{tot}} \approx 0.85$ W cm⁻³ of the total input power P_{tot} . After ICRF heating, the near-central radiation increases continuously at a rate much faster than it does during ICRF heating. This increase is more noticeable at smaller radii, leading to a centrally peaked radiation profile. It is probable, near the center of the plasma during and after ICRF heating, that the radiative losses are not small enough to be negligible in the discharge power balance, being responsible for the rapid decrease in the electron temperature as seen in Fig. 1(b).

Central accumulation of metallic impurities that has been observed so far in tokamak experiments usually ended in plasma disruptions following excessive radiation losses in the central region of the plasma.^{9,10} This cause-and-effect relationship is not clearly established in the present experiments, however. The present accumulation, which takes place during ICRF heating as indicated by the spectroscopic and soft-x-ray data in Figs. 2(b) and 3(b), does not lead even to excessive radiation losses in the central region; the radiation profile $W_{\text{rad}}(r)$ is not centrally peaked during ICRF heating. This may be ascribed to the low level of metallic impurities in the discharge. The metallic impurity concentrations are reduced with graph-

ite limiters, and further reduced as a result of strong gas puffing and additional current rise. Following the initiation of ICRF heating, the impurity concentrations in the discharge increase progressively owing to large additional influxes of impurities which are then transported to the central region of the plasma. The profile $W_{\text{rad}}(r)$ eventually becomes centrally peaked toward the end of ICRF heating, and thereafter becomes more and more centrally peaked.

Neither substantial increase nor decrease of impurity concentrations takes place in the discharge after ICRF heating, as indicated by the spectroscopic and soft-x-ray data in Figs. 2(b) and 3(b). The substantial increase in the near-central radiation after ICRF heating is consistent with the sequential peaking of the emission from the highest to the lowest ionization stages of iron as seen in Fig. 2(b); this radiation increase is probably related to an increase of the radiation efficiencies of impurities with decreasing electron temperature.^{31,32}

The data in Figs. 1–4 are the results for D₂ discharges with 3% H₂ minority, toroidal magnetic field $B_T = 28.8$ kG, maximum plasma current $I_{pm} = 240$ kA, and ICRF heating power $P_{\text{rf}} = 500$ kW. Similar results were obtained for the following wide range of discharge conditions: working gas D₂ with 3–20% H₂ minority, $B_T = 26.4$ – 30.0 kG, $I_{pm} = 240$ – 290 kA, and $P_{\text{rf}} = 500$ – 800 kW.

IV. DISCUSSION AND CONCLUSIONS

In the present ICRF heating experiments with strong gas puffing and additional current rise, the evidence for preferential accumulation of intrinsic iron in the central region of the plasma is essentially as follows: the line intensities of high ionization stages such as FeXXIV rise substantially during ICRF heating [Fig. 2(b)], though the electron temperature is decreasing in the central region where the high stages radiate [Fig. 1(b)]. This intensity rise is much faster than the electron-density increase [Fig. 1(b)]. The iron concentration in the discharge increases considerably during ICRF heating owing to a large additional influx of iron into the plasma, as indicated by a substantial rise in all the line intensities of different ionization stages [Fig. 2(b)]. However, the electron-temperature decrease in the central region should result in a marked decrease of the fractional abundances of high ionization stages such as FeXXIV. Therefore, if the iron concentration did not increase preferentially in the central region, but increased at almost the same rate throughout the plasma, the intensity rise during ICRF heating would be less noticeable in the higher ionization stages.

Recent measurements of soft-x-ray spectra in the present discharges have shown that FeXXV is scarcely produced, i.e., FeXXIV is the terminal stage of ionization.³³ After the highest ionization stage FeXXIV attains the peak intensity toward the end of ICRF heating, the lower stages attain their peak intensities at successively later times [Fig. 2(b)]; each line intensity drops after reaching its own peak. This sequential peaking of the emission reflects the decrease in the electron temperature [Fig. 1(b)] and the concurrent recombination into succes-

sively lower stages without substantial changes in the iron concentration. It appears that the iron, which has flowed into the plasma and accumulated in its central region during ICRF heating, is retained in the plasma with relatively long confinement times after ICRF heating.

Similar features of impurity line radiation have been observed in ISX-B (Impurity Study Experiment—B tokamak at Oak Ridge National Laboratory) discharges with Ohmic heating only^{4,6} and with counter-NBI,^{6,8,9,11} for intrinsic titanium and iron and for silicon, argon, and titanium introduced as tracer elements. Substantial increases in the central-chord line radiances appeared first in the highest ionization stages and later showed up in the lower stages, while the plasma interior cooled rapidly. These effects were particularly clear in the counter-NBI discharges. Recombination does not explain the radiation increase in the highest ionization stages. The ISX-B group has insisted, as in the present paper, that impurity accumulation and long confinement times must be taken into account in order to explain their experimental observations. In PLT (Princeton Large Torus) discharges with counter-NBI and with co-NBI where significant amounts of molybdenum were injected,³⁴ the line radiances of low ionization stages were observed to increase with time as the plasma interior cooled and the ionization balance changed. In TFR (Tokamak de Fontenay-aux-Roses) discharges the line radiances of different ionization stages of intrinsic nickel were observed to increase during ICRF heating.¹³ Following the start of plasma interior cooling toward the end of ICRF heating, the radiance of the highest ionization stage began to decrease and then a disruption occurred. It was indicated that the metallic impurity concentrations in the discharge increased as the ICRF heating caused strong influxes of such impurities which in turn penetrated to the plasma interior.

The evidence for central accumulation of iron in the present ICRF heating experiments is further reinforced by comparing the experimental results with the predictions of time-dependent modeling calculations as described in Refs. 35–37. The comparison is made between the measured and calculated central-chord radiances of the iron-ion resonance lines in Fig. 2. The calculations treat a set of coupled one-dimensional continuity equations for all the ionization stages of iron which include transport as well as ionization and recombination. Cylindrical symmetry is assumed in the calculations; r represents the minor radial coordinate of the toroidal tokamak plasma. The radial flux density Γ_Z of the iron ions of charge Z is taken to have the form $\Gamma_Z = -D_A \partial n_Z / \partial r - (r/a) V_A n_Z$, where n_Z is the iron-ion density of charge Z , and a is the minor radius of the plasma. The diffusion coefficient D_A and the inward convection velocity V_A are two adjustable transport parameters independent of radius r and ion charge Z .

The ionization rate coefficients are given by Lotz's formula with his values for the subshell binding energies.³⁸ The contribution of autoionization to the total ionization rate is taken into account for FeXVI and XV, according to the calculations of Cowan and Mann.³⁹ The radiative recombination rate coefficients are given by the modification of the formula for H-like ions proposed by von

Goeler *et al.*⁴⁰ The dielectronic recombination rate coefficients are given by Burgess's formula,⁴¹ where two resonance transitions of the recombining ion are considered, the atomic data being taken from the tables of Breton *et al.*³² For ions less ionized than the Ar-like sequence, two resonance transitions, a $\Delta n=0$ and a $\Delta n=1$, are taken into account, the atomic parameters being calculated with the formulas used by Pořt *et al.*³¹

The boundary conditions imposed are $(\partial n_Z/\partial r)_{r=0,t} = 0$ and $n_Z(a,t) = 0$, where $a = 23$ cm is the limiter radius. The scrape-off-layer plasma is not considered. It is assumed that iron ions leaving the plasma at $r=a$ are not recycled, and that the iron coming from the walls enters the plasma at $r=a$ as neutral atoms with a constant inward velocity V_0 . The incoming neutral atoms are ionized in a narrow shell just inside $r=a$, so that the influx of neutral atoms into the plasma is accounted for by taking their quasisteady density distribution $n_0(r)$ with the inward flux density $n_0(r)V_0$.^{26,35} The incoming neutral-iron flux density Γ_0 at $r=a$, $\Gamma_0 = n_0(a)V_0$, is the third adjustable parameter in the calculations. The velocity V_0 , is taken to be 10^5 cm s⁻¹, corresponding to the neutral-iron kinetic energy of 0.29 eV.

Given the radial profiles of the electron density n_e and temperature T_e , the coupled continuity equations are solved numerically for $n_Z(r,t)$ with the chosen values of D_A , V_A , and Γ_0 . The time-dependent functional forms of $n_e(r)$ and $T_e(r)$, determined on the basis of the experimental measurements by Thomson scattering, are employed as input to the calculations. Figure 5 shows the input radial profiles $n_e(r)$ and $T_e(r)$ at various times which have the features described in Sec. III with regard to Fig. 1(b). Here the electron density and temperature at the edge of the plasma were taken as $n_e(a) = 0.1n_e(0)$ and $T_e(a) = 20$ eV. No measurements of $n_e(r)$ and $T_e(r)$ were done after 155 ms; the relative density profile $[n_e(r) - n_e(a)]/[n_e(0) - n_e(a)]$ was assumed to change gradually to the form $[1 - (r/a)^2]$ in 10 ms after 155 ms and then remain unchanged, with the value of the line-average density \bar{n}_e measured by microwave interferometry; the relative temperature profile $[T_e(r) - T_e(a)]/[T_e(0) - T_e(a)]$ was assumed to remain unchanged after 155 ms, with the value of $T_e(0)$ measured from second-harmonic electron cyclotron emission.

The calculations are started at $t = 118$ ms, the time of the initiation of ICRF heating which lasts 35 ms from 118 to 153 ms. The iron is initially distributed among different ionization stages as in coronal ionization equilibrium, the total iron density n_{Fe} being taken as $n_{Fe}(r) = 10^{-5}n_e(r)$. The results of the calculations at the time of the experimental measurements concerned, $t \geq 130$ ms, are insensitive to the initial ionization-stage distribution. Once the iron-ion densities $n_Z(r,t)$ have been obtained, the radiances of the iron-ion resonance lines concerned, originating from $\Delta n=0$ transition, are calculated by assuming coronal population equilibrium: the upper level of the transition is populated by electron-impact excitation from the ground level, and is depopulated by spontaneous radiative decay. The electron-impact excitation rate coefficients are given by the formula for optically allowed transitions suggested by Van Regemort-

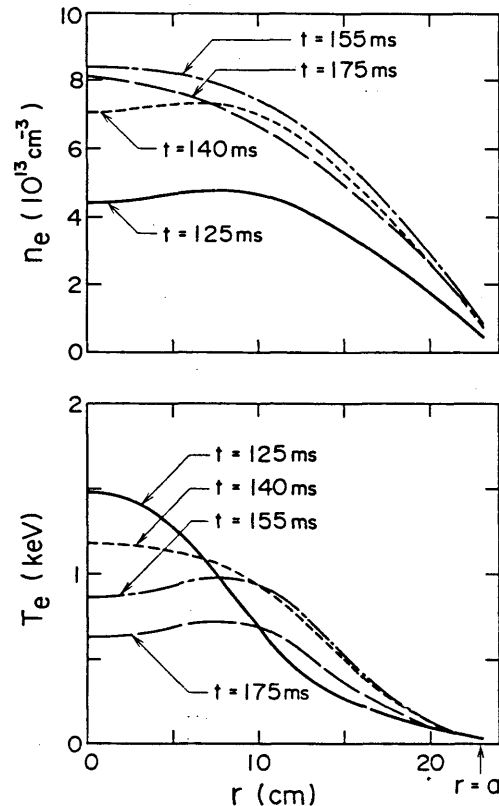


FIG. 5. Input radial profiles of the electron density n_e and temperature T_e at various times. Here $a = 23$ cm is the limiter radius. The time-dependent functional forms of $n_e(r)$ and $T_e(r)$, determined on the basis of the experimental measurements by Thomson scattering for the ICRF heated discharge of Fig. 1(b), are employed as input to the modeling calculations.

er,⁴² with the interpolation formula for the effective Gaunt factor proposed by Mewe.⁴³ The atomic data are taken from the tables of Fuhr *et al.*,²² including the radiative transition probabilities.

By varying the two transport parameters D_A and V_A and by simultaneously adjusting the incoming flux Γ_0 in the numerical computation, it is attempted to achieve the best agreement between the measured and calculated line radiances. Figure 6 shows the calculated time evolution of the central-chord radiances of the iron-ion resonance lines that is in good agreement with the measured one in Fig. 2(b). In calculating the Fe XXIII radiance, the blending of the Fe XXIII and XX 132-Å lines was taken into account. For the case of Fig. 6, the values of D_A , V_A , and Γ_0 were first chosen in such a way as to simulate the time and amplitude of the Fe XXIV radiance peak and to follow the Fe X radiance evolution; after $t = 153$ ms, the time of the termination of ICRF heating, the values were chosen in such a way as to simulate the times of the Fe XVIII and XVI radiance peaks and to reproduce the Fe X radiance. Thus, the curves before 153 ms were obtained with $D_A = 100$ cm² s⁻¹, $V_A = 1200$ cm s⁻¹, and $\Gamma_0 = 9 \times 10^{11}$ cm⁻² s⁻¹ until 140 ms and then increasing linearly by a factor of 1.5 in 13 ms; the curves after 153 ms were obtained with $D_A = 100$ cm² s⁻¹, $V_A = 400$ cm s⁻¹, and $\Gamma_0 = 0$. The following discrepancies still remain between the measured and calculated radiance evolutions. The cal-

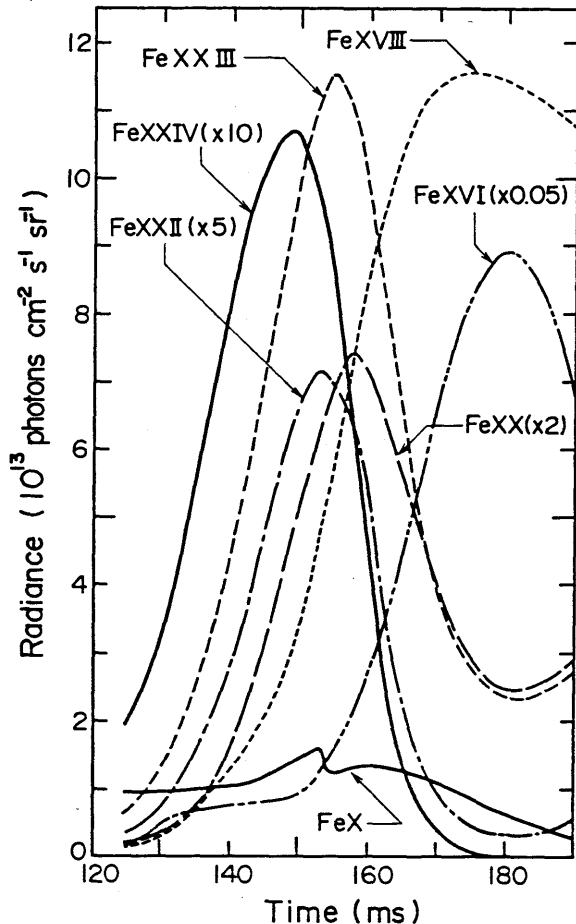


FIG. 6. Calculated time evolution of the central-chord radiances of the iron-ion resonance lines which is compared with the measured one in Fig. 2(b). In calculating the FeXXIII radiance, the blending of the FeXXIII and XX 132-Å lines was taken into account. The time-dependent modeling calculations were started at $t=118$ ms, the time of the initiation of ICRF heating which lasts 35 ms from 118 to 153 ms.

culated amplitude of the FeXXII radiance peak is about a factor of 3 smaller than the measured one; the calculated amplitude of the FeXVI radiance peak is about a factor of 6 larger than the measured one. The calculated FeXVIII radiance drop after the peak is too small as compared to the measured one. The FeX radiance rise and peak after about 160 ms, observed in the experiments, are not well reproduced in the calculations. Otherwise the agreement is quite good.

At present there are various uncertainties in both the experimental measurements and the modeling calculations that tend to make quantitative comparisons tenuous: experimental uncertainties of spectrometer calibration, of plasma shot-to-shot reproducibility, and of electron density and temperature profiles; theoretical uncertainties of the transport model including influx and recycling, and of atomic processes with their rates. In view of these uncertainties and the difficulties in trying to reproduce the signals of different ionization stages perfectly, the overall agreement can be considered satisfactory between the

measured and calculated line radiances in Figs. 2(b) and 6. Figure 7 shows the calculated radial profiles of the total iron density $n_{\text{Fe}} (= \sum_Z n_Z)$ at various times for the case of Fig. 6, giving a picture of large influx and central accumulation of iron. The iron density n_{Fe} increases progressively until $t=153$ ms, the time of the termination of ICRF heating, owing to the large influx Γ_0 of iron which is then transported to the central region by inward convection. Here the convection parameter $S = aV_A/2D_A$,³⁰ which describes the relative importances of inward convection and diffusion in the iron flux, is very large: $S=138$ before 153 ms and $S=46$ after 153 ms. Diffusion tends to produce flat profiles of n_{Fe} , whereas inward convection tends to produce centrally peaked ones; the dimensionless parameter S gives a measure of the peaking of $n_{\text{Fe}}(r)$. The iron density profile $n_{\text{Fe}}(r)$ is flat or hollow at first; then $n_{\text{Fe}}(r)$ evolves toward a centrally peaked profile as the iron arrives and accumulates in the central region. After 153 ms, the iron continues to accumulate with $\Gamma_0=0$, which is accompanied by a reduction of n_{Fe} near the edge at $r=a$.

At $t > 150$ ms, the calculated central iron density $n_{\text{Fe}}(0)$ is of the order of 10^{10} cm^{-3} . The corresponding radiated power densities, estimated from the theoretical radiation efficiencies for coronal equilibrium distributions of iron^{31,32} and the measured electron densities and temperatures, are much smaller than the measured ones

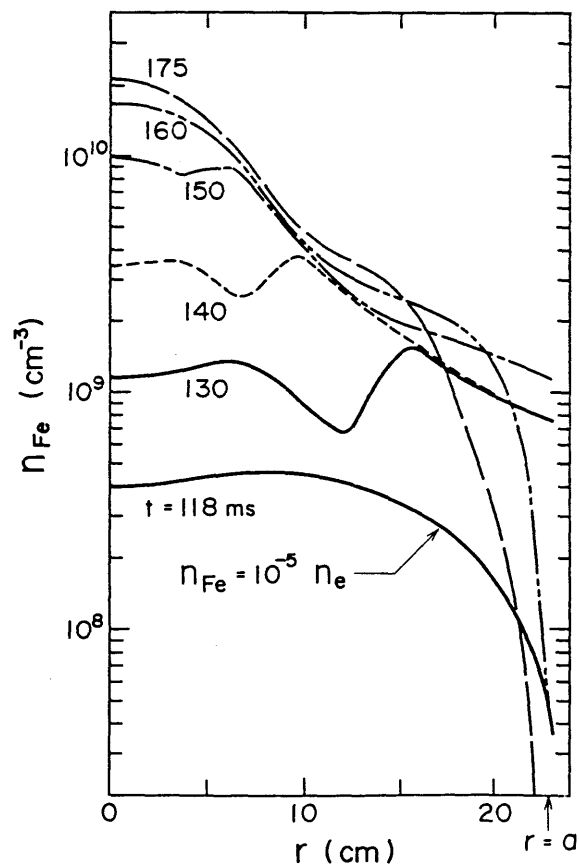


FIG. 7. Calculated radial profiles of the total iron density $n_{\text{Fe}} (= \sum_Z n_Z)$ at various times for the case of Fig. 6. Here $a=23$ cm is the limiter radius.

$W_{\text{rad}}(0)$ in Fig. 4(b). This difference may be due to radiation from titanium, oxygen, and carbon that are the primary intrinsic impurities besides iron in the present experiments. Further improvements in the modeling calculations are now in progress, including the estimation of the radiated power, to clear up the causes of the discrepancies between the measurements and calculations described above.

In conclusion, we have spectroscopically investigated the iron-ion line radiation in the xuv region during ICRF heating experiments in the JIPP T-II-U tokamak. Attention has been focused on the radiation increase during ICRF heating and on the subsequent sequential peaking of the radiation from the highest to the lowest ionization stages. The rf-power injection was accompanied by strong gas puffing and additional current rise, which raised the electron density and concurrently lowered the central electron temperature. The electron-temperature decrease in the central region, which was further promoted by radiative losses due to metallic impurities, continued after ICRF heating. The spectroscopic observations are interpreted as showing that the ICRF heating causes a large additional influx of iron into the plasma, and that the iron accumulates preferentially in the plasma interior with long confinement times. The sequential peaking of the radiation reflects the decrease in the electron temperature

and the concurrent recombination into successively lower stages. These interpretations are supported by the soft-x-ray and bolometric measurements, and confirmed by the modeling calculations that reproduce the iron-ion line radiances. Impurity accumulation is not typical of most tokamak experiments; in the present experiments, moreover, impurity levels are relatively low and accumulation is not serious. However, the present results emphasize that a deeper understanding of impurity transport and confinement as well as of impurity generation may be needed for near-future tokamak experiments with higher-power, longer-pulse ICRF heating. Further investigations will be required to reveal the mechanisms responsible for impurity accumulation during ICRF heating⁴⁴ as observed in the present experiments.

ACKNOWLEDGMENTS

Three of us (K.O., T.O., and Y.U.) would like to thank Professor J. Fujita and Professor M. Otsuka of Nagoya University and Professor T. Oda of Hiroshima University for providing the opportunity to participate in the JIPP T-II-U ICRF heating experiments. They would also like to thank Dr. M. Iwamoto and Dr. Y. Murai of Mitsubishi Electric Corporation for encouragement during this work.

*Present address: Products Development Laboratory, Mitsubishi Electric Corporation, Tsukaguchi-honmachi, Amagasaki 661, Japan.

¹R. C. Isler, *Nucl. Fusion* **24**, 1599 (1984).

²W. Engelhardt *et al.*, in *Plasma Physics and Controlled Nuclear Fusion Research*, Proceedings of the 7th International Conference, Innsbruck, 1978 (IAEA, Vienna, 1979), Vol. 1, p. 123.

³K. Toi *et al.*, *Nucl. Fusion* **19**, 1643 (1979).

⁴R. C. Isler *et al.*, *Phys. Rev. Lett.* **47**, 333 (1981).

⁵G. L. Jahns *et al.*, *Nucl. Fusion* **22**, 1049 (1982).

⁶R. C. Isler *et al.*, *Nucl. Fusion* **23**, 1017 (1983).

⁷S. Tsuji *et al.*, *Nucl. Fusion* **25**, 305 (1985).

⁸R. C. Isler *et al.*, *Phys. Rev. Lett.* **47**, 649 (1981).

⁹R. C. Isler, E. C. Crume, and D. E. Arnurius, *Phys. Rev. A* **26**, 2105 (1982).

¹⁰C. E. Bush *et al.*, *Nucl. Fusion* **23**, 67 (1983).

¹¹R. C. Isler, P. D. Morgan, and N. J. Peacock, *Nucl. Fusion* **25**, 386 (1985).

¹²D. Q. Hwang, G. Grotz, and J. C. Hosea, *J. Vac. Sci. Technol.* **20**, 1273 (1982).

¹³Equipe TFR, *Plasma Phys.* **24**, 615 (1982).

¹⁴S. Suckewer *et al.*, *Nucl. Fusion* **21**, 981 (1981).

¹⁵H. Kimura *et al.*, in *Plasma Physics and Controlled Nuclear Fusion Research*, Proceedings of the 9th International Conference, Baltimore, 1982 (IAEA, Vienna, 1983), Vol. 2, p. 113.

¹⁶Equipe TFR, *Plasma Phys. Contr. Fusion* **26**, 165 (1984).

¹⁷B. C. Stratton *et al.*, *Nucl. Fusion* **24**, 767 (1984).

¹⁸K. Toi *et al.*, in *Plasma Physics and Controlled Nuclear Fusion Research*, Proceedings of the 10th International Conference, London, 1984 (IAEA, Vienna, 1985), Vol. 1, p. 523.

¹⁹C. Breton *et al.*, *Plasma Phys. Contr. Fusion* **27**, 355 (1985).

²⁰K. Sato *et al.*, *Nucl. Fusion* (to be published).

²¹K. Sato, M. Otsuka, and M. Mimura, *Appl. Opt.* **23**, 3336 (1984).

²²J. R. Fuhr, G. A. Martin, W. L. Wiese, and S. M. Younger, *J. Phys. Chem. Ref. Data* **10**, 305 (1981).

²³TFR Group, *Nucl. Fusion* **17**, 1297 (1977).

²⁴E. Hinnov *et al.*, *Nucl. Fusion* **18**, 1305 (1978).

²⁵J. Fujita *et al.*, in *Plasma Physics and Controlled Nuclear Fusion Research*, Proceedings of the 7th International Conference, Innsbruck, 1978 (IAEA, Vienna, 1979), Vol. 1, p. 247.

²⁶R. C. Isler, E. C. Crume, and H. C. Howe, *Nucl. Fusion* **19**, 727 (1979).

²⁷E. Hinnov *et al.*, *Nucl. Fusion* **22**, 325 (1982).

²⁸M. Ichimura *et al.*, *Nucl. Fusion* **24**, 709 (1984).

²⁹R. J. Hawryluk *et al.*, *Nucl. Fusion* **19**, 1307 (1979).

³⁰F. H. Seguin, R. Petrasso, and E. S. Marmor, *Phys. Rev. Lett.* **51**, 455 (1983).

³¹D. E. Post *et al.*, *At. Data Nucl. Data Tables* **20**, 397 (1977).

³²C. Breton, C. De Michelis, and M. Mattioli, *J. Quant. Spectrosc. Radiat. Transfer* **19**, 367 (1978).

³³J. Fujita *et al.*, in *Controlled Fusion and Plasma Physics*, Proceedings of the 12th European Conference, Budapest, 1985 (European Physical Society, Budapest, 1985), Vol. 9F, Pt. III, p. 702.

³⁴S. Suckewer *et al.*, *Nucl. Fusion* **24**, 815 (1984).

³⁵T. Amano and E. C. Crume, Oak Ridge National Laboratory Report No. ORNL/TM-6363, 1978 (unpublished).

³⁶TFR Group, *Nucl. Fusion* **23**, 559 (1983).

³⁷C. Breton *et al.*, *J. Phys. B* **16**, 2627 (1983).

³⁸W. Lotz, Max-Planck-Institut für Plasmaphysik, Garching, Report No. IPP 1/56, 1967 (unpublished); Report No. IPP

- 1/76, 1968 (unpublished).
- ³⁹R. D. Cowan and J. B. Mann, *Astrophys. J.* **232**, 940 (1979).
- ⁴⁰S. von Goeler *et al.*, *Nucl. Fusion* **15**, 301 (1975).
- ⁴¹A. Burgess, *Astrophys. J.* **141**, 1588 (1965).
- ⁴²H. Van Regemorter, *Astrophys. J.* **136**, 906 (1962).
- ⁴³R. Mewe, *Astron. Astrophys.* **20**, 215 (1972).
- ⁴⁴V. S. Chan, S. C. Chiu, and S. K. Wong, *Nucl. Fusion* **25**, 697 (1985).

REPRINTED FROM

JOURNAL OF NUCLEAR MATERIALS

Volume 123 (1984)

IMPURITY ORIGIN DURING ICRF HEATING IN THE JIPP-1111 TOKAMAK

N. NODA, I. WAKAYARI, K. TOHME, K. KAKO, K. SAITO, K. OHKUBO, K. KAWAHARA,
H. OGAWA, T. FURUSUKI, S. YAMAHASHI, S. HIROKURA, Y. TANIGUCHI, Y. KAWASUMI,
R. ANDO and H. FUJIKI

Institute of Plasma Physics, Nagoya University, Nagoya 464, Japan

pp. 302-309

NORTH-HOLLAND PUBLISHING - AMSTERDAM

ELSEVIER

IMPURITY ORIGIN DURING ICRF HEATING IN THE JIPP T-IIU TOKAMAK

N. NODA, T. WATARI, K. TOI, E. KAKO, K. SATO, K. OHKUBO, K. KAWAHATA,
I. OGAWA, T. TETSUKA, S. TANAHASI, S. HIROKURA, Y. TANIGUCHI, Y. KAWASUMI,
R. ANDO and J. FUJITA

Institute of Plasma Physics, Nagoya University, Nagoya 464, Japan

Key words: impurity, ICRF heating, JIPP T-II U, graphite limiter

Replacing stainless steel limiters by graphite limiters, we found that radiations from iron and titanium ions were significantly reduced. Total radiation and loop voltage also decreased. This indicates that the limiters are the major impurity sources both in the ohmic and RF heating phases. Although titanium radiations increased with RF power injected by an antenna with a titanium Faraday shield, the maximum intensity was much smaller than in the experiment where the titanium-flashed stainless steel limiters were used. Thus it has been found that the Faraday shield is less important as an impurity source than limiters. Toroidal asymmetry observed for O II radiation suggest that the energetic charge-exchange neutrals play a role in releasing oxygen from the wall and that those energetic particles are relatively abundant in the toroidal sections near the antenna.

The $H_{\alpha} + D_{\alpha}$ radiation decreases during the RF pulse around the limiter, which may be due to the change in hydrogen/deuterium recycling at the limiter. The reduction of $H_{\alpha} + D_{\alpha}$ is greater with graphite limiters than with stainless steel limiters. The relation between recycling and impurity release is briefly discussed.

1. Introduction

High frequency-wave heating is one of the promising techniques of further heating in future large tokamaks. Wave heating at the ion-cyclotron range of frequencies (ICRF) is especially attractive because it shows a good efficiency for ion heating [1–4]. It has been reported, however, that RF heating causes a relatively large amount of impurity contamination compared to other heating techniques [5,6]. The impurity contamination makes the plasma column unstable and the maximum input power is often limited by disruption due to peaking of the current distribution caused by radiation cooling in the peripheral region. It has also been observed that the central electron temperature goes down during the ICRF pulse [1,4]. Thus, for successful RF heating, it is important to understand the mechanism which dominates the impurity generation and to find a method to reduce the impurity contamination. As the first step of the impurity study, we carried out a series of ICRF heating experiments with the JIPP T-IIU tokamak, especially focusing our attention on the identification of the origin of the impurity.

2. Experimental setup

JIPP T-IIU is a tokamak device constructed by modifying the JIPP T-II stellarator/tokamak. The major radius of the vacuum vessel is 93 cm and the minor radius is 32 cm. The plan view of JIPP T-IIU is shown in fig. 1. It has 20 toroidal coils and each toroidal section is numbered as P1, P2... P20 in the figure. Two sets of poloidal limiters are mounted at sections P7 and

P17. Three antennas on the high field side were used as ICRF launchers in this series of experiments. These antennas are located at P4, P14 and P15. The device has two bellows sections and, on each side of the bellows section, auxiliary limiters are set as a bellows guard. In fig. 2 is shown a sectional view of the vacuum vessel. Usually the center of the plasma-current channel is feedback-controlled to locate at $R = 91$ cm. The minor radius of the plasma is limited to 22.5 cm by the inner limiters. The minor radius of the guard limiters, which are not shown in fig. 2 is 25 cm. The vacuum vessel, the main limiters and Faraday shields are made of stainless steel SUS 304. The guard limiters are made of molybdenum. During these experiments, both sets of the main limiters were replaced by graphite limiters of the same shape and size. The Faraday shield was also changed to a titanium one. Titanium gettering was applied in the course of the experiments with the stainless steel (SUS) limiter. The locations of Ti balls are also shown in fig. 1. Hydrogen and impurity radiations were measured and their variations were compared with each other. Toroidal variation of the $H_{\alpha} + D_{\alpha}$ line radiation and that of O II 4415 Å were studied by means of a simple device consisting of an interference filter and a photodiode. The full width at the half maximum of the filters is 30 Å, which is narrow enough to separate the $H_{\alpha} + D_{\alpha}$ or O II lines from other radiations. A grazing incidence spectrometer was used at P6 for measurements of the radiation in the vacuum ultraviolet region. Total radiation intensity was monitored with pyroelectric detectors and metallic bolometers. A set of two Langmuir probes are on the section P8 and the distances from the axis of the vacuum vessel are 27 and 28 cm.

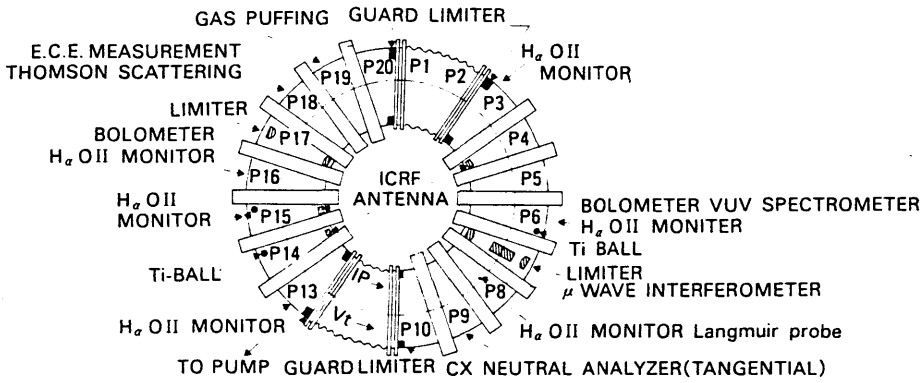


Fig. 1. Plan view of the JIPP T-IIU.

3. Results and discussions

3.1. Parameters of target plasmas and ICRF heatings

This series of experiments was concentrated on a hydrogen-minority heating with antennas on the high field side and the toroidal field B_0 of 2.94 T (see fig. 2). A mixture of 10% H_2 and 90% D_2 was used. Typical plasma parameters are tabulated in table 1. The loop voltage necessary for the same plasma current with the graphite limiters was a half of that with the SUS limiters. Thus, the plasma resistivity is significantly reduced by using the graphite limiters even in the ohmic heating phase. The impurity radiations with the graphite limiters were compared to those with the SUS limiters under the conditions where the ohmic input power of the target plasmas was almost equal. The applied RF frequency is 38.5 MHz for P4 antenna and 40.0 MHz for P14 and P15 antennas. The maximum RF power absorbed by the plasma is 400 kW per each antenna. In an optimized case with the SUS limiters, RF power as large as 500 kW could be injected without causing any minor disrup-

tion. The ion temperature and the electron temperature rose up to 1.1 keV in this case. Electron-heating efficiency was greater with the graphite limiters than with the SUS limiters and the electron temperature went up to as high as 1.8 keV with 250 kW RF injection.

3.2. Effects of limiter materials

The impurity study has been carried out for RF power levels up to 300 kW. Fig. 3 shows relative changes of impurity radiations as a function of RF power. The radiation intensities with the SUS limiters and with the graphite limiters are plotted. It can clearly be seen that the radiations from iron and titanium ions are significantly reduced by using the graphite limiters. The titanium-gettering had been applied 3 months before the measurements of the radiations in fig. 3. Both SUS limiters were covered with titanium on their electron sides (see the location of Ti balls in fig. 1). A significant decrease in Ti VIII indicates that most of the titanium impurity was generated from the SUS limiters covered with titanium. The radiations from the impurities of

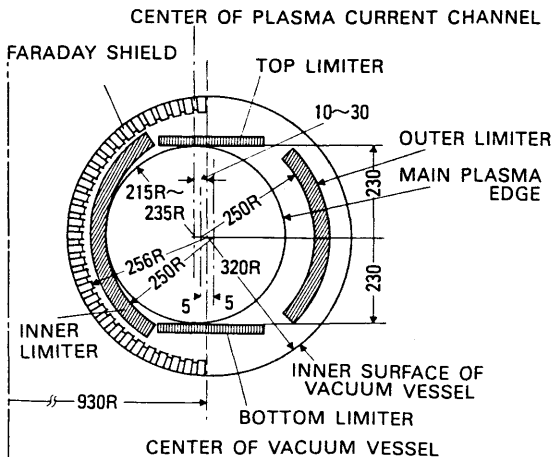


Fig. 2. Sectional view of the vacuum vessel.

Table 1

Parameters of ohmic plasmas and temperatures with ICRF. The power of RF is 500 kW for the SUS-limiter case and 250 kW for the graphite-limiter case

	SUS limiter	C limiter
Toroidal field B_0	2.94 T	2.94 T
Plasma current I_p	170 kA	240 kA
Loop voltage V_l	4.0 V	2.5 V
Ohmic input	680 kW	600 kW
Line averaged electron density ($\times 10^{13} \text{ cm}^{-3}$)	2.5	3.5
Central electron temperature $T_e(0)$		
without ICRF	700 eV	1100 eV
with ICRF	1100 eV	1800 eV
Central ion temperature $T_i(0)$		
without ICRF	400 eV	400 eV
with ICRF	1100 eV	800 eV

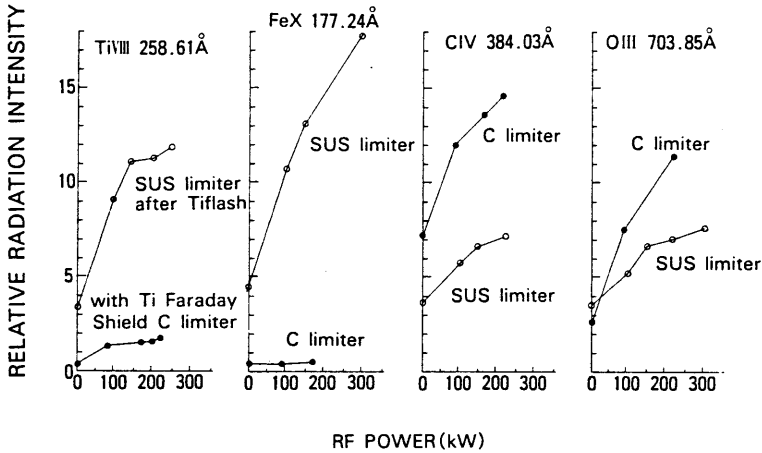


Fig. 3. Intensity of impurity radiations as a function of RF power. Open circles are the radiation intensity with the SUS limiters and the closed circles are that with the graphite limiters.

limiter materials increased with RF power and did not reach saturation within this power level.

The measurements with the graphite limiters were done using the P4 antenna with a Faraday shield made of titanium. Although the titanium radiation increases with RF heating by a factor of 5, the radiation intensity is still much smaller than that obtained with the

titanium-flashed SUS limiters. As is shown in fig. 2, the front surface of the Faraday shield is 11 mm behind the front of the main limiter. The results shown in fig. 3 indicate that, under such conditions, impurity generation on the Faraday shield is less important than that on the limiter. This conclusion is similar to that obtained for H-minority heating in PLT [7]. On the other hand, this is different from the results obtained in the TCA tokamak with the Alfvén wave heating, where the main origin of the impurities is concluded to be RF-antenna [6]. This difference is thought to be due to the fact that the heating mechanisms are quite different in ICRF heating and Alfvén wave heating. The intensity of C IV increased by a factor of two with the graphite limiter, compared to that in the SUS limiter, both the ohmic and ICRF heating phases. We think that the difference in the C IV intensities shown in fig. 3 is the net increase caused by introducing the graphite limiters. It should be noted, however, that the signal of C IV with SUS limiters is possibly blended with some impurity radiations other than carbon and then the net intensity of C IV is not clear in this case.

The total radiation measured with bolometers was 500 kW in the ohmic phase with the SUS limiter and decreased to 260 kW when graphite was used. A considerable amount of molybdenum radiation was observed in discharges with the SUS limiter. Both the iron and the molybdenum radiations may be responsible for the total radiation in the discharges with the SUS limiter. The intensity of the molybdenum radiation decreased with the graphite limiters by a factor of 8, compared to that with the SUS limiters.

3.3. Effect of titanium gettering with SUS limiters

Titanium gettering was once applied in the course of the experiments with the SUS limiters. In fig. 4 the radiations of O V and Ti VIII are compared for the

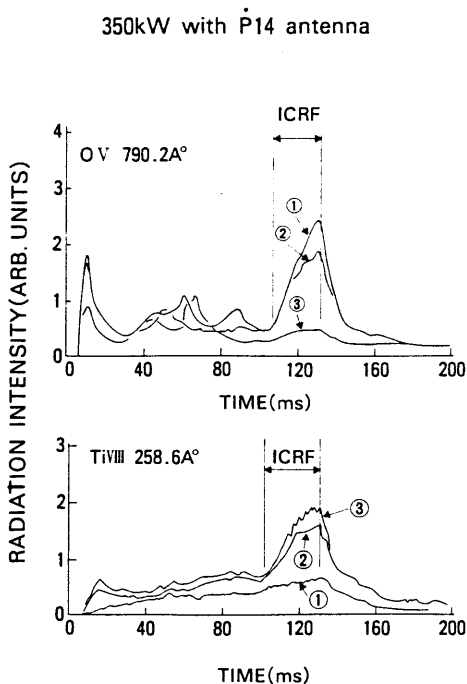


Fig. 4. Change in oxygen and titanium radiations before and after titanium gettering. The RF power is 350 kW with the P14 antenna. The first gettering is between shot Nos. 10726 and 10727. After shot No. 10735 the gettering was applied in every interval of discharge. (top) O V: (1) No. 10726, (2) No. 10727, (3) No. 10763; (bottom) Ti VIII: (1) No. 10713, (2) No. 10730, (3) No. 10766.

discharges before and after the gettering. The gettering was applied for the first time between the discharges of shot Nos. 10726 and 10727. The Ti ball of the P14 section was used and about 20 mg of Ti was flashed. Fig. 4(a) shows that the increase in the oxygen radiation during RF heating was suppressed by this first gettering trial. The gettering was applied in every interval of discharges after shot No. 10735. After several tens of discharges, the oxygen radiation was significantly reduced. In the course of the repetitive gettering, titanium radiations gradually increased up to the levels shown in fig. 4(b).

It was found that the electron density n_{es} in the scrape-off layer also increased during RF heating. Before the gettering, the density with the RF heating was 5 times larger than that in the ohmic phase. After the gettering, the density-increase rate was reduced to 1.6, indicating that the density-increase in the scrape-off layer strongly correlated with the increase of the oxygen radiations. A considerable part of the increased electrons probably came from oxygen.

The iron impurity radiation was not much reduced and still determined the plasma properties. The plasma parameters such as loop voltage, n_e , T_e , T_i , etc. did not change as a result of the gettering. The influence of the increased titanium on the plasma properties is not clear.

3.4. Behavior of O II and $H_\alpha + D_\alpha$ radiations

The radiation O II 4415 Å showed no significant toroidal asymmetry in the ohmic heating phase. This suggests that oxygen originates from a broad area of the first wall. With the SUS limiters, we found a clear toroidal asymmetry in O II intensity during RF heating.

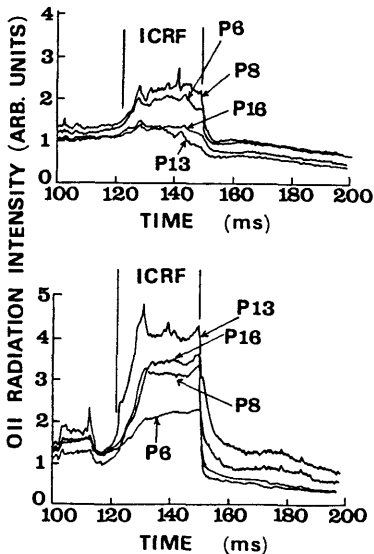


Fig. 5. Toroidal variation of O II with RF heating. P6-P16 indicate location of the detectors. (top) 150 kW with P4 antenna. (bottom) 350 kW with P14 antenna.

Typical results are shown in fig. 5. Fig. 5(a) shows behaviors of OII at the P6, P8, P13 and P16 sections with an RF power of 150 kW launched from the tenna at P4. The radiation increase is clearly seen at P6 and P8, which are closer to the antenna than P16. On the other hand, fig. 5(b) shows that increase in O II is largest at P13, which is just next to the antenna used. These results indicate that the oxygen influx is relatively large in the region close to the antenna. This can be interpreted as follows: (i) oxygen is released from the first wall by charge exchange neutrals. (ii) By ICRF heating, the energy and particle intensity of the neutrals and ions are increased. (iii) Absorption of RF power is toroidally localized in vicinity of the antenna. (iv) Ions are accelerated perpendicularly and a considerable fraction of the accelerated ions is also localized as trapped ions, which results in a relatively high density of energetic ions around the antenna region.

In the case of using the graphite limiter, the limiter can be another important source of oxygen. Different from the case with the SUS limiter, the intensity of O II was not small at P16 even though the P4 antenna was used. In fig. 6, typical results obtained with the graphite limiters are shown. As for the OII radiation, the following

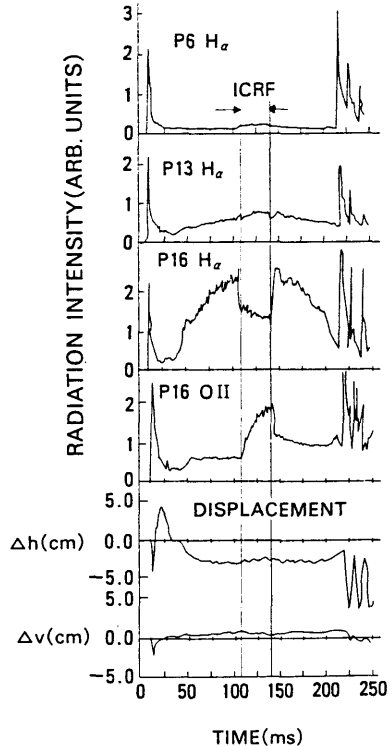


Fig. 6. Behavior of $H_\alpha + D_\alpha$, OII radiations, horizontal placement Δh and vertical displacement Δv . The RF power 220 kW with P4. The detector at P16 looks directly at the limiter at P17. The detector at P6 looks at 14–15 cm distance from the limiter at P7.

ing points are remarkable: (i) The increase in O II radiation is large at a toroidal location close to the limiter and far from the antenna. (ii) The rise time of O II with the RF heating is longer than that in the case of using SUS limiters. (iii) The intensity level is higher after the RF power is off than that before injection. These phenomena are not found with the SUS limiters and suggest some chemical processes which release oxygen from the graphite limiter.

In fig. 6, the behaviors of $H_{\alpha} + D_{\alpha}$ radiation are also shown. After initiation of the discharge, the radiation increases significantly at P16 as the plasma column is shifted inward. As the detector at P16 looks directly at the inner limiter surface, this increase shows that strong hydrogen and deuterium recycling takes place there. It can clearly be seen that the radiation decreases during the RF heating. The plasma position is feedback-controlled and does not shift outward. This decrease is presumed to be due to a change of recycling. As is shown in section 3.5, the electron temperature in the scrape-off layer rises during the RF heating and this can be the main reason which reduces the recycling. This causes the increase of the surface density of H and D on the graphite limiter, which results in oxygen and carbon release through chemical processes.

It should be noted that the $H_{\alpha} + D_{\alpha}$ signal at P6 is small in the recycling phase in fig. 6. This is because the line of sight at P6 was not directly on the inner limiter at P7 but more than 10 cm away from the limiter. Here we can see that the $H_{\alpha} + D_{\alpha}$ radiation increases during the RF heating. It has also been observed that $H_{\alpha} + D_{\alpha}$ increases at P13 when the antenna at P14 is used as the RF launcher. During the RF heating the $H_{\alpha} + D_{\alpha}$ radiation usually increases at the location close to the antenna. Here is another mechanism of hydrogen/

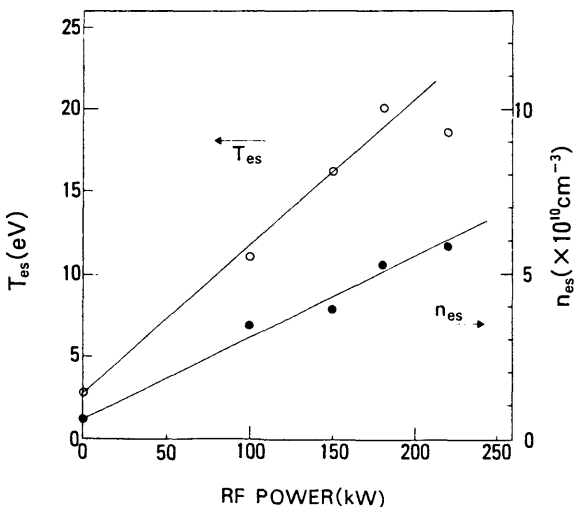


Fig. 7. Electron temperature T_{es} and density n_{es} in the scrape-off layer as a function of the RF power at a distance of 6.5 cm from the plasma edge.

Table 2

Electron density n_{es} and T_{es} in the scrape-off layer with graphite limiters. Parameters of ohmic plasma are shown in table 1. The input power of ICRF is 220 kW

	Ohmic heating		ICRF heating	
	6.5 cm	7.5 cm	6.5 cm	7.5 cm
n_{es} ($\times 10^{10} \text{ cm}^{-3}$)	0.54	0.23	7.8	1.9
T_{es} (eV)	9.2	6.4	19.2	11.8

deuterium recycling different from that on the limiter, and it may have a relation to charge-exchange neutrals on the high energy component generated by the RF heating.

3.5. Electron density and temperature in the scrape-off layer

Plasma parameters in the scrape-off layer are important because they may have close relations to impurity behaviors. Electron density n_{es} and temperature T_{es} in the scrape-off layer were measured as a function of RF power. The results are shown in fig. 7. The probe was located at 27 cm from the axis of the vessel. The center of the plasma-current was at $R = 91$ cm and the minor radius of the plasma was 22.5 cm. Thus, the probe was located at $r = 6.5$ from the plasma edge.

In table 2, typical values of n_{es} and T_{es} are shown. In the ohmic heating phase, n_{es} at $r = 6.5$ cm was $5.4 \times 10^9 \text{ cm}^{-3}$ for the plasma densities $\bar{n}_e = 2.5 \times 10^{13} \text{ cm}^{-3}$. The density at $r = 7.5$ cm was $2.3 \times 10^9 \text{ cm}^{-3}$. If the density decay can be assumed to be exponential in the scrape-off layer, the density at the plasma edge is $1.4 \times 10^{12} \text{ cm}^{-3}$ and the e-folding length is 1.2 cm. During the ICRF heating, the gradient of electron density in the scrape-off layer increases (see table 2). As is mentioned in section 3.3, the increase of the density is partly due to oxygen contamination. The relative increase in T_{es} with RF heating is of great importance because it is possibly one of the causes of the reduction of hydrogen recycling of the limiter and of the impurity increase during the RF heating.

4. Conclusions

- (1) Limiters are the major sources of metallic and carbon impurities both in the ohmic heating and the RF heating. The radiation from impurity ions originates from the limiter surface increases strongly with injected RF power. The plasma behavior was affected by impurities released from the stainless steel limiter.
- (2) Faraday shield of the ICRF antenna is less important as an impurity source than the limiter.
- (3) Using graphite limiters, contamination of the plasma

with metal impurities was significantly reduced, which resulted in an improvement of the parameters in ohmically heated plasmas. However, the increase of oxygen impurity during RF heating was so large that it limited the maximum RF power which could be delivered without disruption. There is an indication that the graphite limiter is the source of oxygen impurities during the RF heating.

- (4) With the stainless steel limiter, an increase of OII radiation by RF heating is large in the vicinity of the antenna. This may be due to a local increase of the flux of energetic charge-exchange neutrals.
- (4) It has been found that the $H_{\alpha} + D_{\alpha}$ radiation at the main limiter decreases with RF heating. This is probably due to a change in recycling at the limiter surface. The main reason for the change in recycling may be the observed increase of the electron temperature during the RF heating. This has probably a close relation to the oxygen-impurity on the graphite limiters.

Acknowledgments

The authors are indebted to Messrs. S. Ishiguro and M. Mugishima for their assistance with the JIPP T-IIU

operation. The authors are also grateful to Professor A. Miyahara and Dr K. Akaiishi for their stimulating discussions.

References

- [1] T. Amano et al., in: Plasma Physics and Controlled Nuclear Fusion Research, Proc. 9th Intern. Conf. Baltimore, 1982, Vol. I (IAEA, Vienna, 1983) p. 219.
- [2] D. Hwang et al., in: Plasma Physics and Controlled Nuclear Fusion Research, Proc. 9th Intern. Conf. Baltimore, 1982, Vol. I (IAEA, Vienna, 1983) p. 3.
- [3] H. Kimura et al., in: Plasma Physics and Controlled Nuclear Fusion Research, Proc. 8th Intern. Conf. Brussels, 1980, Vol. II (IAEA, Vienna, 1981) p. 105.
- [4] Equipe TFR, in: Plasma Physics and Controlled Nuclear Fusion Research, Proc. 8th Intern. Conf. Brussels, 1980, Vol. II (IAEA, Vienna, 1981) p. 75.
- [5] S. Suckewer et al., Nucl. Fusion 21 (1981) 981.
- [6] R. Behn et al., Plasma Physics and Controlled Fusion 26 (1984) 173.
- [7] J. Hosea et al., Proc. 4th Intern. Symp. on Heating in Toroidal Plasmas, Rome, 1984, to be published in: Heating in Toroidal Plasmas, Commission of the European Communities, Brussels.

Effect of *In Situ* Carbon Coating on ICRF-Heated Tokamak Plasmas Relating to Radiation Loss by Iron-Impurities in JIPP T-IIU

Nobuaki NODA,* Yuichi OGAWA, Kuniaki MASAI, Isamu OGAWA,
Ritoku ANDO, Satoru HIROKURA, Eiji KAKO, Yoshiyuki TANIGUCHI,
Ryuichi AKIYAMA, Yoshiaki KAWASUMI, Kazuo KAWAHATA, Kazuo TOI,
Tetsuo WATARI, Shugo TANAHASHI, Keisuke MATSUOKA and Yasuji HAMADA

Institute of Plasma Physics, Nagoya University, Nagoya 464

(Received March 11, 1986; accepted for publication April 26, 1986)

The effect of the C-coating has been demonstrated for tokamak plasmas with high power heating. *In situ* carbon coating has been made with a glow discharge in a methane/hydrogen mixture gas. Without C-coating, iron contamination has been so severe in megawatts of ICRF heating that the total radiation loss exceeds the rf-heating power, and the electron temperature, after once heating up, then decreases continuously during the latter half of 55 ms rf pulse. With C-coating, the radiation loss is reduced to be one fifth of the rf power and the electron temperature T_e becomes stationary at the end of the rf pulse. As a result of this change in T_e , the total stored energy increases more than the one without C-coating.

§1. Introduction

Carbon coating is a promising method to avoid metal impurity contamination for high temperature plasmas in fusion experimental devices. Using this method, we can make a thin carbon film which covers all the in-vessel components, such as limiters, rf antennas, liners and the inner surface of the vacuum vessel itself. Thickness of the film is expected to be several thousand angstroms. In 1979, pioneer work was carried out in JAERI (Japan Atomic Energy Research Institute) on applying the *in situ* carbon coating to DIVA tokamak.¹⁾ Good effects of the C-coating on tokamak discharges were observed in this experiment, however, the work was done just before the shutdown of the DIVA tokamak and no further study on the C-coating was done for 5 years until 1983, mainly because of the lack of effective methods to remove the C-layer once it had formed in the torus vessel. The carbon removal is important in the experimental phase of fusion research in which any variety in wall condition must be investigated. During the interim 5 year period, many improvements were made in discharge cleaning techniques, in which carbon on the inner surface of the vessel can be efficiently removed.²⁻⁵⁾ Based on development of the carbon-removal method, Winter and the Jülich group recently started an intensive study on the C-coating of TEXTOR tokamak.^{6,7)} It has been reported that the C-coating has favorable effects on tokamak discharge in TEXTOR including suppression of the metal-impurity contamination.^{8,9)} However, total radiation loss has not yet been measured and evaluated in TEXTOR and no careful study has been made on the radiation loss and its effect on the energy balance of ICRF heated plasmas. In JIPP T-IIU, radiation loss has been a serious problem of ICRF heating with megawatt level power.¹⁰⁾ Although 1.6 MW rf power was delivered to the plasma without disruption, the radiation loss ex-

ceeded the rf power at the end of the rf pulse of 55 ms, and the electron temperature, after once heating up, decreased continuously during the latter half of the rf pulse. The *in situ* carbon coating was applied to JIPP T-IIU to solve this problem. Typical experimental results are presented in this paper.

§2. Experiment

The vacuum vessel of JIPP T-IIU is made of stainless steel SUS 304 and all of the limiters are made of graphite. Six ICRF antennas are installed on the high-field side of the torus vessel and their Faraday shields are all made of stainless steel. Minor radius of the main limiter is 24.5 cm and that of the Faraday shield is 25.6 cm. The ICRF heating has been applied to H/D plasmas with H-minority concentration of around 15%. Toroidal field on the axis is 2.95 T and the frequency of the rf is 40 MHz.

The carbon coating was carried out with a glow discharge in a methane/hydrogen mixture gas. A helical electrode is inserted into the torus as an anode. The torus vessel is grounded and acts as a cathode. The glow discharge is triggered by 10 MHz/1 kW rf power and sustained by DC voltage of 400 V between the anode and the vessel. The vessel is not heated up but is left at room temperature during the coating procedure. Methane ions in the plasma are accelerated in the cathode sheath, hit the surfaces of the wall, limiters and antennas and form carbon films on them. Total pressure of CH₄/H₂ mixture is 4×10^{-3} mbar and the ratio of CH₄:H₂ is 1:4. The working gas is introduced through a single gas feed into the torus. Typical carbonization time is 4 hours. According to nuclear reaction analysis of the samples exposed to the glow discharge, the thickness of the carbon films is 300–900 Å and toroidal uniformity of the thickness is sufficiently good.* There is a little problem of density control with the carbonized wall, that is, hydrogen recycling rate is so large that it is difficult to obtain low density

*Present address: Plasma Physics Laboratory, Kyoto University, Gokasho, Uji 611.

*Private communications with Susumu Amemiya in Department of Nuclear Engineering, Nagoya University, Nagoya 464.

plasma of less than $5 \times 10^{13} \text{ cm}^{-3}$ of line-averaged electron density. It is worth noting that the carbon-coating process is carried out at room temperature. We have not met any problem so far due to the wall temperature being not heated.

§3. Results and Discussion

In Fig. 1, typical time behavior of plasma parameters is plotted. Plasma current I_p and line-averaged electron density \bar{n}_e are controlled to have the same waveform with and without C-coating. ICRF power of around 1.0 MW is applied from 110 ms to 165 ms in both cases. The density increase due to the rf heating is also indicated in the figure. A marked difference can be seen in the behavior of the total radiation power P_{rad} measured by a bolometer without collimation and on the behavior of the central electron temperature T_e measured by electron cyclotron emission. Without C-coating, the radiation P_{rad} increases during the rf pulse, reaches a level larger than the rf power and is not saturated during the rf pulse. The electron temperature first rises by the rf heating but then decreases continuously in the latter half of the rf pulse. Loop voltage V_L rises toward the end of the pulse due to the reduction of T_e and the increase in the effective ionic charge of the plasma. With C-coating, the radiation P_{rad} is considerably low and becomes saturated in the later phase of the heating. The electron temperature reaches to an equilibrium state of around 1.3 keV at the end of the rf pulse; this is almost the same as the value of ion

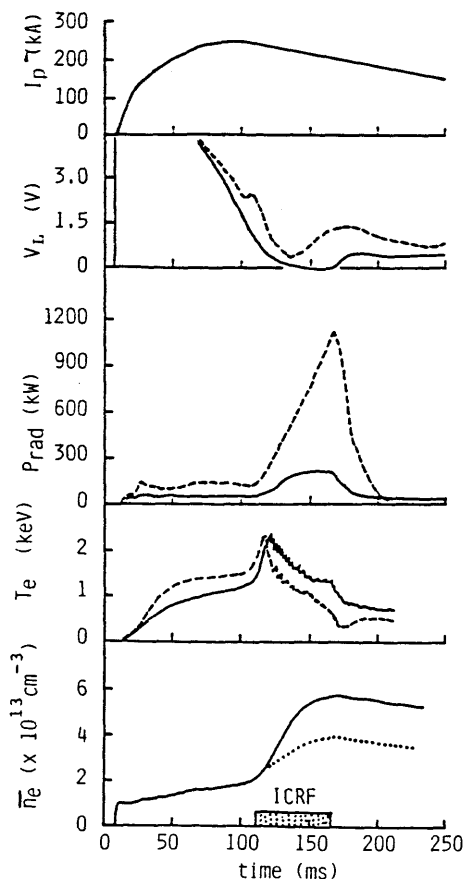


Fig. 1. Time behavior of plasma parameters. Broken lines are those without C-coating and solid lines are with C-coating. Behavior of plasma current and electron density is the same with and without C-coating. Dotted line in \bar{n}_e shows the density without ICRF heating.

temperature. In this C-coated case, the decrease in T_e observed in the middle phase of the heating is mainly due to the density rise, which causes a large energy flow from electrons to ions.

The total radiation loss P_{rad} is plotted in Fig. 2 as a function of the rf power P_{rf} injected into the torus. The line-averaged density is from $4-6 \times 10^{13} \text{ cm}^{-3}$ without C-coating and the scattering of the data in Fig. 2 is mainly due to the difference in the density. Here, one can see that the radiation loss is suppressed by the C-coating to levels of 1/4-1/5 the rf power. According to an observation of the spatial radiation profile by a collimated bolometer array, the decreasing rate of the radiation-power density is the largest at the central region of the plasma, $\sim 1/20$. By spectroscopic measurement, the dominant radiation loss is attributed to iron impurities without C-coating. Relative changes in iron impurity radiations are summarized in Table I. These are all derived from maximum values of each radiation with the ICRF heating of $\sim 1.0 \text{ MW}$. With C-coating, decrease in the intensity of Fe XIX-Fe XXIV is 1/16-1/30, which is well correlated to the change in central radiation intensity obtained by the bolometer array. Intensity of Fe X-Fe XIII also decreases to 1/20 of the intensity without C-coating. These radiations probably make the dominant contribution to the total radiation loss without C-coating. Their reduction rate is larger than the reduction rate of P_{rad} , which indicates that, with C-coating, the main radiation loss is no longer attributable to iron impurities but to low Z impurities. Intensity of CV is 1.6 times larger with C-coating than the intensity without C-coating, which suggests that the increase in carbon im-

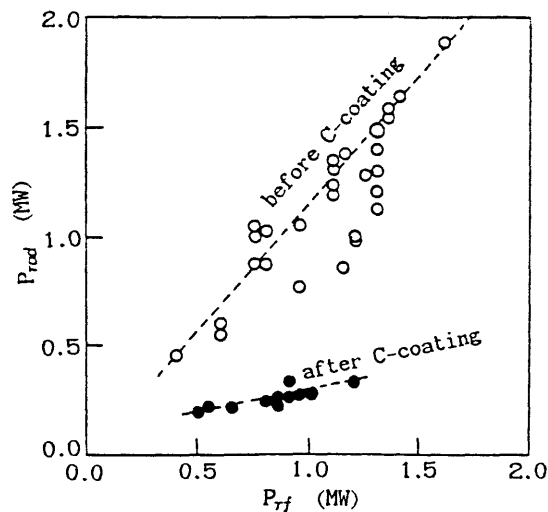


Fig. 2. Total radiation power as a function of the rf power.

Table I. Iron-radiation intensities with C-coating relative to those without C-coating.

line	(wavelength)	intensity
Fe X	(175 Å)	0.054
Fe XIII	(204 Å)	0.037
Fe XVI	(335 Å)	0.013
Fe XIX	(108 Å)	<0.082
Fe XXII	(117 Å)	0.056
Fe XXII	(114 Å)	0.061
Fe XXIV	(192 Å)	0.033

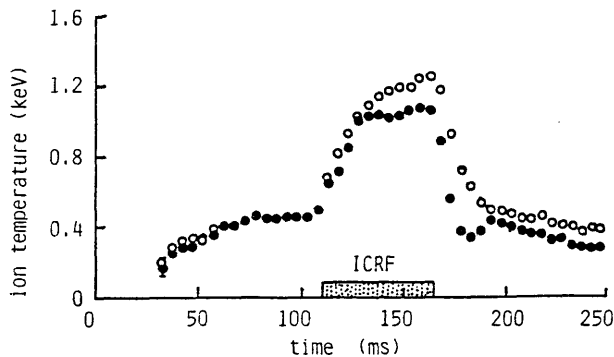


Fig. 3. Ion temperature estimated from charge exchange neutral analysis. Solid circles: without C-coating, open circles: with C-coating.

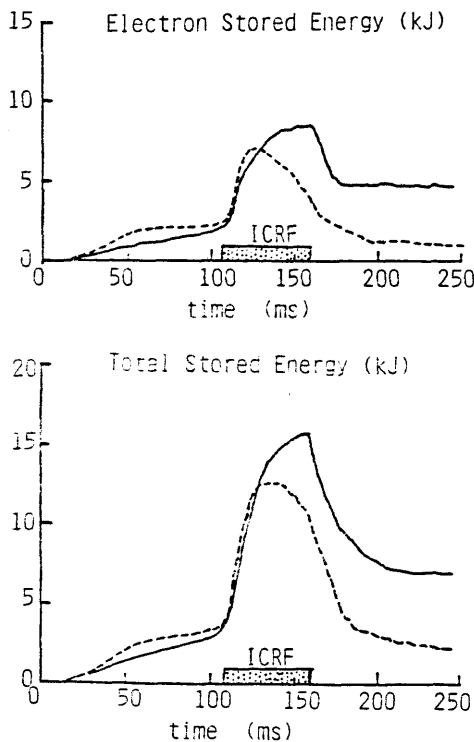


Fig. 4. Electron and total stored energy. Dashed line: without C-coating, solid line: with C-coating.

purity due to the carbonization is not significant. However, more systematic investigation will be needed to evaluate the effect of carbon impurity with the C-coating.

Figure 3 shows the time evolution of ion temperature T_i by charge-exchange neutral analysis. This is determined by the energy spectra from 1500 to 5000 eV. The absolute values of the central ion temperature may be underestimated here in this high n_e range. Although a small difference can be seen between two sets of the T_i data in this figure, relative change of T_i with and without C-coating is not clear in general. At least we can say that the ion-heating efficiency and confinement is not deteriorated by the C-coating.

Total and electron stored energy are estimated from a radial temperature profile measured by polychromator of the electron cyclotron radiation; the results are shown in Fig. 4. Profiles of the density and the ion temperature are assumed to be parabolic. At 160 ms, just before the end of heating, the total energy W_{tot} is 11 kJ without C-

coating and 15 kJ with C-coating. An improvement in global energy balance has been achieved by the C-coating. Using the values of P_{rad} in Fig. 1 and the time derivative of W_{tot} in Fig. 4, we obtain 660 kW as the power loss through conduction and convection without C-coating and 860 kW with C-coating. These both correspond to 17 ms of the energy confinement time with conduction/convection loss only. This suggests that the energy loss due to diffusion processes is not much different in the cases with and without C-coating.

§4. Conclusion

It has been demonstrated that *in situ* carbon coating is very effective to suppress metal-impurity contamination and radiation. The iron-impurity radiation is reduced by one order of magnitude and the total radiation loss is reduced to one fifth of the rf power by the C-coating, which results in sustaining of electron temperature and an increase in stored energy with megawatts of ICRF heating. Heating efficiency and conduction/convection loss are not significantly changed by the C-coating.

Acknowledgements

The first author is grateful to Dr. J. Winter in Kernforschungsanlage Jülich GmbH for generous communication on his experiences with C-coating in TEXTOR. The authors would like to thank Messrs S. Amemiya and Y. Hori for their work on surface analysis. They are also grateful to Professors A. Mohri and A. Miyahara for their stimulating discussions.

References

- 1) S. Sengoku, T. Matsuda, H. Matsumoto, T. Abe, H. Ohtsuka, T. Arai, K. Ohasa, S. Yamamoto, K. Odajima, H. Kimura, S. Kasai, K. Kumagai, K. Takahashi and Y. Shimomura: *J. Nucl. Mater.* **93 & 94** (1980) 178.
- 2) H. F. Dylla: *J. Nucl. Mater.* **93 & 94** (1980) 61.
- 3) Y. Sakamoto, Y. Ishibe, S. Ishii, K. Okazaki, H. Oyama, K. Yano, N. Noda, K. Kawahata, Y. Kawasumi and S. Tanahashi: *J. Nucl. Mater.* **111 & 112** (1982) 485.
- 4) N. Noda, S. Hirokura, Y. Taniguchi and S. Tanahashi: *J. Vac. Sci. Technol.* **A1** (1983) 1430.
- 5) F. Waelbroeck, J. Winter and P. Wienhold: *J. Vac. Sci. Technol.* **A2** (1984) 1521.
- 6) J. Winter, F. Waelbroeck, P. Wienhold, H. G. Esser, L. Könen, M. Braun, B. Emmoth, H. E. Säterblom: *J. Nucl. Mater.* **128 & 129** (1984) 841.
- 7) K. H. Besocke, G. Flentje, J. Winter, P. Wienhold and H. G. Esser: *J. Nucl. Mater.* **136** (1985) 124.
- 8) A. Pospiesznyk, H. L. Bay, P. Bogen, D. Rusbüldt, U. Samm, J. Schlüter, B. Schweer: *Proc. 12th Europ. Conf. on Controlled Fusion and Plasma Physics, Budapest, 1985* (European Physical Society, Budapest, 1985), Vol. 9F, Part II, p. 523.
- 9) J. Schlüter, E. Graffmann, L. Könen, F. Waelbroeck, G. Waidmann, J. Winter and the TEXTOR Team: *Proc. 12th Europ. Conf. Controlled Fusion and Plasma Physics Budapest, 1985* (European Physical Society, Budapest, 1985), Vol. 9F, Part II, p. 627.
- 10) J. Fujita, T. Watari, K. Toi, T. Amano, R. Ando, Y. Hamada, S. Hirokura, E. Kako, K. Kawahata, Y. Kawasumi, S. Kitagawa, K. Masai, K. Matsuoka, K. Matsuura, Y. Mizuno, S. Morita, H. Naitou, A. Nishizawa, N. Noda, I. Ogawa, Y. Ogawa, K. Ohkubo, M. Sasao, K. Sato, K. N. Sato, S. Tanahashi, Y. Taniguchi, T. Tetsuka, K. Yamazaki: *Proc. 12th Europ. Conf. Controlled Fusion and Plasma Physics, Budapest, 1985* (European Physical Society, Budapest, 1985), Vol. 9F, Part II, p. 702.